IPP-Report

Max-Planck-Institut
für Plasmaphysik

Stefan Kapser

Deuterium Permeation Through Tungsten Driven by Plasma-Based Low-Energy Ion Implantation

IPP 2019-01
Januar 2019

Technische Universität München
Fakultät für Physik

Deuterium Permeation Through Tungsten Driven by Plasma-Based Low-Energy Ion Implantation

Stefan Kapser

Vollständiger Abdruck der von der Fakultät für Physik der Technischen Universität München zur Erlangung des akademischen Grades eines

Doktors der Naturwissenschaften (Dr. rer. nat.)

genehmigten Dissertation.

Vorsitzende:	Prof. Dr. Nora Brambilla
Prüfende/-r der Dissertation:	1. Prof. Dr. Rudolf Neu
	2. Prof. Dr. Johannes Barth

Die Dissertation wurde am 03.07.2018 bei der Technischen Universität München eingereicht und durch die Fakultät für Physik am 03.12.2018 angenommen.

Kurzfassung

Die von plasmabasierter Ionenimplantation mit niedrigen einfallenden Energien getriebene Permeation von Deuterium durch Wolfram wurde untersucht. Dazu wurde eine Methode entwickelt, die es ermöglicht die Permeation bei der Plasmaexposition in einer Plasmaquelle, die typischerweise für Experimente zur Deuteriumrückhaltung genutzt wird, zu messen. Die Messergebnisse wurden verwendet, um den Einfluss der Entstehung von Schäden unter der Oberfläche auf den Permeationsfluss zu untersuchen.

Für die Permeationsmessungen wurde eine Sammelschicht aus entweder Zirconium, Titan oder Erbium auf einer Seite der Wolframproben abgeschieden. Anschließend wurde die andere Seite der Proben Deuteriumplasma ausgesetzt. Deuterium das während der Plasmaexposition durch das Wolfram permeierte wurde in der Sammelschicht akkumuliert. Die Deuteriummenge, die sich nach der Plasmaexposition in der Sammelschicht befand wurde mit ex-situ Ionenstrahlanalyse bestimmt. Ein Abdeckschichtsystem auf der Sammelschicht verhinderte eine direkte Aufnahme von Deuterium in die Sammelschicht aus dem Hintergrunddeuteriumgas, das während der Deuteriumplasmaexposition vorhanden war. Es ermöglichte des Weiteren eine Unterscheidung von Deuterium in der Sammelschicht und an der Oberfläche des Abdeckschichtsystems in der Ionenstrahlanalyse.

Die Methode wurde validiert und angewandt, um die Deuteriumpermeation durch etwa 25 µm dicke Wolframfolien bei 300 K und 450 K zu messen, die von Deuteriumplasmaexposition mit einfallenden Energien im eV-Bereich hervorgerufen wurde. Der resultierende gemessene stationäre Deuteriumpermeationsfluss war für beide Expositionstemperaturen im Rahmen der Datenstreuung ununterscheidbar und hatte einen Wert von rund 1.7×10^{14} D/(m^2 s). Auch die Messung noch kleinerer Permeationsflüsse erscheint mit der dargestellten Methode im Prinzip möglich.

Ein Vorteil der präsentierten Methode ist, dass sie die Messung der permeierten Deuteriummenge räumlich und zeitlich von der Plasmaexposition entkoppelt. Dadurch können bestehende Plasmaanlagen, die sonst für Deuteriumrückhaltungsversuche genutzt werden, auch für plasmagetriebene Permeationsexperimente verwendet werden, ohne einen komplexen Aufbau für in-situ Permeationsmessungen an die Anlagen anbauen zu müssen.

Die Ergebnisse der Permeationsmessungen wurden mit Ergebnissen von Mikrostrukturanalysen und Messungen der Deuteriumrückhaltung kombiniert. Dadurch konnte der Einfluss von unter der plasmaexponierten Oberfläche entstehenden Schäden auf die Permeation untersucht werden. Eine erhöhte Deuteriumrückhaltung unter der plasmaexponierten Oberfläche korrelierte mit der Beobachtung von unter der Oberfläche entstehenden Schäden. Sie wurde Fangstellen (englisch: traps) zugeschrieben, die in der Nähe der beobachteten Schäden unter der Oberfläche entstehen.

Sowohl die Entstehung von Schäden unter der Oberfläche als auch die erhöhte Deuteriumrückhaltung wurden nur für 300 K Expositionstemperatur beobachtet. Dennoch war der Permeationsfluss für 300 K und 450 K im Rahmen der experimentellen Datenstreuung

ununterscheidbar. Dies war der Fall obwohl die abgeschätzte obere Grenze für den Verlust von Deuterium aus der Lösungsphase in sich entwickelte Fangstellen in der gleichen Größenordnung lag wie der stationäre Permeationsfluss.

Dieses Phänomen wurde mit eindimensionalen Diffusion-Einfang-Simulationen modelliert, reproduziert und untersucht. Diffusionslimitierte Randbedingungen an der plasmaexponierten und der Permeationsseite und eine Implantationsverteilung und ein Reflexionskoeffizient, die basierend auf Implantationssimulationen gewählt wurden, ergaben eine gute Übereinstimmung des simulierten stationären Permeationsflusses mit dem experimentell bestimmten Wert. Um den simulierten stationären Permeationsfluss vollständig an den experimentell ermittelten Wert anzupassen war für den besten Satz von Implantationssimulationsparametern nur eine geringfügige Korrektur des Reflexionskoeffizienten notwendig. Das sich entwickelnde Profil von Fangstellen unter der Oberfläche wurde basierend auf Messungen der Deuteriumrückhaltung in die Simulation implementiert. Die Diffusion-Einfang-Simulationen zeigten ferner, dass ein stärkerer Abfall des stationären Permeationsflusses zu erwarten wäre, wenn die Fangstellen tiefer unter der deuteriumplasmaexponierten Wolframoberfläche entstehen würden.

Die maximalen Verhältnisse von gelösten Deuterium- zu Wolframatomen, die während der Deuteriumplasmaexposition bei 300 K und 450 K vorhanden waren, wurden unter Verwendung des gemessenen stationären Permeationsflusses abgeschätzt. Diese Werte werden möglicherweise in künftigen Versuchen nützlich sein Modelle zu entwickeln und zu testen, die die Entwicklung von Schäden und zugehörigen Fangstellen unter der Oberfläche von Wolfram auf Grund von Deuteriumplasmaexposition beschreiben. Ein detaillierter Vergleich der experimentell bestimmten und simulierten Deuteriumrückhaltung nach der Plasmaexposition deutete auf Grenzen des aktuellen Diffusion-Einfang-Modells hin, welche Hinweise für künftige Modellverbesserungen geben können.

Die in dieser Arbeit präsentierten Ergebnisse tragen zu einem verbesserten Verständnis des Einflusses der Entstehung von Schäden unter der Oberfläche von Wolfram durch Deuteriumplasmaexposition auf die Deuteriumpermeation bei und bilden eine solide Grundlage für weitere Untersuchungen zur plasmagetriebenen Permeation von Deuterium durch Wolfram.

Abstract

The permeation of deuterium through tungsten driven by plasma-based ion implantation with low incident energies has been investigated. For this purpose, a method was developed that enables to measure the permeation during plasma exposure in a plasma source typically used for deuterium retention experiments. The measurement results were used to investigate the influence of sub-surface damage evolution on the permeation flux.

For the permeation measurements, a getter layer consisting of either zirconium, titanium or erbium was deposited on one side of the tungsten samples. Subsequently, the opposite side of the samples was exposed to deuterium plasma. Deuterium that permeated through the tungsten during the plasma exposure was accumulated in the getter layer. The deuterium amount present in the getter layer after plasma exposure was determined by ex-situ ion-beam analysis. A cover layer system on top of the getter layer prevented direct uptake of deuterium into the getter layer from the background deuterium

gas present during deuterium-plasma exposure. Furthermore, it enabled a distinction of deuterium in the getter layer and at the surface of the cover layer system in the ion-beam analysis.

The method was validated and applied to measure the deuterium permeation through about 25 µm thick tungsten foils at 300 K and 450 K that was caused by deuterium-plasma exposure with incident energies in the eV-range. The resulting measured steady-state deuterium permeation flux was for both exposure temperatures indistinguishable within the experimental data scatter and had a value of about 1.7×10^{14} D/(m^2 s). Also the measurement of even lower permeation fluxes appears in principle possible with the presented method.

An advantage of the presented method is that it decouples the measurement of the permeated deuterium amount spatially and temporally from the plasma exposure. Thus, existing plasma devices typically used for deuterium-retention experiments can also be used for plasma-driven permeation experiments without the necessity to attach a complex in-situ permeation measurement setup to the devices.

The results of the permeation measurements were combined with the results of microstructural analyses and measurements of the deuterium retention. Thereby, the influence of sub-surface damage evolution on the permeation flux could be investigated. An increased deuterium retention below the plasma-exposed surface was correlated with the observation of sub-surface damage evolution. It was ascribed to traps evolving in the vicinity of the observed sub-surface damage.

Sub-surface damage evolution as well as increased deuterium retention were only observed for 300 K exposure temperature. Still, the permeation flux at 300 K and 450 K was indistinguishable within the experimental data scatter. This was the case although the estimated upper limit of deuterium loss from the solute phase to evolving traps was of the same order of magnitude as the steady-state permeation flux.

This phenomenon was modeled, reproduced and investigated with one-dimensional diffusion-trapping simulations. Diffusion-limited boundary conditions at plasma-exposed and permeation side and an implantation distribution and reflection yield chosen based on implantation simulations resulted in a good agreement of the simulated steady-state permeation flux with the experimentally determined value. To fully match the simulated to the experimental steady-state permeation flux, only a minor correction of the reflection yield was necessary for the best set of implantation-simulation input parameters. The evolving sub-surface trap profile was implemented based on deuterium retention measurements. The diffusion-trapping simulations also showed that a stronger decrease of the steady-state permeation flux would have to be expected for trap evolution deeper below the deuterium-plasma-exposed tungsten surface.

The maximum ratios of solute-deuterium to tungsten atoms present during deuterium-plasma exposure at 300 K and at 450 K were estimated using the measured steady-state permeation flux. These values may be useful in future attempts to develop and test models that describe damage and associated trap evolution below the surface of tungsten caused by deuterium-plasma exposure. A detailed comparison of the experimentally determined and simulated deuterium retention after plasma exposure indicated limitations of the current diffusion-trapping model, which can give indications for future model improvements.

The results presented in this thesis contribute to an improved understanding of the influence of sub-surface damage evolution in tungsten due to deuterium-plasma exposure on deuterium permeation and form a solid basis for further investigations of the plasma-driven permeation of deuterium through tungsten.

Contents

1. Introduction

An expected growing demand for energy [1] and, at the same time, desired reduction of climate-damaging greenhouse gas emissions [2], such as CO_2 emissions [3], make further development of existing energy sources, but also the development of new energy sources necessary. Taking the sun as a role model [4], nuclear fusion is investigated as a promising future energy source. There, nuclei of light elements undergo nuclear fusion reactions in a hot plasma and thus release energy [4]. High temperatures in the plasma are necessary to give the reactants sufficient kinetic energy to overcome the electrostatic repulsion between them [5]. Including the construction and decommissioning phases, nuclear fusion is associated with only very low CO_2 emissions over the entire power-plant life cycle [3].

A nuclear fusion reaction of the hydrogen isotopes deuterium and tritium is considered to be one of the most promising reactions for future nuclear fusion power plants because it possesses a large reaction cross-section [5, 6]. In this process, deuterium (D) and tritium (T) form helium-4 (^{4}He) and a neutron (n) by the reaction

$$\mathrm{D} + \mathrm{T} \rightarrow {}^4\mathrm{He} + \mathrm{n}, \tag{1.1}$$

in which an energy of 17.6 MeV is released. 14 MeV of this released energy are converted into kinetic energy of the emitted neutron (compare, e.g., [5, 6]).

In order to make nuclear fusion usable as an energy source on earth, two fundamental differences to the energy production in the sun need to be addressed in addition to a large number of other challenges. First, the gravitational confinement of the plasma present in the sun [4] can, of course, not be utilized on earth. Instead, confining the plasma with magnetic fields is currently considered to be one of the most promising approaches [5, 6]. Second, a fusion reactor on earth will need some kind of vessel [4] and thus a wall, which is capable to withstand the extreme conditions present at the edge of a burning fusion plasma [7, 8].

The hot plasma and the fusion reactions lead to a flux of hydrogen isotopes, helium and neutrons to the wall of a magnetic-confinement nuclear fusion reactor [9, 10]. Also, additional impurities in the plasma, which result from erosion of wall material or intentional impurity seeding, contribute to the particle flux to the wall [11, 12].

To ensure a safe operation, but also to prevent fuel loss, hydrogen isotope retention in and permeation through the wall must be minimized. This is especially true with respect to the rare and radioactive tritium, which is at the same time a precious resource and a major safety concern [9].

Over the past years, tungsten has emerged as one of the most promising candidates as plasma-facing material in future fusion reactors [13–16]. This is due to a number of favorable properties, such as a low sputtering yield, high melting point and low hydrogen solubility [9]. Consequently, tungsten is used as a plasma-facing material in several fusion

experiments such as ASDEX Upgrade (AUG) [16] and the Joint European Torus (JET) [17]. It is also foreseen for use in the International Thermonuclear Experimental Reactor (ITER) [18] and considered one of the most promising candidates as plasma-facing material in a future demonstration nuclear fusion power plant [19], which is typically referred to as DEMO. Knowledge about the interaction of hydrogen-isotope plasmas with tungsten is thus of crucial importance for the design of future nuclear fusion experiments and reactors.

Numerous complex effects occur simultaneously at the wall of such devices. These include effects of incident hydrogen isotopes, helium and different impurities as well as neutrons. The interaction of incident hydrogen-isotope ions with tungsten is, therefore, frequently investigated in simpler laboratory experiments, which address different aspects of this interaction. Based on these laboratory experiments, theoretical models are developed, which can describe the observations made in the laboratory experiments and finally be used to predict the situation in a future fusion reactor.

Because of the hazards associated with the handling of tritium, such laboratory experiments are typically performed with deuterium (e.g. [20–35]). In contrast to the most abundant hydrogen isotope protium [36], deuterium has the advantage that it is one of the reactants in the fusion reaction usually foreseen for future nuclear fusion power plants (Equation 1.1) and that it additionally occurs in the environment in significantly smaller concentrations than protium [36]. This enables measurements with a much lower background level.

Deuterium retention and diffusion in as well as permeation through tungsten can be heavily influenced by material defects (compare, e.g., [9, 21, 37–39] and references therein). Due to the low solubility of hydrogen in tungsten [40], the deuterium retention after plasma exposure is typically dominated by immobile deuterium trapped at material defects. The interstitially dissolved solute deuterium, which is responsible for diffusion and permeation during the deuterium-plasma exposure, usually leaves the sample quickly after the plasma exposure is terminated [9, 41].

The situation during deuterium-plasma exposure is complicated by the fact that deuterium from the plasma does not only interact with existing defects, but can also lead to a modification of the defect structure in tungsten [9, 35, 42]. This can result in a complex interplay [38] of, on the one hand, defect evolution due to deuterium in the tungsten lattice and, on the other hand, the influence of defects on the deuterium retention, diffusion and permeation. Although a conclusive physical model for defect evolution in tungsten exposed to deuterium plasma has not yet been developed, it is generally assumed that the solute deuterium concentration plays a crucial role not only in diffusion and permeation, but also in defect evolution [39]. This makes information about the solute even more valuable.

Unfortunately, studies in the literature usually do not report on all the effects associated with deuterium implantation into tungsten. In fact, they typically report only either on the deuterium retention after deuterium implantation (e.g. [20, 24, 31, 32]), on microstructural modifications due to the implantation (e.g. [28, 42]), on deuterium permeation (e.g. [23, 26, 30]) or on a combination of two of these effects (e.g. [22, 25, 29, 33–35, 43–45]). The subsequent analysis and interpretation of the experiments is in these cases additionally complicated by an important piece of information being not available. If only the

deuterium retained after implantation, typically trapped at defects, is measured, information about the solute deuterium and the tungsten microstructure is missing. Investigations of only the microstructural modifications generated by deuterium ion implantation completely lack information about the whereabouts of the deuterium. Measurements of the permeation flux alone yield no information about microstructural modifications, which can in general have a significant influence on the permeation flux, and offer no direct access to trapped deuterium. Limited, indirect conclusions about trapped deuterium can, however, possibly be drawn based on the time evolution of the permeation flux, as it was done, e.g., in [23, 30]. If only retention and microstructural evolution are measured, no access to the important solute deuterium is provided. For this case, the appendix in [22] describes nicely how the maximum solute deuterium concentration can at least be roughly estimated based on simulations and literature data. A combination of retention and permeation measurements yields quite complete information about the whereabouts of the implanted deuterium, but lacks information about possible microstructural modifications that can affect deuterium retention and permeation. Finally, measurements of only permeation and microstructural modifications still lack direct information about the retained deuterium trapped at defects.

The current state of knowledge about the effects associated with the implantation of deuterium into tungsten has been gained mainly based on such laboratory experiments, even though they typically did not include investigations of all three of the above mentioned effects, i.e. deuterium retention, permeation and microstructural modification. Still, investigations that address all these issues in a single set of experiments on well characterized samples appear to be the best way to investigate the complex interplay resulting from all these contributions. The combination of information about solute and trapped deuterium, as it can be derived from permeation and retention measurements, with a microstructural analysis yields data that can in particular also be valuable for the development of a physical model that describes defect evolution due to the presence of deuterium in the tungsten lattice.

The present thesis attempts to contribute to an improved understanding of the interplay of the above-mentioned effects during the plasma-based low-energy ion implantation of deuterium into tungsten. It reports on deuterium retention and permeation measurements as well as microstructural analyses performed on about 25 µm thick tungsten foil samples exposed to low-energy deuterium plasma at 300 K and 450 K.

After a short description of the most important fundamental theoretical concepts relevant for the understanding of subsequent chapters in Chapter 2, the materials and methods used for the experiments are presented in Chapter 3. A method developed to measure plasma-driven deuterium permeation through tungsten in existing plasma devices typically used for retention experiments, without the need for device modification, is presented in Chapter 4, together with measurement results for the permeated deuterium amount over time. The results of the permeation measurements are combined with results from deuterium-retention measurements and microstructural analyses in Chapter 5. Together, they are used to study the influence of sub-surface damage evolution on the permeation. The sub-surface damage evolution represents a modification of the tungsten's defect structure and leads to increased deuterium retention in the tungsten. Also, estimates for the maximum ratios of solute-deuterium to tungsten atoms present in the tungsten samples

during the deuterium-plasma exposure in the presence and absence of sub-surface damage evolution are reported in Chapter 5. They were determined based on the measured steady-state permeation flux. Subsequently, simulations that describe and elucidate the experimental observations are presented in Chapter 6. Besides reporting experimental or simulation results, Chapters 4, 5 and 6 also include a discussion of these results. Additionally, conclusions are drawn at the end of each of these chapters. Finally, Chapter 7 summarizes the results of the thesis.

If not stated otherwise, the experiments and simulations presented in this thesis were performed at the Max-Planck-Institut für Plasmaphysik (IPP) in Garching, Germany. A large part of the results presented in this thesis has already previously been published in [46, 47], the first author of which is the author of this thesis.

2. Fundamental theoretical concepts

This chapter gives an overview of important theoretical concepts that are relevant for the understanding of subsequent chapters. Most of the topics have been described in great detail by various authors before and shall only shortly be repeated here. Further details can be found in the references given.

After an introduction to the microstructure of solid metals in Section 2.1, the interaction of incident ions with solids is discussed in Section 2.2. Finally, the interaction of hydrogen isotopes with metals is described in Section 2.3. Although mainly general concepts are presented, the discussion focuses on those topics relevant for the understanding of subsequent chapters and does not attempt to give a full overview of each field.

2.1. The microstructure of tungsten and other metals

Metals in solid state can have a wide variety of microstructural configurations. As described in detail, e.g., in [48–50], the most simple case is a perfect or ideal crystal. In this configuration, the metal consists of a large number of unit cells, which are arranged in a regular pattern. Each of these unit cells incorporates the same number of atoms in the same configuration. The resulting atom lattice has a short- as well as long-range order. Various lattice types with different complexity exist, among them the body centered cubic (bcc) structure. It is also the structure of the stable modification of tungsten [51] and has two atoms per unit cell [52].

In-between regular lattice sites, where the atoms of the lattice are located, other sites, the so-called *interstitial sites*, exist. They are typically named after the structure of the neighboring lattice atoms. Two of the most prominent types of interstitial sites are the *tetrahedral sites* (T sites) and *octahedral sites* (O sites) with 4 and 6 nearest neighbor lattice atoms, respectively [53]. For bcc metals, such as tungsten, the number of interstitial sites per unit cell is 12 for T sites and 6 for O sites. This results in 6 T sites and 3 O sites per lattice atom for the bcc crystal structure [52].

While the ideal single crystal is an important theoretical concept, it is typically not encountered in reality because real metals usually incorporate a large number of material defects, which disturb the regularity of the lattice. As described, e.g., in [48], a first subdivision is typically made between crystalline, polycrystalline and amorphous metals. A real metal single crystal shows comparatively small deviations from the ideal crystal described above, but usually has a number of defects such as those described further below. A polycrystalline material consists of many regions with different crystal orientations, the so-called *grains*. Each of these grains has a crystalline structure, but the crystal orientations of individual grains can be oriented randomly with respect to each other. The grains are separated by so-called grain boundaries. If the order in the material is

reduced further, and the atoms possess no long-range order beyond the nearest neighbors, the metal is typically considered as amorphous.

Within a real single crystal or within the grains of a polycrystalline material, various types of defects with different dimensionality are typically present. As described in detail in [54, 55], point defects are for example vacancies, which means the absence of lattice atoms at certain lattice sites, or interstitials, which are lattice or foreign atoms located at interstitial sites. Line defects are represented by different types of dislocations, while plane defects are, e.g., grain boundaries or stacking faults. Finally, also volume defects, such as voids, can occur [55].

As discussed, e.g., in [56], the microstructure of metals can be modified by annealing. Thus, material defects generated during the production process, e.g. by cold rolling, can, depending on the annealing temperature, be healed out partially. For polycrystalline tungsten, a heat treatment at 1500 K and above is known to lead to a significant modification of the atomic microstructure, resulting in recrystallization and grain growth [57].

In sum, the microstructure of metals can have different degrees of complexity, determined by the type of metal, but also affected by, e.g., the manufacturing process and subsequent heat treatments.

2.2. Ion-solid interactions

The interaction of incident ions (also referred to as projectiles) with solid target materials is relevant for this thesis not only regarding the interaction of incident deuterium ions from a plasma with tungsten, but also for some of the technologies used for sample preparation and analysis that will be described in Chapter 3. The flux of incident ions is characterized by its composition, its incident energy distribution and its flux density, which is the number of ions incident per unit time and area. Integration of the flux density over time yields the fluence, which is also frequently used to compare different experiments.

2.2.1. Nuclear and electronic stopping

As described in detail, e.g., in [58–60], incident ions reaching the target interact with the nuclei of the target material via electrostatic forces. This interaction is repulsive and typically leads to elastic scattering. However, for kinetic energies that are high enough, the repulsion can be overcome, such that nuclear forces between the ion and a target nucleus contribute significantly to the interaction. This can lead to inelastic scattering due to nuclear reactions between the two nuclei [61]. The discussion in this section will focus on the simpler case of elastic scattering, which is relevant for most of the applications presented in this thesis. Since nuclear reactions were, however, used in nuclear reaction analysis, some additional information on this topic will be given in Section 3.7.2, where this analysis method is described.

The elastic scattering of projectiles and target nuclei, discussed, e.g., in [58–60], can be described quite well by classical mechanics in a wide energy range. The momentum and energy transfer in a collision is determined by the interaction potential of projectile and

target nucleus, their relative positions and their velocities. In this interaction, screening of the nuclei by surrounding electrons bound to them typically leads to a modification of the interaction potential of the pure nuclei. It must also be noted that limitations of this classical treatment may occur at very low energies due to quantum mechanical effects [62].

The overall deceleration of the projectiles resulting from elastic scattering with target nuclei is referred to as *nuclear stopping*. It can be described by the nuclear stopping power $\left(\frac{\mathrm{d}E}{\mathrm{d}x}\right)_{\mathrm{nuclear}}$, which is the energy loss per unit length due to nuclear stopping or, if the description shall be made independent of the material density, the nuclear stopping cross-section $\sigma_{\mathrm{nuclear}}$ [58–60]. Due to statistical variations in the interactions, the energy distribution of the projectiles broadens with penetration depth, an effect referred to as nuclear straggling [60].

For certain orientations of the crystal structure, the projectiles can penetrate much deeper into the material than for other orientations, because they have a strongly reduced scattering probability if they are moving parallel to certain crystal plains. This effect is known as channeling [59].

On their way through the metal, moving ions do not only interact with the target nuclei via their possibly shielded interaction potentials, but also with electrons in the conduction and valence band. In contrast to nuclear stopping, this interaction is mainly based on inelastic collisions of projectiles with electrons. It leads to energy loss of the projectiles, which is typically approximated as quasi-continuous. The resulting deceleration of the projectiles is referred to as *electronic stopping* [59, 60, 63].

Different concepts have been developed to describe electronic stopping in metals. Two of the most common approaches used are the ones of Oen and Robinson [64] as well as Lindhard and Scharff [65]. While the Lindhard-Scharff model describes electronic stopping as a continuous non-local energy loss, the Oen-Robinson model takes the electron density around the atom into account and thus attempts to give a description of the local energy loss. In practical calculations and simulations, an equipartition of both models is frequently used [66].

To describe electronic stopping, an electronic stopping power $\left(\frac{\mathrm{d}E}{\mathrm{d}x}\right)_{\mathrm{electronic}}$ and cross-section $\sigma_{\mathrm{electronic}}$ can be defined [59, 60, 63] in analogy to nuclear stopping described above.

Since individual ions do not undergo exactly the same electronic collisions, the electronic stopping power gives only an average description and has an uncertainty due to the statistical nature of the interaction processes. The resulting broadening of the energy distribution of the ions is referred to as electronic loss straggling [60].

2.2.2. Reflection, implantation and sputtering

The path of a projectile in the sample is determined by nuclear and electronic interactions. As described in detail, e.g., in [60], these can cause the projectile to come to rest inside the target (implantation), leave the target again through the implantation surface (reflection) or through another surface (transmission). It is important to note that also target atoms set in motion by recoil interaction with a projectile undergo similar nuclear and electronic collisions, which determine their movement through the sample. These target atoms can again set other target atoms in motion and thus create a *collision cascade*. The target

atoms may come to rest at a different location inside the sample (displacement) or leave the sample (sputtering).

Implantation, displacement and sputtering lead to a modification of the target microstructure and can thus create some of the material defects described in Section 2.1, as discussed in detail, e.g., in [67]. This kinetic defect creation is limited to a depth defined by the collision cascades, which is typically of the order of magnitude of the projectile range.

2.2.3. The binary collision approximation (BCA) and the simulation code SDTrimSP

The interaction of incident ions with matter can be simulated with different kinds of computer models. Two frequently used approaches are simulations using the *binary collision approximation* (BCA) [62] and molecular dynamics (MD) [68], which are both based on classical mechanics. MD calculations take interactions with all surrounding atoms into account, which makes them computationally very expensive [69]. This results in very long calculation times, which make, e.g., parameter studies or the sampling of complex energy distributions, which need to be modeled by many subsequent simulation runs, difficult.

Simulations using the BCA are typically much faster and thus enable extensive parameter studies with complex energy distributions in a reasonable computation time. As described in detail, e.g., in [62], only binary collisions of two particles are taken into consideration within the framework of the BCA, while simultaneous interactions involving more than two particles are neglected. The paths of the collision partners are approximated by their asymptotic trajectories and the simulation is typically performed assuming free atoms, thus neglecting binding to surrounding target atoms. Therefore, the effects of binding need to be taken into account in additional steps in the simulation process, where they are introduced, e.g., via a bulk binding energy, a displacement energy and a surface binding energy, as discussed in detail, e.g., in [70]. The choice of these energies is often not trivial and makes approximations necessary. The surface binding energy is, e.g., frequently approximated based on the heat of sublimation [70]. It is important to note that the surface binding energy, if implemented as a potential step, does not only lead to binding and deceleration of projectiles and target atoms leaving the target, but also to an acceleration of incident projectiles [70].

For the interaction potential in BCA simulations, which is relevant for nuclear interactions, but also for local electronic loss models, such as the Oen-Robinson model, screened Coulomb potentials such as the KrC [71], Molière [72], ZBL [58] or Nakagawa-Yamamura [73] potential are frequently used [74].

A limitation of the validity of the BCA at low energies results from neglecting the interaction with additional target atoms in the collision process. However, this limitation only leads to a gradual loss of validity and does not represent a sudden full breakdown of the concept at a certain energy threshold [62]. The applicability of the BCA at low energies thus needs to be judged individually depending on the situation.

Because moving atoms may never come to rest fully in a simulation, e.g. due to numerical noise, a certain cutoff energy needs to be defined, below which the movement of

the atoms is assumed to have stopped [70]. Obviously, a high cutoff energy can lead to shorter computation times, but may hide important effects at lower energies, if chosen too high.

A well-established computer code for BCA simulations is SDTrimSP [75], which was used in version 5.07 for the simulations of deuterium implantation from a plasma into tungsten presented later in this thesis. As described in detail in [75], SDTrimSP uses a randomized one-dimensional target at a temperature of 0 K. This means that the next collision partner is determined randomly in a so-called Monte Carlo approach, the target is assumed to consist of layers that are infinitely large and homogeneous in the directions parallel to the surface, and thermal motion of the target atoms is neglected. Despite the one-dimensional target structure, the trajectories of projectiles and moving target atoms are followed in three dimensions. SDTrimSP partially compensates the effect of neglecting the influence of surrounding target atoms on the collision process by the concept of so-called weak simultaneous collisions [75].

SDTrimSP simulations can be performed in a static or dynamic mode. While the static approach neglects modifications of the target structure and composition due to the ion bombardment, these effects are taken into account in the dynamic approach. In the static approach, subsequently incident projectiles thus always interact with the same target, while in the dynamic approach, the target is modified over time [75]. The static approach is computationally less expensive and can be used if sputtering and displacement of target atoms are expected to be negligible, e.g. for light projectiles at low incident energies, or have negligible influence on the output quantity of interest. It can yield valuable information mainly about the range distribution and reflection of projectile ions incident on the target and is typically well applicable as long as the target composition is not substantially modified by the incident ions.

2.3. Hydrogen isotopes in tungsten and other metals

The interaction of hydrogen isotopes, in particular deuterium, with metals, in particular tungsten, is central to this thesis. Therefore, the most important concepts of this interaction will be described in this section, not giving a full overview of this intensively studied field, but focusing on the concepts relevant for the understanding of subsequent chapters. The term hydrogen will be used synonymously with the term hydrogen isotopes, while the most abundant hydrogen isotope ^{1}H, which is often referred to as ordinary hydrogen, will be referred to as protium.

2.3.1. Solution from the gas phase

In the most simple case, a metal is exposed to a gaseous hydrogen atmosphere. As described, e.g., in [76], a thermal equilibrium evolves, in which hydrogen adsorption on the metal surface from the gas, dissociation and dissolution in the metal are balanced by the processes of transition from the metal bulk to the surface, recombination and desorption to the gas phase. Omitting the details of the intermediate processes, the dynamic equilibrium of the gaseous and solute hydrogen phases can be abbreviated as

$$\frac{1}{2}\mathrm{H_2(gas)} \leftrightarrow \mathrm{H(solution)} \tag{2.1}$$

(compare, e.g., [76, 77]).

The dissociation of molecular hydrogen is necessary, because, in a metal, hydrogen is typically stored in atomic form at interstitial lattice sites. The solution process is controlled by the chemical potentials of hydrogen atoms in the gas phase $\frac{1}{2}\mu_{\mathrm{H_2(gas)}}$ and in solution in the metal $\mu_{\mathrm{H(solution)}}$, which need to be equal in thermodynamic equilibrium [76, 77]:

$$\frac{1}{2}\mu_{\mathrm{H_2(gas)}} = \mu_{\mathrm{H(solution)}}. \tag{2.2}$$

The chemical potential of hydrogen atoms bound in molecules in the gas phase $\frac{1}{2}\mu_{\mathrm{H_2(gas)}}$ can, for the assumption of an ideal gas, be written as

$$\frac{1}{2}\mu_{\mathrm{H_2(gas)}} = \frac{1}{2}RT\ln\left(\frac{p_{\mathrm{H_2}}}{p_{\mathrm{H_2},0}}\right) + \frac{1}{2}\mu_{\mathrm{H_2(gas),0}} = RT\ln\left(\sqrt{\frac{p_{\mathrm{H_2}}}{p_{\mathrm{H_2},0}}}\right) + \frac{1}{2}\mu_{\mathrm{H_2(gas),0}} \tag{2.3}$$

with hydrogen gas pressure $p_{\mathrm{H_2}}$, temperature T and ideal-gas constant R (compare, e.g., [77]). The constants $\mu_{\mathrm{H_2(gas),0}}$ and $p_{\mathrm{H_2},0}$ define the zero reference of the chemical potential.

In the limit of low hydrogen concentrations ($c_{\mathrm{H}} \to 0$), where the number of hydrogen atoms N_{H} is much smaller than the number of metal atoms N_{M} and interactions between hydrogen atoms are negligible, the chemical potential of solute hydrogen atoms in the metal can be written as

$$\mu_{\mathrm{H(solution)}} = RT\ln\left(\frac{r_{\mathrm{H}}}{\beta}\right) + \mu_{\mathrm{H(solution),0}} \tag{2.4}$$

with the atomic ratio of hydrogen and metal atoms $r_{\mathrm{H}} = \frac{N_{\mathrm{H}}}{N_{\mathrm{M}}}$ and the number of interstitial sites per lattice atom $\beta = \frac{N_{\mathrm{i}}}{N_{\mathrm{M}}}$, where N_{i} is the total number of interstitial sites (compare, e.g., [77]). Of course, the zero reference of the chemical potential must be identical in Equations 2.3 and 2.4. This is ensured by choosing the constant $\mu_{\mathrm{H(solution),0}}$ such that the zero reference of the chemical potential in Equation 2.4 is identical with the zero reference defined by the constants $\mu_{\mathrm{H_2(gas),0}}$ and $p_{\mathrm{H_2},0}$ in Equation 2.3.

In addition to the hydrogen concentration c_{H} and the ratio of hydrogen and metal atoms r_{H}, the atomic fraction of hydrogen atoms $\zeta_{\mathrm{H}} = \frac{N_{\mathrm{H}}}{N_{\mathrm{M}}+N_{\mathrm{H}}}$ is also frequently used in the context of hydrogen in metals. In the limit of low hydrogen concentrations, ζ_{H} is approximately equal to r_{H}:

$$\zeta_{\mathrm{H}} \approx r_{\mathrm{H}} \text{ for } N_{\mathrm{H}} \ll N_{\mathrm{M}}. \tag{2.5}$$

It must be noted that the term atomic concentration, which is actually defined with respect to volume [78, 79], is frequently used for the atomic fraction ζ_{H} or the atomic ratio of hydrogen-isotope to metal atoms r_{H} in the literature concerned with hydrogen isotope retention in tungsten (e.g. [29, 43, 80]). However, with respect to r_{H}, and in the low concentration limit $\zeta_{\mathrm{H}} \approx r_{\mathrm{H}}$ also with respect to ζ_{H}, this inconsistency brings in only a constant factor, which depends on the metal density ρ_{M} and molar mass M_{M} as well

as the Avogadro constant N_A. The relationship between hydrogen concentration c_H and atomic ratio r_H is a proportionality described by

$$c_H = r_H \cdot \frac{\rho_M \cdot N_A}{M_M}. \tag{2.6}$$

For the deuterium concentrations in tungsten present during the experiments reported in this thesis, Equation 2.5 can be considered valid, which is why a direct comparison of atomic fractions and atomic ratios is, in this case, possible and they can, in this framework, be regarded as practically synonymous.

Inserting Equations 2.3 and 2.4 in Equation 2.2 and using Equation 2.6 results in the well known *Sieverts' law* [76, 77, 81], which can be expressed in terms of the concentration as

$$c_H = S \cdot \sqrt{p_{H_2}} \tag{2.7}$$

or in terms of the atomic ratio as

$$r_H = \tilde{S} \cdot \sqrt{p_{H_2}}, \tag{2.8}$$

for sufficiently dilute solutions. Sieverts' constant S or $\tilde{S}$ is also referred to as the (equilibrium) solubility [82]. S and $\tilde{S}$ differ by only a constant factor, which is defined by Equation 2.6. The square root in Equation 2.7 results from the factor $\frac{1}{2}$ in Equation 2.2 and is thus a consequence of the dissociation of hydrogen molecules into atoms before solution [76, 77, 81].

Tungsten has a very low hydrogen solubility S_W, for which only a very limited number of measurements exists [37, 38]. The most widely accepted literature value [37] is the one determined by Frauenfelder [40]. However, it has been measured at high temperatures between 1100 K and 2400 K, which is why an extrapolation to room temperature is associated with a large uncertainty.

2.3.2. Diffusion in perfect metal lattices

When dissolved in a perfectly crystalline metal lattice, hydrogen atoms in general do not remain at one interstitial site, but can move through the metal lattice from interstitial site to interstitial site, for sufficiently high temperatures. The probability and nature of the transition of a hydrogen atom from one interstitial site to another strongly depends on temperature. Different regimes reaching from quantum mechanical tunneling at very low temperatures to nearly unbound movement at high temperatures exist, as described in detail, e.g., in [83].

According to DFT calculations reported in [84], classical diffusion behavior of hydrogen in tungsten can be expected for temperatures above about 200 K. Since 200 K is significantly below the temperatures present during the experiments reported in this thesis, this section focuses on a classical description of diffusion. In this classical regime, the transition of hydrogen atoms between interstitial sites is described as a thermally activated jump over a potential barrier of energy E_D [83]. All equations will be given in their one-dimensional form, as they can be used to describe samples that may be assumed

to be homogeneous and infinitely long in all directions orthogonal to the concentration gradient.

The diffusion flux density $\jmath$ resulting from a concentration gradient $\frac{\partial c_\mathrm{H}}{\partial x}$ can be described by *Fick's first law*

$$\jmath = -D \cdot \frac{\partial c_\mathrm{H}}{\partial x} \tag{2.9}$$

with the *diffusion coefficient* D (compare, e.g. [83, 85–87]). D is also referred to as the chemical diffusion coefficient and must be distinguished from the intrinsic or tracer diffusion coefficient, which describes the random walk of a single hydrogen atom in the metal lattice. However, in the limit of low hydrogen concentrations, where the interaction between hydrogen atoms is negligible, the chemical and the tracer diffusion coefficient become equal [83, 87].

In classical diffusion theory, the temperature dependence of D can be described by an Arrhenius equation

$$D = D_0 \cdot \exp\left(-\frac{E_D}{k_B T}\right) \tag{2.10}$$

with a dependence of the prefactor D_0 on the hydrogen isotope mass m_HI described by

$$D_0 \propto \frac{1}{\sqrt{m_\mathrm{HI}}} \tag{2.11}$$

(compare, e.g., [88]).

Experimental data of the hydrogen diffusion coefficient in tungsten is sparse and the values reported in different studies show a large data scatter [37, 38]. As in the case of the Sieverts' constant, also here the value reported by Frauenfelder [40] is the most widely accepted literature value [37, 38]. However, since Frauenfelder's diffusion coefficient has, such as his Sieverts' constant, been determined based on measurements at high temperatures between 1100 K and 2400 K, an extrapolation to room temperature also has a large uncertainty.

In the absence of sources and sinks, conservation of mass yields the *continuity equation*

$$\frac{\partial c_\mathrm{H}}{\partial t} + \frac{\partial \jmath}{\partial x} = 0. \tag{2.12}$$

(compare, e.g., [85, 87]).

Inserting Equation 2.9 into Equation 2.12 yields *Fick's second law*, which is also referred to as the *diffusion equation*

$$\frac{\partial c_\mathrm{H}}{\partial t} = \frac{\partial}{\partial x} \cdot D \cdot \frac{\partial c_\mathrm{H}}{\partial x}. \tag{2.13}$$

and can be simplified for the case of D independent of x to

$$\frac{\partial c_\mathrm{H}}{\partial t} = D \cdot \frac{\partial^2 c_\mathrm{H}}{\partial x^2} \tag{2.14}$$

(compare, e.g., [85, 87]).

Assuming that the metal sample has a finite length L in x-direction and that the hydrogen in the metal is in local thermodynamic equilibrium with hydrogen gas of pressure p_{front} and p_{back} at the front and back surface, respectively, the boundary conditions at both surfaces can be described with Sieverts' law (Equation 2.7). Using these boundary conditions in the solution of Fick's first law (Equation 2.9) yields the steady-state permeation flux density

$$J_{\mathrm{perm}} = -D\frac{\Delta c_{\mathrm{H}}}{\Delta x} = -D\frac{\Delta c_{\mathrm{H}}}{L} = -D \cdot S \cdot \frac{\sqrt{p_{\mathrm{front}}} - \sqrt{p_{\mathrm{back}}}}{L} \tag{2.15}$$

for gas-driven permeation. In the case of $p_{\mathrm{back}} \approx 0$ follows

$$J_{\mathrm{perm}} = -D \cdot S \cdot \frac{\sqrt{p_{\mathrm{front}}}}{L} = -\Phi \cdot \frac{\sqrt{p_{\mathrm{front}}}}{L}, \tag{2.16}$$

where $\Phi = D \cdot S$ is the *permeability* [86].

2.3.3. Ion implantation

In metals with a low hydrogen solubility, such as tungsten, only very small amounts of hydrogen are dissolved in thermal equilibrium at moderate temperatures and hydrogen pressures. However, if the hydrogen isotopes are implanted with sufficiently high energies, e.g. as ions from a plasma, they can enter the material directly without undergoing the dissolution process described above. Thereby, much higher concentrations than in thermal equilibrium can be reached inside the metal, which can lead to an oversaturation with hydrogen [9, 22]. The resulting hydrogen concentrations depend on the implantation conditions (compare Section 2.2), but also on the out-diffusion of hydrogen isotopes from the sample as described in Sections 2.3.2 and 2.3.4. From the resulting concentrations, equivalent equilibrium pressures can be calculated. These pressures can become extremely high, even up to the GPa range [9].

It is important to note that the permeability Φ (compare Equation 2.16) is not applicable for the case of ion-driven permeation, because it includes Sieverts' constant S and is thus only applicable in thermal equilibrium, which is in general not present during ion implantation.

Different regimes of ion-driven steady-state hydrogen permeation can be distinguished based on the boundary conditions present at the implantation side and the other side (permeation side) of the sample. The boundary conditions are usually classified based on the rate determining steps for desorption present at both surfaces. These are typically distinguished as being either diffusion to the surface or recombination at the surface. The resulting regimes for a delta-peak implantation distribution are described in detail, e.g., in [89–92]. As is described there, the hydrogen concentration during steady-state permeation depends linearly on the position x on both sides of the implantation depth, where a maximum value $c_{\mathrm{H,max}}$ of the hydrogen concentration is reached. Depending on the regime, the linear function of the hydrogen concentration may also have zero slope. In the subsequent discussion of the different regimes, which follows [91], it shall be assumed that the dissolution of hydrogen in the metal from hydrogen gas that possibly surrounds the sample is negligible, which is frequently a good assumption for tungsten due to its

low hydrogen solubility. Furthermore, the diffusion coefficient D shall be assumed to be temperature dependent, but spatially invariant in the whole sample and the implantation depth d_{impl} shall be assumed to be much smaller than the sample thickness L ($d_{\mathrm{impl}} \ll L$).

For recombination limited desorption at both sides, the steady-state permeation flux can, according to [91], be written as

$$J_{\mathrm{perm}} = \frac{k_{\mathrm{p}}}{k_{\mathrm{i}} + k_{\mathrm{p}}} \cdot J_{\mathrm{impl}}, \tag{2.17}$$

where J_{impl} is the implanted flux. k_{i} and k_{p} are the recombination coefficients at the implantation side and permeation side, respectively. One important quantity influenced by the boundary conditions is, besides the absolute value of the permeation flux J_{perm} during ion implantation, also its temperature dependence. If the desorption at both sides is recombination limited, the steady-state permeation flux will be independent of temperature assuming that the recombination coefficients on both sides have the same temperature dependence. Else, it will depend on temperature via the temperature dependencies of the recombination coefficients.

If the desorption is recombination limited at the implantation side, but diffusion limited at the permeation side, the steady-state permeation flux can, according to [91], be written as

$$J_{\mathrm{perm}} = \frac{D}{L} \cdot \sqrt{\frac{J_{\mathrm{impl}}}{k_{\mathrm{i}}}}. \tag{2.18}$$

The steady state permeation flux in this regime will depend on temperature via the recombination coefficient at the implantation side and the diffusion coefficient.

In the most simple case of diffusion-limited boundary conditions at both sides, the concentrations directly below both surfaces are zero, if solution from surrounding hydrogen gas is negligible. Then, the hydrogen concentration in the sample decreases linearly from $c_{\mathrm{H,max}}$ at the implantation depth to zero at both surfaces. In this case, the value of $c_{\mathrm{H,max}}$ is defined purely geometrically by implantation and out-diffusion. The steady-state permeation flux in this regime can, according to [91], be written as

$$J_{\mathrm{perm}} = \frac{d_{\mathrm{impl}}}{L} \cdot J_{\mathrm{impl}}. \tag{2.19}$$

The permeation flux in this regime is independent of temperature because neither the temperature dependence of the diffusion coefficient D nor the temperature dependence of the recombination coefficients enter into the equation.

2.3.4. Diffusion in defective metals

The description of solution and diffusion of hydrogen in metals presented in Sections 2.3.1 and 2.3.2 was based on the assumption that all hydrogen atoms in the metal lattice are located at and diffuse predominantly via a single type of interstitial sites with an energy barrier height E_D between neighboring interstitial sites, as it can be reasonably assumed for a perfect crystalline lattice at low hydrogen concentrations. However, as described in Section 2.1, real metals are typically not perfect single crystals, but incorporate a large number of different material defects.

These material defects can strongly affect the amount of hydrogen present in the metal at a certain temperature as well as the hydrogen diffusion. They can cause additional sites where hydrogen atoms can be stored at a lower energy level than at interstitial sites and thus bind hydrogen atoms in their vicinity, a process referred to as *trapping* [41, 52, 93]. These traps can be saturable or unsaturable, depending on the number of hydrogen atoms, which can be stored in a trap simultaneously [52].

By offering additional, energetically lower sites for hydrogen, a larger amount of hydrogen can in principle be stored in the metal at a given temperature. The Sieverts' constant S defined by Equation 2.7, is in general regarded as a material property, which should be independent of the microstructure and describe the solution in regular interstitial lattice sites. The total hydrogen amount stored in the metal at interstitial and trap sites is, therefore, often described by using the term *hydrogen retention* (compare, e.g., [9, 41]).

As described, e.g., in [41, 52, 94], the hydrogen in the material is, for a theoretical description and modeling, typically divided into the two populations of interstitially dissolved *solute hydrogen* and *trapped hydrogen* located at sites with lower energies in the vicinity of material defects. Hereby, it is, furthermore, assumed that only the solute hydrogen is mobile and can thus diffuse through the metal, while the trapped hydrogen is immobile and can only diffuse after entering the solute by thermally activated *detrapping*. In this picture, the transport of hydrogen atoms between traps thus always requires the following steps: detrapping from the initially occupied trap site, diffusion via the solute, and (re-)trapping at the new trap site.

The processes of trapping and detrapping for saturable traps can be included in the description of diffusion by adding additional terms to the simplified diffusion Equation 2.14. Also a source term $\sigma(x,t)$ that models, e.g., ion implantation can be added. As described, e.g., in [41, 94], this results in the *diffusion-trapping equation*

$$\frac{\partial c_{\mathrm{H}}^{\mathrm{solute}}(x,t)}{\partial t} = \underbrace{D(T(t)) \cdot \frac{\partial^2 c_{\mathrm{H}}^{\mathrm{solute}}(x,t)}{\partial x^2}}_{\text{solute diffusion}} + \underbrace{\sigma(x,t)}_{\text{source}} - \underbrace{\sum_{n=0}^{N_{\mathrm{traps}}-1} \frac{\partial c_{\mathrm{H},n}^{\mathrm{trapped}}(x,t)}{\partial t}}_{\text{(de-)trapping}}, \tag{2.20}$$

where N_{traps} is the number of different trap types, $c_{\mathrm{H}}^{\mathrm{solute}}$ is the solute hydrogen concentration and $c_{\mathrm{H},n}^{\mathrm{trapped}}$ is the hydrogen concentration in trap type n.

Strictly speaking, Equation 2.20 differs from the equation reported in [41, 94] because the equation given in the references is based on the convention mentioned in Section 2.3.1 with concentrations given as atom density fractions or atomic fractions. This difference, however, corresponds only to a constant factor (compare Equation 2.6) in the limit of low hydrogen concentrations, which is why Equation 2.20 can also be written based on the atomic ratio definition as

$$\frac{\partial r_{\mathrm{H}}^{\mathrm{solute}}(x,t)}{\partial t} = \underbrace{D(T(t)) \cdot \frac{\partial^2 r_{\mathrm{H}}^{\mathrm{solute}}(x,t)}{\partial x^2}}_{\text{solute diffusion}} + \underbrace{\tilde{\sigma}(x,t)}_{\text{source}} - \underbrace{\sum_{n=0}^{N_{\mathrm{traps}}-1} \frac{\partial r_{\mathrm{H},n}^{\mathrm{trapped}}(x,t)}{\partial t}}_{\text{(de-)trapping}}, \tag{2.21}$$

where $r_{\mathrm{H}}^{\mathrm{solute}}(x,t)$ is the atomic ratio of solute-hydrogen to metal atoms and $r_{\mathrm{H},n}^{\mathrm{trapped}}(x,t)$ is the atomic ratio of trapped hydrogen to metal atoms for trap type n.

The source term $\tilde{\sigma}(x,t)$ introduces hydrogen into the system. For a normalized source distribution ξ with $\int_0^\infty \xi(x)\mathrm{d}x \equiv 1$ and a total source flux of Γ, it can be written as

$$\tilde{\sigma}(x,t) = \frac{\Gamma}{\rho_{\mathrm{M}}} \cdot \xi(x), \tag{2.22}$$

with the atomic density of the metal ρ_{M} [41].

The (de-)trapping term describes the change of the trapped concentration in each trap type n as the difference of a trapping rate $\Psi_{\mathrm{trapping},n}$ and a detrapping rate $\Psi_{\mathrm{detrapping},n}$

$$\frac{\partial r_{\mathrm{H},n}^{\mathrm{trapped}}(x,t)}{\partial t} = \Psi_{\mathrm{trapping},n}(x,t) - \Psi_{\mathrm{detrapping},n}(x,t) \tag{2.23}$$

with trapping rate

$$\Psi_{\mathrm{trapping},n}(x,t) = \frac{D(T(t))}{a_0^2 \beta} \cdot r_{\mathrm{H}}^{\mathrm{solute}}(x,t) \cdot \left(\eta_n^{\mathrm{tr}}(x,t) - r_{\mathrm{H},n}^{\mathrm{trapped}}(x,t)\right) \tag{2.24}$$

and detrapping rate

$$\Psi_{\mathrm{detrapping},n}(x,t) = r_{\mathrm{H},n}^{\mathrm{trapped}}(x,t) \cdot \nu_n \cdot \exp\left(-\frac{E_n^{\mathrm{detrap}}}{k_{\mathrm{B}} T(t)}\right), \tag{2.25}$$

where η_n^{tr} is the number of traps of type n per metal atom, β is the number of available interstitial sites per lattice atom, a_0 is the lattice constant approximated by $a_0 = \sqrt[3]{\rho_{\mathrm{M}}}$ with the atomic density of the metal ρ_{M}, ν_n is the frequency pre-factor for detrapping from trap type n, E_n^{detrap} is the detrapping energy for trap type n and k_{B} is the Boltzmann constant [41, 94]. The factor $\frac{D(T(t))}{a_0^2\beta}$ in Equation 2.24 originates from the frequently made simplifying assumption that a transition from an interstitial site to a neighboring trap site occurs with the same probability as the transition to a neighboring interstitial site (compare [39, 94]). For tungsten, hydrogen diffusion is assumed to proceed via tetrahedral sites (T sites) [84, 95]. Considering the bcc crystal structure of tungsten, this results in $\beta = 6$ (compare Section 2.1).

The presented diffusion trapping model was implemented in the form of a Mathematica script named TESSIM [41, 94] by Klaus Schmid (Max-Planck-Institut für Plasmaphysik). TESSIM, which has already been applied successfully by other researchers to model deuterium loading of tungsten (compare, e.g., [41, 96]), was also used for the diffusion-trapping simulations presented in this thesis. Since it describes diffusion in one dimension, possible two- or three-dimensional effects, such as enhanced diffusion along grain boundaries, are neglected.

2.3.5. Interface effects

In analogy to Equation 2.2, which describes the thermodynamic equilibrium of hydrogen gas with hydrogen dissolved below a metal surface, the equilibrium of hydrogen dissolved

at both sides of an interface between different metals can be described by equality of the chemical potentials of hydrogen atoms dissolved in each of the metals:

$$\mu_{\text{metal 1}} = \mu_{\text{metal 2}}. \tag{2.26}$$

This condition in general leads to a discontinuity in the hydrogen concentration across the interface, which can be motivated in the framework of Sieverts' law by a gedankenexperiment as described in [97]. In [97], a small cavity filled with hydrogen gas is assumed to be present at the interface, which is in local thermal equilibrium with the hydrogen dissolved near the cavity in both metals. This can be described via the chemical potentials as

$$\mu_{\text{metal 1}} = \frac{1}{2}\mu_{\text{H}_2\text{(gas)}} = \mu_{\text{metal 2}} \tag{2.27}$$

according to Equation 2.2.

Using Sieverts' law (Equation 2.7), the hydrogen concentrations near the cavity in the metals can consequently be expressed as functions of the hydrogen pressure p in the cavity as

$$c_{\text{H,1}}^{\text{solute}} = S_1 \cdot \sqrt{p} \quad \text{and} \quad c_{\text{H,2}}^{\text{solute}} = S_2 \cdot \sqrt{p}, \tag{2.28}$$

with the solute-hydrogen concentration $c_{\text{H,1}}^{\text{solute}}$ and Sieverts' constant S_1 in metal 1 and the solute-hydrogen concentration $c_{\text{H,2}}^{\text{solute}}$ and Sieverts' constant S_2 in metal 2. Solving Equations 2.28 for $\sqrt{p}$ yields

$$\sqrt{p} = \frac{c_{\text{H,1}}^{\text{solute}}}{S_1} = \frac{c_{\text{H,2}}^{\text{solute}}}{S_2} \tag{2.29}$$

and thus a boundary condition for the interface. It defines a ratio of the hydrogen concentrations at the interface, which is determined by the equilibrium solubilities in both metals [97].

Since the equilibrium assumed in the gedankenexperiment is only local, the diffusion flux between metals 1 and 2 must be considered in addition. Conservation of mass requires

$$\jmath_1(x_0) = \jmath_2(x_0), \tag{2.30}$$

where x_0 is the position of the interface. Using Equation 2.9, Equation 2.30 can be written in terms of concentrations as

$$D_1 \cdot \left.\frac{\partial c_{\text{H,1}}^{\text{solute}}}{\partial x}\right|_{x_0} = D_2 \cdot \left.\frac{\partial c_{\text{H,2}}^{\text{solute}}}{\partial x}\right|_{x_0}, \tag{2.31}$$

where D_1 and D_2 are the diffusion coefficients in metal 1 and 2, respectively [97].

In sum, the hydrogen concentrations at the interface in both metals are determined by two processes. These are the solution of hydrogen in the metals described by their Sieverts' constants and the diffusion to and from the interface. The combination of these two processes is represented by the combination of Equations 2.29 and 2.31.

2.3.6. Modification of the microstructure

As described in Section 2.2.2, the hydrogen ion implantation into metals can, for sufficiently high energies, lead to material defects being created due to a collision cascade. However, defect creation due to hydrogen isotope implantation in tungsten has also been reported even far beyond the implantation range [9, 35, 42]. The most reasonable explanation for this defect creation appears to be an oversaturation of the metal with hydrogen far above the equilibrium value [9, 22, 98] that can extend deep into the material carried by diffusion. In the extreme case, even bubbles filled with hydrogen gas, can be formed below the surface and lead to surface elevations, so-called "blisters" [42, 98].

Numerous theoretical and experimental studies (e.g. [45, 99–103]) were performed to investigate the evolution of defects and associated traps in tungsten due to the interaction of hydrogen isotopes with tungsten. Still, the underlying microscopic processes behind the nucleation and development of such defects are not entirely understood yet. However, the solute hydrogen-isotope concentration is expected to be a key factor in the defect evolution [9, 39, 44, 104]. Therefore, knowledge about the solute and possibly trapped hydrogen concentrations present during defect evolution is expected to be of crucial importance to develop a conclusive theory that is capable to quantitatively describe the microscopic processes that lead to defect evolution due to the presence of hydrogen isotopes in tungsten.

As already mentioned in Chapter 1, the defect evolution during hydrogen isotope implantation into tungsten cannot be interpreted isolated from the effect of the evolving defects on the hydrogen isotope retention and diffusion (see Section 2.3.4). The complex interplay [38] of these effects needs to be investigated further in order to obtain a comprehensive understanding of the phenomena associated with hydrogen isotopes implanted into tungsten, a task to which this thesis attempts to contribute.

3. Materials and methods used for sample preparation and analysis

This chapter provides an overview of the materials and methods used for sample preparation and analysis. The explanations focus on the devices used and facts relevant for the understanding of subsequent chapters, rather than giving a full overview of the respective field. More detailed general information about the methods can be found in the references given.

3.1. High temperature treatments

Two vacuum furnaces called MOMO and HADES were used for heat treatments of samples.

In MOMO, a schematic drawing of which is displayed in Figure 3.1, the samples are placed in a box made of molybdenum (Mo) sheets that is mounted inside the furnace. The box is heated by thermal radiation from electrically heated molybdenum wires located above and below the box. The electric current is set by a proportional-integral-derivative (PID) controller such that the temperature measured with a thermocouple touching the inside of the molybdenum box is matched to a set value. The hot zone of the furnace is surrounded by multiple layers of molybdenum foils that serve as heat shields. MOMO, which can reach temperatures up to about 1200 K, is used as a general purpose furnace for heat treatments of various metals and other materials. It can reach a base pressure down to almost 10^{-5} Pa at room temperature. For higher temperatures, the pressure is increased and affected by possible outgassing from samples. For sample exchange, the furnace must be vented completely, which was done with nitrogen.

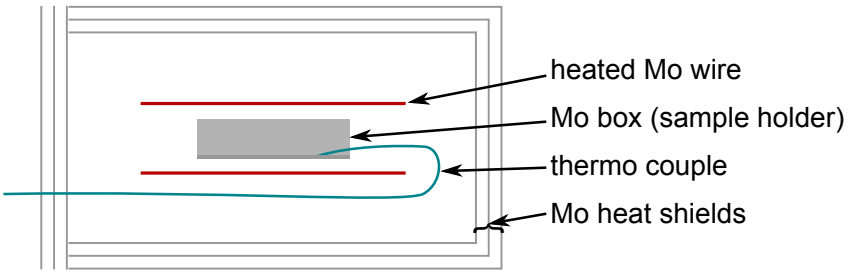

Figure 3.1.: Schematic drawing of the vacuum furnace MOMO. MOMO is a general-purpose vacuum furnace intended to anneal various kinds of metals and other materials at temperatures up to about 1200 K.

A schematic drawing of the high temperature furnace HADES is displayed in Figure 3.2.

For insertion into HADES, the samples are placed on a round tungsten plate with about 50 mm diameter. The plate is then put on the sample holder table, which is also made of tungsten. The temperature of the sample holder, which is assumed to be very close to the sample temperature, is measured with a thermocouple located inside the sample holder. In contrast to MOMO, HADES has a load lock into which the sample holder can be retracted. Thus, the vacuum in the main chamber does not need to be broken for sample exchange. The main chamber of HADES is usually kept at a pre-heating temperature of roughly 400 K to minimize adsorption of species from residual gas in the hot zone of the furnace. At this pre-heating temperature, a base pressure down to around 5×10^{-9} Pa can be reached. After transfer of sample holder and samples to the main chamber, they are heated by thermal radiation from an electrically heated tungsten meander that surrounds the sample holder. The hot zone of the furnace is surrounded by one layer of tungsten foil and additional layers of molybdenum foil, which serve as heat shields. After a typical heating ramp and a temperature treatment at the maximum design temperature of 2000 K for 30 min, the pressure in the main chamber is usually around 10^{-5} Pa with tungsten foil samples on the sample holder. In contrast to MOMO, HADES is almost exclusively used to anneal pure tungsten samples in order to avoid any possible cross-contamination from preceding heating runs.

The pressure values reported were in both furnaces determined using pressure gauges that are located outside of the heat shields. However, since the heat shields do not have vacuum-tight connections, the measured values are assumed to be representative also for the pressure in the hot zone.

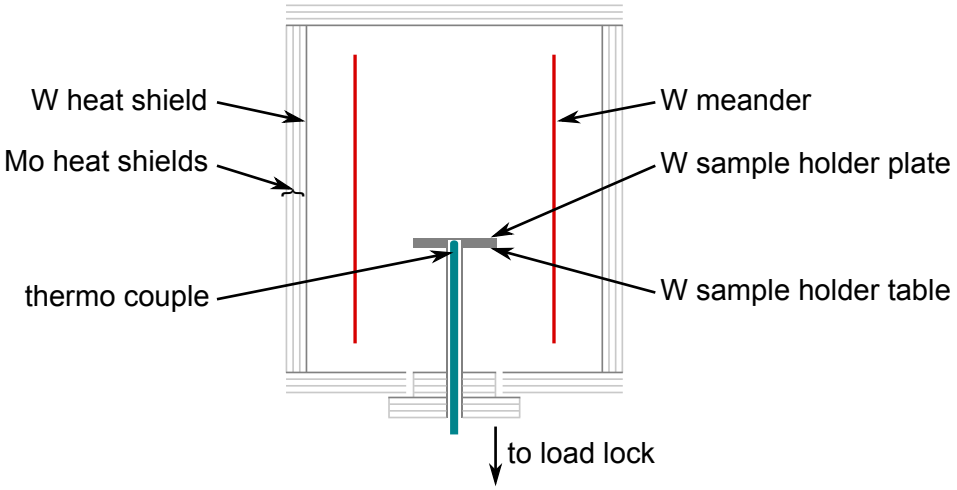

Figure 3.2.: Schematic drawing of the vacuum furnace HADES. HADES is almost exclusively used to anneal pure tungsten samples at temperatures up to 2000 K.

3.2. Magnetron sputter deposition

Thin metal and oxide layers were deposited by magnetron sputtering, using a Discovery 18 device manufactured by Denton Vacuum LLC (USA). A schematic drawing of this device

is displayed in Figure 3.3.

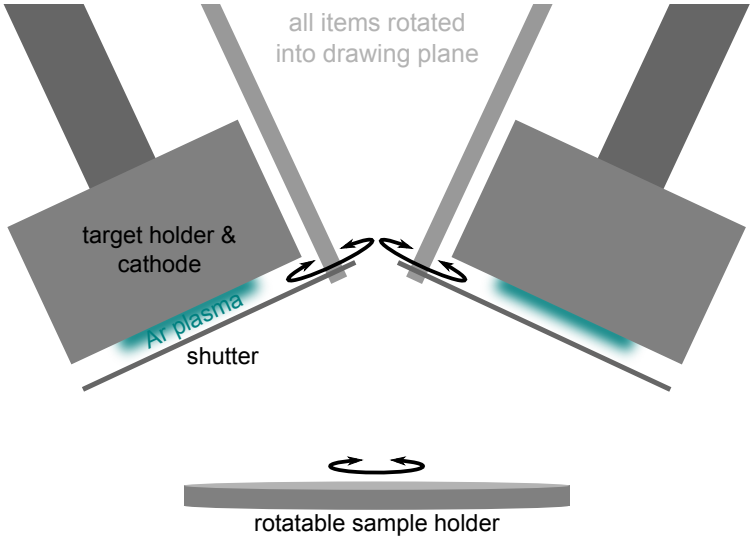

Figure 3.3.: Schematic drawing of the Denton Discovery 18 magnetron sputter device. A part of the atoms eroded from the targets by argon sputtering is deposited on samples located on the sample holder. Chemical compounds can be deposited by reactive sputter deposition, for which a reactive gas is admixed to the argon sputter gas.

As described in detail, e.g., in [105, 106], the principle of magnetron sputter deposition is as follows: a plasma generated by a direct current (DC) or radio frequency (RF) electric field and intensified by a magnetic field orthogonal to the electric field is used to erode a frequently metallic target by sputtering. The plasma is usually generated with argon gas and the target is typically clamped to a water cooled target holder. A part of the eroded target atoms can reach the samples located on the sample holder and be deposited there.

In the Discovery 18, shutters in front of the two target holders are available to interrupt and thus control deposition. For the depositions reported in this thesis, the shutter was kept closed for a few minutes after ignition of the plasma in front of the target in order to remove possible contaminations from the target surface before starting the deposition. The sample holder was set in continuous rotation to ensure a homogeneous deposition. By applying an RF electric field to the sample holder, an argon plasma could also be ignited around the sample holder, which was used to clean the samples before deposition.

By admixture of a reactive gas to the argon sputtering gas, chemical compounds consisting of target atoms and atoms of the admixed gas can be deposited. This process, which is also described, e.g., in [105, 106], is referred to as reactive sputter deposition. Using this approach, e.g. metal oxides can be deposited by admixture of oxygen gas during erosion of a pure metal target.

The metal layers for this thesis were deposited by DC magnetron sputtering with rates of about 0.3 nm/s for tungsten, 0.9 nm/s for copper, 1.0 nm/s for zirconium, 0.6 nm/s for titanium, 1.7 nm/s for erbium and 0.5 nm/s for aluminum. Erbium oxide was deposited by RF magnetron sputtering with a rate of about 0.06 nm/s. The sample holder was unbiased during the depositions.

3.3. Sputter x-ray photoelectron spectroscopy (sputter-XPS)

X-ray photoelectron spectroscopy (XPS) in combination with ion-beam sputtering, referred to as sputter-XPS, was used to investigate element depth profiles for a number of samples. The investigations were performed in the so-called SAX setup, which is based on a Perkin Elmer PHI5600 ESCA system. It is equipped with aluminum and magnesium x-ray sources and a hemispherical electron energy analyzer as well as an additional WF 421 Microfocus Ion Gun from Atomika. A schematic drawing of the SAX setup is displayed in Figure 3.4.

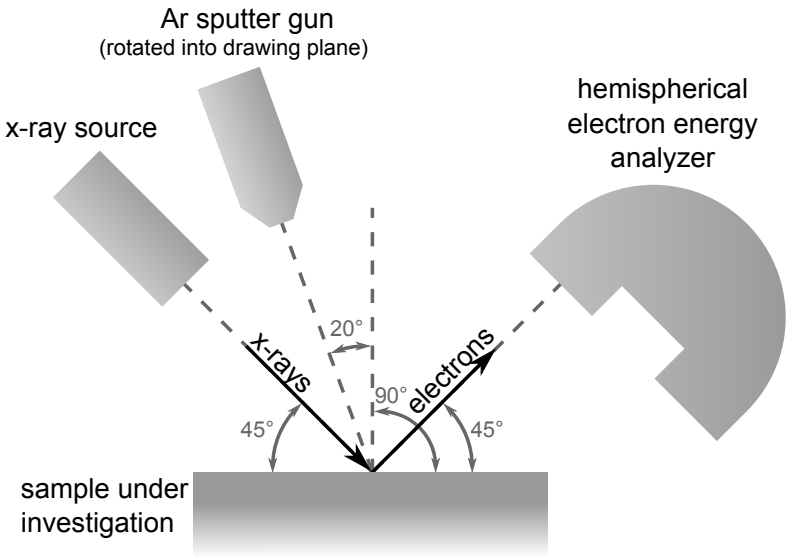

Figure 3.4.: Schematic drawing of the SAX device used for sputter-XPS measurements. The energy spectrum of electrons emitted from the sample due to incident x-rays can be analyzed to gain information about the elemental composition and chemical binding in the sample. Alternating XPS measurements and argon sputtering enables depth profiling.

In XPS measurements, as described in detail, e.g., in [107, 108], incident x-rays cause emission of electrons from up to a few nm below the sample surface. The emitted electrons typically originate from inner atomic shells. Their energy spectrum is determined by the elemental composition of the sample as well as the chemical binding of the sample atoms from which the electrons are emitted. A spectrum typically contains multiple peaks per element, which correspond to different electron shells and are named after the element and shell, e.g. as O1s peak for the 1s shell of oxygen. Different chemical binding can lead to a slight peak shift. Typically, lithium and heavier elements can be detected. Thus, hydrogen isotope atoms cannot be detected by XPS.

As described, e.g., in [107], information about regions in the sample that are deeper than the XPS information depth of a few nm can be gained by an iterative process of alternating XPS measurements and sputter erosion. Care must be taken in the interpretation of these

measurements because different sputter yields of different elements as well as forward implantation of sample atoms into deeper regions can lead to a deviation of the measured depth profile from the initial depth distribution of the elements in the sample before sputtering. In the SAX setup, the sputtering is performed with the ion gun typically using Argon and an acceleration voltage of 10 kV.

3.4. Microstructural analysis by SEM and FIB

A HELIOS NanoLab 600 dual-beam device manufactured by FEI was used for microstructural analysis. It is capable of performing scanning electron microscopy (SEM) and equipped with a focused ion beam (FIB) column. Furthermore, it includes a stage that can be used for sample positioning in three dimensions as well as rotation and tilt. A schematic drawing of the HELIOS NanoLab 600 is displayed in Figure 3.5.

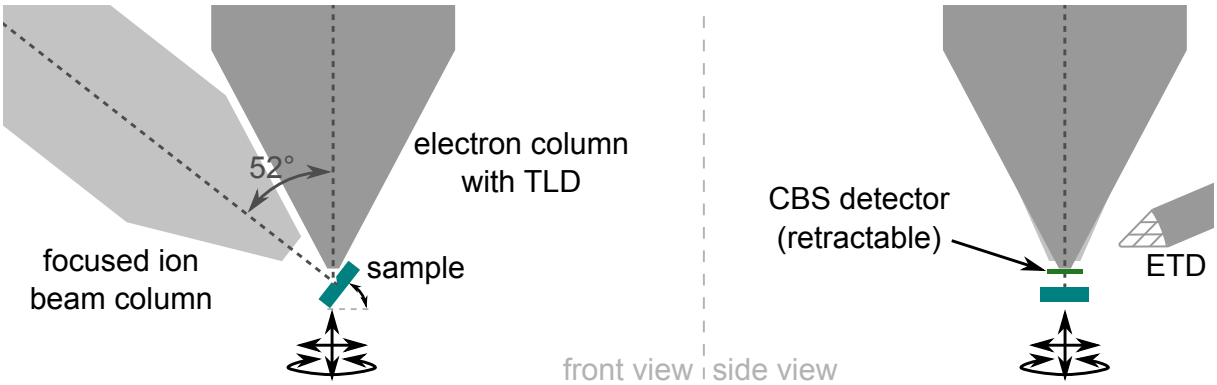

Figure 3.5.: Schematic drawing of the Helios NanoLab 600 dual-beam device, which includes a scanning electron microscope and a focused ion beam column for microstructural analysis. Electron detectors used to record the images presented in this thesis are also shown. The focused ion beam cannot only be used for imaging, but also for micro- and nanostructuring.

3.4.1. Scanning electron microscopy (SEM)

As described in detail, e.g., in [109, 110], the interaction of an incident electron beam with a sample is used in scanning electron microscopy (SEM) to gain information about the sample's microstructure. After emission from a cathode, which is in the case of the NanoLab 600 a Schottky field emission gun, the electrons are accelerated and manipulated by electrostatic and magnetic fields to finally generate a nearly monochromatic electron beam, which is focused on the sample surface.

At and below the sample surface, incident electrons undergo different interactions with the sample atoms, which lead to emission of electrons and electromagnetic radiation. Two of the most important contributions used for analysis are backscattered electrons (BSE), which are incident electrons that are re-emitted from the sample after a number of collisions, and secondary electrons (SE), which are electrons emitted from up to a few

nm below the sample surface due to interaction with incident or backscattered electrons. While the BSE have an energy range nearly up to the incident energy, the energies of SE are typically much lower and by convention defined as those emitted electrons with a kinetic energy below 50 eV. The electrons are not only emitted from the surface and sub-surface region of the beam spot, but from a possibly much larger interaction volume [109, 110].

To generate a two-dimensional image of the sample surface, the electron beam spot is scanned over the sample in a regular pattern. Simultaneously, the electron emission is recorded with different kinds of detectors and an image is generated by correlating the brightness of a pixel with the signal at the corresponding beam position [109, 110]. Since the electron emission at each location is strongly affected by, e.g., sample material, topography and crystallographic orientation, different types of contrast reflecting these properties evolve in the recorded images [109, 110].

The HELIOS NanoLab 600 is equipped with a number of different detectors for electrons as well as electromagnetic radiation, which is why the subsequent description of the detectors shall be limited to the detectors used to generate the images presented in this thesis.

An Everhart-Thornley detector (ETD) [111], is essentially a scintillator combined with a photomultiplier and can be used to detect BSE and SE. As described, e.g., in [109, 110], the detection of SE can be enhanced or reduced by biasing a metal grid in front of the detector entrance. While BSE detection is nearly unaffected by reasonable bias voltages due to the high energy of the BSE, the trajectories and thus detection of SE, which have a lower kinetic energy, can be strongly influenced by a voltage applied to the ETD's entrance grid. If not stated otherwise, ETD images presented in this thesis were recorded with an acceleration voltage for the incident electrons of 5 kV and the ETD operating in SE mode, which means that the entrance grid of the ETD was positively biased to about 250 V in order to attract SE and thus enhance SE detection.

A through-the-lens detector (TLD) can be used to detect secondary electrons that are emitted from the sample into the electron column. In the column, the electrons are separated from the electrons of the incident beam and guided to a detector [109, 110], which is in the case of the HELIOS NanoLab 600 using the detection principle of an ETD. If not stated otherwise, the acceleration voltage for images recorded with the TLD, presented in this thesis, was 5 kV and an additional magnetic immersion lens was used to gain a higher resolution.

A segmented concentric backscatter (CBS) detector was used to detect BSE. The CBS detector is a solid state detector which uses the principle of electron-hole-pair generation by electrons in a semiconductor diode, as described in detail, e.g., in [109, 110]. It can be used to generate images with different kinds of contrast enhanced or suppressed by adding or subtracting the signals from different segments. In the HELIOS NanoLab 600, the CBS detector is divided into two rings, of which the outer ring is again divided in three equally sized parts. Images intended to display topographic contrast were generated by taking the difference of the signals from two parts (compare also, e.g., [109, 110]) of the outer ring and are subsequently referred to as *topographic-contrast images*. They were, if not stated otherwise, recorded with an electron acceleration voltage of 5 kV. Images generated by summing up the signals from all parts of the CBS detector are typically used

to display material contrast [109, 110]. They are then referred to as Z-contrast images. However, when recorded on a pure polycrystalline material, they can also be used to display the contrast generated by the different crystal orientations of individual grains [109, 110]. Since this was the case for the present thesis, they are subsequently referred to as *orientation-contrast images*. If not stated otherwise, the orientation-contrast images presented in this thesis were recorded with an electron acceleration voltage of 30 kV.

3.4.2. Focused ion beam (FIB) analysis

In focused ion beam (FIB) analysis, as described in detail, e.g., in [112, 113], the interaction of an ion beam incident on a sample is used to investigate the sample microstructure. Ions, typically from a liquid metal source, which is in the case of the HELIOS NanoLab 600 a Ga^+ ion source, are accelerated and manipulated by electrostatic and magnetic fields to generate a focused ion beam that impinges on the sample. Secondary electrons emitted due to the collision cascade caused by the incident ions can be detected [112, 113], e.g., using the ETD described in Section 3.4.1.

Due to the processes described in Section 2.2, such as implantation and sputtering, the focused ion beam analysis leads to a modification of the sample. It is thus, in contrast to SEM, destructive. However, these processes can also be utilized to modify the microscopic structure of the sample in a desired way, thus enabling the creation of microstructures, e.g. by controlled local erosion of sample material [114].

One typical application of microstructuring by FIB is the production of cross-sections [114, 115], which enables the investigation of the sub-surface microstructure of various kinds of samples. In the HELIOS NanoLab 600, the FIB column is tilted 52° with respect to the vertical SEM column. Thus, the SEM observes the cross-section generated by FIB under an angle of 38° with respect to the surface normal of the cross-section. To avoid rounding of the cross-section's top edge and to improve the smoothness of the cross-section, a protective layer can be deposited in-situ before the FIB cut by electron- or ion-beam-assisted deposition [114, 116]. In the HELIOS NanoLab 600, a methylcyclopentadienyl (trimethyl) platinum precursor is used to deposit thin protective layers, which contain carbon, platinum, hydrogen and, if deposited by ion-beam-assisted deposition, also gallium.

3.5. Tungsten foil

The tungsten samples used for the experiments presented in this thesis were cut from a cold-rolled tungsten foil manufactured by Plansee SE (Austria). The nominal purity and thickness of the foil were specified by the manufacturer as 99.97 % by weight and (25 ± 3) µm, respectively. All tungsten samples were cleaned in an ultrasonic bath first in ultra-pure acetone and subsequently in deionized water before they were rinsed in flowing deionized water and blown dry with air from bellows.

SEM investigations revealed a fine grained microstructure, as displayed in the left part of Figure 3.6.

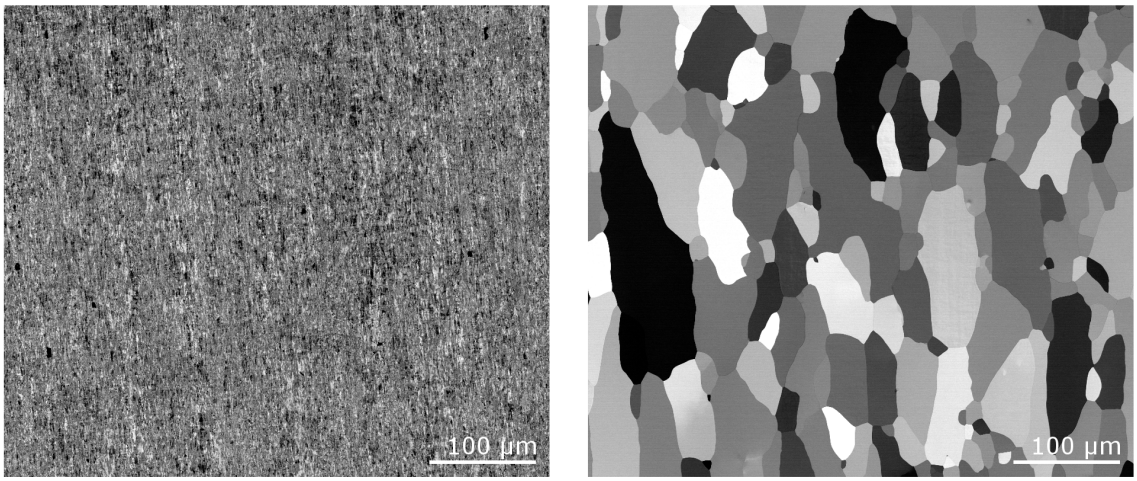

Figure 3.6.: Topview orientation-contrast SEM images of tungsten sample surfaces, recorded with an electron acceleration voltage of 5 kV. The sample displayed in the right image was annealed in the vacuum furnace HADES at 2000 K for 30 min, while the sample displayed in the left image was not annealed. (Images recorded by Gabriele Matern, Max-Planck-Institut für Plasmaphysik)

It is known that heat treatments at 1500 K and above can lead to a significant modification of the defect structure of tungsten, including recrystallization and grain growth, and thereby reduce the overall density of various kinds of defects [57]. To achieve such a reduction of the initial defect density, the tungsten samples were annealed at 2000 K for 30 min in the vacuum furnace HADES before the experiments. As is shown in Figure 3.6, this heat treatment did, as expected, cause recrystallization and a significantly increased average grain size in the samples.

As already previously reported in [47], eight samples were intentionally cleaved after the experiments to create a cross-section of each sample. These cross-sections were used for measurements of the sample thickness. SEM images were recorded at five positions on each cross-section and the sample thickness was measured at five locations in each SEM image. The results of these measurements are displayed in Figure 3.7. Due to the equal number of measurements in each image and on each cross section, the mean value of the sample thickness could simply be determined by calculating the mean value of all measured thicknesses. This resulted in a mean sample thickness L of about 24.5 µm [47]. The minimum measured foil thickness was 22 µm and the maximum 27 µm [47]. Uncertainties in the thickness measurement, which may result from uncertainties in the length calibration and possible small drifts of the SEM as well as a possible tilt of the foil and foil deformation, were estimated to be small compared to the observed variations of the sample thickness.

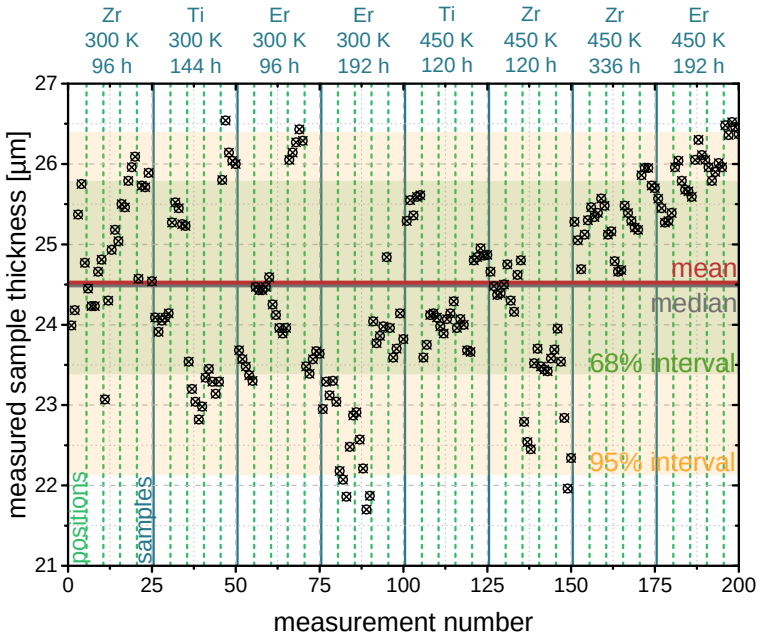

Figure 3.7.: After all other experiments were finished, thickness measurements were performed for eight samples by intentionally cleaving the samples and subsequently investigating the resulting cross-sections by SEM. On the cross section of each sample (separated by solid blue lines) electron micrographs were taken at five positions (separated by dashed green lines). The sample thickness indicated by the black datapoints was measured at five locations in each SEM image. The mean and median as well as intervals including 68 % and 95 % of the thickness measurements are also displayed. The 68 % and 95 % intervals exclude the upper and lower 16 % and 2.5 % of the measurement distribution, respectively. The information given in blue above the plot specifies the getter-layer material and deuterium-plasma exposure conditions for each of the samples. These parameters will be discussed in detail in Chapter 4.

3.6. Low-energy-deuterium-plasma exposure

The deuterium-plasma exposures reported in this thesis were performed in the laboratory plasma source PlaQ. PlaQ has been used for a large number of studies on hydrogen isotope retention in tungsten before (e.g. [21, 22, 34, 42, 57]) and was described in detail in [117]. A schematic drawing of PlaQ is displayed in Figure 3.8.

The plasma in PlaQ is generated using the principle of electron cyclotron resonance (ECR), which is described in detail, e.g., in [118, 119]. Microwave radiation of frequency 2.45 GHz is transmitted into the vacuum chamber through a microwave compatible window parallel to a static magnetic field [117]. A typical advantage of ECR plasma sources is their relatively high ion flux at low ion energies [118]. As described in [117], the region of plasma generation in PlaQ is confined by a metal cage. This cage has a hole at the bottom through which a plasma beam is emitted. The hole is covered with a coarse metal grid that is intended to avoid microwave emission through the hole. The plasma beam

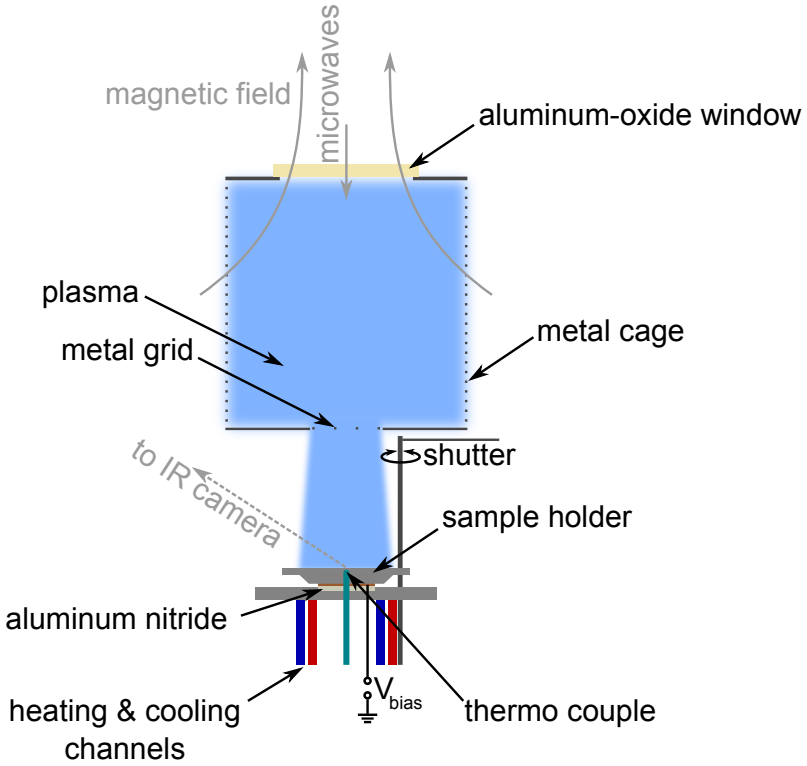

Figure 3.8.: Schematic drawing of the ECR plasma source PlaQ, of which a detailed description can be found in [117]. PlaQ was used for all deuterium-plasma exposures reported in this thesis. The plasma is generated by resonant microwave radiation transmitted into the vacuum chamber parallel to a static magnetic field and confined by a metal cage. A plasma beam is emitted through a hole in the cage and impinges on the sample holder.

impinges on a tungsten-coated sample holder, which is shielded from the microwaves by the metal cage and the coarse metal grid. It can be blocked with a rotatable shutter. Usually, the shutter is kept closed after ignition of the plasma for a certain amount of time to delay the exposure until the plasma has reached stable operating conditions [117]. This so-called burn-in phase [117] was typically 30 min for the exposures described in this thesis.

The energy of the ions incident on the samples can be controlled by biasing the sample holder, keeping it grounded or keeping it at floating potential [117]. The temperature of the sample holder can be controlled using one of two thermostats, of which one operates with ethanol and one with oil. The resulting sample holder temperature is measured with a K-type thermocouple pressed against the backside of the sample holder [117].

As already previously reported in [46], the PlaQ setup was slightly modified since its description in [117]. One important modification was a replacement of the quartz microwave window by one made of aluminum oxide, which was expected to have a better resistance to erosion by the plasma. Furthermore, the microwave source was replaced by one with the same frequency and a similar working power.

All deuterium-plasma exposures reported in this thesis were performed with the sample holder at floating potential. The resulting differential ion-flux density to the sample holder was, as in [117], determined using a retarding field analyzer (RFA). It is displayed in Figure 3.9.

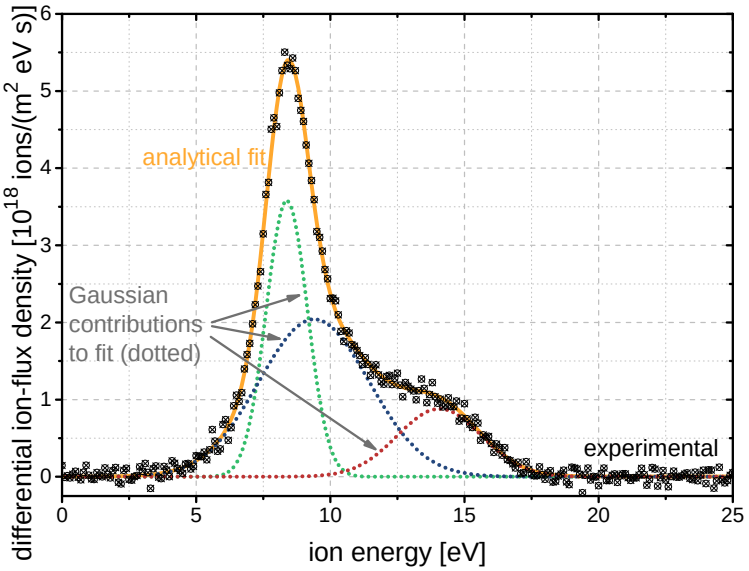

Figure 3.9.: Differential ion-flux density from the deuterium plasma measured with a retarding field analyzer. A fit of the data with a sum of three Gaussians plus a constant offset is also included (solid line) as well as the three Gaussians contributing to the fit result (dotted lines).

As already previously reported in [47], the experimentally determined differential ion-flux density was fitted with a smooth analytical function to enable an implementation of the energy distribution of incident deuterium ions into implantation simulations. This was necessary to avoid an influence of noise, especially in the high energy tail of the distribution, on the simulation result. A sum of three Gaussians plus a small constant offset resulted in an excellent fit of the measured data. The fit result is also included in Figure 3.9 together with the contributions of the individual Gaussians to the total fit result. The small offset was ascribed to a small drift of the measurement system and, therefore, subsequently neglected. It must be emphasized that the used fit function was not intended to represent any physical model, but was chosen purely due to its simplicity and its good fit to the experimental data.

To calculate the differential deuteron-flux density from the differential ion-flux density, the relative abundances of the different ion species reported in [117][1] for the sample holder at floating potential were used, as already previously reported in [47]. These were about 94 % for D_3^+, 3 % for D_2^+ and 3 % for D^+. The assumption of unchanged relative abundances appears justified because the deuterium pressure during plasma exposure was identical to the standard value of 1 Pa reported in [117], where the deuterium pressure

[1]Please also see the note on the relative abundances reported in [117] that is given in the reference list of [120].

had also been identified as the main parameter influencing the relative abundances. The differential deuteron-flux density carried by each ion species was calculated based on the fit to the differential ion-flux density, taking the number of deuterons in the ions of each species as well as the relative abundances of the ion species into account and assuming that the ion energy is shared equally between the deuterons in each ion. The total differential deuteron-flux density to the sample holder was then calculated by summing up the contributions from the individual ion species. It is displayed in Figure 3.10 together with the contributions carried by the individual deuterium-ion species and cumulative integrals of the curves. Integration of the displayed total differential deuteron-flux density yields a total incident deuteron-flux density of $J_{\text{incident}} = 6.0 \times 10^{19}$ D/(m^2 s) [47]. Uncertainties in this value may arise, e.g., from the reproducibility of the plasma source conditions, uncertainties in the RFA measurement as well as a variation of the flux density across the sample holder.

It must be noted that, as described in [117], a flux of neutral deuterium atoms originating from the plasma reaches the sample holder in addition to the ion flux. The deuteron flux carried by these neutral atoms is at least one order of magnitude higher than that carried by ions [117]. However, since the neutral deuterium atoms typically possess energies of far less than 1 eV [57], they are expected to lead to adsorption at the tungsten surface rather than implantation into the tungsten. As will be discussed in Section 6.1.2, the incident neutral deuterium atoms did not appear to contribute significantly to deuterium permeation and were, therefore, neglected in the analysis. A contribution from the neutral atoms to the deuterium retention in tungsten was also not observed in [57].

3.7. Accelerator-based ion-beam analysis (IBA)

Two methods of accelerator-based ion-beam analysis (IBA) were used for sample analysis. The structure and composition of thin layer systems was investigated by Rutherford backscattering spectroscopy (RBS). Nuclear reaction analysis (NRA) was used to investigate the deuterium distribution in the samples.

The IBA measurements were performed in the experiment chamber "Rückstreutopf" (RKS). A schematic drawing of the measurement geometry of RKS is displayed in Figure 3.11. The incident ions originated from the 3 MV tandem accelerator at the Max-Planck-Institut für Plasmaphysik, to which RKS is attached. The ^{3}He ion beam used for the measurements had a beam spot size on the sample of about 1 mm^2 and consisted of positively charged $^3He^+$ ions.

The computer program SIMNRA [121] in version 7 [122] was used to simulate spectra resulting from the RBS and NRA measurements. As described in detail in [121, 122], SIMNRA assumes a target consisting of layers with constant composition, which may also have complex features such as roughness.

3.7.1. Rutherford backscattering spectroscopy (RBS)

In Rutherford backscattering spectroscopy (RBS), the number and energy distribution of particles backscattered due to elastic collisions with sample atoms (compare Section 2.2)

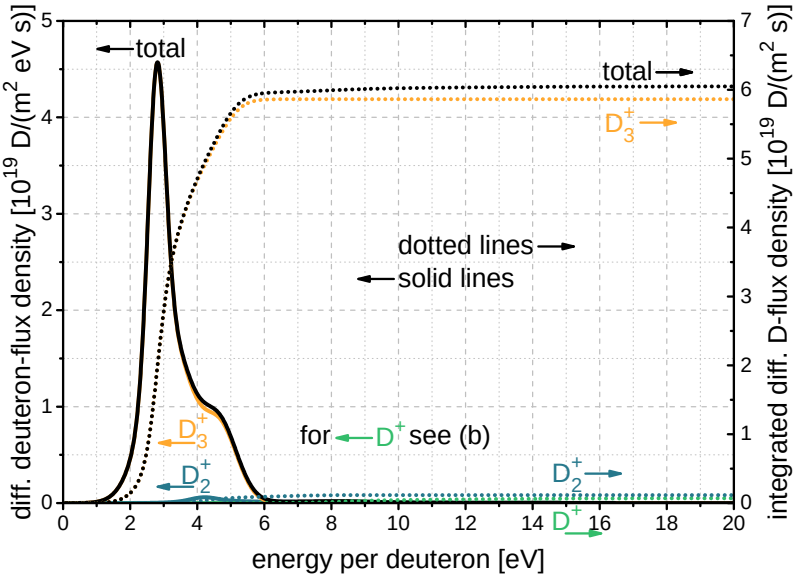

(a)

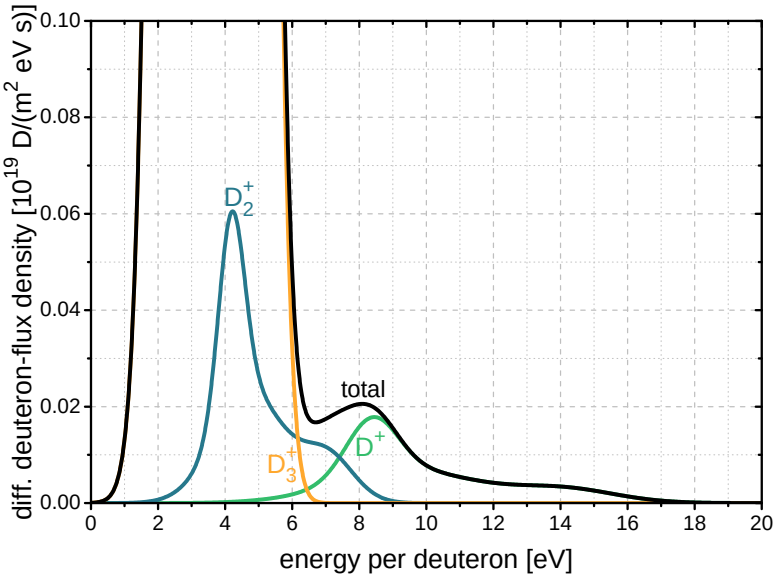

(b)

Figure 3.10.: (a) Total differential deuteron-flux density to the floating sample holder in PlaQ determined based on an analytical function fitted to the differential ion-flux density (presented in Figure 3.9) and using the relative abundances of the deuterium-ion species reported in [117]. The contributions carried by the individual deuterium-ion species are also included as well as the cumulative integrals of all curves. (b) shows the same differential deuteron flux densities as (a), but with rescaled vertical axis to focus on the contributions of D_2^+ and D^+. The data was already previously displayed in [47].

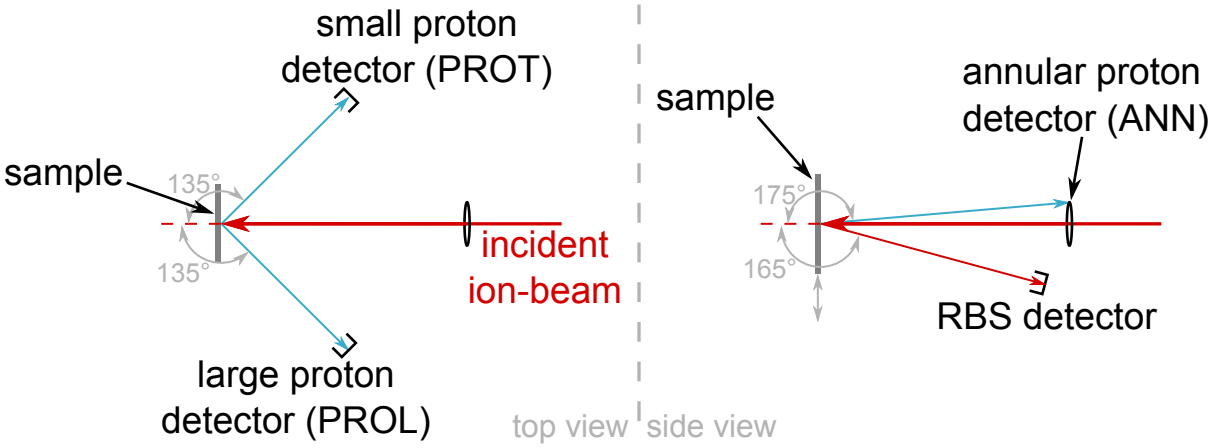

Figure 3.11.: Schematic drawing of the measurement geometry of the ion-beam analysis setup RKS including the detectors used for the experiments presented in this thesis. The incident ion beam from a 3 MV tandem accelerator interacts with the sample atoms. A RBS detector is used to measure the energy spectra of backscattered ions. Three proton detectors with different sizes and shapes are used to determine the energy distribution and number of protons reaching the detectors after they were generated in nuclear reactions of incident ions and sample atoms.

into a solid angle element can be used to determine a depth profile of the elemental composition of the sample's sub-surface region, as described in detail, e.g., in [123, 124]. Due to the kinematics of RBS, it is especially well suited for the detection of heavy elements [123]. A big advantage of RBS compared to other techniques is that a simple analytical formula is available for the differential scattering cross-section. It enables a quantitative measurement without standards [123, 124] and can be written as

$$\left(\frac{\mathrm{d}\sigma}{\mathrm{d}\Omega}\right)_{\mathrm{CMS}} = \left(\frac{Z_1 \cdot Z_2 \cdot e^2}{16 \cdot \pi \cdot \epsilon_0 \cdot E_{\mathrm{CMS}}}\right)^2 \frac{1}{\sin^4\left(\frac{\theta_{\mathrm{CMS}}}{2}\right)} \tag{3.1}$$

in the center of mass system (CMS) [123, 124]. Z_1 and Z_2 are the atomic numbers of projectile and target atom, respectively, e is the elementary charge, ϵ_0 is the vacuum permittivity, E_{CMS} is the kinetic energy in the system, and θ_{CMS} is the scattering angle in the center of mass system.

As already previously described in [47], backscattered ^{3}He ions were detected in RKS using a solid-state detector with a solid angle of 1.1 msr under a scattering angle of 165°. The resulting data was analyzed by simultaneously fitting simulated RBS spectra to experimental spectra recorded with different incident ^{3}He energies in a multiparameter optimization using MultiSIMNRA [125], which uses SIMNRA [121, 122] for physics calculations. The objective function used in the fitting procedure was chosen to be the regular χ^2 instead of the reduced χ^2, which was used in [125].

As an example, the experimental RBS spectrum resulting from the interaction of a 3200 keV ^{3}He ion beam incident on a multilayer system (compare Chapter 4 and [46, 47] for

layer system) is displayed in Figure 3.12. The counts of detected backscattered particles are grouped into so-called channels, which represent certain energy intervals. Details on the energy calibration, which links the channel numbers to the particle energies, will be given in Section 4.4.1. Figure 3.12 also includes a simulation result from SIMNRA using a layer structure determined with MultiSIMNRA. In the MultiSIMNRA optimization, the displayed and an additional RBS spectrum recorded for a different incident ^{3}He energy at the same position of the sample were fitted simultaneously. Roughness for substrate and first layer were included in the fitting procedure. Contributions resulting from the individual target elements are also plotted. Experiment and simulation are in very good agreement. Further details regarding the evaluation procedure used will be given in Section 4.4.1.

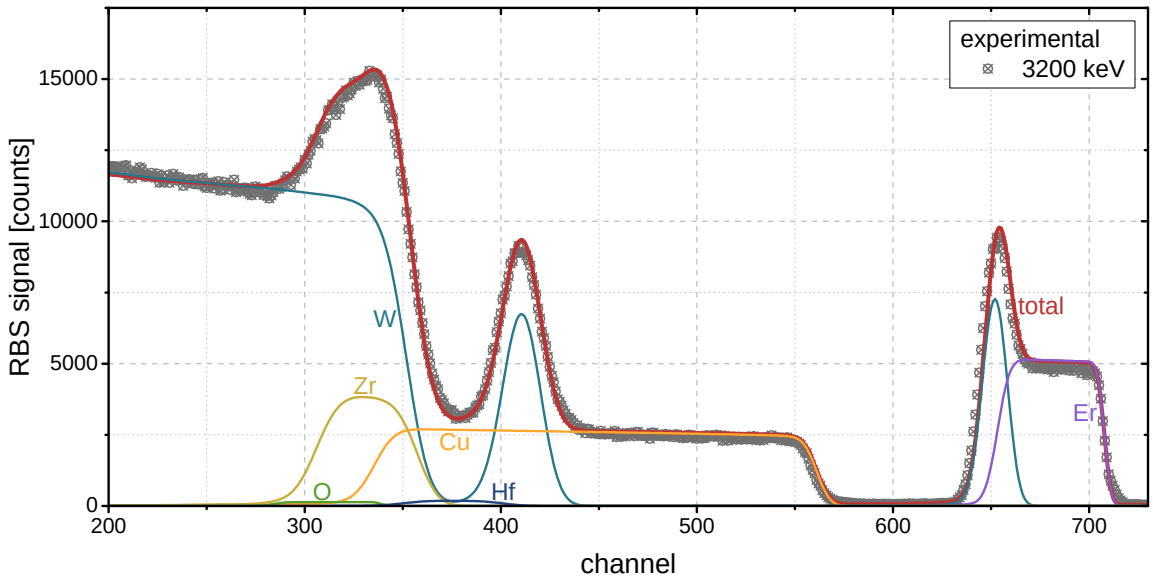

Figure 3.12.: Experimental RBS data and SIMNRA [121, 122] simulation result for 3200 keV ^{3}He ions incident on a multilayer system (compare Chapter 4 and [46, 47] for layer system). The layer structure used in the simulation was determined by simultaneously fitting this and an additional RBS spectrum with MultiSIMNRA [125], including roughness in the substrate and first layer. Also the contributions by individual elements are displayed. The total spectrum is also included in Figure 4.7, in the discussion of which additional details will be given.

Note: SIMNRA applies pile-up correction only to the total spectrum, but not to the individual elemental spectra. This can lead to seemingly unlogical effects, such as the tungsten contribution (blue) being larger than the total spectrum (red) near channel 200 [126]. The slight shift between the simulated and experimental peak near channel 650 originates from the simultaneous fitting of multiple RBS spectra (compare Figure 4.7).

3.7.2. Nuclear reaction analysis (NRA)

As already mentioned in Section 2.2, incident ions that have a sufficiently high energy to overcome the electrostatic repulsion can undergo nuclear reactions with nuclei in the sample. As described in detail, e.g., in [61], a number of reaction products is created and emitted in this process. In contrast to elastic collisions, the energy of the emitted particles is not simply determined by conservation of the kinetic energies of projectile and target atoms, but has an additional contribution by the energy released or absorbed in the nuclear reaction, the so-called Q-value. The reaction cross-sections for nuclear reactions used in NRA can, in contrast to the scattering cross-section used in RBS (Equation 3.1), not be described by a simple analytical formula. Therefore, measured cross-sections reported in the literature that were determined for the reaction and experimental conditions of interest are usually used. A strength of NRA compared to RBS is its superior capability to detect light elements.

The use of the nuclear reaction D(^{3}He,p)^{4}He of incident ^{3}He ions with deuterium in a sample is well established for the determination of depth profiles of deuterium in different materials [127] and has been used in numerous studies on deuterium retention in tungsten (e.g. [21, 29, 34, 41, 43]). Therefore, this reaction was also used for deuterium detection and quantification by NRA in experiments reported in this thesis. For the deuterium detection by NRA presented here, the reaction cross section reported in [128] was used. Protons emitted due to the reaction were detected with the large and small proton detectors of the RKS setup, which are referred to as PROL and PROT, respectively. Both detectors are mounted under a reaction angle of 135° and have solid angles of 77.5 msr for the PROL detector and 30.3 msr for the PROT detector. Data recorded with an additional annular proton detector, abbreviated as ANN, with a solid angle of 13.3 msr and mounted under a reaction angle of 175° was unfortunately not usable for most measurements. All proton detectors have a foil in front of their entrance slit which can easily be passed by the high energy protons, but prevents reflected ^{3}He ions and other reaction products from reaching the detector.

The detection of protons is energy resolved. This means that the counts of detected protons are grouped into so-called channels, which represent an energy interval $E + \Delta E$. Thus, an energy spectrum in the form of the number of protons per channel is recorded. The correlation between channel number and proton energy must be determined by calibration measurements. One frequently used method is the detection of protons originating from a thin layer deposited on a substrate that does not contribute to the proton signal. The advantage of a very thin layer is that stopping of incident and emitted particles in the layer can often be assumed to be negligible. Protons emitted from an about 12 nm thin amorphous deuterated carbon (a-C:D) layer [129] on a tungsten substrate were used for energy calibration for the NRA measurements presented in this thesis.

Deuterium as well as carbon atoms contained in the a-C:D layers react with incident ^{3}He ions by the nuclear reactions D(^{3}He,p)^{4}He [127, 128] and ^{12}C(^{3}He,p)^{14}N [130], respectively. Channel numbers and energies of the resulting proton-peak maxima were determined from experiments and SIMNRA simulations, respectively, for a number of selected ^{3}He energies. For the determination of the exact peak positions, the proton spectra were fitted with analytical functions. A peak in the proton spectrum, simulated with SIMNRA for

the conditions of the PROL detector, resulting from the reaction of 1800 keV ^{3}He with deuterium in a thin a-C:D layer is displayed in Figure 3.13a. It was fitted with a Gaussian function

$$y = a \cdot \mathrm{e}^{-\frac{(x-b)^2}{2c^2}} + d \tag{3.2}$$

as well as an asymmetric Gaussian function consisting of a two-piece normal distribution

$$y = \begin{cases} a \cdot \mathrm{e}^{-\frac{(x-b)^2}{2c_1^2}} + d & \text{for } x \leq b \\ a \cdot \mathrm{e}^{-\frac{(x-b)^2}{2c_2^2}} + d & \text{for } x > b, \end{cases} \tag{3.3}$$

(compare [131]), which are also included in the figure. Both fits were performed by non-linear least-squares fitting weighted according to Poisson statistics. Weights of infinity arising due to zero counts in a channel were replaced by one, similar to [125].

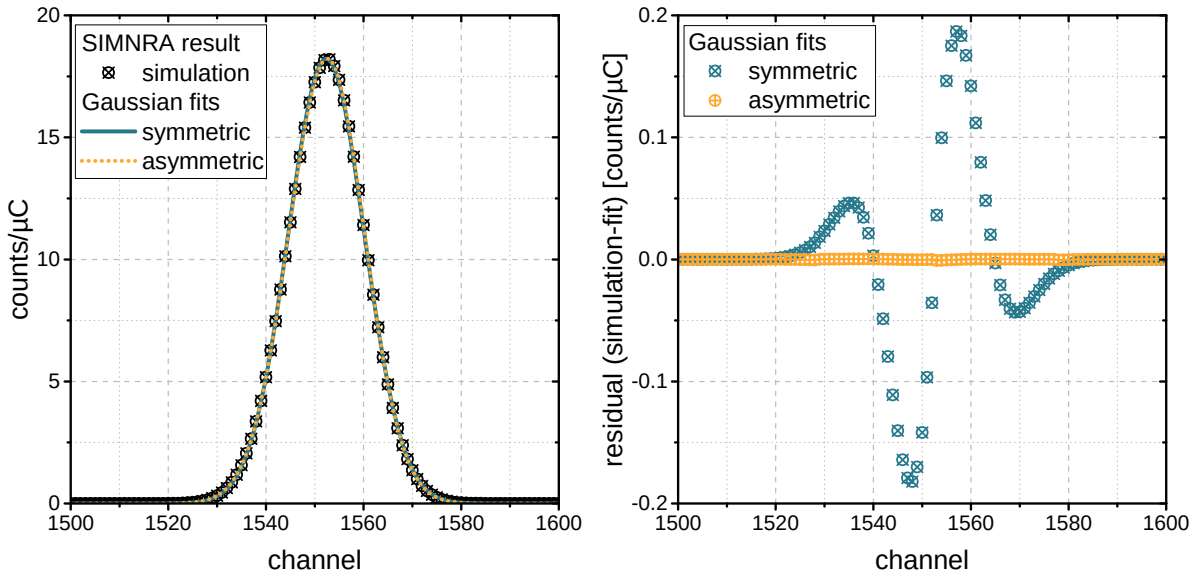

(a) (b)

Figure 3.13.: SIMNRA simulation of the proton peak resulting from the nuclear reaction of incident ^{3}He ions with deuterium in an approximately 12 nm thin a-C:D layer. The simulations were performed for 1800 keV incident ^{3}He energy, the conditions of the PROL detector and a known energy calibration. The simulated data is shown together with a fitted Gaussian as well as a fitted asymmetric Gaussian curve in (a). The residuals, defined as the difference of simulated data and fit, of both fits plotted in (b) reveal a significantly better fit with the asymmetric Gaussian.

While both fits appear to match the data well, their residuals, plotted in Figure 3.13b, reveal a significantly better fit using the asymmetric Gaussian. This asymmetry in the proton spectrum at least partially results from an asymmetry in the energy distribution of the ^{3}He ions caused by energy loss in the thin a-C:D layer (compare [131]). Consequently,

the asymmetric Gaussian was finally used in the determination of the proton-detector calibrations based on simulated and experimental data.

In the case of the simulated spectra, the energy calibration is known. It was simply chosen close to the expected experimental energy calibration. The desired peak energies could thus be easily determined based on the simulated peak position in channels and the known energy calibration in the simulations. An example of a fit to an experimental proton spectrum is displayed in Figure 3.14a.

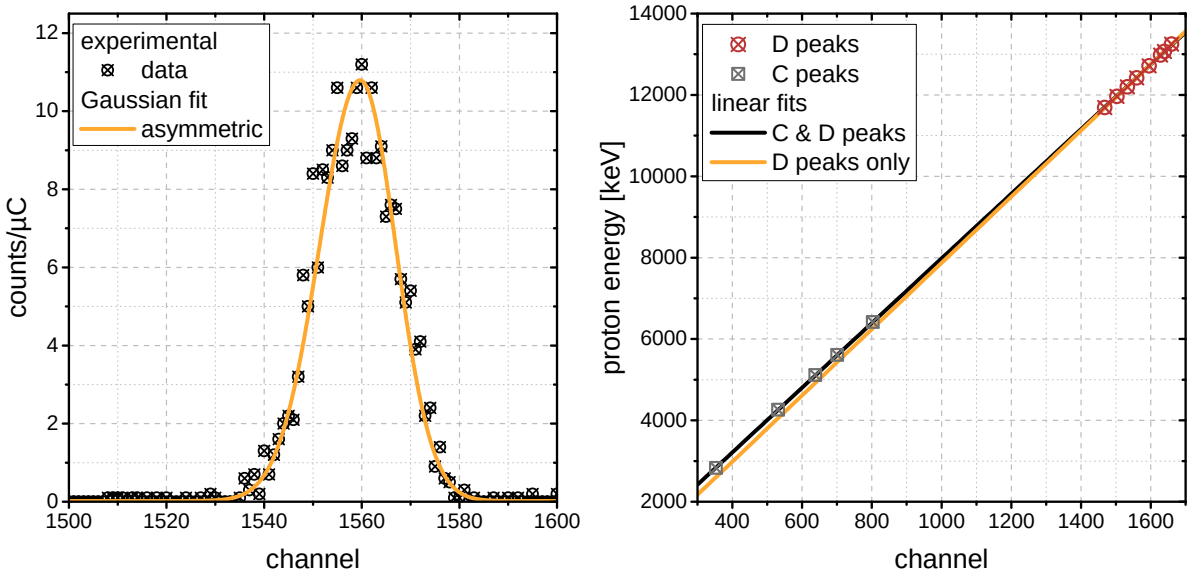

(a) (b)

Figure 3.14.: (a) Proton spectrum from the nuclear reaction of ^{3}He with deuterium in a thin a-C:D layer measured using the PROL detector, 1800 keV incident ^{3}He energy and a collected charge of 10 µC. An asymmetric Gaussian curve fitted to the data is also included. (b) Determination of the PROL detector's energy-calibration using a thin a-C:D layer. Positions of peaks resulting from ^{3}He reactions with C and D are shown. Linear fits to the C and D data as well as only the D data are included.

With this method, pairs of channels and corresponding proton energies were determined based on experimental and simulated proton peaks. The reaction of ^{3}He with deuterium in the a-C:D layer led to one peak in each of the proton spectra for the relevant energy range of 500 keV to 4500 keV incident ^{3}He energy. In contrast, the reaction of ^{3}He with carbon in the a-C:D layer yielded zero, one or more peaks, depending on the incident ^{3}He energy. This effect results from the fact that the reaction of ^{3}He with ^{12}C can occur with different Q values that originate from the ground and different excited states of the ^{14}N product nucleus [130]. An example of the resulting correlation of channels and proton energies is displayed in Figure 3.14b. Due to the high energies of the emitted protons, the energy calibration of the proton detector is typically approximated with a linear function [126, 132], which is determined by fitting this data. Such linear fits were performed for the peak positions resulting from reactions of ^{3}He with carbon and

deuterium (C & D peaks) as well as for peak positions resulting from reactions with deuterium only (D peaks only), using the linear least-squares method. The linear-fit results are also included in Figure 3.14b. The linear fit using C and D peaks appears to give a good fit over the whole range of channels, while the fit taking only the D peaks into account gives a good representation in the region of the D peaks, but not in the region of the C peaks. Still, the fit based only on the D peaks was used for the final energy calibrations of the proton detectors, because it gave a better local approximation of the real non-linear detector calibration function in the region where the peaks of actual deuterium retention measurements were located.

Since the proton spectrum resulting from a certain deuterium depth distribution in a sample can be simulated using SIMNRA, it is possible to check whether a certain depth profile can yield an experimentally determined proton spectrum. However, since the proton spectrum is a convolution of the depth distribution and the energy dependent reaction cross section, the determination of a depth profile from a proton spectrum recorded at a single incident energy is typically only possible with a very poor resolution. Therefore, a set of proton spectra recorded with a series of incident ^{3}He energies is typically used for the determination of deuterium depth profiles [127].

To determine the depth profile of a trace impurity, e.g. deuterium, in a sample, spectra resulting from IBA can be analyzed using the computer program NRADC [133]. It uses SIMNRA for physics calculations and has been used by different researchers to determine deuterium depth profiles in tungsten based on NRA data for a number of studies (e.g. [21, 34, 41, 104]). The large number of physics calculations using SIMNRA that would be required to fit the simulated to the experimental proton spectra would be computationally expensive. Therefore, NRADC reduces the determination of the proton spectra for a certain depth profile to a simple matrix multiplication, with the matrix determined based on a single set of SIMNRA simulations [133].

As described in detail in [133], NRADC uses the following procedure for this purpose: to determine the required matrix, the sample is divided into a set of layers, subsequently referred to as sub-layers, of constant composition, as required by SIMNRA. The IBA signal resulting from a certain trace element atomic fraction in a certain sub-layer, with the atomic fraction of the trace element being zero in all other sub-layers, is then determined for each sub-layer using SIMNRA. The results of these simulations are used to determine the elements of the matrix that correlates a certain trace-element atomic fraction in a certain sub-layer to the resulting counts in the simulated IBA spectrum. When applied to a depth profile with certain atomic fractions in the sub-layers, the resulting IBA spectrum can subsequently be determined by a simple multiplication of the matrix with a vector representing the trace-element depth profile. However, this procedure is only applicable, if the influence of the trace impurity on stopping is negligible. This assumption is fulfilled for the deuterium atomic fractions in tungsten reported in this thesis (compare the results in Chapter 5 with [133]). With this computationally inexpensive way to determine the IBA spectra resulting from a certain trace-element depth profile, NRADC attempts to determine the most probable depth profile given the experimental data. To avoid the fitting of noise, NRADC does not simply determine the depth profile which yields the smallest deviation of simulated and experimental spectra, but bins sub-layers together in thicker layers using a statistical approach. The most probable number of layers in

which the sub-layers should be binned is determined by using Markov-Chain Monte Carlo (MCMC) optimization and marginalization, also known as Occam's razor, in a maximum likelihood approach. Given the most probable number of layers, the most probable depth profile is determined also by MCMC optimization, however with a fixed number of layers equal to the most probable number of layers. This final optimization step yields the most probable trace-element depth profile given the experimental IBA spectra.

An example set of proton spectra, all appended to each other in a single vector by NRADC, which were measured with the PROL and PROT detector for incident ^{3}He energies of 500 keV, 690 keV, 800 keV, 1200 keV, 1800 keV, 2400 keV, 3200 keV and 4500 keV on a tungsten sample that had been exposed to deuterium plasma, is displayed in Figure 3.15a. Besides the experimental data, also the final fit result determined with NRADC is included to demonstrate the very good agreement of experimental and simulated proton spectra. The most probable depth profile determined with NRADC for this set of proton spectra is displayed in Figure 3.15b. This step profile, which results from the assumption of layers of constant composition made by SIMNRA, is of course only an approximation to an expected continuous real depth profile.

As already previously reported in [47], the determination of uncertainties for the depth profile is challenging, because uncertainties in the trace element atomic fraction in each layer as well as uncertainties in the layer thicknesses must be taken into account. The uncertainty of the atomic fraction in a certain sub-layer can be assessed based on the probability distribution for the atomic fraction in this sub-layer, which is determined by NRADC in the final MCMC optimization run. Since this probability distribution can be complex, e.g. possess multiple local maxima, a representation by, e.g., uncertainty bands can usually only be a simplified representation of the full probability distribution. However, especially when multiple depth profiles shall be compared, such a simplified representation appears useful for a clear visualization. Therefore, 95 % uncertainty bands, which exclude the upper and lower 2.5 % of the probability distribution for the deuterium atomic fraction in each sub-layer, were included in the plots of deuterium depth profiles in this thesis together with the most probable depth profiles determined with NRADC. Consequently, the uncertainty bands are not discretized based on the layer structures of the most probable depth profiles, but based on the finer resolved sub-layer structures.

3.8. Thermal desorption spectroscopy (TDS)

In thermal desorption spectroscopy (TDS), as described in detail, e.g., in [134], a sample is typically heated with a certain temperature ramp in vacuum while desorbing species are detected with a quadrupole mass spectrometer (QMS). If the species of interest are not only located at the sample surface, but also retained in the sample bulk, the desorption flux may be determined not only by surface reactions, but also affected by bulk effects such as diffusion and trapping [135]. The temperature dependence of the desorption of different species can be used to investigate the energetics of surface processes [134, 136, 137] and bulk binding [135]. In the literature, TDS is also referred to as temperature programmed desorption (TPD) [136, 137], which is sometimes defined slightly different [134], and occasionally also as thermal desorption technique [135] or thermal effusion

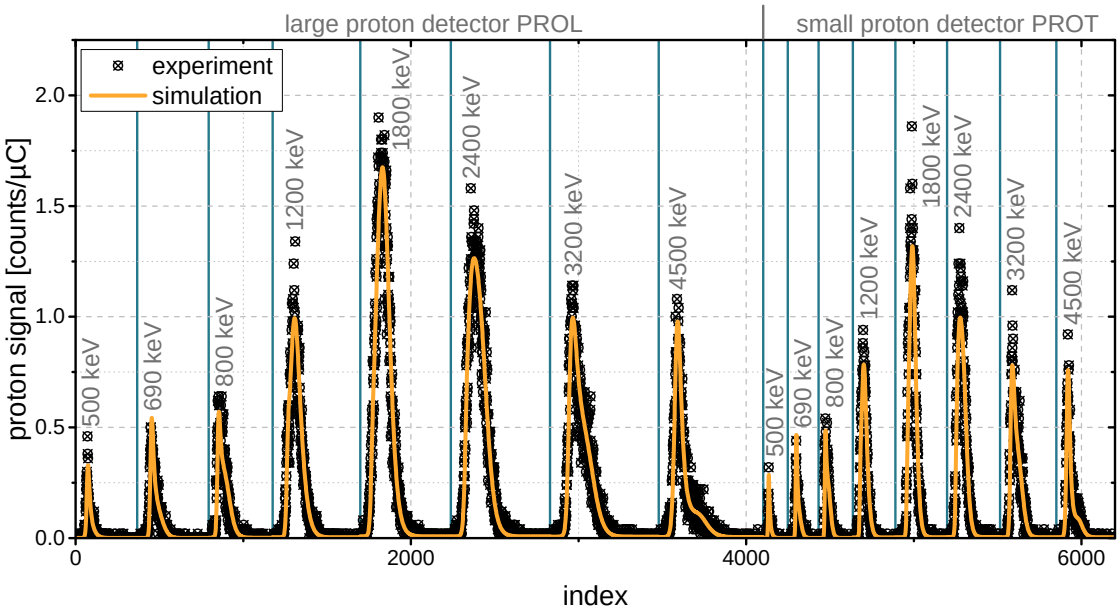

(a)

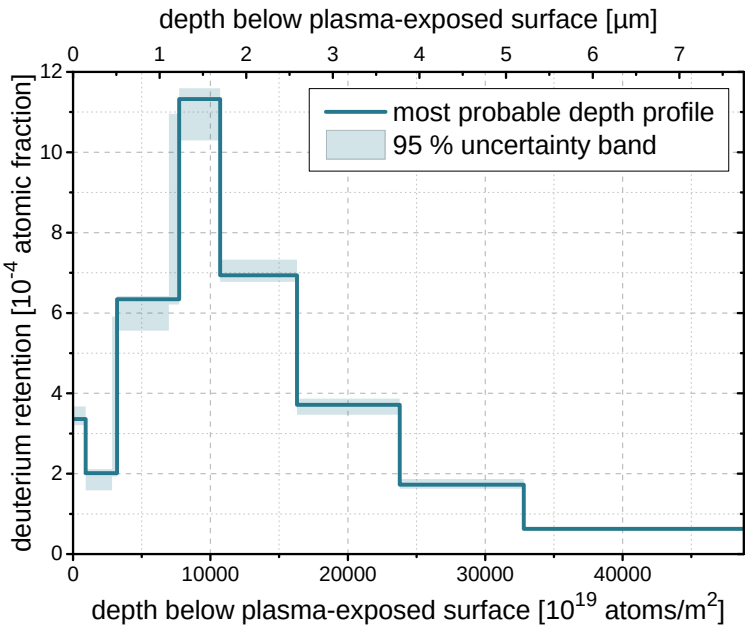

(b)

Figure 3.15.: (a) Experimental proton spectra recorded with the PROL and PROT detector for ^{3}He of different energies incident on a deuterium-plasma exposed tungsten sample. Also included is the simulation result for the corresponding most probable deuterium depth profile, which was determined using NRADC and is displayed in (b). The data in (b) was already previously displayed in [47]. Additional details on the sample from which this depth profile originates will be given in the discussion of Figure 5.6, in which this depth profile is included as the 336 h depth profile.

spectroscopy (TES) [138]. The TDS measurements presented in this thesis were performed to investigate the deuterium retention in tungsten after plasma exposure.

3.8.1. Measurement setup

The TDS measurements presented in this thesis were performed in the quartz-glass tube of the TESS setup, which is described in detail in [138]. A schematic drawing of TESS, which includes the most important components for measurements with samples in the quartz-glass tube, is presented in Figure 3.16. It includes also some of the modifications made since the description in [138].

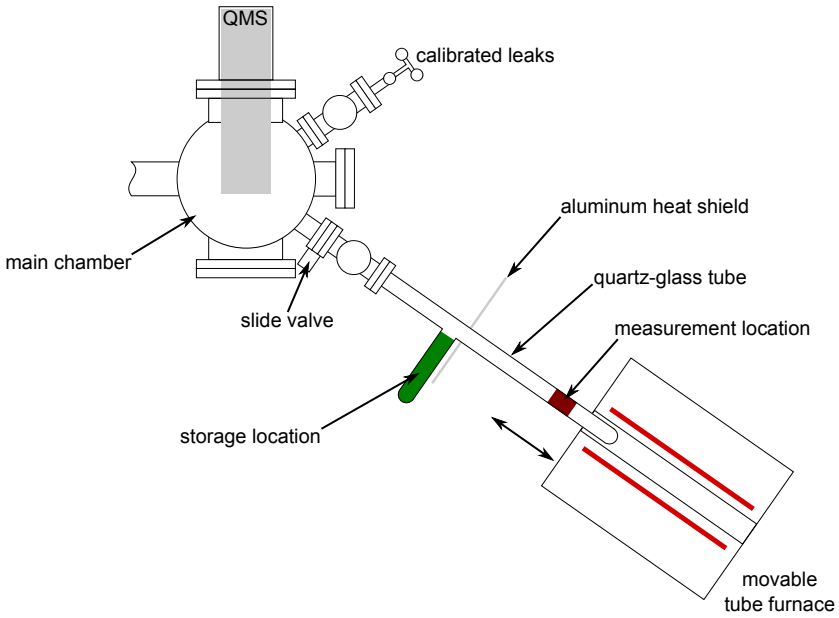

Figure 3.16.: Schematic drawing of the TESS setup used for TDS. It includes the components most important for measurements in the quartz-glass tube, which was used for the TDS measurements presented in this thesis. Important modifications since a detailed description in [138], such as a side arm of the quartz-glass tube, are included.

The samples to be investigated are stored in a side arm (storage location) of a quartz-glass tube, which is attached to the main vacuum chamber of TESS. They can be moved between the storage location and the measurement location without breaking the vacuum using a magnet outside and a ferromagnetic metal block inside the glass tube as in [138]. A movable tube furnace can be positioned such that the measurement location of the glass tube is inside the furnace [138]. While the sample located at the measurement location is heated by the furnace, the samples in the storage location remain approximately at ambient temperature. Species desorbing from the heated sample can be detected using a QMS attached to the main chamber without direct line of sight to the sample. Thus, detected species typically underwent a large number of collisions with the chamber walls before they reached the QMS [138]. This has a strong influence on the detection of species

that have a large sticking probability to the chamber walls, such as water [138, 139].

3.8.2. Temperature calibration and background subtraction

The dependence of the furnace temperature on time is determined by the selected heating ramp, except for small deviations caused by thermal inertia of the furnace. Typically a linear ramp to a certain temperature is chosen and the final temperature is then held for an additional amount of time. The furnace temperature ramp used for the TDS measurements described in this thesis was 15 K/min up to a temperature of 1050 °C, which was then held constant until cooldown. In contrast to the furnace temperature, the sample temperature is not directly measured during TDS measurements and can deviate significantly from the furnace temperature, as can be seen in an example displayed in Figure 3.17a. Therefore, the dependence of the sample temperature on the furnace temperature and thus time must be determined by calibration measurements. The temperature calibration measurement separate from the TDS measurements helps to avoid undesired effects such as a possible loss of deuterium from the sample due to a temperature increase caused by spot-welding a thermocouple to the sample.

Following the same procedure as described in [138] for the temperature calibration, a thermocouple is spot-welded to a sample, for which the TDS measurement has already been performed. The sample is mounted in the glass tube and heated with the same furnace temperature ramp as used for the TDS measurements, resulting in a measurement of furnace and sample temperature with a common time scale.

The furnace temperature ramp, which was nearly identical in all TDS and temperature calibration runs, was used to define a common time scale. Therefore, one temperature calibration measurement, whose furnace-temperature ramp is also included in Figure 3.17a, was selected as a time reference. The time scales of all other measurements were then shifted by a certain amount of time, to match the linear parts of the furnace temperature ramps to the reference. Thereby, also other measured signals like the desorption fluxes in TDS measurements or the sample temperature in temperature calibration measurements (see example in Figure 3.17a) were of course shifted.

To determine a possible temperature-dependent background in the QMS signals, TDS measurements without sample at the measurement location were performed. After they were shifted to the common time scale, the resulting background measurements were post-processed to prepare them for background subtraction, using the cubic spline interpolation procedure described in [140] implemented into a computer code by Udo von Toussaint (Max-Planck-Institut für Plasmaphysik). Afterwards, the interpolated backgrounds were subtracted from the corresponding TDS measurements, finally yielding background subtracted TDS measurements with a common time scale and known sample temperature evolution. An example of background subtraction is displayed in Figure 3.17b.

3.8.3. Desorption flux calibration

Using a QMS, only the number and mass-over-charge ratio of detected particles can be determined. Their chemical species cannot be determined directly. This leads to two issues that must be resolved in order to determine the desorption flux of a certain species

from a sample. First, different species with nearly identical mass-over-charge ratios that cannot be distinguished by the QMS exist in many cases. One example are D_2 molecules and ^4He atoms with the same charge state, which both have an atomic mass of about 4 u. This ambiguity makes reasonable assumptions regarding the desorbed and detected species necessary. For the present case of desorption from tungsten that was exposed to a deuterium plasma, the mass 4 u signal, assuming a charge state of plus one, was attributed to D_2. Similarly, signals at mass 3, 19 and 20 were assumed to be the deuterium-containing molecules HD, HDO and D_2O, respectively, again assuming a charge state of plus one. It is important to mention that these assumptions only need to take atoms and molecules desorbed from the sample into consideration, because contributions of species with similar mass-over-charge ratios to the background are removed by background subtraction at least if their appearance with respect to the heating ramp is reproducible.

The deuterium-containing molecular species are assumed to be formed at the sample surface, incorporating deuterium that effuses from the deuterium-plasma-exposed tungsten. While the D_2 molecules can safely be assumed to be formed by two effusing deuterium atoms that react at the sample surface, the H in HD and HDO is assumed to originate from residual hydrogen gas that adsorbs on the tungsten surface. A significant contribution from protium in the tungsten samples is not expected because the amount of protium remaining in the tungsten after the heat treatment described in Section 3.5 is expected to be negligible. The oxygen in the heavy water species may originate from a native oxide formed on the tungsten due to exposure to air or adsorbed H_2O that also results from the air exposure. Protium contained in adsorbed H_2O may also contribute to the protium contained in HD and HDO. However, also a formation of heavy water by reaction of D_2 or HD with H_2O molecules adsorbed at the chamber walls cannot be excluded. By such exchange reactions, even a conversion of D_2 into HD might occur at other locations than the sample surface.

The second issue is the necessity to determine a relationship between the number of particles detected by the QMS per unit time (in counts per second) and the desorption flux from the sample. This relationship is typically determined based on calibration measurements. For the present thesis, the number of counts per second of the mass 4 u signal recorded by the QMS for the known deuterium flux from a calibrated deuterium leak manufactured by Laco Technologies was used to calculate the desired calibration factor for D_2.

The calibration factor for HD was estimated based on the measured D_2 calibration factor using the ratio of the HD and D_2 calibration factors reported in [139], which were also measured in the TESS setup.

Calibration for the heavy water species HDO and D_2O is significantly more challenging, because sticking to the chamber walls is, in contrast to HD and D_2, not expected to be negligible for these species [139]. The sticking leads to adsorption of a part of the heavy water at the chamber walls, which can then not be detected by the QMS. The adsorbed heavy water may even desorb again later, if, e.g., the temperature of the chamber wall increases. This can lead to peaks in the TDS spectrum that are not related to desorption from the sample. This release may in the worst case even occur in a subsequent measurement of a different sample. To still get a rough estimate of the HDO and D_2O desorption flux, the calibration factors for HDO and D_2O were assumed to be identical

to that of H_2O, which was estimated based on the measured D_2 calibration factor using relative sensitivity factors reported in [141]. However, it must be noted that the thus determined calibration factors for heavy water have a large uncertainty and thus need to be used with caution [141].

As an example, the desorption fluxes of HD, D_2, HDO and D_2O molecules from a tungsten sample that was exposed to deuterium plasma, are displayed in Figure 3.18a normalized to the plasma-exposed area. Using the time evolution of the corresponding sample temperature, determined with the procedure described in Section 3.8.2, the molecule fluxes in molecules per time and area can be converted to molecules per temperature interval and area, as displayed in Figure 3.18b.

With the number of deuterium atoms per molecule of the individual species, the deuteron flux carried by each of the aforementioned molecular species can be calculated based on the corresponding molecule flux. The total deuteron flux results from summing up the contributions from the individual species. It is also included in Figure 3.18b. Frequently, the deuterium amount carried by heavy water is much smaller than the amount carried by D_2 (compare, e.g., [57, 139]). Unfortunately this is not the case for the experiments presented in this thesis, due to the overall low deuterium amount retained in the recrystallized tungsten samples after plasma exposure. Therefore, the uncertainties associated with the contributions from heavy water are unfortunately not negligible. The occurrence of a peak around 650 K for all species in Figure 3.18b suggests that this peak has the same origin for all species. In contrast, the long tail in the HDO signal is not present in the D_2 signal. This suggests that its origin is unique to heavy water. It might, e.g., result from a delayed transport of some HDO molecules to the QMS possibly due to sticking to and delayed re-desorption from certain parts of the setup.

Due to the uncertainties associated with the heavy water contributions and additional uncertainties due to possible desorption of other deuterium containing molecules that are not taken into consideration, a quantitative interpretation of the TDS results must be made with caution. Nevertheless, especially the peak positions of the D_2 signal may be affected only little by these uncertainties and thus the TDS data still appears suitable for a cautious interpretation, however, keeping the associated uncertainties in mind.

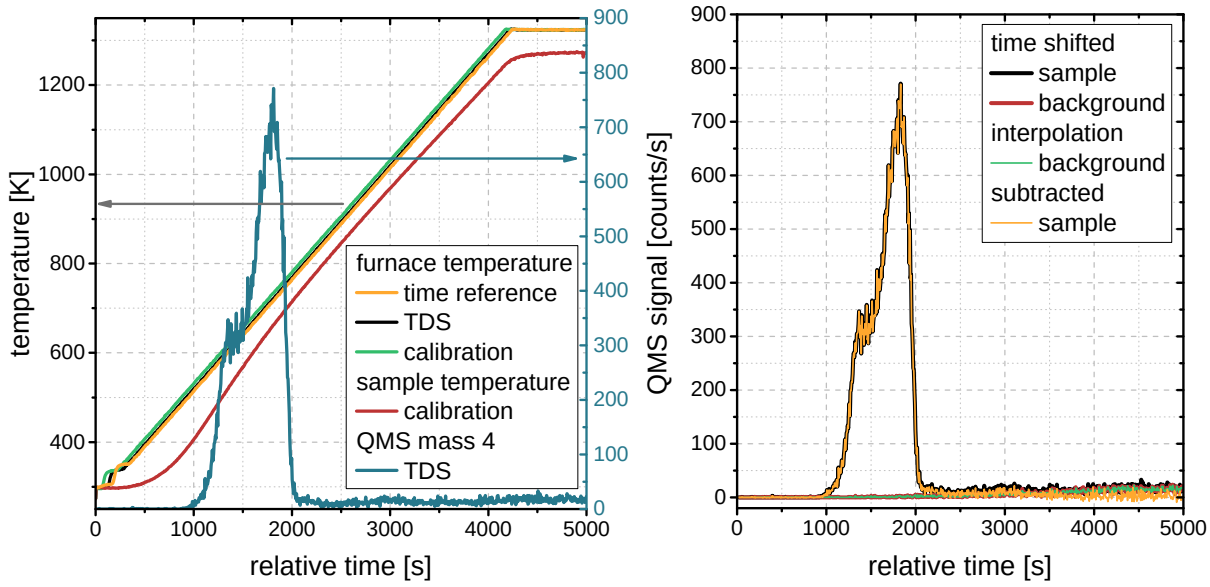

(a) (b)

Figure 3.17.: (a) Example for temperature calibration: The deviation of the sample temperature (red) from the furnace temperature (green), measured in a temperature calibration run with a thermocouple attached to a sample, demonstrates the necessity of temperature calibration. The time scales of TDS and temperature calibration measurements were matched by shifting their time scales such that the linearly increasing sections of the furnace temperature ramps (TDS: black, temperature calibration: green) were in coincidence with a common time reference furnace-temperature ramp (orange). Thereby, also the sample temperature of the temperature calibration measurement (red) and the desorption spectra of the TDS measurements (e.g. the mass 4 u signal represented by the blue line) were shifted to the common time scale. (b) Example for background subtraction: The result of a background measurement without sample (red) was interpolated (green) and subtracted from a TDS measurement result (black) to eliminate contributions that did not originate from the sample and thus gain a background-subtracted TDS signal (orange).

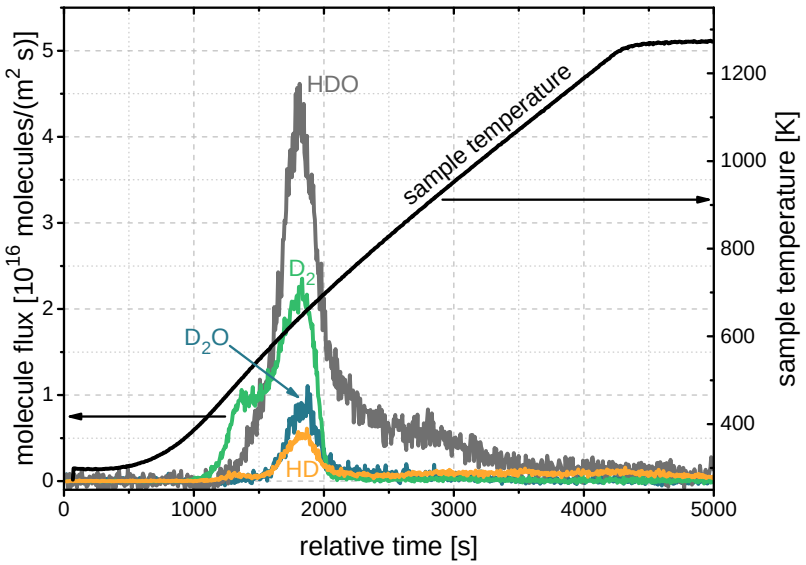

(a)

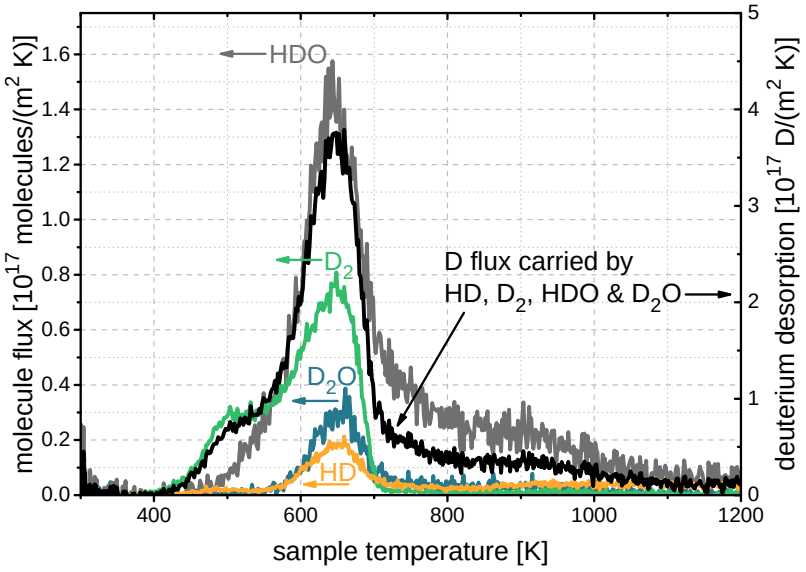

(b)

Figure 3.18.: (a) Desorption fluxes normalized to plasma-exposed area of deuterium containing molecules over time during TDS analysis for a tungsten sample that was exposed to deuterium plasma. Due to the overall low deuterium retention, a significant fraction is carried by heavy water species, which are difficult to quantify and thus have large uncertainties. Sub-figure (b) displays the same molecule fluxes, but this time converted to molecules per temperature interval and area, and the deuteron flux calculated from the molecule fluxes. The deuteron flux in (b) was already previously displayed in [47]. Additional details on the sample from which this data originates will be given in the discussion of Figure 5.9, in which the deuteron flux is included as the 300 K, 192 h data.

4. Measuring plasma-driven deuterium permeation through tungsten with a getter layer

The results presented in this chapter were in large parts already previously published in [46, 47].

Knowledge about the behavior of solute hydrogen isotopes in tungsten is crucial for the operation and especially safety of future nuclear fusion reactors with tungsten as plasma-facing material (compare Chapter 1). In general, permeation measurements are a commonly applied technique to get access to information about solute hydrogen isotopes in metals.

Unfortunately, the standard approach of gas-driven permeation measurements, where hydrogen gas is applied to one side of a sample and the permeation flux is measured on the other side typically by mass spectrometry, is challenging for tungsten especially near room temperature and below due to the very low solubility of hydrogen in tungsten in this temperature range. Gas-driven hydrogen-isotope permeation measurements on tungsten are, therefore, typically performed only at significantly higher temperatures (e.g., [27, 142–144]). By using a tritium tracer technique, Ikeda et al. [145] were able to perform gas-driven permeation measurements for tungsten near room temperature. They used natural hydrogen with a small added fraction of tritium and determined the permeated amount of tritium using a liquid scintillator on the permeation side of the sample. However, this method requires to work with radioactive tritium and thus imposes a severe safety hazard. Furthermore, the detection of a tracer instead of the predominant hydrogen isotope in the gas mixture may cause unpredictable deviations from the expected behavior [46]. For example, hydrogen isotope exchange in traps in tungsten, which can be expected to be present during tracer diffusion, is a complex phenomenon and a topic of on-going research (e.g. [39, 146–148]).

However, permeation measurements near room temperature are highly interesting because a large number of laboratory experiments regarding hydrogen isotope retention and microstructural modifications in tungsten after plasma exposure were performed also down to this temperature range (e.g. [20, 22, 24, 32, 57]). As already discussed in Chapter 1, such retention experiments are typically performed with deuterium, because it does not have the high natural abundance of protium [36] and is, in contrast to tritium, not radioactive [36].

An alternative to gas-driven permeation measurements are electrochemical permeation measurements. An electrochemical hydrogen permeation measurement technique was suc-

cessfully applied by Manhard et al. [149] for sputtered tungsten on a palladium substrate. However, sputtered tungsten is known to be significantly different compared to other tungsten grades with respect to hydrogen isotope retention [34] and thus may also not be fully comparable with, e.g., rolled tungsten with respect to permeation [46].

Another alternative are ion-driven permeation measurements. They appear suitable also for the use near room temperature, because hereby much higher solute hydrogen concentrations below the loading side and thus permeation fluxes than for gas-driven permeation can be achieved. The low solubility and corresponding low permeability of hydrogen in tungsten do not directly affect this kind of measurement. Nevertheless, such measurements were so far typically reported for higher temperatures (compare, e.g., [23, 26, 30, 150–152]).

Such ion-driven permeation measurements typically require a complex permeation measurement setup, which needs to be attached to the plasma or ion-beam source and usually includes a quadrupole mass spectrometer for hydrogen isotope detection. Unfortunately, such a setup is typically not attached to most ion-beam and plasma sources used to study hydrogen isotope retention in tungsten. Also, such an in-situ permeation measurement setup can probably often not be added easily to existing devices because of, among other reasons, limited space.

This chapter describes a method for plasma-driven deuterium-permeation measurements on tungsten near room temperature that can be applied with existing plasma devices used for retention studies without a need for device modification. It has been published already previously in [46] and an application plus some improvements were reported in [47]. Using a layer system deposited on the tungsten samples before plasma exposure, the actual measurement of the permeated deuterium amount, which is accumulated in a getter layer, is performed ex-situ after the plasma exposure is finished.

Following an explanation of the measurement principle in Section 4.1, details of the individual steps and their validation will be presented in Sections 4.2 to 4.4.

4.1. Measurement principle

The method used for the plasma-driven deuterium-permeation measurements presented in this chapter was already previously published in [46] and is summarized in Figure 4.1. Its basic principle is based on experiments reported by Möller et al. on stainless steel [153] and Børgesen et al. on nickel [154], where permeated deuterium was accumulated in a getter layer and subsequently analyzed by nuclear reaction analysis (NRA). The permeation measurement is hereby basically converted into a retention measurement.

The permeation measurements presented in this thesis were performed on the tungsten foil samples described in Section 3.5 after they were recrystallized at a temperature of 2000 K for 30 min in the vacuum furnace HADES. This annealing procedure was performed to reduce the defect density and thus the number of traps in the tungsten samples [46]. A low trap concentration was desired because it was expected to lead to a shorter time until the onset of permeation.

As in [153, 154], a getter layer of either zirconium (Zr), titanium (Ti) or erbium (Er) was deposited on the tungsten samples used for permeation measurements. The thickness of

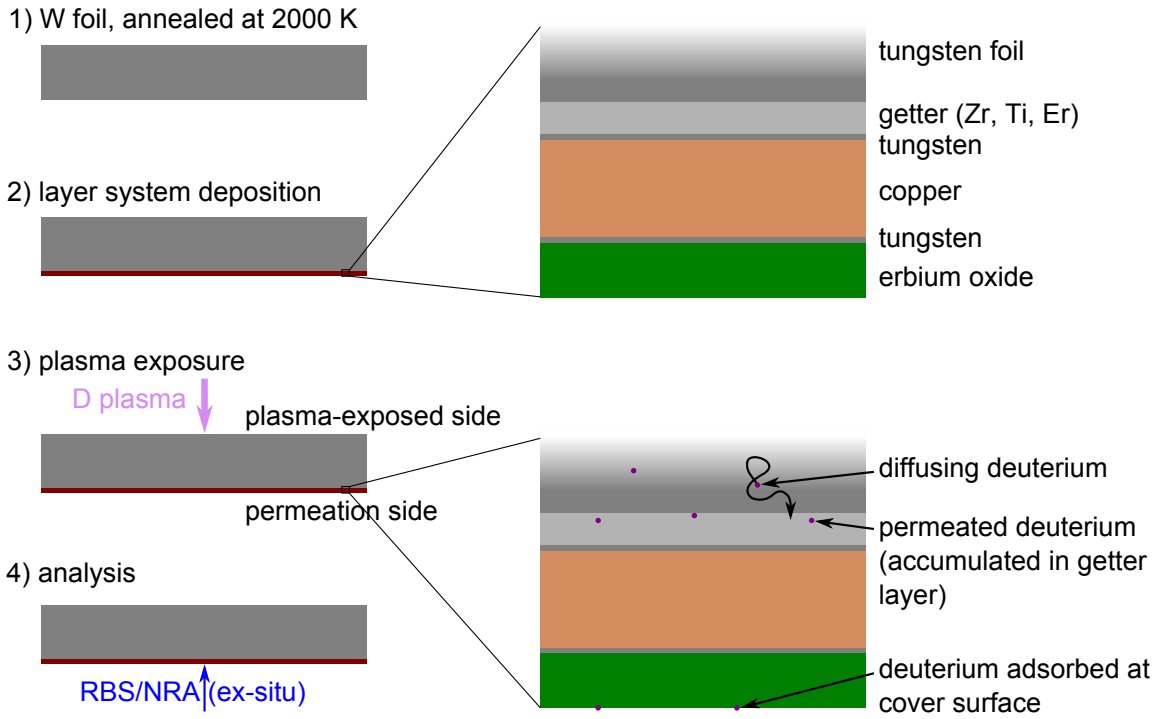

Figure 4.1.: Main steps of the method used to measure the deuterium permeation through tungsten near room temperature under deuterium-plasma exposure, which has already been published previously in [46]. 1) Tungsten samples are annealed to reduce the defect density and thus minimize the delay till an onset of the permeation flux caused by trapping. 2) Layer system deposition by magnetron sputtering. 3) Deuterium-plasma exposure and accumulation of permeated deuterium in the getter layer. The cover layer system prevents a direct loading of the getter from the deuterium background gas during plasma exposure and allows a distinction of deuterium in the getter and at the cover surface during the subsequent ion-beam analysis (4) by Rutherford backscattering spectroscopy (RBS) and nuclear reaction analysis (NRA) performed to determine the deuterium amount in the getter layer after plasma exposure.

the getter layers was chosen to be about 300 nm and thus of the same order of magnitude as in [153, 154], but the deposition was performed by magnetron sputter deposition [46], which is in contrast to the references, where evaporation was used. The side on which the getter layer for accumulation of permeated deuterium was deposited will subsequently be referred to as the *permeation side*. Additional details about the sample preparation and layer deposition will be presented in Section 4.2.

The uncoated side of the samples, which was later exposed to deuterium plasma, will subsequently be referred to as the *plasma-exposed side*. In contrast to [153, 154], deuterium loading of the samples was performed with a deuterium plasma instead of ion-beam loading. One advantage of plasma loading is that lower ion energies can be used, which was expected to diminish the generation of damage by collision cascades generated in the tungsten by the incident ions. Another advantage is the possibility to expose multiple samples at the same time to the plasma, which is especially interesting for comparative studies [46]. All deuterium-plasma exposures were performed in the laboratory plasma source PlaQ at floating potential to ensure a low energy of the incident deuterium ions. Additional details about the performed deuterium-plasma exposures will be presented in Section 4.3.

Since the deuterium-plasma exposures were performed at a much higher background pressure than typical ion-beam loading experiments, it was necessary to deposit a cover (see Figure 4.1) on the getter layer, to avoid a direct uptake of deuterium from the background gas into the getter during plasma exposure [46]. The top layer of the developed multilayer cover consists of erbium oxide, which was reported to be a good permeation barrier for hydrogen isotopes [155]. A copper (Cu) layer, located between getter and erbium oxide, is relevant for the ion-beam analysis used for deuterium detection as will be described in one of the following paragraphs. Thin tungsten layers between getter and copper as well as copper and erbium oxide were introduced to avoid interdiffusion of the other layers [46]. The tungsten interlayer between getter and copper was necessary because previous experiments had indicated interdiffusion of erbium and copper at 450 K, which was one of the exposure temperatures. Due to the immiscibility of erbium and tungsten [156] as well as copper and tungsten [157] in the temperature range of 300 K to 450 K relevant for the experiments presented in this thesis, a tungsten interlayer was a reasonable choice. In contrast to erbium, the zirconium-tungsten [158, 159] and titanium-tungsten [160, 161] phase diagrams indicate a miscibility also in the relevant temperature range. However, preliminary experiments did not indicate significant interdiffusion in the relevant temperature range, which is also important with respect to the interface of getter and tungsten foil. The tungsten interlayer between copper and erbium oxide was introduced because interdiffusion of the two had been observed already directly after deposition.

The amount of permeated deuterium stored in the getter layer was detected and quantified by nuclear reaction analysis (NRA) using the nuclear reaction $D(^3He,p)^4He$ (compare Section 3.7.2), as in [153, 154]. In contrast to [153, 154], the tungsten samples were typically not loaded with deuterium multiple times alternating with NRA measurements, but usually used for only one deuterium-plasma exposure with subsequent ion-beam analysis. This was done to exclude that defects and thus traps created in the tungsten foil below the getter layer by the incident ^3He analysis beam could affect the permeation measurements

with longer exposure times, as it had been reported to be a problem for stainless steel in [153]. Additionally, this strategy excludes that measurements with longer exposure times are affected by a possible loss of deuterium from the sample due to heating of the sample by the ^{3}He analysis beam. However, no indications for such an outgassing were found and it would in any case be expected to be strongly diminished by the cover layer system [46].

The cover layer system made also a different approach in the IBA necessary. The layer structure and composition had to be determined before the deuterium amount retained in the getter layer could be determined based on the NRA measurements. This is because the energy spectrum and number of protons emitted due to nuclear reactions of ^{3}He with deuterium in the getter depend on the energy spectrum of the ^{3}He ions from the analysis beam at the depth of the getter and the energy of the ^{3}He ions at the depth of the getter is affected by the layer system. The structure and composition of the layer system were, therefore, determined based on RBS measurement results [46].

By protecting the getter from environmental influences, the cover layer system made it possible that the IBA was, in contrast to [153, 154], performed ex-situ, which means the plasma device was not attached to the accelerator used for IBA. Since no indications for loss of deuterium from the getter were found even for measurements that were repeated after ten months of sample storage, this approach spatially and temporally decouples the determination of the permeated deuterium amount from the plasma exposure. It thus enables the use of existing plasma devices without a permeation setup for permeation experiments [46]. The determination of the permeated deuterium amount by IBA can thus in principle even be performed at a different institution than the plasma exposure, what dramatically increases the number of plasma sources that can potentially be used for the deuterium loading.

A certain amount of deuterium was typically present at the surface of the cover after the deuterium plasma exposure. The copper layer mentioned before, together with the other cover layers, caused stopping of the incident ^{3}He ions of the analysis beam and thus led to different energies of protons detected for reactions in the getter and at the cover surface. The resulting peak separation in the signal from the proton detectors can be used to distinguish these contributions. Copper was chosen for this purpose because it could be deposited much faster than erbium oxide [46]. This appeared favorable in order to minimize the temperature increase of the samples during deposition and thus further reduce the probability of interdiffusion. A cover purely made of copper, however, appeared unsuited, because permeation of deuterium through copper into the getter had been observed in such a preliminary experiment.

To ensure a permeation measurement with well interpretable data, it is desirable that all deuterium that reaches the permeation side is stored in the getter. Since all solute deuterium in the tungsten at the permeation side is then lost to the getter, this corresponds to a zero-concentration boundary condition for the solute at the permeation side. In contrast to typical permeation measurements with detection by mass spectrometry, recombination limitation can be excluded with the getter method, because the deuterium atoms do not need to recombine to molecules in order to be detected. However, also no diffusion barrier that impedes the uptake of deuterium into the getter may be present at the interface and the combination of dissolution and redistribution of deuterium in the getter must ensure that a possible accumulation of deuterium at the interface is limited

to a maximum concentration that still ensures that the solute concentration in the tungsten at the interface is negligible. If no diffusion barrier is present, the situation at the tungsten-getter interface, located at $x = L$, can be described using Equations 2.29 and 2.31 as

$$\frac{c^{\text{solute}}_{\text{D,W}}(L)}{S_{\text{D,W}}} = \frac{c^{\text{solute}}_{\text{D,getter}}(L)}{S_{\text{D,getter}}} \tag{4.1}$$

and

$$D_{\text{D,W}} \cdot \left.\frac{\partial c^{\text{solute}}_{\text{D,W}}}{\partial x}\right|_L = D_{\text{D,getter}} \cdot \left.\frac{\partial c^{\text{solute}}_{\text{D,getter}}}{\partial x}\right|_L , \tag{4.2}$$

with Sieverts' constant $S_{\text{D,W}}$, diffusivity $D_{\text{D,W}}$ and solute concentration $c^{\text{solute}}_{\text{D,W}}$ of deuterium in the tungsten and Sieverts' constant $S_{\text{D,getter}}$, diffusivity $D_{\text{D,getter}}$ and solute concentration $c^{\text{solute}}_{\text{D,getter}}$ of deuterium in the getter.

For $S_{\text{D,W}} \ll S_{\text{D,getter}}$, the hydrogen concentration at the interface in the tungsten will always be much smaller than the concentration at the interface in the getter:

$$S_{\text{D,W}} \ll S_{\text{D,getter}} \Rightarrow c^{\text{solute}}_{\text{D,W}}(L) \ll c^{\text{solute}}_{\text{D,getter}}(L). \tag{4.3}$$

Regarding the diffusivities, the two limiting cases

$$D_{\text{D,W}} \gg D_{\text{D,getter}} \Rightarrow \left.\frac{\partial c^{\text{solute}}_{\text{D,W}}}{\partial x}\right|_L \ll \left.\frac{\partial c^{\text{solute}}_{\text{D,getter}}}{\partial x}\right|_L \tag{4.4}$$

and

$$D_{\text{D,W}} \ll D_{\text{D,getter}} \Rightarrow \left.\frac{\partial c^{\text{solute}}_{\text{D,W}}}{\partial x}\right|_L \gg \left.\frac{\partial c^{\text{solute}}_{\text{D,getter}}}{\partial x}\right|_L \tag{4.5}$$

can be considered.

The situation during deuterium-plasma exposure can be described by assuming an initially deuterium-free sample (consisting of tungsten and a getter layer), where a fixed sub-surface deuterium concentration $c^{\text{solute}}_{\text{D,W}}(x = d_{\text{impl}}) = c_{\text{s}}$ is generated directly below the plasma-exposed tungsten surface ($d_{\text{impl}} \ll L$) and no deuterium can leave the sample through the backside of the getter, corresponding to $\jmath(x = L+d_{\text{getter}}) = 0$, due to the cover layer system. The general shape of the resulting solute-deuterium concentration profiles during steady-state permeation expected for the two limiting cases for the diffusivities (Equations 4.4 and 4.5) are sketched in Figure 4.2.

In the case of Equation 4.4, the diffusion of deuterium deeper into the getter is slower than the diffusion in the tungsten. Therefore, the concentration of deuterium increases locally in the getter near the tungsten-getter interface because it is not redistributed fast enough in the getter. Despite Equation 4.3, the solute-deuterium concentration in the tungsten at the interface can in this case increase significantly and reach, at maximum, the value of the sub-surface concentration c_{s}.

In the case of Equation 4.5, deuterium that reaches the getter is quickly redistributed in the getter. This keeps the deuterium concentration at the interface in the getter low. Together with Equation 4.3 this ensures

$$c^{\text{solute}}_{\text{D,W}}(L) \approx 0 \tag{4.6}$$

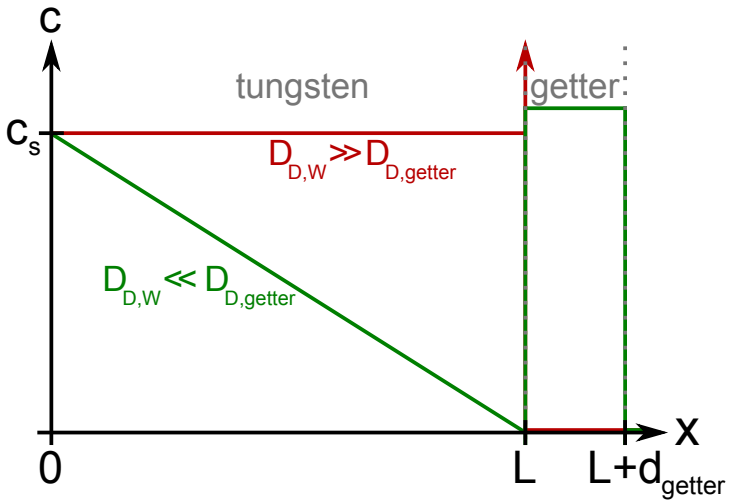

Figure 4.2.: Expected general shape of the solute-deuterium concentration profiles in the tungsten-getter system during steady-state permeation for two limiting cases of the diffusion coefficients. A much higher hydrogen solubility in the getter compared to tungsten has been assumed.

and thus for the ratio of solute-deuterium to tungsten atoms

$$r_{\mathrm{D,W}}^{\mathrm{solute}}(L) \approx 0 \tag{4.7}$$

in the tungsten at the permeation side even for quite large amounts of deuterium stored in the getter. This is the most favorable case because it ensures that a simple zero-concentration boundary condition can be assumed at the permeation side of the tungsten and all deuterium that reaches the getter is stored there. Since, in this case, the diffusion of deuterium in the tungsten to the interface determines the rate with which deuterium is accumulated in the getter, the described boundary condition can also be referred to as diffusion-limited.

The exact situation present in the real tungsten-getter system is difficult to predict. Zirconium, titanium and erbium all have complex phase diagrams with different hydride phases [162–164]. During hydride formation, the metal-hydrogen system undergoes a phase transition, which can also modify the crystal structure of the metal [165]. The normal solid-solution phase and a hydride phase can even exist in parallel at the same time, which additionally complicates the situation. Taking the phase diagrams for the getter materials in [162–164] into account, this appears also possible in the temperature range of the permeation measurements, which were performed at 300 K and 450 K. The comparison of the hydrogen solubilities and diffusion coefficients is additionally complicated by large uncertainties associated with these values, e.g. due to extrapolation from measurements at higher temperatures. Since the getter layers are sputtered films and not bulk material, possible effects resulting from the deposition process must also be taken into account. The generated defect structure in the getter may change the amount of deuterium that can be retained due to trapping or generate fast diffusion paths in the getter.

Sieverts' constants and diffusion coefficients in tungsten, zirconium and titanium as reported in the literature [40, 166–171] are displayed in Figure 4.3. At both temperatures

of interest for the experiments reported later, 300 K and 450 K, the Sieverts' constant of hydrogen in tungsten is many orders of magnitude lower than in zirconium and titanium. Based on the fact that erbium is also a hydride forming metal, it appears reasonable to expect this to be true also for erbium even though no corresponding literature data was found. The Sieverts' constants were determined based on literature data for the solid solution phase without hydride formation. Possible hydride formation may modify the difference between the Sieverts' constants in tungsten and in the getter materials. Still, since the difference of the Sieverts' constants for hydrogen in tungsten and in the getter materials determined based on the above-mentioned literature data is enormous, it appears in any case reasonable to assume that the desired situation described by Equation 4.3 is fulfilled for all three getter materials.

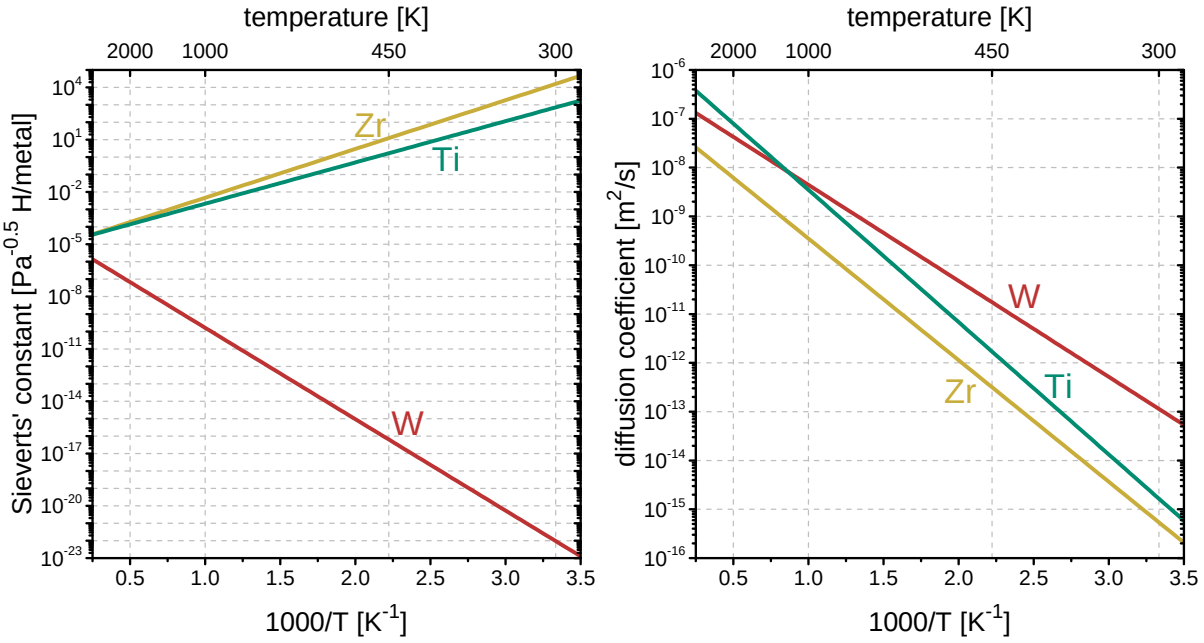

Figure 4.3.: (a) Sieverts' constants (solubilities) and (b) diffusion coefficients of hydrogen in tungsten, zirconium and titanium as reported in the literature. The Sieverts' constants are based on [40] (using the converted formula given in [37]) for W, [166] for Zr and [167] (as cited in [168]) for Ti. The diffusion coefficients are based on [40] for W, [169] for Zr and [170] (as cited in [171]) for Ti.

In contrast to the Sieverts' constants, the diffusion coefficients calculated based on literature data do not fulfill the desired condition of Equation 4.5. However, also Equation 4.4 is not as clearly fulfilled as in the case of the solubilities, especially when considering the large uncertainties associated with the extrapolation from literature data measured at higher temperatures. As in the case of the Sieverts' constants, no literature value was found for the diffusion coefficient in erbium.

Despite the ambiguities in the given situation, the enormous difference of the Sieverts'

constants in tungsten compared to the getter materials is expected to dominate the situation and thus ensure that Equations 4.6 and 4.7 are valid even if the diffusion coefficient is lower in the getter than in the tungsten. This assumption is supported by the fact that the permeated deuterium amounts measured with different getter materials are in agreement within the observed data scatter [46], as will be shown in Section 4.4.2. If not all deuterium that reaches the permeation side would be stored in the getter, the deuterium amounts accumulated with the different getter materials would be expected to be different because of differences in their Sieverts' constants and diffusion coefficients.

Based on the given explanation of the measurement principle, the following sections will present additional details regarding the practical application of the method and report on its validation as well as obtained measurement results.

4.2. Preparation of tungsten samples and layer system

All tungsten samples used for permeation experiments were prepared according to the procedure described in Section 3.5, including a heat treatment at 2000 K for 30 min in the vacuum furnace HADES. As already mentioned in Section 4.1, the layer system was deposited by magnetron sputtering. Before deposition, the foils were clamped into a stainless steel holder, which masked the edges of the samples to avoid deposition of material at the edges and on the other side of the samples, which was later exposed to deuterium plasma. This was done to avoid a contamination of the plasma-exposed surface with sputter-deposited material and to exclude a possible shortcut for diffusion from the plasma-exposed side to the permeation side.

Since only two sputter targets could be mounted in the sputtering device simultaneously (compare Section 3.2), a deposition of the whole layer system in one run was not possible. The sputter device was vented for sputter-target exchange after the about 300 nm thick getter layer of zirconium, titanium or erbium, and an about 50 nm to 75 nm thin tungsten interdiffusion barrier had been deposited. In the next deposition run, the about 950 nm thick copper layer and another about 50 nm to 75 nm thin tungsten interdiffusion barrier were deposited. After another venting for sputter-target exchange, the about 400 nm thick erbium oxide permeation barrier was deposited [46]. A SEM image of a FIB-prepared cross section of a layer system with erbium getter, recorded with the TLD, is displayed in Figure 4.4.

The thickness of the getter layer was chosen to be a bit larger, but of the same order of magnitude as in [153, 154]. The erbium oxide layer thickness of about 400 nm appeared to be well suited based on preceding experiments. The copper thickness was chosen based on preceding SIMNRA [121, 122] simulations. The thickness of the tungsten interdiffusion barriers was chosen to be large enough to probably suppress interdiffusion of the other layers, but also thin enough to avoid the buildup of large stress in the material. This limitation of the tungsten-layer thickness was necessary because bending of the tungsten foils was observed for thicker layers [46].

To ensure good contact between the deposited layers and the substrate, the samples were pre-sputtered with an argon plasma before each deposition run [46]. Before the deposition of the getter layer, this pre-sputtering was intended to remove the native

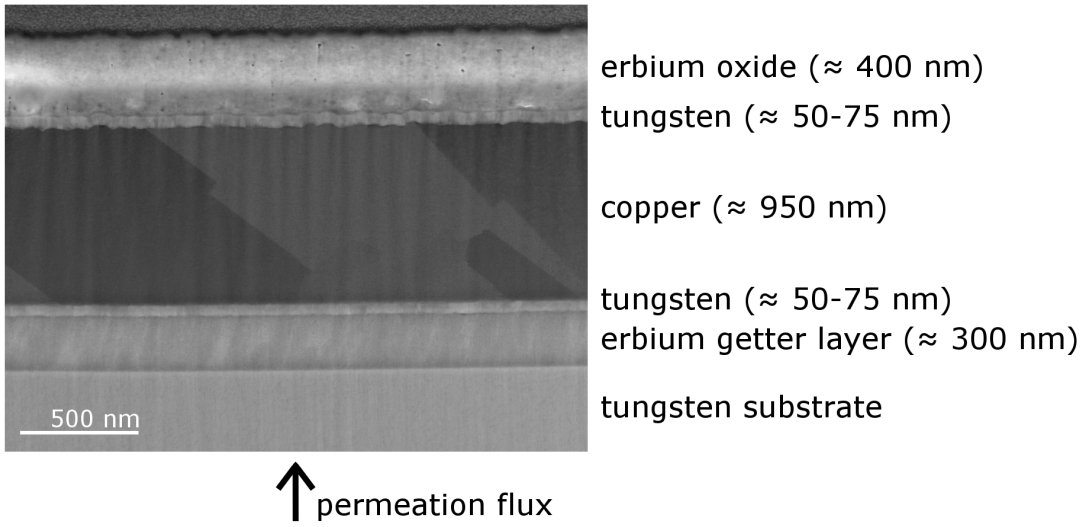

Figure 4.4.: SEM image of a FIB-prepared cross-section of a layer system with erbium getter, recorded with the TLD (Image recorded by Gabriele Matern, Max-Planck-Institut für Plasmaphysik). The observation direction is tilted 38° with respect to the cross-section's surface normal. An image of a very similar layer system with a zirconium getter was already previously displayed in [46].

oxide layer formed on the tungsten samples due to exposure to air and to remove also other unwanted contaminants [46], in order to avoid a possible permeation barrier at the tungsten-getter interface. To prevent contamination of the samples with foreign material from the sample holder during pre-sputtering before layer deposition, the sample holder had a coating of tungsten.

The effectiveness of the pre-sputtering procedure used for a first set of samples in removing the native oxide at the tungsten-foil surface was investigated because indications for remaining oxygen at the interface of tungsten and getter had been found by sputter-XPS [46]. For this purpose, several tungsten samples were coated with about 35 nm thin aluminum (Al) layers (see Figure 4.5a) after undergoing pre-sputtering procedures with different parameter sets or none at all. A possible remainder of oxygen at the interface was investigated by performing sputter-XPS on these samples after deposition. In the XPS analysis, the O1s peak was used for oxygen detection and the W4f and Al2s peaks were used to determine when the interface between tungsten and aluminum was reached. As already mentioned in Section 3.3, the combination of number and letter after the element symbol describes the electron orbital from which the peak in the XPS spectrum originates.

The development of the O1s peak integral with argon fluence imposed during sputter-XPS, and thus depth, is displayed in Figure 4.5b for a sample without pre-sputtering before layer deposition. A dataset of the O1s data smoothed with a fourth-order Savitzky-Golay filter is also included to guide the eye. A bump in the oxygen signal, marked with a black ellipse, corresponding to oxygen in the interface region is clearly visible. The interface region is indicated by the normalized W4f and Al2s peak integrals, which are

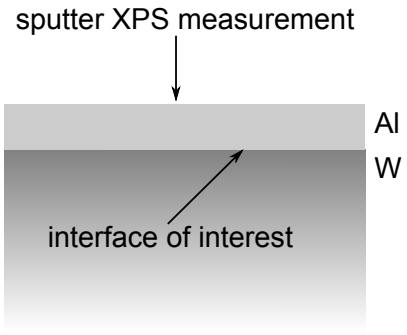

(a) schematic drawing of the test-sample structure used for the interface investigations

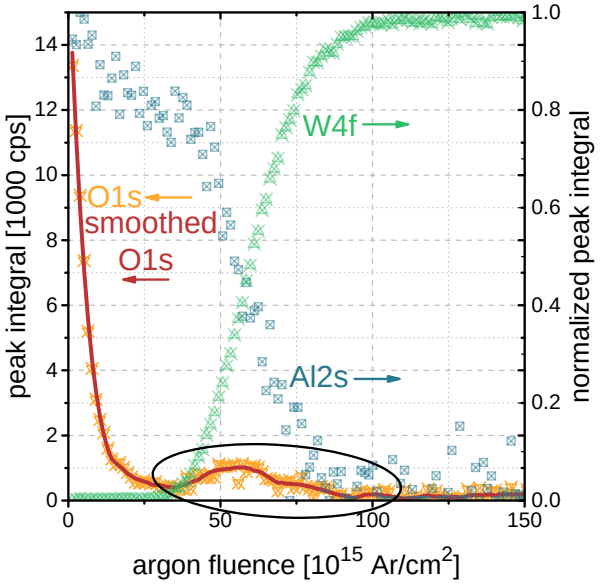

(b) not pre-sputtered

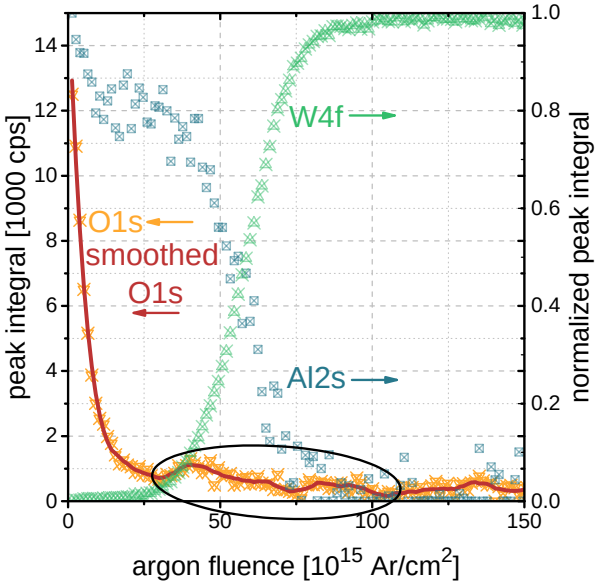

(c) pre-sputtered 8 W, 900 s

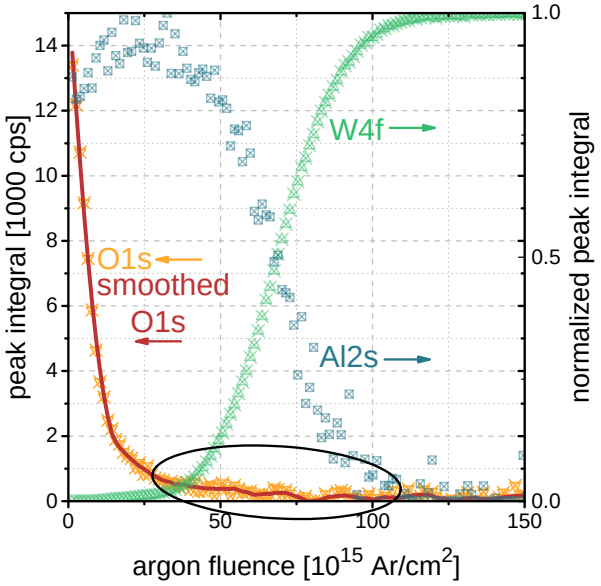

(d) pre-sputtered 100 W, 600 s

Figure 4.5.: Sputter-XPS measurement results for a number of test samples used to investigate the removal of oxygen at the interface between deposited layer and tungsten substrate with different pre-sputtering parameters. (a) shows a schematic drawing of the test-sample structure consisting of an about 35 nm thin aluminum layer on the tungsten substrate. The other images show the O1s peak integrals and normalized W4f and Al2s peak integrals resulting from sputter-XPS measurements on samples that were not pre-sputtered before layer deposition (b), pre-sputtered for 900 s with a nominal input power of 8 W (c) and pre-sputtered for 600 s with a nominal input power of 100 W (d).

also included in the plots of Figure 4.5.

The pre-sputtering procedure used in the production of a first set of permeation samples, to which all samples reported in [46] belong, had a nominal input power of 8 W for 900 s. It is subsequently referred to as the "old pre-sputtering procedure". The sputter-XPS results of a test sample with aluminum layer and this pre-sputtering procedure are displayed in Figure 4.5c. The data indicates that the oxygen at the interface was not completely removed by this pre-sputtering procedure.

The pre-sputtering procedure for the production of a second set of samples was, therefore, improved [47]. Sputter-XPS data obtained on a sample pre-sputtered with an input power of 100 W for 600 s before aluminum-layer deposition is displayed in Figure 4.5d. It indicates a nearly complete removal of the oxygen at the interface. The pre-sputtering procedure for a second set of samples was, therefore, chosen to be 100 W for 900 s. It is subsequently referred to as the "new pre-sputtering procedure".

As will be discussed in Section 4.4.2, no indications for inconsistencies of the permeation measurement results from both sets of samples were found [47]. This is not surprising, because hydrogen diffusion is known to be rapid in tungsten oxide [172] and thus a remaining thin tungsten oxide layer at the interface would not be expected to act as a permeation barrier [46].

It must finally be noted that a certain amount of argon is expected to have been incorporated in the deposited layers (compare, e.g., [173]). Also damage of the tungsten substrate's sub-surface region and implantation of argon into the tungsten substrate during pre-sputtering are possible. Since the sputter-XPS measurements used sputtering with argon, detection of argon in the layer system could not be included in the sputter-XPS measurements described above. In any case, the argon incorporated in the deposited layer system can be assumed to be unimportant because the layer system performs as desired, which will be shown later in this chapter. Damage and implantation in the tungsten substrate due to the pre-sputtering can also be assumed to have no effect on the permeation measurements because otherwise inconsistencies in the permeation measurements for samples with different pre-sputtering procedure would be expected. As already mentioned above as well as in [47] and as will be discussed again in Section 4.4.2, no such inconsistencies were found.

4.3. Deuterium-plasma exposures

The plasma exposures for the permeation measurements were performed in the plasma device PlaQ (compare Section 3.6). The tungsten foil samples were clamped to a tungsten-coated sample holder made of copper, which had also been used for retention experiments before. Except for a thin tungsten-coated stainless steel frame, which firmly clamped the foil samples to the sample holder and defined plasma exposed regions of about (10×10) mm^2 on each sample, no modifications of the plasma device were necessary for the permeation experiments. This indicates that the presented procedure for permeation measurements may also enable permeation experiments in other existing plasma devices used for retention experiments, without the need for device modification [46].

Before the deuterium-plasma exposure, the sample holder temperature was first brought

to the desired value using an oil or ethanol thermostat. Subsequently, the sample surfaces were cleaned in-situ using an argon plasma [46] with the sample holder at -100 V bias. Unfortunately, damage creation and argon implantation in the tungsten's sub-surface region during this step cannot be excluded. However, the step still appeared clearly favorable compared to undefined surface conditions with a surface oxide and possible contaminants. Afterwards, the samples were exposed to deuterium plasma with the sample holder at floating potential. The resulting differential deuteron flux density to the sample holder was already shown in Figure 3.10. The low energies of the incident deuterium ions, and thus deuterons, at floating potential were chosen to avoid kinetic defect creation by collision cascades during the deuterium implantation.

Before all plasma exposures, the shutter was kept closed for a so-called burn-in phase of 30 min after plasma ignition in order to allow the plasma to stabilize before sample exposure (compare [117]).

All deuterium-plasma exposures were performed without interruption, except for those samples exposed for 336 h. These were the samples that were exposed for 192 h and exposed again for 144 h after a first ion-beam analysis [46, 47]. To preserve the advantage of individual samples for different time steps (compare Section 4.1) as much as possible also for the 336 h data, care was taken to minimize the overlap of the measurement regions in the two IBA analyses within the experimental possibilities. No inconsistencies were found that would point towards an impact of the first ion-beam analysis on the permeation during the second deuterium-plasma exposure.

The deuterium-plasma exposures were performed at sample holder temperatures of 300 K and 450 K. No indications for a significant temperature increase of the sample holder surface due to the deuterium-plasma exposure were found by infrared camera. Since the samples were firmly clamped to the sample holder and the deuterium-plasma exposures were performed at floating potential, it appears justified to assume that the sample temperatures were at all times of the deuterium-plasma exposure very close to the measured sample holder temperature [47], which will subsequently be given as the exposure temperature. After termination of the deuterium-plasma exposures performed at 450 K, the samples were immediately cooled to room temperature, reaching 300 K after about 20 min.

4.4. Measurement of the permeated deuterium amount by IBA

The permeated deuterium amount stored in the getter after deuterium-plasma exposure was determined by ion-beam analysis (IBA) with a ^{3}He ion beam under normal incidence and incident ion energies of 1200 keV, 1800 keV and 3200 keV performed in the RKS setup described in Section 3.7. An ion dose of 20 µC was accumulated in each measurement with a beam spot size of about 1 mm^2. The two proton detectors PROL and PROT as well as the RBS detector and the annular proton detector ANN were used to detect emitted particles. As already mentioned in Section 3.7 and [46], the data from the annular proton detector, which has a higher depth resolution but smaller solid angle than the other proton

detectors, was unfortunately not usable for most measurements.

The layer structure of each sample was first determined based on Rutherford backscattering spectroscopy (RBS) data. It was then used to determine the deuterium amount retained in the getter based on nuclear reaction analysis (NRA) data [46].

4.4.1. Determination of the layer structure by RBS

Before the deuterium amount in the getter could be determined based on NRA data, the layer structure had to be determined based on RBS data. This is a non-trivial task, because the layer properties (e.g. thicknesses) as well as the setup properties (e.g. energy calibration) represent a large number of parameters, which need to be determined. The RBS data recorded at 1200 keV, 1800 keV and 3200 keV incident ^{3}He energy for one position on each sample was used for the determination of the layer structure [46, 47]. The analysis procedure for the RBS data presented in [46], where the spectra were analyzed directly with SIMNRA [121, 122], was improved [47] by using MultiSIMNRA [125]. MultiSIMNRA was used to determine the layer structure by fitting multiple RBS spectra simultaneously as well as optimizing the selected parameters simultaneously. In contrast to the standard setting described in [125], the normal instead of the reduced χ^2 was selected as objective function for this fit. Also, a small amount of hafnium (Hf) in the zirconium (Zr) layer, which resulted from a small amount of hafnium in the zirconium sputter target, was now included in the improved analysis [47].

RBS spectra recorded for all three incident ^{3}He energies at one location on each sample were first used to determine the energy calibration of the RBS detector (which links the detector channels to particle energy intervals) based on the high energy edge of the erbium (Er) signal originating from erbium in the erbium-oxide cover layer. For this purpose, the parameters of a quadratic energy calibration function, as an approximation to the unknown non-linear energy calibration function [132], were determined using MultiSIMNRA. While all other areal densities in the target were kept constant, the oxygen content in the erbium oxide was also included as a fit parameter in this step, in order to match the edge height of simulation and experiment. For the energy calibration, the regions of interest (ROIs) for the optimization were chosen to include only the high-energy erbium edge and a small part of the flat top of the erbium signal from the erbium oxide.

Using this energy calibration, the structure and composition of the layer system were subsequently determined by fitting the RBS spectra recorded at one location on each sample for 1800 keV and 3200 keV incident ^{3}He energy. The 1200 keV data was excluded from this analysis step because it appeared to be significantly affected already at energies slightly below the high energy Er edge by effects that are not perfectly represented in the SIMNRA simulations (e.g. multiple scattering). Additionally, the largest part of the RBS spectra recorded for 1200 keV was outside of the energy range for which the energy calibration had been determined. An example of a fit without roughness resulting from the described analysis procedure, showing the experimental and simulated spectra for 1800 keV and 3200 keV incident ^{3}He energy, is displayed in Figure 4.6. For the determination of the layer system, the ROIs were chosen much larger than for the energy calibration, including as many relevant features as possible. They were, however, at both ends limited by non-ideal features. A small non-ideal section of the high energy edge,

probably originating from the detector, was excluded because it otherwise led to a shift in the erbium edge in the fitting process. Low energy data had to be excluded due to effects that are not perfectly described by the physical model implemented in SIMNRA, such as multiple scattering.

Due to the large number of spectra combined with the multiple-parameter optimization, the inclusion of roughness in the MultiSIMNRA optimization procedure appeared computationally unfeasible [47], in contrast to the old SIMNRA-based analysis presented in [46]. The multiple-parameter optimization with MultiSIMNRA was still considered to be advantageous compared to the pure SIMNRA analysis including roughness, because in MultiSIMNRA the fit to different features and especially also to multiple spectra is optimized simultaneously [47].

To estimate the influence of neglecting roughness in the RBS analysis, data of a few samples was fitted including roughness for the substrate and the erbium oxide layer [47]. RBS fit results with and without roughness for one RBS data set are displayed in Figure 4.7 as an example. The RBS fit is significantly improved by the inclusion of roughness especially regarding the peak heights resulting from the tungsten interlayers and getter (compare Figure 4.6 for the peaks associated with the different layers). However, the deuterium amounts in the getter, and thus the quantity of interest, determined by NRA using the RBS fit results with and without roughness differed by only about two percent [47]. This error appears negligible compared to other uncertainties and especially also compared to the overall data scatter (compare Section 4.4.2).

4.4.2. Determination of the permeated deuterium amount by NRA

As described in Section 4.1, the cover layer system was used not only as a permeation barrier to prevent direct loading of the getter from deuterium background gas during plasma exposure, but also to enable a distinction of permeated deuterium retained in the getter and deuterium present at the cover surface after plasma exposure [46]. The deuterium at the cover surface is probably stored in a deuterium-containing adsorbate or possibly in the first atomic layers of the erbium oxide [46].

The peaks originating from deuterium in the getter and at the cover surface are separated in the proton spectra recorded with incident ^{3}He ions of 1200 keV [46], as can be seen in the examples for 300 K and 450 K exposure temperature displayed in Figures 4.8a and 4.8c, respectively. In contrast, in proton spectra recorded with incident ^{3}He ions of 1800 keV, the peaks resulting from deuterium in the getter and at the cover surface are not clearly separated [46], as the examples displayed in Figures 4.8b and 4.8d demonstrate.

While this drawback of the spectra recorded for 1800 keV incident ^{3}He energy is obvious, also the 1200 keV spectra have a drawback. Unfortunately, the deuterium distribution over the getter layer thickness is not known. This is a problem for the 1200 keV measurements, since they are more sensitive to comparatively small variations of this depth distribution than the 1800 keV measurements because the steep low-energy edge of the reaction cross-section [128] is reached in the getter layer for 1200 keV, while it is reached in the tungsten foil behind the getter for 1800 keV. Therefore, a comparatively small deviation between simulation and experiment regarding the deuterium depth distribution or the energy of the ^{3}He ions at the depth of the deuterium in the getter for 1200 keV incident

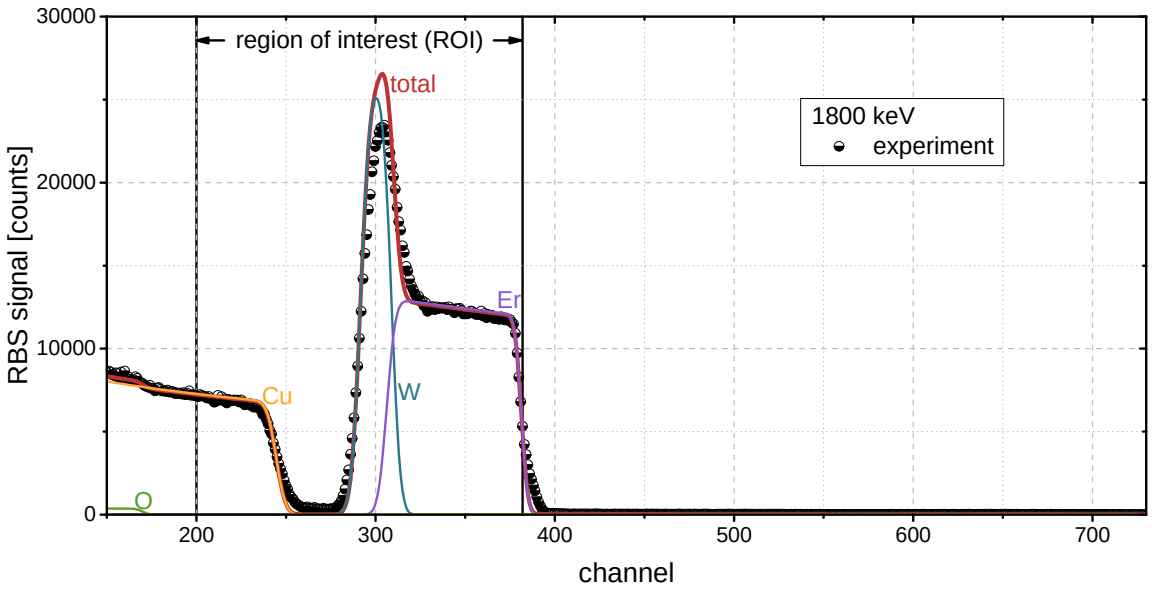

(a)

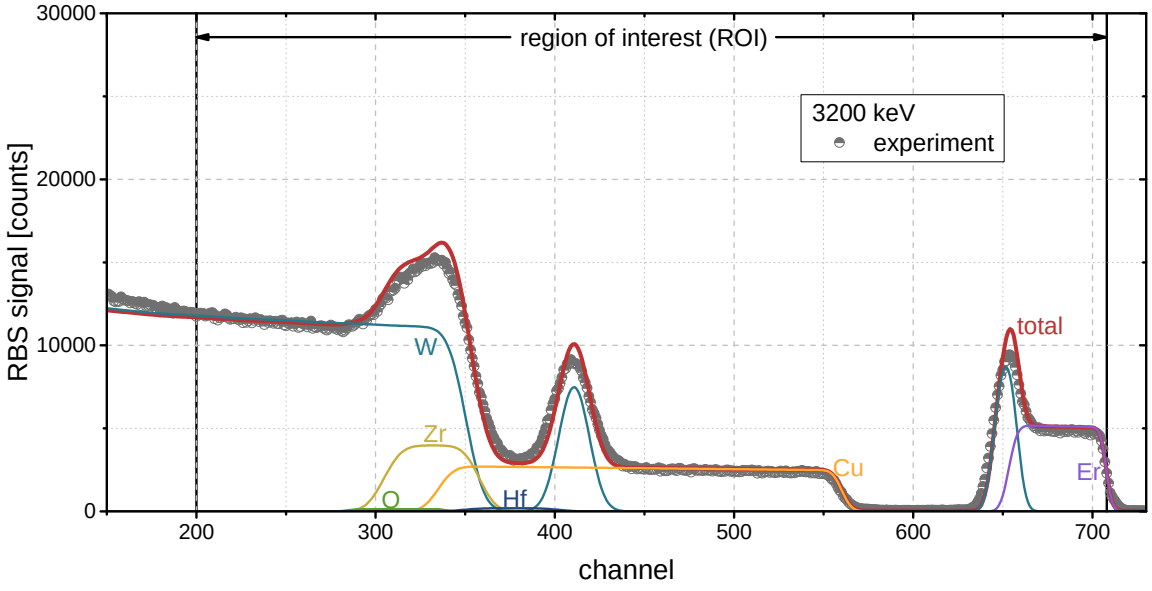

(b)

Figure 4.6.: Fit without roughness of RBS spectra recorded with (a) 1800 keV and (b) 3200 keV incident ^{3}He energy for a layer system with zirconium getter on a sample exposed to deuterium-plasma for 96 h at 300 K. Individual element contributions are also included.

Note: SIMNRA applies pile-up correction only to the total spectrum, but not to the individual element spectra. This can lead to seemingly unlogical effects, such as the tungsten contribution being larger than the total spectrum near channel 200 in (b) [126].

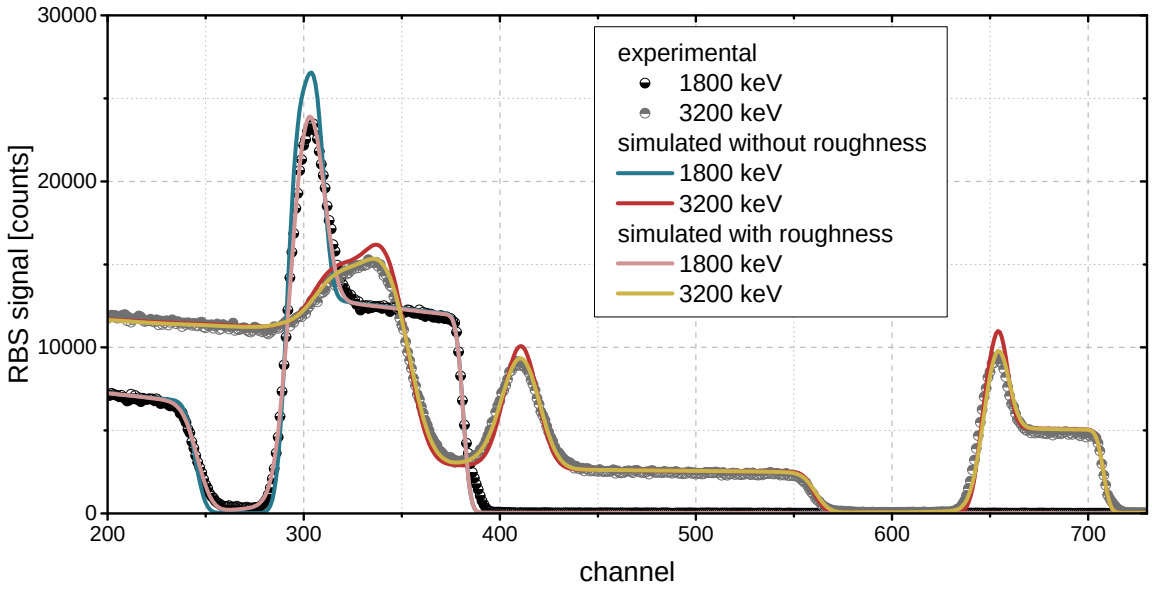

Figure 4.7.: Comparison of RBS spectra of a layer system with zirconium getter recorded with 1800 keV and 3200 keV incident ^{3}He energy fitted with roughness included for substrate and erbium-oxide layer and without roughness using MultiSIMNRA [125]. The data without roughness is the same as in Figure 4.6. The inclusion of roughness improves the result, but makes the fitting procedure significantly slower such that roughness could not be included in the fits for all samples.

^{3}He energy can lead to a significant error in the determined permeated deuterium amount especially if permeated deuterium is accumulated at the interface between tungsten and getter. This potential error is much smaller for 1800 keV incident ^{3}He energy.

To combine the strengths of the 1200 keV and 1800 keV measurements, the following evaluation procedure [46] was used. First, the deuterium amount at the cover surface was determined based on experimental and simulated spectra for 1200 keV incident ^{3}He energy. Subsequently, this amount was used to determine its contribution to the total spectrum for 1800 keV incident ^{3}He energy based on simulations. Finally, the deuterium amount in the getter was determined based on the proton spectra for 1800 keV incident ^{3}He energy, taking the contribution by the surface deuterium into account. In this analysis, the deuterium amounts were determined by matching simulated and experimental peak integrals, which means the sum of all counts in a peak [46]. This strategy appeared promising to ensure a robust analysis, because small uncertainties in, e.g., the layer structure or energy calibration, could else have led to a peak shift, which could have perturbed peak fitting. Improving the procedure reported in [46], data from both proton detectors, PROL and PROT, was used [47]. In determining the deuterium amounts based on SIMNRA simulations, spectra were not simulated for each individual deuterium amount present in a sample, but only for selected reference amounts based on the proton peak integrals of which the deuterium amounts in the samples were determined assuming a proportionality between deuterium amount and proton peak integral. The assumption

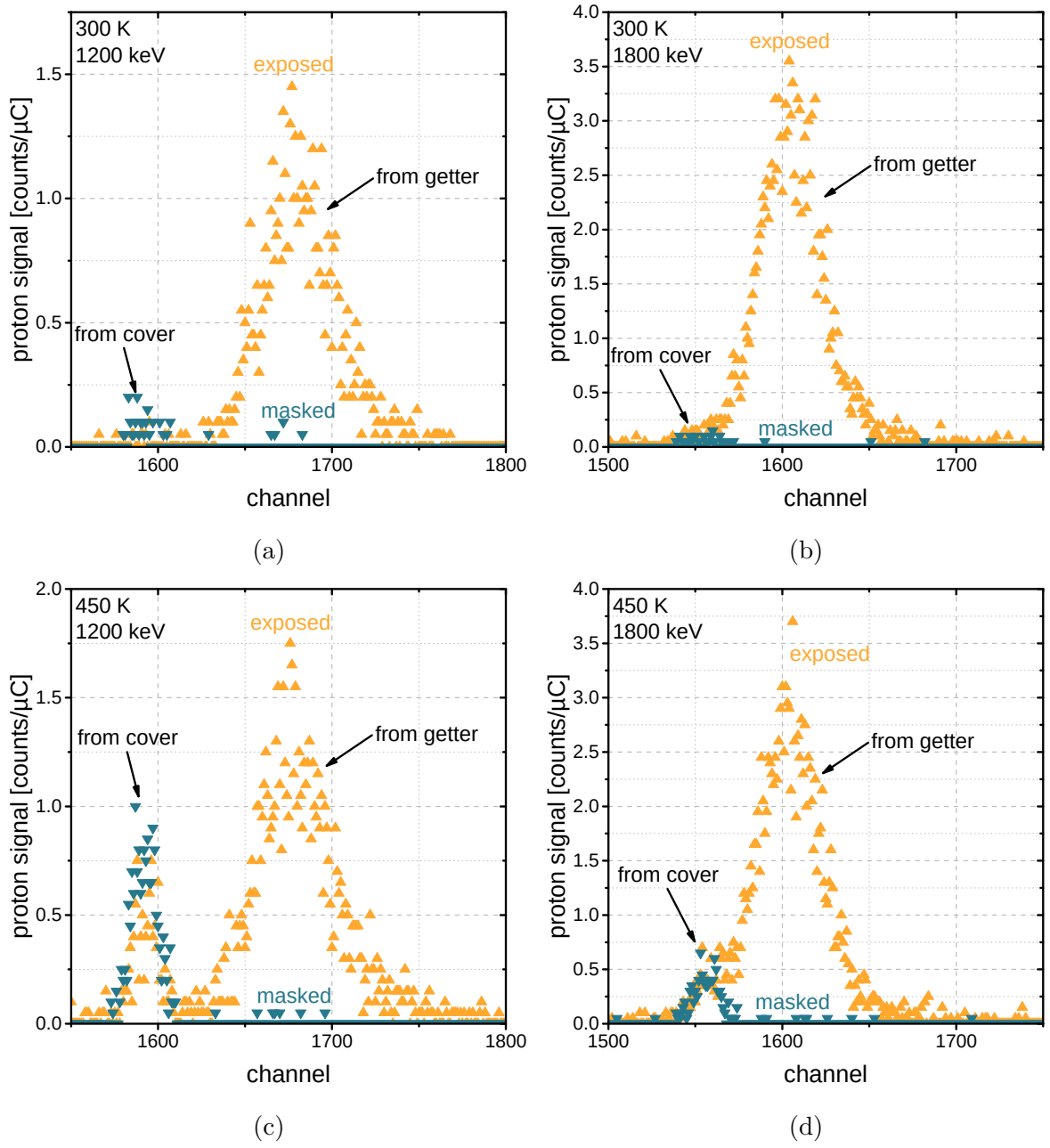

Figure 4.8.: NRA proton spectra recorded on the permeation side of samples exposed to deuterium plasma for 120 h at 300 K and 450 K with the PROL detector for incident ^{3}He energies of 1200 keV and 1800 keV. The samples exposed at 300 K and 450 K had a getter layer of Zr and Er, respectively. Proton peaks originating from deuterium in the getter and at the cover surface are well separated for 1200 keV incident ^{3}He energy, but not for 1800 keV. Spectra measured for samples that were masked during plasma exposure, and thus only exposed to the deuterium background gas but not to incident deuterium ions, show only a negligible amount of deuterium in the getter.

of this proportionality is based on an assumed negligible effect of the deuterium on the stopping. It is considered to be well justified based on SIMNRA simulations performed to test this assumption [46].

Figure 4.9 shows experimental and simulated proton spectra for 1200 keV and 1800 keV incident ^{3}He energy, taking only deuterium at the cover surface into account in the simulation for 1200 keV, and deuterium at the cover surface and in the getter for 1800 keV. The experimental cover-surface peak is very well represented for both incident ^{3}He energies, however, the peak caused by deuterium in the getter in the 1800 keV signal is slightly shifted in the simulations compared with the experiment. This shift may be caused, e.g., by uncertainties in the RBS analysis of the layer system or the limited knowledge about the deuterium distribution over the getter thickness. As Figure 4.9b shows, assuming a homogeneous deuterium distribution over the getter thickness or an accumulation of deuterium at the interface between tungsten foil and getter leads to a different peak shift in the simulated spectrum compared with experiment. The peak position of the simulation assuming a homogeneous deuterium distribution over the getter thickness is closer to the experimental peak position. However, due to the overall very small peak shift, the data still appears to be insufficient to clearly deduce a deuterium distribution over the getter thickness that could be used in improved simulations. This is also because both simulated peaks from deuterium in the getter are shifted to the same side of the experimental peak while an experimental peak position between the two simulated ones would be expected. The peak shift in these spectra, therefore, appears to be dominated by experimental uncertainties, because no obvious physical reason exists for an accumulation of deuterium in the getter further from the interface, as this data would indicate.

A spectrum recorded with the annular proton detector, in which the differences of the simulated peaks resulting from homogeneous distribution and accumulation at the tungsten-getter interface are more significant, is displayed in Figure 4.10. The comparison of the simulations with the experimental result appears to indicate a deuterium distribution over the getter thickness that is closer to a homogeneous distribution than to an accumulation at the interface between getter and tungsten foil. However, the real distribution probably lies somewhere in between and thus represents a partial filling [46]. The simulated deuterium amount in the getter was also here chosen such that the peak integrals of experiment and simulation are in agreement.

For lack of knowledge about the exact distribution of deuterium over the getter layer thickness, a homogeneous distribution was assumed in the simulations used to prepare the subsequently presented results. The maximum error introduced by this assumption was estimated by comparing simulations with deuterium homogeneously distributed over the getter layer thickness and accumulated at the interface between getter and tungsten foil, both with peak integrals matched to the experimental spectra. The resulting maximum overestimation of the permeated deuterium amount turned out to be roughly ten percent [46].

To ensure that the deuterium detected in the getter layer had permeated through the tungsten foil sample and not through the cover layer system, some samples were masked with a tungsten foil during plasma exposure [46]. They were thus exposed to the deuterium background gas under the same conditions as other samples, but shielded from the impinging deuterium ion flux. NRA proton spectra recorded for such samples

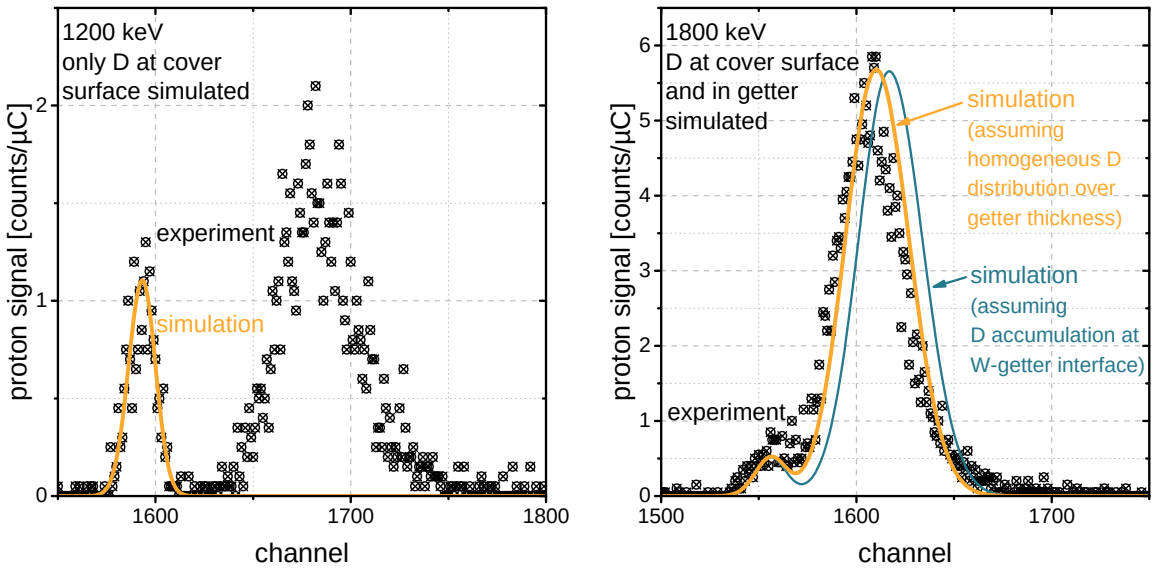

(a) (b)

Figure 4.9.: Comparison of experimental and simulated proton spectra for the PROL detector and incident ^{3}He energies of (a) 1200 keV and (b) 1800 keV for a sample with zirconium getter exposed to deuterium plasma for 192 h at 450 K. The peak resulting from deuterium at the cover surface is well reproduced in the simulations, but a slight peak shift is observed for the peak resulting from deuterium in the getter. The data does not allow to draw a certain conclusion about the distribution of deuterium over the getter layer thickness.

are also included in Figure 4.8. They show that the proton peak caused by deuterium at the cover surface is present for plasma-exposed as well as masked samples, but that the proton peak resulting from deuterium in the getter is negligible for masked samples. This clearly demonstrates the nearly perfect impermeability of the cover layer system and thus a background-free measurement of the amount of permeated deuterium [46].

As described in Section 4.3, the samples were clamped to the sample holder using a frame that also defined the plasma-exposed area on the samples. The area coated with the layer system was defined by the mask used during layer deposition and was larger than the plasma-exposed area. Therefore, it was necessary to investigate whether lateral diffusion in the getter could decrease the measured permeated deuterium amount stored in the getter below the plasma-exposed region. Approximately half of the plasma-exposed area of a sample with Zr getter was masked with a tungsten foil during deuterium-plasma exposure for 120 h at 300 K. NRA proton spectra recorded with 1800 keV incident ^{3}He energy along a line orthogonal to the edge of the masked region on both sides of this sample resulted in the normalized peak integrals plotted over position in Figure 4.11. This data shows that the plasma-exposed region correlates very well with the region in which permeated deuterium was detected in the getter layer and demonstrates that no lateral diffusion in the getter from the plasma-exposed into the masked region was observed. The increased retention measured in the masked region on the plasma-exposed side at positions

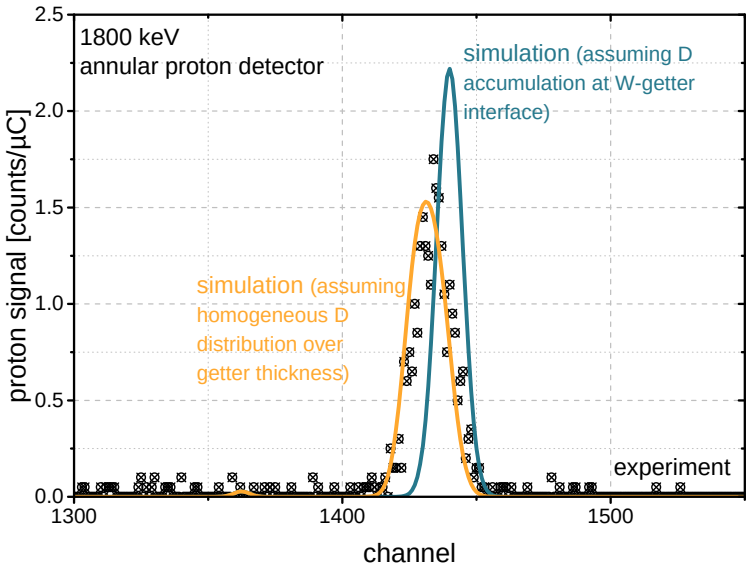

Figure 4.10.: Proton spectrum recorded with the annular detector on a sample with zirconium getter exposed to deuterium plasma for 96 h at 300 K and SIMNRA simulations assuming a homogeneous distribution of deuterium over the getter thickness and an accumulation of deuterium at the tungsten-getter interface. As already previously mentioned in [46], the data appears to indicate a partial filling closer to a homogeneous distribution than to an accumulation at the interface.

55 mm and 57 mm is assumed to result from some kind of imperfections in the masking, which did, however, apparently not lead to permeation in this region and thus did not affect the investigation of the lateral diffusion in the getter. The NRA measurements were performed using a flippable sample holder, such that the sample positions can be assumed to have been nearly identical for the measurements on both sides. A slight misorientation of the edge of the masked region to the positioning direction in the NRA scan could have led to a broadening of the edge and possibly a shift between the edges observed in both measurements. However, since no indications exist for any of these effects, the alignment can be assumed to have been well adjusted [46].

For the interpretation of the data of this lateral scan, the spot size diameter of the ion beam, which was roughly 1 mm, must be taken into consideration. As already discussed in [46], the data demonstrates, in agreement with [174], a very limited lateral diffusion of deuterium in the getter layer and thus shows that the problems mentioned above, which might have occurred due to such a lateral diffusion, can be assumed to be absent. This is assumed to be also valid for experiments with other getter materials and an exposure temperature of 450 K, because no inconsistencies, which might have resulted from such an effect, were found in the results shown subsequently.

NRA measurements to determine the permeated deuterium amount were performed at multiple locations on each of the permeation samples [46, 47]. Besides measurements at a central location with all three incident ^{3}He energies mentioned above in the context

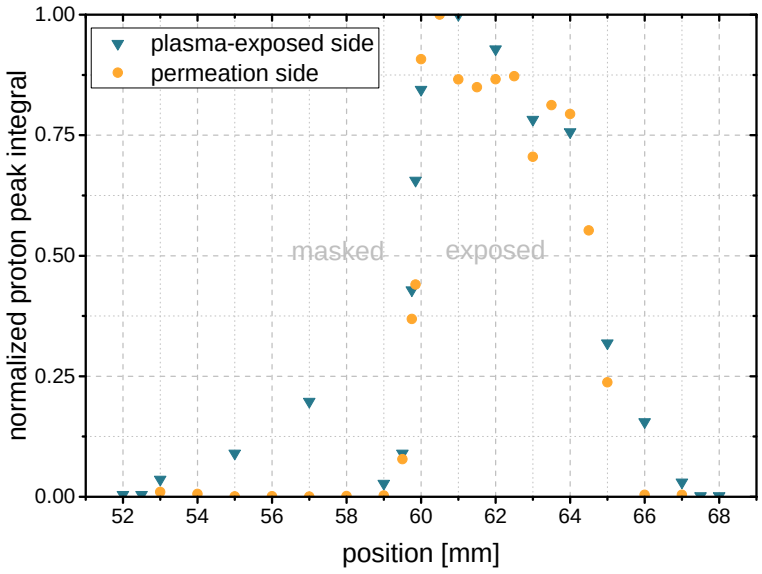

Figure 4.11.: Normalized proton peak integrals resulting from NRA measurements performed along a line orthogonal to the mask edge on both sides of a sample with zirconium getter that was approximately half masked during deuterium-plasma exposure at 300 K for 120 h. The data, which was recorded with an incident ^{3}He energy of 1800 keV and already previously displayed in [46], demonstrates no or only a very limited lateral diffusion of deuterium in the getter layer [46].

of RBS, additional measurements were performed on both sides of this central location. Measurements with 1800 keV were typically performed at four additional locations at distances of 1 mm and 2 mm along a line in two opposite directions from the central location. Additional measurements with 1200 keV incident ^{3}He energy were performed at some of the 1800 keV locations. For those locations where only spectra with 1800 keV were recorded, the deuterium amount at the surface was inter- or extrapolated based on 1200 keV measurements at the other locations. The permeated deuterium amount determined for each measurement location based on this measurement procedure is displayed as an individual data point in the plots of the permeated deuterium amount over deuterium-plasma-exposure time in Figure 4.12. There, measurement results for exposure temperatures of 300 K and 450 K are presented, most of which were already previously displayed in [47]. Most of the 300 K data originates from measurements that were already used to produce the permeation data displayed in [46].

For the permeation measurements, typically one sample with each getter material was exposed to deuterium plasma for each combination of the exposure temperatures 300 K and 450 K and the selected exposure times. Therefore, the combination of getter material, deuterium-plasma exposure time and exposure temperature is in almost all cases a unique identifier of the sample. The only exceptions are for 300 K exposure temperature the 72 h exposures with all getter materials and the 48 h exposure with Zr getter and for 450 K the 72 h exposure with Zr getter. The combination of the above-mentioned three

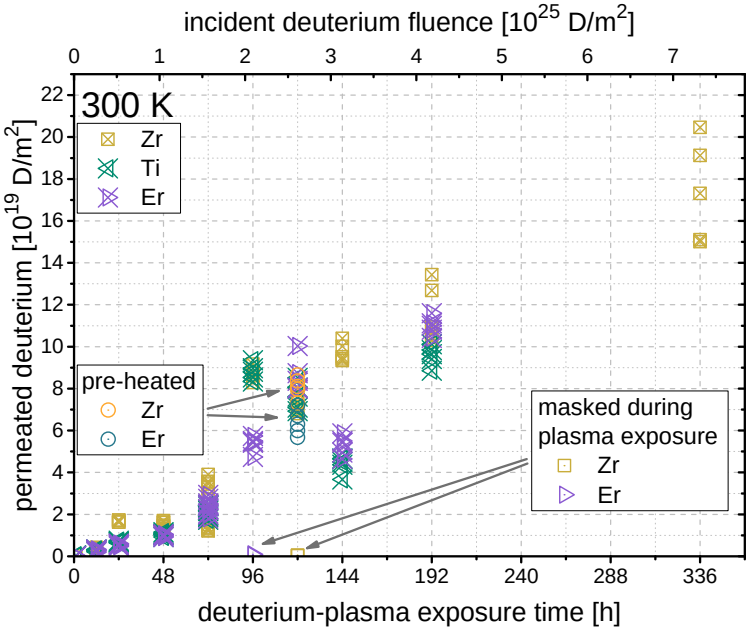

(a)

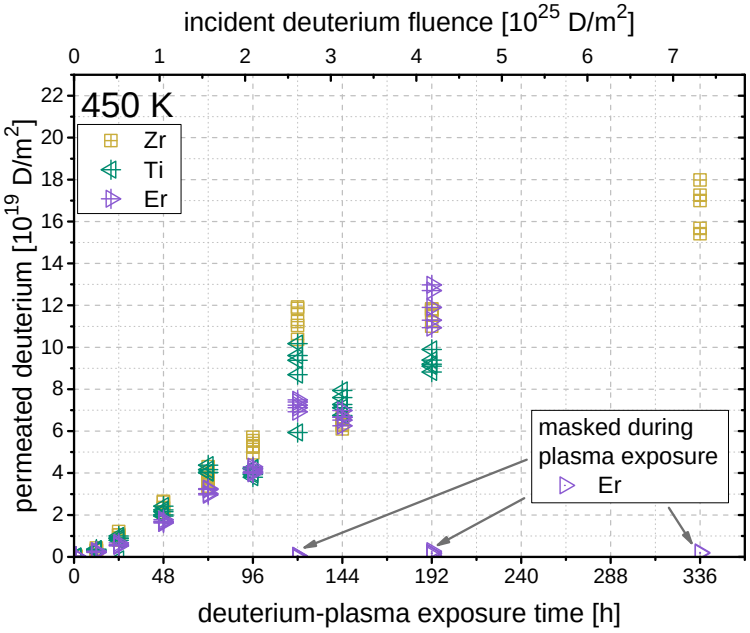

(b)

Figure 4.12.: Permeated deuterium amount accumulated in the getter layer of various samples plotted against deuterium-plasma exposure time for exposure temperatures of (a) 300 K and (b) 450 K. For most of the samples, data from measurements at five locations is included. For 300 K, also measurements on samples shortly pre-heated at 573 K, as suggested in [154, 174], are included. For both exposure temperatures, also data from samples masked during plasma exposure is included. Except for the pre-heated data, the data was already previously displayed in [47]. Most of the 300 K data results from NRA measurements that were already used to generate data displayed in [46].

parameters will be used to refer to the corresponding samples also in the context of retention measurements and microstructural analysis in the next chapter. Exposures with masked, partly masked or pre-heated (see discussion of pre-heating later in this section) samples may have identical combinations of the above mentioned parameters as other samples, however, they are only referred to if such a treatment is explicitly specified. Deuterium-plasma exposures for the highest exposure time of 336 h were only performed for samples with a Zr getter. As already mentioned above, the 336 h were reached by exposing the samples that were exposed to deuterium-plasma for 192 h for another 144 h after a first ion-beam analysis. All other exposure times were reached without interruption.

The agreement of the deuterium amount measured with the different getter materials, within the observed data scatter, indicates that the assumption made in Section 4.1 that all deuterium that reaches the getter layer is stored there is valid. This is because different getter materials would otherwise be expected to collect different deuterium amounts [46] because of differences in their Sieverts' constants and diffusion coefficients.

As already mentioned above, a number of samples was masked during deuterium-plasma exposure in order to expose them to the background deuterium gas but prevent impact of incident deuterium ions. This was done to test the impermeability of the cover. Measurement results originating from such samples are also included in Figure 4.12. They demonstrate the negligible amount of deuterium in the getter of these samples and show that no distortion of the measurements by permeation through the cover is present [46, 47].

According to [154, 174], pre-heating of the samples for a short time at 270 °C to 300 °C before deuterium loading was necessary to eliminate a permeation barrier between the substrate and the getter. Therefore, the influence and necessity of such a pre-heating step was assessed. Pre-heating of a number of selected samples at 573 K (= 300 °C) for 10 min was, in contrast to [154, 174], performed ex-situ [46] in the vacuum furnace MOMO. Since any possibly resulting modification of the microstructure would be expected to be permanent and the getter was additionally protected by the cover during transport from MOMO to PlaQ, the fact that the pre-heating was performed ex-situ is not expected to make a difference [46]. In contrast to [174], no significant deviation in the deuterium amount in the getter was found for samples with and without this pre-heating [46], as displayed in Figure 4.12a. Consequently, the pre-heating step was not performed for any other samples. Possible reasons for this difference to the results of [154, 174] are the different substrate (tungsten instead of nickel) and the different getter deposition technology (sputter deposition instead of evaporation) [46].

Also the influence of the pre-sputtering procedure before layer deposition, as discussed in Section 4.2 with respect to sputter-XPS measurements, shall be discussed here again based on the permeation results. While most of the permeation data for an exposure temperature of 300 K was measured on samples prepared with the old pre-sputtering procedure, most of the permeation data for an exposure temperature of 450 K was measured on samples prepared with the new pre-sputtering procedure. No indications for a systematic deviation between results from samples of both batches were found [47]. For example the 120 h data points (without pre-heating) in the 300 K graph (Figure 4.12a) were recorded on samples produced with the new pre-sputtering procedure and are, within the data scatter, consistent with the 96 h and 144 h data points for 300 K, which were gained

from samples prepared with the old pre-sputtering procedure. Consequently, all data points can be assumed to be equally valid, independent of the pre-sputtering procedure used for sample production [47].

Another point that needs to be mentioned is the fact that the deuterium amount in the getter is strictly speaking not exactly identical to the integral of the deuterium permeation flux over deuterium-plasma exposure time, because the solute deuterium present in the sample at the end of the plasma exposure will partially enter the getter layer and thus increase the amount stored there. However, due to the linear decrease of the solute-deuterium concentration during deuterium-plasma exposure from a maximum below the plasma-exposed surface to zero at the permeation side, most of this solute deuterium can be expected to leave the sample through the plasma-exposed surface based on geometric considerations and the assumption of a random walk of deuterium in tungsten. Also diffusion-trapping simulations such as those presented in Chapter 6 indicate that this additional contribution is negligible for basically all exposure durations, especially when the data scatter is taken into consideration [47].

Also deuterium retained in the tungsten foil close to the getter layer can in principle make a small contribution to the amount measured by NRA. However, this contribution can be assumed to be negligible due to the low retention of deuterium in tungsten at the permeation side (compare Section 5.2.1).

Unfortunately, the origin of the significant data scatter in the permeation data could not be finally clarified. The total data scatter includes scatter of the measurement results gained on each individual sample as well as scatter of the measurement results gained on different samples with nominally equal exposure conditions. An obvious guess would have been that variations in the foil thickness may have contributed to the scatter, but a comparison of Figures 4.12 and 3.7 does not reveal a clear correlation between scatter and sample thickness. For example, the permeated deuterium amount measured for 96 h exposure at 300 K (see Figure 4.12a) is significantly different for the samples with Zr and Er getter. However, the thickness-measurement results for these samples displayed in Figure 3.7 do not reveal a corresponding difference in the sample thickness.

A full uncertainty estimate for the permeated deuterium amount is challenging because the total uncertainty results from various statistical as well as possible systematic uncertainties in a large number of parameters, e.g. foil thickness, stopping power, roughness and detector energy calibration. The main systematic uncertainty is assumed to result from the assumption of a homogeneous deuterium distribution over the getter thickness and amounts to roughly ten percent [46], as was already mentioned above. The observed data scatter appears to be a good indication for the total statistical uncertainty [47].

4.5. Summary and conclusions for the getter-layer-based permeation measurements

This chapter presented a method to measure plasma-driven deuterium permeation through tungsten near room temperature, which was already previously published in [46] and improved as reported in [47]. This temperature range is difficult to access with common

gas-driven permeation methods due to the low solubility and thus permeability of hydrogen in tungsten.

As in [153, 154], where ion-beam-driven deuterium permeation measurements were reported for stainless steel and nickel, permeated deuterium was accumulated in a getter layer of zirconium, titanium or erbium and the permeated deuterium amount was determined by ion-beam analysis. The permeation measurement was thus basically converted into a retention measurement. Since the deuterium implantation was performed by plasma exposure in the present case, an additional cover layer system had to be deposited on the getter. It prevented direct loading of the getter with deuterium from the background gas, the pressure of which was higher than in typical ion-beam experiments as used in [153, 154]. The design of the cover layer system also enabled the distinction of deuterium in the getter and at the cover surface. The use of plasma for ion implantation enabled the simultaneous exposure of multiple samples, a homogeneous implantation and low ion energies that can avoid kinetic defect creation [46].

Permeation measurements were performed at exposure temperatures of 300 K and 450 K [47]. Since the permeation flux resulting from ion implantation is in the most simple case of diffusion-limited boundaries expected to be independent of temperature (compare Section 2.3.3), also measurements at lower temperatures appear possible. For significantly higher exposure temperatures, the applicability of the method will be limited by loss of deuterium from the getter. In [154, 174], measurements with the getter method were reported to be possible up to about 600 K, depending on the getter material. Since a loss of deuterium is in the present case additionally impeded by the cover layer system, maybe even higher temperatures can be reached.

The presented permeation-measurement method has been proven to detect a permeation flux of the order of 10^{14} D/(m^2 s) (compare Section 5.4.1 and [46, 47]) with exposure times of up to 336 h. This permeation flux is of the order of the lower limit of ion-driven hydrogen isotope permeation fluxes through tungsten measured with a quadrupole mass spectrometer reported in the literature [23, 26, 30, 150–152]. In principle, an even lower permeation flux should be detectable because the measured signal in the NRA proton spectra was well above noise level. The sensitivity could be improved even further by using longer exposure times or proton detectors with larger solid angles. Since the permeated deuterium is stored in the getter in atomic form, recombination limitation cannot occur in contrast to measurements using mass spectrometry. Unfortunately, the permeation measurements had a significant data scatter, the origin of which could not be finally clarified. Possibly, the data scatter can be reduced in the future by further investigations of the uncertainties and variations associated with the experiments.

Since the measurement of the permeated deuterium amount can be performed ex-situ, the method can also be used with existing plasma devices, where no space is available for a complex in-situ permeation measurement setup. The determination of the permeated deuterium amount is temporally and spatially decoupled from the plasma exposure. Thus, the plasma device does not even need to be in proximity to the accelerator used for ion-beam analysis [46].

The described method can be applied to study various effects that influence the permeation flux, such as microstructural evolution, surface effects or impurity seeding. If an appropriate nuclear reaction is available, it should also be usable with other hydro-

gen isotopes, for example using the nuclear reaction of nitrogen-15 with protium [175]. The method might even be usable in future fusion experiments and reactors to ensure a safe operation by monitoring the permeation of hydrogen isotopes through the wall. When used with tritium, the detection procedure could be simplified to a measurement of the radioactivity generated by tritium in the getter, which would, however, need to be distinguished somehow from radioactivity resulting from tritium retained in tungsten.

5. Experimental results for microstructural evolution, deuterium retention and permeation

The results presented in this chapter were in large parts already previously published in [47].

As discussed in Chapter 1, investigations on the phenomena associated with the implantation of deuterium into tungsten typically focus on either microstructural evolution (e.g. [28, 42]), deuterium retention (e.g. [20, 24, 31, 32]) deuterium permeation (e.g. [23, 26, 30]) or a combination of two of these effects (e.g. [22, 25, 29, 33–35, 43–45]).

This chapter presents results of experiments that addressed all three of these phenomena with measurements on one set of samples. The results of microstructural analyses and deuterium-retention measurements performed on some of the samples used for the permeation measurements (see Figure 4.12) presented in the preceding chapter are reported. In addition, retention measurements on tungsten samples without layer system are presented. In contrast to samples with layer system, this type of samples enabled measurements of the deuterium retention in tungsten near the permeation side and could also be used to measure the thermal desorption of deuterium from tungsten.

Combining the results of the permeation, retention and microstructural investigations, the interplay of sub-surface damage evolution, corresponding to a modification of the tungsten microstructure, deuterium retention and deuterium permeation due to deuterium-plasma exposure of tungsten at 300 K and 450 K could be studied. It was, thereby, possible to investigate the effect of sub-surface damage evolution on the permeation flux. Also, the maximum ratios of solute-deuterium to tungsten atoms, which are proportional to the maximum solute-deuterium concentrations, below the plasma-exposed surface in the presence and absence of sub-surface damage evolution at 300 K and 450 K, respectively, could thus be estimated. Most of the data as well as results presented in this chapter were already previously reported in [47].

As already explained in detail in Section 4.4.2, each combination of exposure time, getter material and exposure temperature was typically given for only one sample, which is why the combination of these three parameters can in most cases be used to uniquely identify the sample from which retention and permeation as well as microstructural analysis data originate. The only exception in the microstructural and retention data displayed in this chapter are the 72 h data points in Figure 5.7. For their parameter combinations, permeation measurements on multiple samples are included in Figure 4.12.

5.1. Sub-surface damage evolution

Figure 5.1 displays orientation-contrast SEM images recorded on the plasma-exposed surface of a number of tungsten samples, for which permeation data was already presented in Figure 4.12, after exposure to deuterium plasma. The samples displayed in Figures 5.1a, c and e were exposed to deuterium plasma at 300 K for 24 h, 96 h and 144 h, respectively. Compared with the image of an unexposed reference tungsten sample displayed in Figure 5.1b, the images recorded after 96 h and 144 h of deuterium-plasma exposure show damage features in the form of local in-grain distortions. Taking Figures 5.1a, c and e into account, the number of damage features appears to increase with exposure time. However, Figure 5.1f, which displays an orientation-contrast image of the plasma-exposed surface of a sample exposed to deuterium plasma at 300 K for 192 h, demonstrates that this trend is not as clear as the aforementioned images may indicate. Despite the longer exposure time, it appears to have a lower areal density of damage features than Figures 5.1c and e. This means, the areal density of damage features observed after deuterium-plasma exposure at 300 K partly appeared to increase continuously with exposure time, but had a significant scatter [47].

It must be noted that the visibility of the observed damage features depended strongly on grain orientation and observation direction [47]. This is demonstrated by the significant differences in orientation-contrast images of the same region on the same sample recorded during different SEM observation sessions, as displayed in Figure 5.2. Caution must, therefore, be taken in any quantitative or semi-quantitative interpretation of the SEM images displayed in Figure 5.1. A full quantitative analysis of the damage-feature areal density based on these SEM images appears unreliable. The sample-surface regions displayed in Figure 5.1 were chosen attempting to give an impression of the variation and mean value of the damage-feature areal density observed in the parts of the sample surfaces that were inspected by SEM [47].

In contrast to Figures 5.1a, c and e that originate from samples with a zirconium getter on the permeation side, Figure 5.1f shows the plasma-exposed surface of a sample with an erbium getter. Due to the consistency of the permeated deuterium amount measured with different getter materials (compare Section 4.4.2), the different getter materials were excluded as the reason for the observed scatter in the areal density of the damage features, as will be discussed in more detail in Section 5.3. More likely, other factors such as variations in the initial tungsten microstructure appear to be responsible for this effect [47].

While damage feature evolution was observed for 300 K exposure temperature, no indications for such damage features were found on samples inspected after deuterium-plasma exposure at 450 K, even for 336 h exposure time (carried out in two steps of 192 h and 144 h) [47], as illustrated by Figure 5.1d.

A comparison of the orientation-contrast image in Figure 5.1e with a topographic-contrast image of the same region, as displayed in Figure 5.3, indicates no surface elevations in the vicinity of the observed damage features. The observed damage features are, therefore, not referred to as “blisters” (compare [98]) [47].

A SEM image of a FIB-prepared cross-section through a number of damage features observed on the sample with zirconium getter exposed to deuterium plasma for 144 h

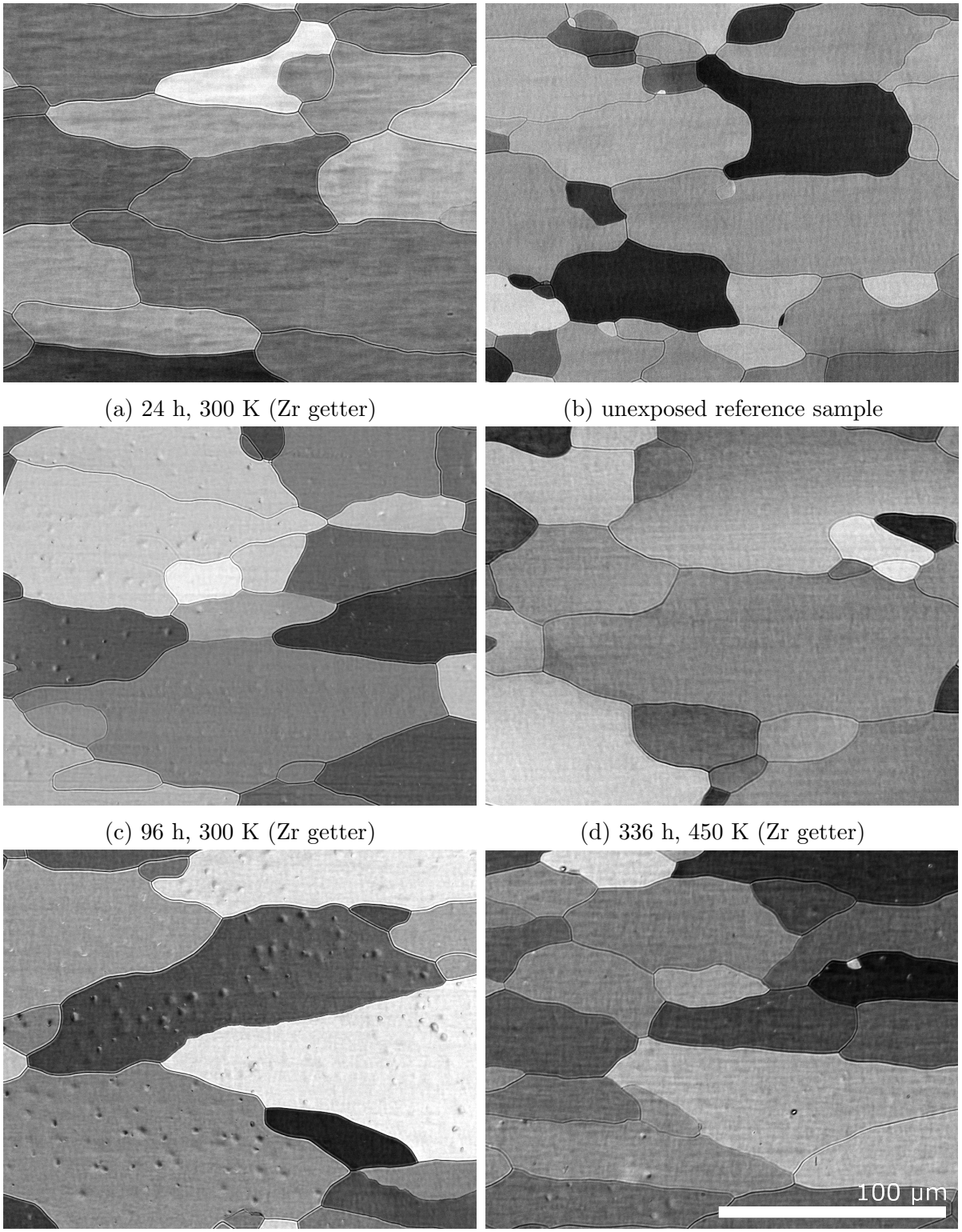

(a) 24 h, 300 K (Zr getter)

(b) unexposed reference sample

(c) 96 h, 300 K (Zr getter)

(d) 336 h, 450 K (Zr getter)

(e) 144 h, 300 K (Zr getter)

(f) 192 h, 300 K (Er getter)

Figure 5.1.: Orientation-contrast SEM images of the surfaces of samples exposed to deuterium plasma for different exposure times at different exposure temperatures and an unexposed reference sample. Brightness and contrast of the images were adjusted during post-processing to improve the comparability. The scale-bar in (f) is valid for all images. The images (a) to (e) include data that was already previously displayed in [47]. (Images recorded by Stefan Elgeti and Martin Balden, Max-Planck-Institut für Plasmaphysik)

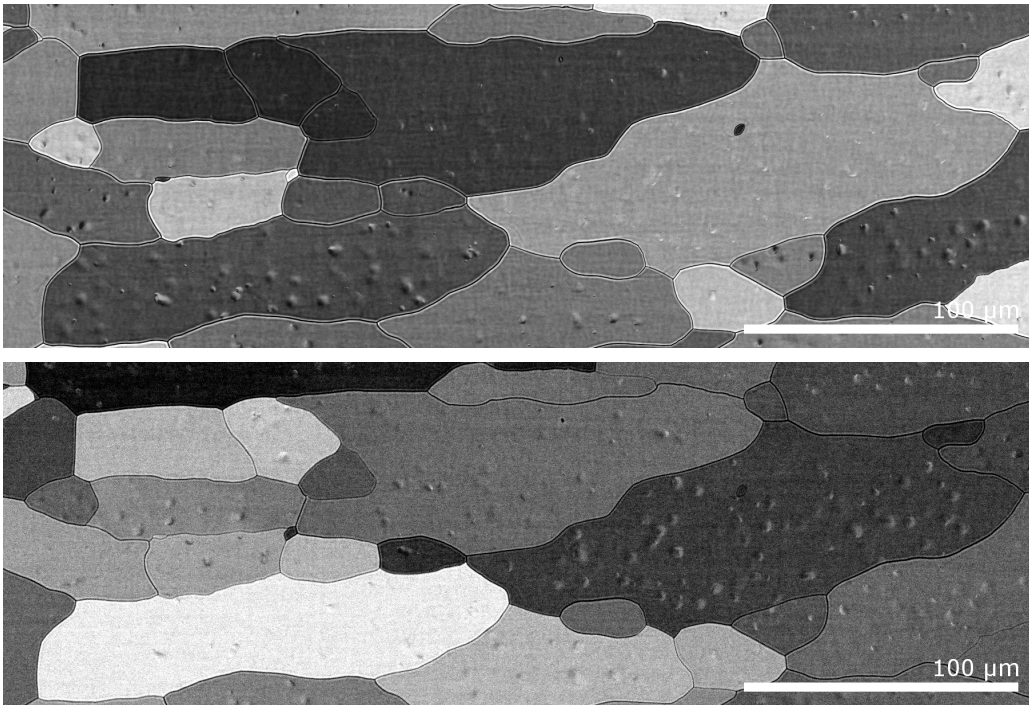

Figure 5.2.: Orientation-contrast SEM images of the same region of the sample with Zr getter exposed to deuterium-plasma for 144 h at 300 K, recorded in two different SEM observation sessions with the sample being re-mounted in between. The slightly different observation direction caused by re-mounting results in a different grain contrast and strongly influences the visibility of damage features. Brightness and contrast of both images were adjusted during post-processing to improve the comparability. The upper image includes data that was already previously displayed in [47]. (Images recorded by Stefan Elgeti, Max-Planck-Institut für Plasmaphysik)

at 300 K is displayed in Figure 5.4. It reveals sub-surface damage in a depth of up to about one µm below the surface at the locations of the cross-sectioned damage features observed in the topview orientation-contrast SEM image. The sub-surface damage appears to look like sub-surface cracks, however, as its nature could not be fully clarified, it will subsequently be referred to with the general term "sub-surface damage" [47].

It currently remains speculation how the observed sub-surface damage may develop for longer deuterium-plasma exposure times and thus higher fluences. Possibly, it represents an initial stage in the formation of gas-filled cavities that lead to the formation of blister-like structures, as they are frequently observed on tungsten after deuterium-plasma exposure (e.g. in [28, 42, 45, 176, 177]). However, to clarify this, deuterium-plasma exposure times that are even significantly longer than those presented here would be necessary.

In sum, sub-surface damage evolution, visible as damage features in topview orientation-contrast SEM images, was observed for deuterium-plasma exposure at 300 K, but not at 450 K. The number of damage features for 300 K exposure temperature partly indicated a continuous increase with exposure time, however, also exceptions from this trend and

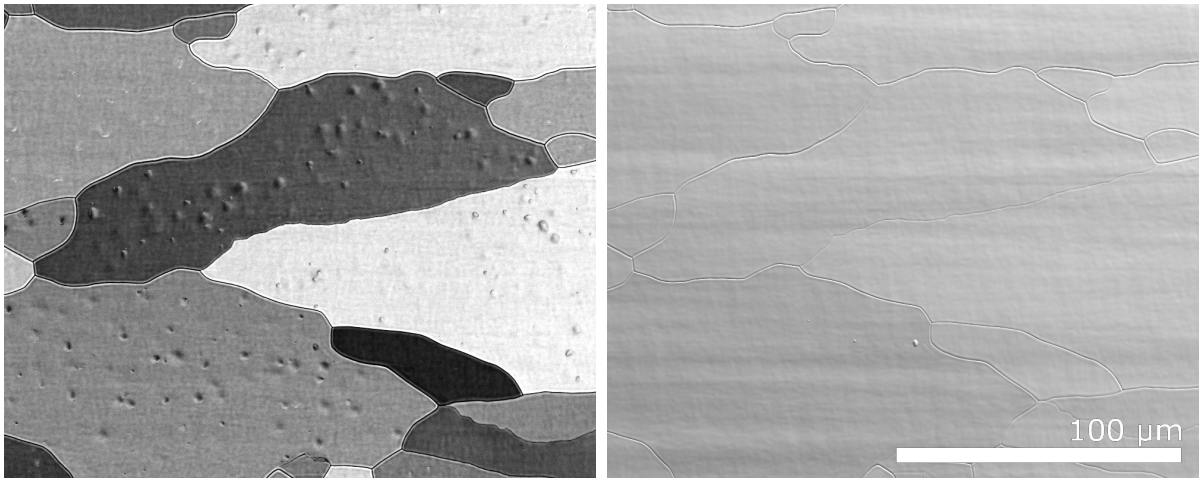

(a) orientation-contrast image (b) topographic-contrast image

Figure 5.3.: Comparison of an orientation-contrast SEM image and a topographic-contrast SEM image of the same region on the surface of the sample with zirconium getter exposed to deuterium plasma at 300 K for 144 h. The topographic-contrast image demonstrates that no surface elevations were observed in the vicinity of the damage features visible in the orientation-contrast image. Brightness and contrast of both images were adjusted during post-processing to improve the visibility of the relevant features. The images include data that was already previously displayed in [47]. Image (a) is identical with Figure 5.1e. The scale-bar in (b) is also valid for (a). (Images recorded by Stefan Elgeti, Max-Planck-Institut für Plasmaphysik)

thus a large scatter in the damage-feature areal density evolution over time were observed.

5.2. Deuterium retention after plasma exposure

The deuterium retention in a number of tungsten samples after plasma exposure was investigated by nuclear reaction analysis (NRA). It is known that the tungsten microstructure can have a significant influence on deuterium retention [29, 57, 178]. Therefore, correlations between the retention-measurement results presented in this section and the results of the microstructural analysis presented in the previous section will be discussed in Section 5.3.

5.2.1. Deuterium retention below plasma-exposed and permeation side

To study the deuterium retention in tungsten below the plasma-exposed as well as the permeation side after deuterium-plasma exposure, samples without layer system were exposed to deuterium plasma for 12 h and 192 h at 300 K and 450 K and subsequently investigated with NRA [47]. The resulting deuterium retention profiles determined using

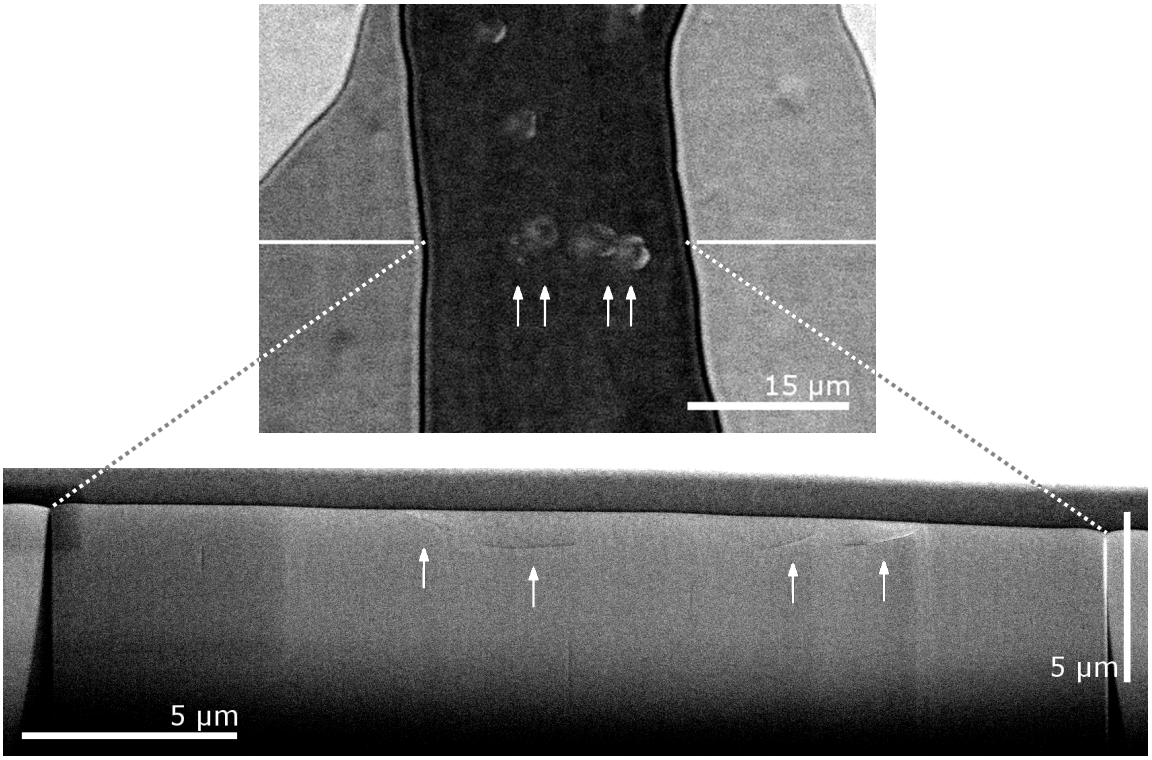

Figure 5.4.: Topview orientation-contrast SEM image of a number of damage features observed on the plasma-exposed surface of the sample with a Zr getter exposed to deuterium plasma for 144 h at 300 K (upper image). Below is an ETD SEM image of a FIB-prepared cross section through some of the damage features. The location of the cross section is marked with solid white lines in the topview image. As indicated by dotted lines, the grain boundaries visible in both images enable a comparison of the lateral positions. Arrows in the lower image mark sub-surface damage observed on the cross-section. The lateral positions of the arrows in the upper image match the lateral positions of the arrows in the lower image. They demonstrate that the lateral positions of sub-surface damage and cross-sectioned damage features are in agreement. The lower image was recorded under an angle of 38° with respect to the surface normal of the cross section. Brightness and contrast in both images were adjusted during post-processing to improve the visibility of the damage features. Both images include data that was already previously displayed in [47]. (Images recorded by Stefan Elgeti, Max-Planck-Institut für Plasmaphysik)

NRADC (compare [133] and Section 3.7.2) are displayed in Figure 5.5. Due to the limited range of the NRA analysis, the deuterium retention in the middle of the sample could not be determined. A linear interpolation was included in Figure 5.5 to guide the eye.

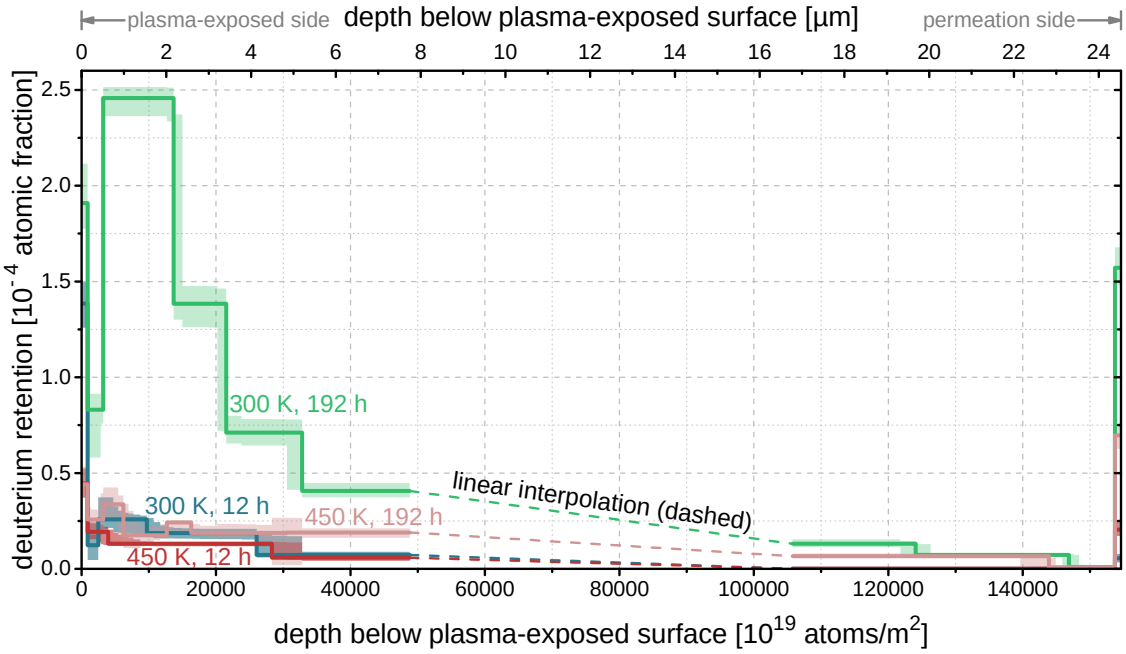

Figure 5.5.: Deuterium retention in tungsten samples without layer system below the plasma-exposed as well as the permeation side after plasma exposure at 300 K and 450 K for 12 h and 192 h. The data was already previously displayed in [47].

Surface retention peaks, as they are visible in the first layer of all depth profiles displayed in Figure 5.5, are typically ascribed to deuterium-containing adsorbates on the surfaces. While the displayed thickness of the surface layers of about 150 nm is limited by the NRA depth resolution, these surface adsorbates are assumed to be actually much thinner [47]. A deuterium-supersaturated layer below the plasma-exposed tungsten surface, as described in [22], can be excluded as the origin of the surface retention peaks due to the low incident energies present during deuterium implantation (compare Figure 3.9 and [22]). Since the deuterium contained in the surface peaks is assumed to have been mainly in an adsorbate and not in the tungsten bulk, it was neglected in the analysis discussed subsequently. This neglect also appears justified, because the deuterium amount contained in the surface peaks was at maximum 3×10^{18} D/m^2 and thus less than a monolayer [47].

The deuterium depth profiles after 12 h of deuterium-plasma exposure are comparable for both exposure temperatures. The retention was approximately equal below the plasma-exposed side and negligible below the permeation side. In contrast, the deuterium depth profiles after 192 h exposure time are significantly different. While the deuterium retention within several µm below the plasma-exposed surface after 192 h deuterium-plasma exposure at 450 K was of the same order of magnitude as the values after exposure for 12 h at both temperatures, the retention after deuterium-plasma exposure for 192 h at

300 K was about a factor of ten higher. It is interesting to note that, despite the difference below the plasma-exposed side, the deuterium retention below the permeation side after 192 h exposure was comparable for both temperatures [47].

5.2.2. Temporal evolution of the deuterium retention below the plasma-exposed surface

The large difference in the deuterium retention below the plasma-exposed surface observed for samples without layer system after exposure for 12 h and 192 h at 300 K is in contrast to the similar retention after both exposure times at 450 K (see Figure 5.5). This demonstrates differences in the temporal evolution of the deuterium retention at the two exposure temperatures, which shall be discussed in more detail in the following paragraphs.

The deuterium amount in the NRA range below the plasma-exposed surface after various exposure times was investigated by NRA. Full depth profiles generated with NRADC were determined based on NRA measurements at eight incident ^{3}He energies (compare Section 3.7.2) for a number of selected samples. The low deuterium retention made it necessary to accumulate 20 µC to 50 µC of incident charge for each incident ^{3}He energy with a beam spot of about 1 mm^2 in order to gain a sufficient number of counts. This led to long measurement times in the hour-range per depth profile [47]. Depth profiles resulting from NRA on the plasma-exposed surface of a number of samples with zirconium getter exposed to deuterium plasma at 300 K for different exposure times are displayed in Figure 5.6. While the sub-surface retention in these samples increased with exposure time, the basic profile shape underwent only a mild variation [47]. When comparing different depth profiles by eye, care must be taken to avoid misinterpretations with respect to the total deuterium retention. It must be considered that a thick layer with a low deuterium atomic fraction may represent the same deuterium amount as a thin layer with a high deuterium atomic fraction.

The number of samples for which a full depth profile could be recorded was limited by the long measurement times mentioned above. To still improve on the number of samples for which information about the deuterium retention below the plasma-exposed side is available, additional samples were investigated with NRA measurements at only 1800 keV and 4500 keV incident ^{3}He energy. These energies were chosen because of the high sensitivity in the sub-surface region for 1800 keV and probing of the full NRA range for 4500 keV. Because of the only mildly varying basic shape of the depth profile, as shown in Figure 5.6, such measurements at two incident ^{3}He energies appeared sufficient to give a good estimate of the deuterium-amount retained below the plasma-exposed surface [47].

The determination of the deuterium amount retained below the plasma-exposed surface based on measurements at two incident ^{3}He energies was carried out with the following procedure [47]: First, proportionality factors for the proton peak integrals recorded with 1800 keV and 4500 keV incident ^{3}He energy and the bulk (excluding the surface peak) deuterium amount determined with NRADC were calculated for samples where a full deuterium depth profile based on NRA measurements with eight incident ^{3}He energies was available. Based on these proportionality factors, mean proportionality factors were

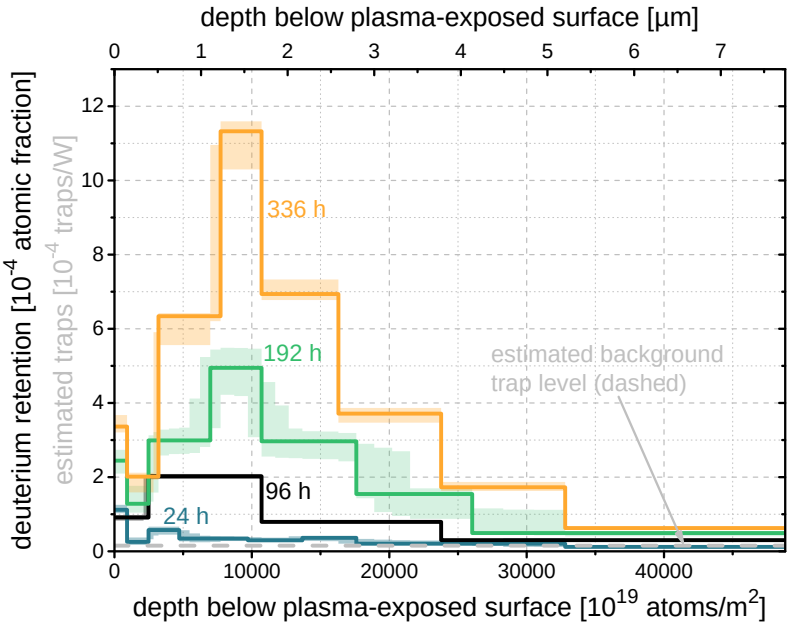

Figure 5.6.: Deuterium depth profiles below the plasma-exposed surface of samples with a zirconium getter after deuterium-plasma exposure at 300 K for different exposure times. The estimated level of background traps per tungsten atom is indicated as a dashed gray line. The data was already previously displayed in [47].

determined for all possible combinations of the two incident energies and the two exposure temperatures. These factors were subsequently used to determine the deuterium amount in the NRA range below the plasma-exposed surface based on the proton-peak integrals recorded with 1800 keV and 4500 keV incident ^{3}He energy for all samples, i.e. for those where a full depth profile determined with NRADC was available as well as for those that were only investigated with two incident ^{3}He energies. The final estimates for the deuterium retention in the NRA range below the plasma-exposed surface based on proton peak integrals were then determined as the mean of the deuterium amounts determined based on the 1800 keV and 4500 keV proton peak integrals for each sample.

The bulk deuterium amounts determined based on full depth profiles generated with NRADC and on only two incident ^{3}He energies are in excellent agreement for those samples where a full depth profile was available (compare Figure 5.7). This demonstrates that also the deuterium-retention values determined for samples that were investigated with only two incident ^{3}He energies can be regarded as reliable in the present case. Small variations of the profile shape are assumed to have been at least partially compensated by the different sensitivity of the two selected energies over depth [47].

Figure 5.7 displays the bulk deuterium amount retained in the NRA range below the plasma-exposed surface over deuterium-plasma exposure time for a number of samples. This includes the samples without layer system, for which depth profiles were presented in Figure 5.5, as well as a number of samples for which the permeated deuterium amount was presented in Figure 4.12.

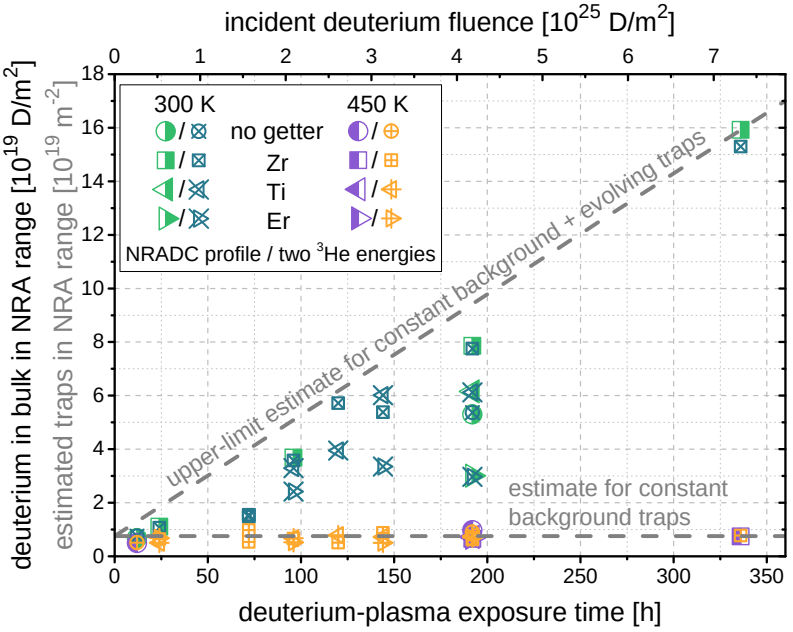

Figure 5.7.: Bulk deuterium amount retained in the NRA range below the plasma-exposed surface plotted against deuterium-plasma exposure time for exposure temperatures of 300 K and 450 K. Half-filled symbols represent data points that result from NRADC depth profiles that were determined based on NRA measurement data recorded with eight incident ^{3}He energies. Open symbols with crosses represent data points that were determined based on NRA measurement data recorded with only two incident ^{3}He energies (see text for details). The data was already previously displayed in [47].

As may already have been expected based on Figures 5.5 and 5.6 as well as the corresponding discussion, Figure 5.7 demonstrates that the deuterium retention below the plasma-exposed side remains constant with exposure time for an exposure temperature of 450 K, while it increases for 300 K exposure temperature. However, the retention increase for 300 K exposure temperature has a large scatter and thus also includes samples for which the retention increase is much lower than for others. Consequently, it appears reasonable to describe the retention increase at 300 K exposure temperature with two limiting cases [47], as will be done later in this section.

The constant retention observed for 450 K exposure temperature could be well explained by assuming a certain intrinsic background trap concentration present in the tungsten, which is filled to an equilibrium value. The average amount of deuterium retained in these background traps was estimated based on the 450 K data resulting from NRADC evaluation for exposure times of 192 h and above, for which the equilibrium was assumed to have been reached. This assumption is supported by the quite flat retention profile below the plasma-exposed side after deuterium-plasma exposure for 192 h at 450 K displayed in Figure 5.5 [47].

Assuming traps that can be occupied by either zero or one deuterium atom, so-called single-occupancy traps, and assuming further that all traps in the NRA range below the

plasma-exposed surface are completely filled, the number of retained deuterium atoms would be equal to the number of traps in the NRA range. However, it has been reported, e.g., in [39, 179] that modeling of hydrogen-isotope exchange in traps in tungsten requires diffusion-trapping models with multi-occupancy traps and fill-level dependent de-trapping energies. Still, in modeling mono-isotopic experiments, these models yield nearly identical results as classical diffusion-trapping models with single-occupancy traps, if the fill levels are simply represented by individual trap types with the corresponding de-trapping energies [39, 179]. Therefore, the assumption of single-occupancy traps still appears reasonable for the interpretation of the present mono-isotopic experiments.

The assumption that all traps below the plasma-exposed surface were nearly completely filled for 450 K exposure temperature is supported by the agreement of the depth profiles after 12 h for 300 K and 450 K in Figure 5.5, because this agreement is only expected if the traps are deep enough such that de-trapping is negligible at both temperatures [47]. Of course, additional traps with significantly lower de-trapping energies than those of the traps containing the retained deuterium observed by NRA may be present. However, since they do not affect the deuterium retention, they are not considered in this description.

Within the assumptions made above, the number of background traps in the NRA range below the plasma-exposed side was estimated based on the average amount of deuterium retained in these background traps after deuterium-plasma exposure at 450 K mentioned above. It is also indicated in Figure 5.7. Based on this estimated number of background traps in the NRA range, an estimate for the number of background traps per tungsten atom in the NRA range of $\eta_0^{\mathrm{tr}} = 1.5 \times 10^{-5}$ [47] was determined. It is assumed to be present not only in the NRA range below the plasma-exposed surface, but everywhere in the sample. The determined value of η_0^{tr} is indicated in Figure 5.6. It appears reasonable based on the depth profiles presented in Figures 5.5 and 5.6. The type of the background traps is not known, but based on literature reports grain boundaries and dislocations appear to be possible candidates [29]. Also impurity atoms or vacancies are a possibility [180]. The deuterium retention at the level of the 450 K data appears to be a reasonable choice also as a lower-limit estimate for the retention after deuterium-plasma exposure at 300 K [47].

The retention increase due to deuterium-plasma exposure at 300 K can be explained by assuming evolving traps below the plasma-exposed surface in addition to the aforementioned background traps [47]. The upper limit of the retention for 300 K exposure temperature was estimated by a linear function starting at exposure time zero from a value corresponding to the level of the background traps and going through the data point determined with NRADC for an exposure time of 336 h at 300 K (see Figure 5.7). Since all other data points are below this linear function, it is indeed a reasonable upper-limit estimate. The slope of this linear function $R_{\mathrm{NRA}}^{\mathrm{D}} = 1.3 \times 10^{14}$ D/(m^2 s) [47] is an upper-limit estimate for the rate with which deuterium gets trapped in evolving traps in the NRA range below the plasma-exposed side. Assuming that, like the background traps, the evolving traps are single-occupancy traps and completely filled, the upper limit of the trap generation rate in the NRA range below the plasma-exposed surface, which is the number of traps generated per unit time and area, corresponds to the slope of the linear function and is $R_{\mathrm{NRA}}^{\mathrm{tr}} = 1.3 \times 10^{14}$ m^{-2} s^{-1} [47]. Up to the maximum fluence of 7.3×10^{25} D/m^2 investigated in the presented experiments, no indications for a saturation

in the sub-surface retention evolution were found. The evolving sub-surface deuterium retention profile and thus trap profile at the upper-limit estimate can be estimated based on the depth profiles for samples with a zirconium getter displayed in Figure 5.6, since the data points corresponding to these profiles in Figure 5.7 are all close to the upper-limit estimate. The depth profiles in Figure 5.6 have a maximum around a depth of about 1.5 µm and also appear to be in good agreement with the estimated number of background traps per tungsten atom η_0^{tr} [47].

The retention profile shape for samples with a sub-surface deuterium retention between the upper- and lower-limit estimates can be assessed based on Figure 5.8, where depth profiles determined with NRADC for samples with different getter materials exposed at 300 K for 192 h are displayed. The depth profiles correspond to the data points for 192 h exposure at 300 K based on NRADC depth profiles displayed in Figure 5.7. They, therefore, give a good representation of the variation in the depth profile shape associated with the data scatter observed for trap evolution. Despite the significant differences in the total retention, the overall profile shape remains similar, i.e. a peaked profile with a maximum around 1.5 µm below the plasma-exposed side.

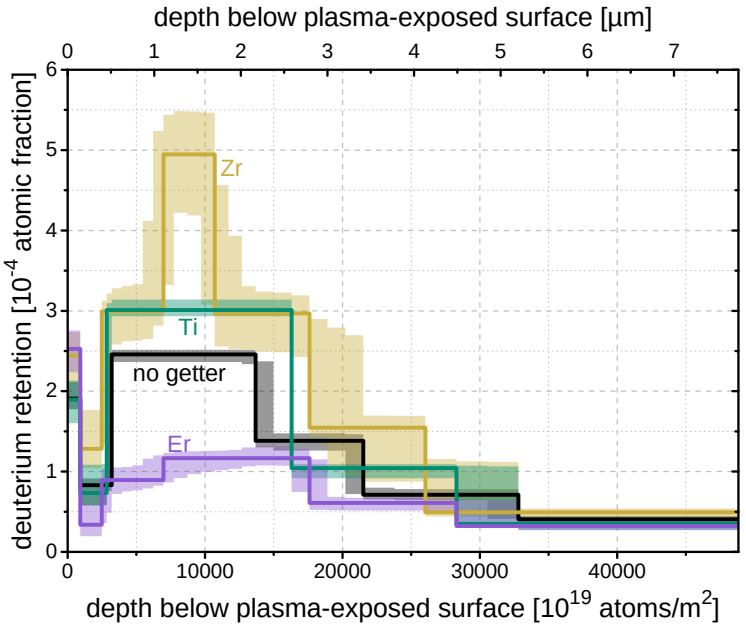

Figure 5.8.: Comparison of deuterium depth profiles below the plasma-exposed side of samples with different getter materials after deuterium plasma-exposure for 192 h at 300 K. The differences between the profiles are assumed to not result from the different getter materials, but from other factors such as variations in the initial tungsten microstructure (see text for further details). The Zr and "no getter" profiles were already previously displayed in [47] and are also included in Figures 5.6 and 5.5, respectively.

The agreement of the permeated deuterium amount measured with different getter materials (compare Section 4.4.2) excludes the different getter materials as the reason for the observed differences in the retention profiles and for the data scatter in the total

retained deuterium amount, as will be discussed in detail in Section 5.3. As in the case of the damage feature evolution, also for the retention other factors such as variations in the initial tungsten microstructure appear more likely to be the reason for the observed data scatter [47].

5.2.3. Thermal desorption spectroscopy measurements

As described in Section 5.2.2, the trap densities in the tungsten were estimated based on NRA measurements of the deuterium retention, making some assumptions. Conclusions about the de-trapping energies of deuterium retained in tungsten are frequently drawn based on thermal desorption spectroscopy (TDS) measurements (e.g. [32, 41, 57]). Diffusion-trapping modeling of the desorption spectra can be used to disentangle the effects of the retention profile, de-trapping energies and diffusion on the desorption flux [41]. In this section, TDS spectra recorded for the samples without layer system (compare Figure 5.5) will be presented and discussed in the framework of the conclusions drawn from the NRA measurements. However, estimates for de-trapping energies determined by diffusion-trapping modeling will not be presented until later in Chapter 6. The effect of defects created by the NRA analysis beam on the TDS spectra [181] is expected to be negligible, because the NRA analysis beam spot of about 1 mm^2 is much smaller than the plasma-exposed area of about (10×10) mm^2.

TDS spectra for the samples without layer system exposed to deuterium plasma for 12 h and 192 h at 300 K and 450 K are displayed in Figure 5.9. The corresponding depth profiles determined based on preceding NRA measurements on these samples were already presented in Figure 5.5. As already discussed in Section 3.8.3, the contributions by heavy water species to the deuterium desorption flux are not negligible due to the overall low deuterium retention. The uncertainties associated with the heavy water desorption that were also already discussed in Section 3.8.3 have to be kept in mind. These uncertainties can cause significant deviations in the absolute and relative peak heights, which is why the peak heights have to be interpreted with extreme caution. Also the peak positions may be affected by heavy water effects. Due to the tails towards high temperatures observed in the total desorption spectra, the positions of the desorption peaks in the spectra resulting from only the D_2 signal (dotted lines in Figure 5.9) were considered to be more reliable.

A peak in the D_2 desorption signal is located around 600 K to 650 K for both exposure temperatures of 300 K and 450 K. Only for 300 K exposure temperature an additional peak is observed around 460 K to 500 K. Both these peak positions are well within the range of literature values reported for deuterium-desorption peak positions from tungsten [31, 37, 182–184]. Assuming that the peak at the higher desorption temperature results from the background traps, as they are the only traps assumed to be active at 450 K, the additional peak or shoulder at a lower temperature may result from evolving traps, as they were only observed at 300 K exposure temperature. Since also the desorption peak at higher temperatures is significantly higher for 192 h exposure at 300 K than at 450 K, evolving traps may also be assumed to contribute to the peak at a higher desorption temperature [47].

In sum, keeping the associated significant uncertainties in mind, the peak at a higher temperature can cautiously be interpreted as resulting from background traps and in

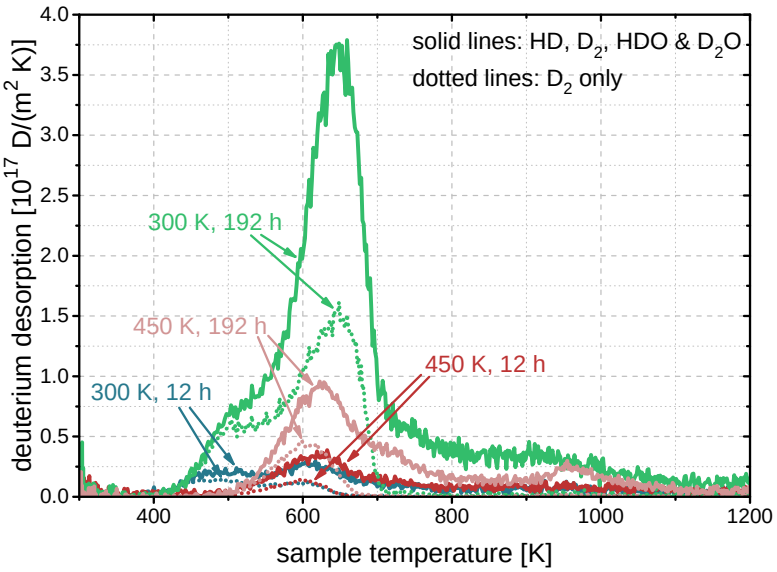

Figure 5.9.: TDS spectra measured for four samples without layer system exposed to deuterium plasma for 12 h and 192 h at 300 K and 450 K. The total deuterium desorption fluxes carried by HD, D_2, HDO and D_2O (solid lines) are displayed together with the fluxes carried by D_2 only (dotted lines). The TDS measurements resulted from the same samples for which depth profiles are displayed in Figure 5.5. The data was already previously shown in [47].

the case of 300 K exposure temperature additionally from a part of the evolving traps. The peak at a lower desorption temperature, which is only present for 300 K exposure temperature, can be cautiously interpreted as resulting from the rest of the evolving traps [47]. A more detailed discussion of the TDS spectra will be made in the context of diffusion-trapping simulations in Chapter 6.

5.3. Correlation between sub-surface damage evolution and deuterium retention

The sub-surface damage evolution presented in Section 5.1 and the retention increase due to an evolving sub-surface trap profile discussed in Section 5.2 have obvious similarities. Sub-surface damage evolution below the plasma-exposed surface was only observed for 300 K exposure temperature, but not for 450 K. Similarly, an evolution of the deuterium retention below the plasma-exposed surface was also only observed for 300 K exposure temperature, but not for 450 K [47].

The number of damage features visible in Figures 5.1a, c and e appears to increase continuously with deuterium-plasma exposure time. Also the deuterium amount retained below the plasma-exposed surface of the samples from which these images originate increased continuously, as the Zr-getter data points with the same exposure times in Figure 5.7 demonstrate. The continuous increase in the number of damage features indicated

by the images mentioned above is in contrast to the areal density of damage features displayed in Figure 5.1f. This image displays a lower areal density of damage features than Figures 5.1c and e although the latter figures were recorded on samples that were exposed to deuterium plasma shorter. However, looking at the retention below the plasma exposed surface in the sample from which Figure 5.1f originates, which is represented by the 192 h Er-getter data point for 300 K exposure temperature in Figure 5.7, it is obvious that also the deuterium amount retained below the plasma-exposed side was lower than in the samples corresponding to Figures 5.1c and e. This indicates a correlation between the areal density of damage features observed in orientation-contrast SEM images of the plasma-exposed surface and the deuterium retention measured in the NRA range below the plasma-exposed surface. This conclusion appears reasonable even though uncertainties due to the dependence of the feature visibility on grain orientation and observation direction need to be taken into account [47].

Based on the preceding discussion, it appears justified to assume that the sub-surface damage evolution results in an increased number of traps, which can be assumed to be located in the vicinity of the observed sub-surface damage. This hypothesis is also supported by the rough agreement of the depth scales on which sub-surface damage (compare Figure 5.4) and increased deuterium retention (compare Figures 5.5, 5.6 and 5.8) occur [47].

While a correlation between sub-surface damage evolution and sub-surface deuterium retention has been found, the origin of the data scatter in both could not be fully clarified. As already briefly mentioned above, the different getter materials have been excluded as the reason for the observed scatter, since the deuterium amount measured with the different getter materials was in agreement (compare Section 4.4.2) [47]. An effect of the getter material on the retention below the plasma-exposed surface could in principle occur via the solute deuterium, however, the agreement of the permeated deuterium amount determined with different getter materials (compare Section 4.4.2) suggests that also the solute deuterium concentration profile in the tungsten was very similar. One example that supports this claim is the retention and permeation data obtained on samples with different getter materials after deuterium-plasma exposure for 192 h at 300 K. While the retention data for these exposure conditions has a very large scatter (see Figures 5.7 and 5.8), the permeated deuterium amount measured with the different getter materials is in good agreement (see Figure 4.12a).

Consequently, other factors are likely to be responsible for the observed data scatter in sub-surface damage evolution and deuterium retention below the plasma-exposed surface. One likely factor are slight variations in the initial tungsten microstructure already present before plasma exposure [47]. A possible lateral inhomogeneity in the deuteron flux from the plasma to the sample holder appears unlikely to be responsible for the scatter, because a significant inhomogeneity would also have disturbed the observed agreement of the permeated deuterium amounts measured with different getter materials.

In sum, the results of the microstructural analysis show the generation of sub-surface damage due to deuterium-plasma exposure that occurs for 300 K exposure temperature, albeit with a significant data scatter, but appears to be absent for an exposure temperature of 450 K. Traps created in the vicinity of the sub-surface damage are assumed to be the reason for increased deuterium retention below the plasma-exposed surface for 300 K

exposure temperature in addition to the deuterium retention in intrinsic background traps present for both exposure temperatures [47].

5.4. Deuterium permeation

Based on the sub-surface damage evolution and the associated trap evolution discussed in Sections 5.1, 5.2 and 5.3 as well as the permeation measurement results presented in Figure 4.12, the influence of sub-surface damage evolution on the permeation flux can be investigated, as will be discussed in Section 5.4.1. In addition, the permeation flux can be used to estimate the maximum ratios of solute-deuterium to tungsten atoms in the samples in the presence of damage evolution at 300 K and the absence of damage evolution at 450 K, as will be shown in Section 5.4.2.

5.4.1. Influence of sub-surface damage evolution and associated trap evolution on the deuterium permeation flux

The results of the permeation flux measurements for 300 K and 450 K presented in Figures 4.12a and 4.12b, respectively, are summarized in Figure 5.10, excluding data points from masked and pre-heated samples.

The data sets of both exposure temperatures were each fitted with a linear function. A linear increase of the permeated deuterium amount corresponds to a constant permeation flux, as it is expected for ion-driven permeation in steady state (compare also, e.g., Section 2.3.3). To account for the data scatter, 95 % confidence bands for the fits were included in the figure. Within the data scatter, the slope and thus the steady-state permeation flux for both exposure temperatures is indistinguishable. Data points with exposure times of less than 48 h were excluded from the fits because a certain lag time until steady-state permeation was expected. Since this lag time is in general temperature-dependent even for identical steady-state permeation fluxes, a mean permeation flux for both data sets could not be determined by fitting the whole data set at once. Instead, a mean experimental steady-state permeation flux of $J_{\mathrm{perm,exp}} = 1.7 \times 10^{14}$ D/(m^2 s) [47] was determined by calculating the mean of the slopes determined for both exposure temperatures, weighted with the number of samples used for each fit. A curve with slope $J_{\mathrm{perm,exp}}$ is also included in Figure 5.10, whereby the vertical axis intercept was for simplicity also chosen as the weighted mean of the intercepts of the fits [47].

As already discussed in Section 2.3.3, a temperature-independent steady-state permeation flux can evolve during ion-driven permeation, e.g. if diffusion-limited boundary conditions can be assumed at plasma-exposed and permeation side. However, this is in general only true if the steady-state permeation flux is not affected by trapping. While this may be a reasonable assumption for a constant trap profile as it was present for 450 K exposure temperature, the continuously evolving trap profile observed for 300 K would be expected to influence the steady-state permeation flux. This is because the trapping of deuterium in evolving traps represents a loss channel for the solute and the concentration profile of the solute determines the permeation flux. As described in Section 5.2.2, the upper-limit estimate for the rate with which deuterium gets trapped in traps evolving in

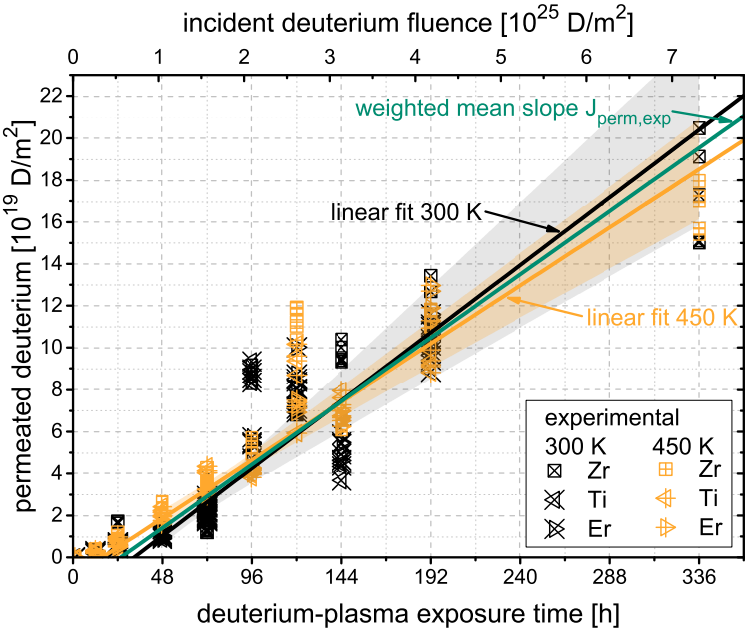

Figure 5.10.: Permeated deuterium amount over deuterium-plasma exposure time. Linear fits with 95 % confidence bands to the 300 K and 450 K experimental data sets are included as well as a linear curve with slope equal to the mean experimental permeation flux $J_{\mathrm{perm,exp}}$ determined based on the fits. The fits included only data points with exposure times of at least 48 h to account for an expected lag time in the onset of the permeation. All this data was already previously displayed in [47]. The experimental data for 300 K and 450 K exposure temperature was already included in Figures 4.12a and 4.12b, respectively. The 300 K experimental data is partially based on measurements that were used to generate the permeation data reported in [46].

the NRA range below the plasma-exposed surface is $R^{\mathrm{D}}_{\mathrm{NRA}} = 1.3 \times 10^{14}$ D/(m^2 s) [47]. Even though this loss of deuterium from the solute is of the same order of magnitude as the experimental steady-state permeation flux $J_{\mathrm{perm,exp}} = 1.7 \times 10^{14}$ D/(m^2 s) [47], the experimental results demonstrate that the evolving sub-surface damage and the associated trap evolution have only a negligible effect on the steady-state permeation flux [47]. This possibly at first sight surprising phenomenon was elucidated with diffusion-trapping simulations, the results of which will be presented in Chapter 6.

5.4.2. Estimate of the maximum ratio of solute-deuterium to tungsten atoms during plasma exposure

As already mentioned in Section 2.3.3, the solute-deuterium concentration during steady-state ion-driven permeation can be assumed to depend linearly on the position between the implantation depth d_{impl} and the permeation side ($x = L$) [89–92]. Using this assumption

and Fick's first law (Equation 2.9), the permeation flux can be written as

$$J_{\mathrm{perm}} = -D \cdot \frac{\Delta c_{\mathrm{D}}^{\mathrm{solute}}}{\Delta x} = -D \cdot \frac{c_{\mathrm{D,max}}^{\mathrm{solute}}}{L}, \tag{5.1}$$

assuming a diffusion-limited boundary condition at the permeation side, which corresponds to $c(x = L) = 0$, and $L \gg d_{\mathrm{impl}}$. The maximum solute-deuterium concentration $c_{\mathrm{D,max}}^{\mathrm{solute}}$ and maximum ratio of solute-deuterium to tungsten atoms $r_{\mathrm{D,max}}^{\mathrm{solute}}$, which are located below the plasma-exposed side, can, therefore, be calculated based on J_{perm} and the diffusion coefficient D via

$$c_{\mathrm{D,max}}^{\mathrm{solute}} = -\frac{J_{\mathrm{perm}} \cdot L}{D} \overset{\text{Eq. 2.6}}{\Longrightarrow} r_{\mathrm{D,max}}^{\mathrm{solute}} = -\frac{J_{\mathrm{perm}} \cdot L}{D} \cdot \frac{M_{\mathrm{M}}}{\rho_{\mathrm{M}} \cdot N_{\mathrm{A}}} \tag{5.2}$$

if the assumptions made above are valid (compare also, e.g., [185]) [47].

As already mentioned in Section 2.3.2, the measurements of the diffusion coefficient of hydrogen in tungsten show a large scatter [37, 38]. With the most accepted literature value for the hydrogen diffusion coefficient in tungsten [37, 38] determined by Frauenfelder [40] divided by $\sqrt{2}$ to take the isotope effect into consideration (compare [41, 179] and Equation 2.11) and the experimental permeation flux $J_{\mathrm{perm,exp}}$ from Section 5.4.1, the maximum ratios of solute-deuterium to tungsten atoms present during deuterium-plasma exposure under the given experimental conditions were estimated to be 8×10^{-7} for 300 K exposure temperature with sub-surface damage evolution and 6×10^{-9} for 450 K without sub-surface damage evolution [47]. It has to be kept in mind though that the uncertainty regarding the diffusion coefficient leads to a significant uncertainty of the estimated ratios [47].

To get an orientation what the determined ratios of solute-deuterium to tungsten atoms mean, they can be compared with the deuterium pressure necessary to generate such ratios by gas loading in thermal equilibrium. However, Sieverts' law (Equation 2.8) cannot be applied in this case because at the resulting high pressures an ideal gas, as assumed in the derivation of Sieverts' law, is not a good approximation for the behavior of deuterium. Taking the non-ideal behavior of hydrogen at high pressures into account, a correlation between equilibrium pressure and ratio of solute-hydrogen to tungsten atoms can be derived [186]. A comparison of the above-mentioned ratios with [186, 187] shows that deuterium pressures in the GPa range would be necessary to reach such high ratios of solute-deuterium to tungsten atoms at the given temperatures. This demonstrates a strong oversaturation with deuterium for both temperatures at the given deuterium-plasma-exposure conditions, which is even significantly larger for the 300 K case than the 450 K case.

5.5. Summary and conclusions for the experimental observations

In this chapter, the results of the deuterium-permeation measurements reported in Chapter 4 were combined with results of microstructural analyses and deuterium retention

measurements after deuterium-plasma exposure. Thereby, insights into deuterium retention in and permeation through tungsten as well as the influence of deuterium on the tungsten microstructure for the given experimental conditions have been gained.

This enabled an investigation of the effect of sub-surface damage evolution due to deuterium-plasma exposure on the deuterium permeation through tungsten. Damage features were observed in topview orientation-contrast SEM images of the plasma-exposed surface of tungsten samples exposed to deuterium plasma at 300 K. A combination of cross-section preparation by FIB and analysis of the cross-section by SEM revealed that they result from sub-surface damage generated in depths of up to about 1 µm below the plasma-exposed surface. Looking at the topview orientation-contrast SEM images, the damage features can easily be confused with blisters, however, since topographic-contrast SEM images show no surface elevation in their vicinity, they cannot be referred to as such. In contrast to tungsten exposed to deuterium plasma at 300 K, no indications for evolving sub-surface damage were observed for 450 K exposure temperature (all for the given experimental conditions) [47].

As for the sub-surface damage evolution, an increased sub-surface deuterium retention was also only observed for 300 K exposure temperature, but not for 450 K. This and correlations in the data scatter of damage evolution and sub-surface deuterium retention observed for 300 K exposure temperature led to the conclusion that traps for deuterium were created in the vicinity of the evolving sub-surface damage [47].

Although sub-surface damage evolution and an associated significant increase of sub-surface deuterium retention were observed only for 300 K exposure temperature, but not for 450 K, the permeation flux at both temperatures was indistinguishable within the experimental data scatter [47]. This possibly surprising effect will be elucidated based on diffusion-trapping-simulation results in Chapter 6.

Furthermore, the maximum ratios of solute-deuterium to tungsten atoms in the tungsten during deuterium-plasma exposure at 300 K and 450 K and thus in the presence and absence of damage evolution, respectively, were estimated based on the measured steady-state permeation flux. For 300 K and 450 K exposure temperature this resulted in estimated maximum ratios of 8×10^{-7} and 6×10^{-9}, respectively [47]. This data can hopefully be of value for the development and validation of future models that describe sub-surface damage evolution and associated trap evolution due to solute hydrogen isotopes in the tungsten lattice. The ratios of solute-deuterium to tungsten atoms were estimated based on a simple analytical formula (Equation 5.2). The main uncertainty in this estimate appears to be the uncertainty of the diffusion coefficient inserted into the formula [47]. Since not only the determined ratios but also the steady-state permeation flux used for their determination is provided, new estimates for the maximum ratios of solute-deuterium to tungsten atoms present for the given experimental conditions can be easily calculated if new, consolidated measurement results for the diffusion coefficient of deuterium in tungsten become available.

6. Modeling of implantation, diffusion, trapping and permeation

The results presented in this chapter were in large parts already previously published in [47].

Diffusion-trapping simulations using the computer code TESSIM [41, 94] were performed in order to elucidate the experimental results presented in Chapter 5 and in particular the negligible influence of the observed sub-surface damage and associated significant trap-evolution on the deuterium permeation flux. TESSIM solves the system of diffusion-trapping equations (Equations 2.21 and 2.23) and requires an implantation source distribution $\sigma(x,t)$ and boundary conditions as input along with other parameters such as the trap distribution and diffusion coefficient.

The implantation distribution profile $\sigma(x,t)$ was determined based on SDTrimSP [75] simulations, the results of which will be described in Section 6.1. Diffusion-limited boundary conditions were used to describe the situation at the surfaces during implantation and TDS, as will be discussed in Section 6.2. Finally, the results of the diffusion-trapping simulations will be presented in Section 6.3, which also includes information about further input parameters.

Most of the data as well as results presented in this chapter were already previously reported in [47].

6.1. Implantation simulation with SDTrimSP

The implantation source distribution $\sigma(x,t)$ for the TESSIM-based diffusion-trapping simulations was determined based on simulations performed with SDTrimSP [75] (compare Section 2.2.3) version 5.07 in static mode and with projectiles at normal incidence to the sample surface. The energy distribution of the incident deuterons from the plasma was implemented in the SDTrimSP simulations based on the differential deuteron flux density displayed in Figure 3.10. The incident deuterium molecule ions were simulated as individual deuterons with a total deuteron flux density of $J_{\text{incident}} = 6.0 \times 10^{19}$ D/(m^2 s) (compare Section 3.6 and [47]).

6.1.1. SDTrimSP input parameters

The influence of various SDTrimSP input parameters on the implantation distribution was tested by parameter variations. One parameter at a time was varied in a set of simulation runs, while the other parameters were kept constant. Their choice was based on a set of initial standard parameters that included a surface-binding energy of 1.1 eV,

the KrC interaction potential [71], an equipartition of the Lindhard-Scharff [65] and the Oen-Robinson [64] inelastic loss models and a cutoff energy of 0.39 eV. The surface-binding energy of 1.1 eV is the atomic surface binding energy of deuterium stored in a table of the SDTrimSP [75] 5.07 software package. The KrC interaction potential as well as the equipartition of the Lindhard-Scharff and the Oen-Robinson inelastic loss model were also used, e.g., in [188]. The cutoff energy was chosen to be 0.39 eV, which is equal to the activation energy of hydrogen diffusion in tungsten reported by Frauenfelder [40] (value converted to eV given, e.g., in [9]). This choice appears reasonable because a transition from the kinetic transport described by SDTrimSP to thermally activated diffusion is expected around this energy.

In the parameter variations, the surface binding energy, inelastic loss model, interaction potential and cutoff energy turned out to have a significant influence on the implantation distribution [47]. A number of simulated implantation profiles for 10^6 incident projectiles and different surface binding energies is displayed in Figure 6.1a. The height and maximum depth of the implantation distribution increase with increasing surface binding energy. This does not result from the surface binding energy hindering reflected projectiles to leave the sample, but from an acceleration of incident projectiles by the surface binding energy (compare [70] and Section 2.2.3). While this acceleration is usually negligible for high-energy projectiles, this is not the case for the present simulations, because the incident energies used here (compare Figure 3.10) are of the order of magnitude of the surface binding energy [47]. The number of particles stopped in the first layer is for most surface binding energies higher than in all other layers and increases with the surface binding energy. This phenomenon results from particles that were not able to overcome the surface binding energy and could thus not leave the sample.

A number of values of the surface binding energy used in the parameter variation resulted from surface binding models (compare [75]) implemented in SDTrimSP [75] version 5.07, which use tabulated values included in the program package. The surface binding energies resulting from these models were 1.1 eV, 4.945 eV and 8.79 eV. Additional surface binding energies of 0 eV, 0.55 eV and 2.2 eV were directly specified using an external input file.

For the variation of the inelastic loss model and the interaction potential, different models included in the SDTrimSP software package were used. They can be selected by assigning the corresponding model number to the associated input variable. Available models and their model numbers are specified in [75]. The interaction potential models used in the present simulations were the KrC [71] (model 1), Molière [72] (model 2), ZBL [58] (model 3) and Nakagawa-Yamamura [73] (model 4) potential (compare [75]). The inelastic loss models used in the present simulations were the Lindhard-Scharff [65] (model 1) and Oen-Robinson [64] (model 2) model, an equipartition of these two models (model 3) (compare [75]) as well as the stopping model by Ziegler and Biersack [63] (model 6), which was implemented by Klaus Schmid from the Max-Planck-Institut für Plasmaphysik and is included in version 5.07 of SDTrimSP in addition to the models mentioned in [75].

The goal of the SDTrimSP parameter variation was to determine a set of input parameters that yields a simulated steady-state permeation flux as close as possible to the experimentally determined value. At this point, it appeared reasonable to exclude trap evolution in the diffusion-trapping simulations to avoid possible complications associated

with its effect on the steady-state permeation flux. A temperature of 450 K was selected for these diffusion-trapping simulations because for this exposure temperature no trap evolution was observed experimentally. Consequently, the SDTrimSP implantation profiles and reflection yields determined in this initial parameter variation study were used in TESSIM simulations with an exposure temperature of 450 K and only constant background traps and the resulting steady-state permeation fluxes were compared with the experimentally determined value $J_{\mathrm{perm,exp}}$ [47]. Further details on the diffusion-trapping modeling will be given in Section 6.3. To implement the profiles resulting from SDTrimSP into TESSIM, they were fitted with a continuous function. A sum of three Gaussians, which was not intended to represent a physical model, was chosen because it resulted in a good fit to the implantation profiles. The number of particles stopped in the first layer was not included in these fits because these deuterium atoms would not be expected to be stopped in the tungsten bulk, but to be adsorbed at the surface. From there, they would have to overcome an energy barrier to enter the tungsten bulk. The probability to overcome this barrier is temperature dependent [96]. Since no temperature dependence of the permeation flux was observed, the contribution of these particles to the permeation flux is assumed to be negligible. Due to the similarity between the depth scale of trap evolution and the sample thickness, which is the relevant length scale for permeation, also the contribution of these particles to the deuterium retention is assumed to be negligible. The reflection yield Y_{refl} used in TESSIM was also determined based on the SDTrimSP results, counting particles stopped in the first layer as reflected. The simulated steady-state permeation flux resulting for different parameter sets of the initial parameter variation study with only constant background traps and 450 K exposure temperature is displayed in Figure 6.1b normalized to the experimental steady-state permeation flux $J_{\mathrm{perm,exp}}$. All simulated permeation fluxes are larger than the experimental value. This deviation would have been even very slightly larger if the deuterium stopped in the first layer would have been included. Figure 6.1b, furthermore, reveals that the surface binding energy has the strongest impact on the permeation flux, when compared to the most influential parameters mentioned above, i.e. inelastic loss model, interaction potential and cutoff energy.

As already previously mentioned in Section 2.2.3, the choice of a reasonable surface binding energy is often difficult, which is why it is frequently approximated by the heat of sublimation [70]. Due to this uncertainty and the observed improvement in the comparison of the simulated and experimental steady-state permeation flux for decreasing surface binding energy [47], a second set of standard parameters was chosen, which is identical to the initial standard parameter set except for the surface binding energy, which was set to 0 eV. A parameter variation study was also performed around this second set of standard parameters. Also in the second parameter variation study, the implantation profiles resulting from the SDTrimSP simulations were fitted with a continuous function that could be implemented in TESSIM for the diffusion-trapping simulations. A sum of five Gaussians, which was again not intended to represent a physical model, was used, because it resulted in a good fit to the simulated implantation profiles. The larger number of Gaussians compared to the first parameter variation study was chosen since a fit with three Gaussians did not yield satisfying results for some implantation profiles of the second parameter variation. The dependence of the ratio of the simulated steady-state permeation flux with only constant background traps and an exposure temperature of

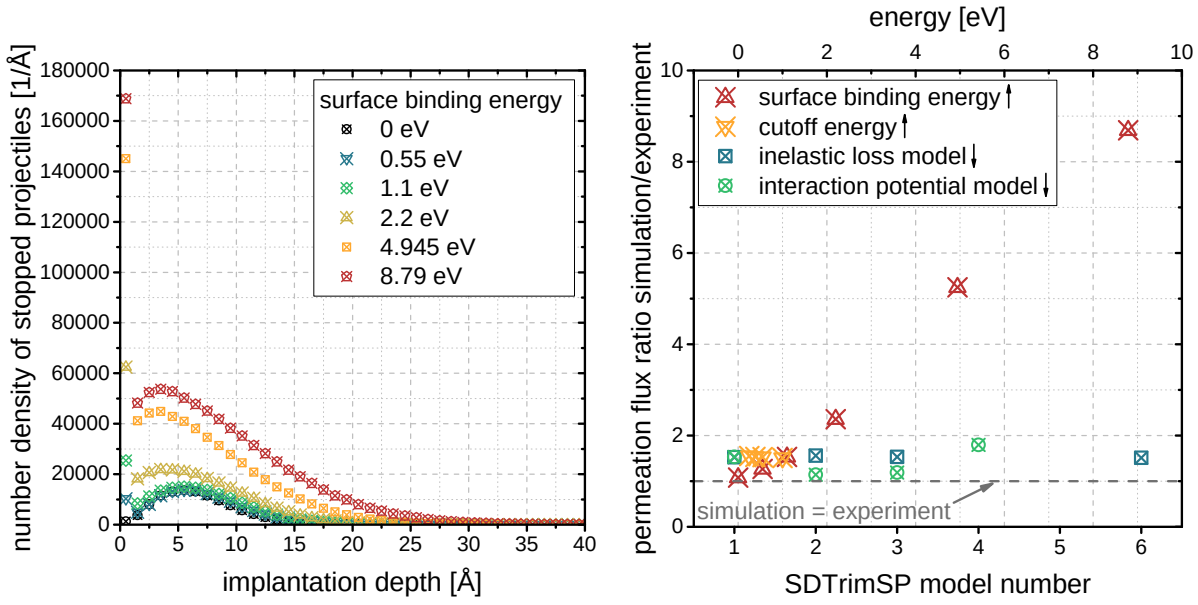

(a) (b)

Figure 6.1.: Initial SDTrimSP [75] parameter variation for 10^6 deuterium projectiles incident on tungsten with an energy spectrum based on the differential deuteron flux density displayed in Figure 3.10. Implantation profiles that resulted from simulation runs with different surface binding energies are displayed in (a). Ratios of the simulated to the experimental steady-state permeation flux that resulted from TESSIM [41, 94] diffusion-trapping simulations that used implantation source functions based on SDTrimSP [75] simulations with different input parameters are displayed in (b). See text for the models associated with the different model numbers and for details on the selection of the surface binding energies.

450 K to the experimental steady-state permeation flux on the choice of parameters in the second parameter variation study is displayed in Figure 6.2a. The figure shows that the inelastic loss model as well as the cutoff energy have only a minor influence on the simulated steady-state permeation flux, which is smaller than the experimental uncertainty that results from the data scatter in the permeation measurements. This justifies keeping the standard setting for the inelastic loss model, which is an equipartition of the Lindhard-Scharff and Oen-Robinson models [75], and the selection of the cutoff energy as Frauenfelder's activation energy for diffusion. With respect to the interaction potential, the KrC potential included in the second set of standard parameters yielded the smallest deviation of the simulated from the experimental steady-state permeation flux.

Based on the results of this second parameter variation study, it was concluded that no further parameter variation studies were required. A final set of SDTrimSP input parameters was chosen identical to the standard parameter set of the second parameter variation study. It included a surface binding energy of 0 eV, together with the KrC interaction potential, inelastic energy loss described by an equipartition of the Lindhard-Scharff and the Oen-Robinson model and a cutoff energy of 0.39 eV [47]. The implantation

profile resulting from this final parameter set is displayed in Figure 6.2b. The SDTrimSP input files used to generate it, which include also all other relevant input parameters, are displayed in Appendix A.1. Figure 6.2b also includes the fit result for the implantation simulation with the final parameter set, which was used to implement the implantation profile into TESSIM. This fit result, the function of which is given in Appendix A.2, was also used in all TESSIM diffusion-trapping simulations presented later in this chapter. The scatter in the permeation results of the second parameter variation displayed in Figure 6.2a can be used to estimate the uncertainties associated with the choice of input parameters.

As already previously mentioned in Section 2.2.3 and [47], the BCA gradually loses its validity at very low energies, but does not undergo a sudden full loss of validity at a certain energy threshold [62]. Despite the low incident energies, the simulated steady-state permeation flux is, for the final parameter set, only about ten percent higher than the experimental steady-state permeation flux. This indicates that the combination of implantation profile and reflection yield determined with SDTrimSP is a reasonable approximation to the real implantation conditions and can thus be used as input for further diffusion-trapping simulations.

A possible reason for such a good result despite the low incident energies is that chemical reactions between tungsten and hydrogen isotopes, which could lead to significant deviations from the assumptions made in the SDTrimSP model, are very limited (compare, e.g., [189]). Also a reasonable agreement of the reflection yield of deuterium incident on tungsten in the relevant energy range predicted by molecular dynamics (MD) and BCA modeling as reported in [190] justifies the confidence in the SDTrimSP results described here.

6.1.2. Correction of the reflection yield

Despite the good agreement of the simulated steady-state permeation flux for the final parameter set with the experimental permeation flux $J_{\mathrm{perm,exp}}$, it appeared reasonable to perfectly match the simulated to the experimental steady-state permeation flux for further diffusion-trapping simulations that were intended to investigate the influence of sub-surface damage evolution on the permeation flux. The reflection yield $Y_{\mathrm{refl}} = 89$ % determined with SDTrimSP was, therefore, increased to 90 % in the TESSIM input, thus matching the simulated steady-state permeation flux at 450 K with only constant background traps perfectly to the experimental steady-state permeation flux $J_{\mathrm{perm,exp}}$. This means that the implanted fraction $(1 - Y_{\mathrm{refl}})$ decreased from 11 % to 10 % [47].

The determined reflection yield of about 90 % is in good agreement with molecular dynamics (MD) simulations for the relevant energy range reported in [190] and for deuterons incident on tungsten with an energy of 10 eV reported in [191]. However, MD simulations reported in [192] suggested a lower reflection yield for the relevant energy range.

In the present case, the simulated steady-state permeation flux was matched to the experimental value by the probably most simple approach: modifying the reflection yield. However, also a modification of the implantation profile shape or shift of the implantation depth could have been performed to achieve the same effect on the permeation flux. The maximum implantation depth is much smaller than the depth of trap evolution and the

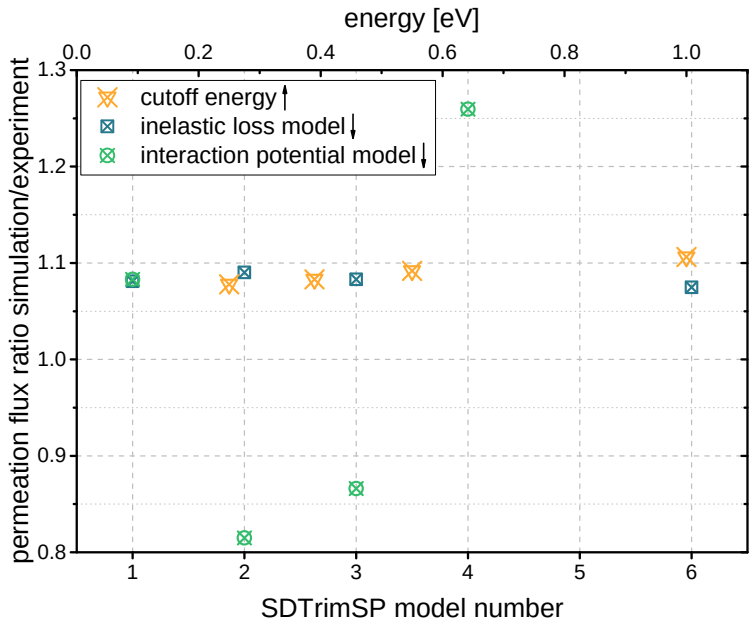

(a)

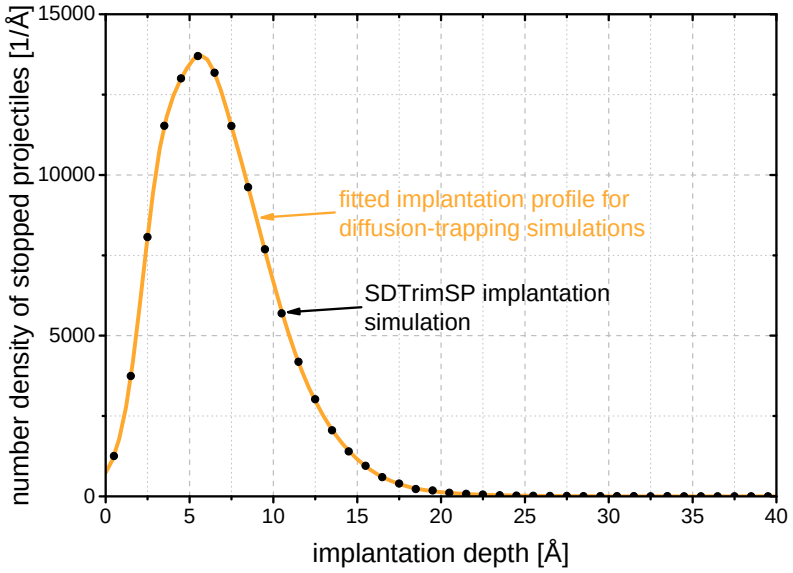

(b)

Figure 6.2.: (a) Ratios of simulated to experimental steady-state permeation flux obtained in the second SDTrimSP [75] input parameter variation study. (b) Implantation profile simulated with SDTrimSP using the final parameter set chosen based on the second parameter variation study. Also an analytical function fitted to the data is included, which was used to implement the implantation profile in TESSIM [41, 94] diffusion-trapping simulations. The data in (b) was already previously displayed in [47].

sample thickness. Therefore, the exact shape of the implantation distribution is of minor importance in studying the influence of sub-surface damage and associated trap evolution on the steady-state permeation flux, as long as the same maximum sub-surface solute deuterium concentration and thus the same steady-state permeation flux without trap evolution is reached [47]. Uncertainties in the implantation conditions are consequently expected to have no effect on the diffusion-trapping simulation results.

As already mentioned in Section 3.6, the samples were, during deuterium-plasma exposure, not only exposed to incident deuterium ions, but also to a flux of neutral deuterium atoms [117]. The average energy of these neutral atoms is expected to be very small, typically much smaller than 1 eV [57]. They are, therefore, expected to mostly not enter the tungsten directly, but be adsorbed at the surface, from where they must overcome a potential barrier to be dissolved in the tungsten bulk (compare [96]). According to [96], this barrier can be overcome at least for the higher exposure temperature of 450 K. However, the good agreement of simulation and experiment (see Section 6.1.1) based on only the incident ions suggests that the contribution of incident atomic deuterium to the permeation flux is negligible. To be precise, the steady-state permeation flux was already overestimated in almost all simulation cases (compare Figures 6.1b and 6.2a) and an additional contribution by neutral atoms could only have increased this overestimation. Even more importantly, the experimentally observed indistinguishable steady-state permeation flux for 300 K and 450 K exposure temperature strongly indicates that the incident deuterium atoms do not contribute significantly to the permeation flux. If they would, the permeation flux should be temperature dependent because the transition of deuterium from the surface to the bulk is temperature dependent [96]. Consequently, the contribution of incident neutral deuterium atoms to the permeation flux is assumed to be negligible for the present experimental conditions.

Since the permeation flux appears to be unaffected by the incident neutral deuterium atoms, the solute deuterium profile in the sample can be assumed to be unaffected as well. Therefore, the incident neutral deuterium atoms are also not expected to have any influence on the filling of traps and are thus assumed to have no effect also on the deuterium retention.

6.2. Boundary conditions for the diffusion-trapping simulations

As input for the diffusion-trapping simulations, boundary conditions for plasma-exposed and permeation side had to be chosen. Due to the large scatter in the data reported in the literature for the recombination coefficient of deuterium on tungsten (compare, e.g., [37, 150]), a choice purely based on literature data is difficult. For the reasons mentioned in the subsequent paragraphs, diffusion-limited boundary conditions were chosen for all diffusion-trapping simulations presented in this thesis, as they were also used, e.g., in [41, 94] for deuterium implanted into tungsten. Assuming that deuterium uptake from the background gas is negligible due to the low solubility of deuterium in tungsten, the

diffusion-limited boundary conditions correspond to the condition

$$c_{\mathrm{D}}^{\mathrm{solute}}(x = 0, t) = c_{\mathrm{D}}^{\mathrm{solute}}(x = L, t) = 0 \tag{6.1}$$

for the solute-deuterium concentration $c_{\mathrm{D}}^{\mathrm{solute}}$ [47]. Using Equation 2.6,

$$r_{\mathrm{D}}^{\mathrm{solute}}(x = 0, t) = r_{\mathrm{D}}^{\mathrm{solute}}(x = L, t) = 0 \tag{6.2}$$

follows consequently for the ratio of solute-deuterium to tungsten atoms $r_{\mathrm{D}}^{\mathrm{solute}}$ at the plasma-exposed ($x = 0$) and permeation ($x = L$) side. The validity of the assumption of diffusion-limited boundary conditions at both surfaces will subsequently be discussed separately for ion implantation and TDS.

Recombination limitation at the permeation side during deuterium-plasma exposure can be excluded if a getter layer is on the permeation side. This is because the deuterium atoms do not recombine, but are stored in the getter as individual atoms. A diffusion barrier at the interface or accumulation of deuterium at the interface in the getter could cause a deviation from the zero concentration condition, but both effects appear improbable because they would be expected to be different for different getter materials and thus to disturb the observed agreement of the permeation flux determined with different getter materials, as discussed in Sections 4.1 and 4.4.2. In contrast, if there is no getter on the permeation side, the permeated deuterium atoms need to recombine before desorption. However, the nearly zero retained deuterium amount directly below the permeation side of the samples without getter after 192 h deuterium-plasma exposure (see Figure 5.5) indicates that the solute-deuterium concentration below the permeation-side surface is approximately zero, because a significant solute concentration would also have led to trapping in this region. Thus, the diffusion-limited boundary condition appears also a reasonable assumption in this case [47].

Also with respect to the plasma-exposed side during deuterium-plasma exposure the assumption of a diffusion-limited boundary condition appears justified for the following reason: Taking the diffusion-limited boundary condition at the permeation side motivated in the preceding paragraph into account, the steady-state permeation flux for diffusion limitation at the plasma-exposed side can be estimated based on Equation 2.19 [91], assuming the incident total deuteron flux density J_{incident}, reflection yield Y_{refl} and sample thickness L defined above as well as an implantation depth d_{impl} chosen based on Figure 6.2b. This results in a steady-state permeation flux that is of the same order of magnitude as the experimentally observed steady-state permeation flux $J_{\mathrm{perm,exp}}$. Also the fact that the experimentally observed steady-state permeation flux is, within the data scatter, indistinguishable for 300 K and 450 K exposure temperature, is in agreement with the temperature independent steady-state permeation flux predicted by Equation 2.19. Consequently, the assumption of diffusion-limited boundary conditions at both sides results in a good representation of the experimental observations. In contrast, assuming recombination limitation at the plasma-exposed side in combination with the diffusion-limited boundary condition at the permeation side motivated above results in significant deviations. Estimating the steady-state permeation flux for this case based on Equation 2.18 [91] with the same input parameters as above, Frauenfelder's diffusion coefficient [40] divided by $\sqrt{2}$ (compare [41, 179] and Equation 2.11) and the combined surface recombination coefficient reported in [152] results in an estimated steady-state permeation flux

that is two to three orders of magnitude larger than $J_{\mathrm{perm,exp}}$ in the relevant temperature range. This difference may result from the fact that the implantation conditions utilized in [152] differed strongly from those reported in this thesis, which may have led to very different surface conditions. For example, in [152] the ions were implanted with much higher energies in the keV-range. The large difference between the steady-state permeation flux estimated for recombination limitation at the plasma-exposed side and the experimental steady-state permeation flux could be reduced by assuming a higher recombination coefficient than reported in [152]. This would be a reasonable assumption based on the scatter of recombination coefficients reported in the literature (compare, e.g., [37, 150]) to which probably also differences in the implantation conditions contribute significantly. However, increasing the assumed recombination coefficient would also lead to a gradual transition to the case of diffusion limitation at the plasma-exposed side, which was already discussed above. In addition, the observed agreement of the measured steady-state permeation flux for 300 K and 450 K exposure temperature is a strong argument against recombination limitation at the plasma-exposed side. If recombination-limited desorption would be present at the plasma-exposed side, this phenomenon could, according to Equation 2.18 [91], only be explained if the temperature dependencies of the input parameters would by coincidence result in a negligible temperature dependence of the permeation flux. However, such an assumption appears to be not justified. Even if the steady-state permeation flux for recombination limitation at the plasma-exposed side would be independent of temperature, it appears doubtful that its value would by chance have the right magnitude to reach a better agreement of the estimated with the experimental steady-state permeation flux than under the assumption of diffusion limitation at both sides described above. In sum, assuming a diffusion-limited boundary condition at the plasma-exposed side results in the best description of the experimental observations, considering the diffusion-limited boundary condition at the permeation side motivated above. In addition to a high recombination coefficient, also sputtering and abstraction of surface deuterium by particles from the plasma may assist in desorption and thus help to ensure that Equation 6.2 is a valid assumption [47].

For the TDS measurements, deviations from the assumed diffusion-limited boundary conditions cannot be excluded. Still, the assumption of diffusion-limited boundary conditions at plasma-exposed and permeation side was for simplicity kept also in the simulations of TDS [47].

6.3. Diffusion-trapping simulation results

As discussed in Chapter 5, the total number of traps per tungsten atom in the tungsten samples was assumed to consist of a constant homogeneous background η_0^{tr} and an additional contribution $\eta_{\mathrm{evolve}}^{\mathrm{tr}}(x,t)$ that evolves during deuterium-plasma exposure. Based on the TDS measurement results presented in Section 5.2.3, the existence of one type of background traps and two types of evolving traps can be cautiously assumed. Within the framework of this assumption, one type of the evolving traps yields a TDS peak in the same temperature range as the background traps. The total number of traps per tungsten

atom can be written as

$$\eta^{\mathrm{tr}}_{\mathrm{total}}(x,t) = \eta^{\mathrm{tr}}_{0} + \eta^{\mathrm{tr}}_{\mathrm{evolve}}(x,t) = \eta^{\mathrm{tr}}_{0} + \sum_{i=1}^{N^{\mathrm{tr}}_{\mathrm{evolve}}} \eta^{\mathrm{tr},i}_{\mathrm{evolve}}(x,t), \tag{6.3}$$

where i represents the i-th evolving trap type and $N^{\mathrm{tr}}_{\mathrm{evolve}}$ is the number of evolving trap types [47].

Based on the experimental results presented in Chapter 5, three cases appear interesting for diffusion-trapping simulations [47]. They are summarized in Table 6.1. The first one, subsequently abbreviated as "case 450Knte", represents the deuterium-plasma exposure at 450 K with no trap evolution. The second one represents the lower-limit estimate for the deuterium retention data measured for 300 K exposure temperature and has also no trap evolution. It is subsequently abbreviated as "case 300Knte". The last experimentally motivated simulation case represents the upper-limit estimate for the retention data measured for 300 K exposure temperature. It includes an evolving sub-surface trap profile and is abbreviated as "case 300Ksstpe".

experimentally motivated simulation cases	
case 450Knte	450 K, no trap evolution
case 300Knte	300 K, no trap evolution (300 K lower-limit estimate)
case 300Ksstpe	300 K, sub-surface trap profile evolution (300 K upper-limit estimate)
additional simulation case	
case 300Khte	300 K, homogeneous trap evolution (same total number of traps as case 300Ksstpe)

Table 6.1.: Model cases [47] simulated with the diffusion-trapping code TESSIM.

Additionally, one more simulation case was defined, for which no experimental motivation from Chapter 5 exists. This case is abbreviated as "case 300Khte". It includes homogeneous trap evolution over the entire sample thickness, and was intended to study the influence of the depth of trap evolution on its impact on the permeation flux. For comparability, the total number of traps evolving in the sample per unit time and area in case 300Khte was chosen equal to the total number of traps evolving per unit time and area in case 300Ksstpe [47].

The cooling after plasma exposure at 450 K mentioned in Section 4.3 was implemented in the simulations based on a measured temperature profile. Simulations of the sample storage at room temperature after plasma exposure resulted in negligible outgassing.

To be exact, it must be mentioned that the TESSIM simulations yielded the ratio of deuterium and tungsten atoms r_{D} as output, while the NRA measurements yielded the atomic fraction of deuterium in tungsten ζ_{D}. However, for the present low atomic fractions both quantities are essentially identical according to Equation 2.5 and will, therefore, be used synonymously also subsequently.

6.3.1. Permeation without trap evolution

In the cases 300Knte and 450Knte, without trap evolution at 300 K and 450 K, respectively, the total trap density can be written as

$$\eta_{\mathrm{total}}^{\mathrm{tr}}(x,t) = \eta_0^{\mathrm{tr}}. \tag{6.4}$$

[47].

A constant permeation flux, corresponding to a linear increase of the permeated deuterium amount, with an only slightly different lag time for the two temperatures, develops in these cases, as Figure 6.3 demonstrates. The simulated permeated deuterium amount is in good agreement with the experimental data, within the experimental data scatter. Regarding the slope and thus steady-state permeation flux, this result is obviously trivial, because the reflection yield was adjusted such that the simulated steady-state permeation flux at 450 K without trap evolution is identical to the experimental steady-state permeation flux (compare Section 6.1.2). But, also the lag times of simulation and experiment are in reasonable agreement within the experimental data scatter [47].

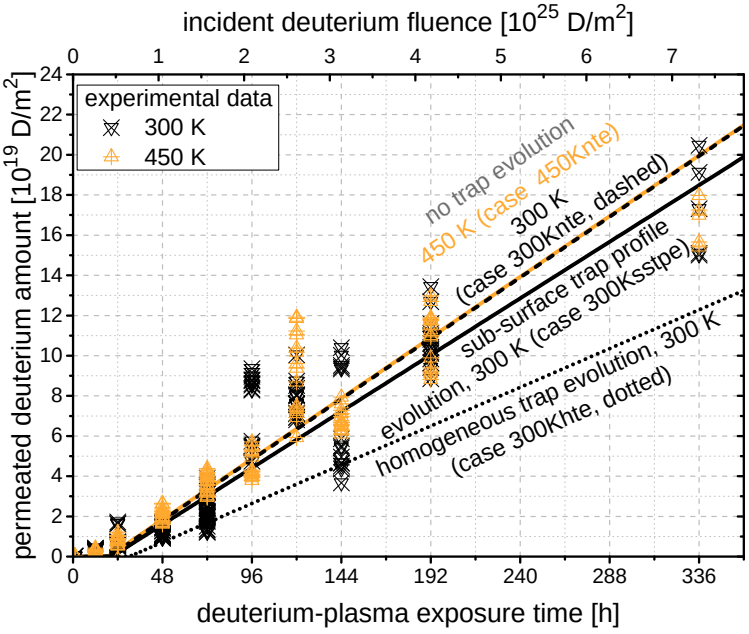

Figure 6.3.: Simulated and experimentally determined permeated deuterium amount over deuterium-plasma exposure time. The data was already previously displayed in [47]. The experimental data was already displayed in Figures 4.12 and 5.10.

The simulated ratios of solute-deuterium to tungsten atoms present in the sample during steady-state permeation after 192 h of deuterium-plasma exposure are plotted against the depth below the plasma-exposed side in Figure 6.4. As predicted in Section 2.3.3 based on [89–92], the ratio of solute-deuterium to tungsten atoms decreases linearly from a maximum $r_{\mathrm{D,max}}^{\mathrm{solute}}$ below the plasma-exposed surface to zero at the permeation side. The maximum ratios of solute-deuterium to tungsten atoms predicted for 300 K and 450 K

exposure temperature in Section 5.4.2, which were 8×10^{-7} for 300 K and 6×10^{-9} for 450 K, also agree with the simulation results [47]. This agreement is expected for the present simulation without trap evolution, since the assumptions made in the derivation of Equation 5.2 (diffusion limitation at the permeation side, no trap evolution) were also made in the simulations and the values of the parameters inserted into Equation 5.2 (diffusion coefficient, steady-state permeation flux, sample thickness) are also the same as in the simulations.

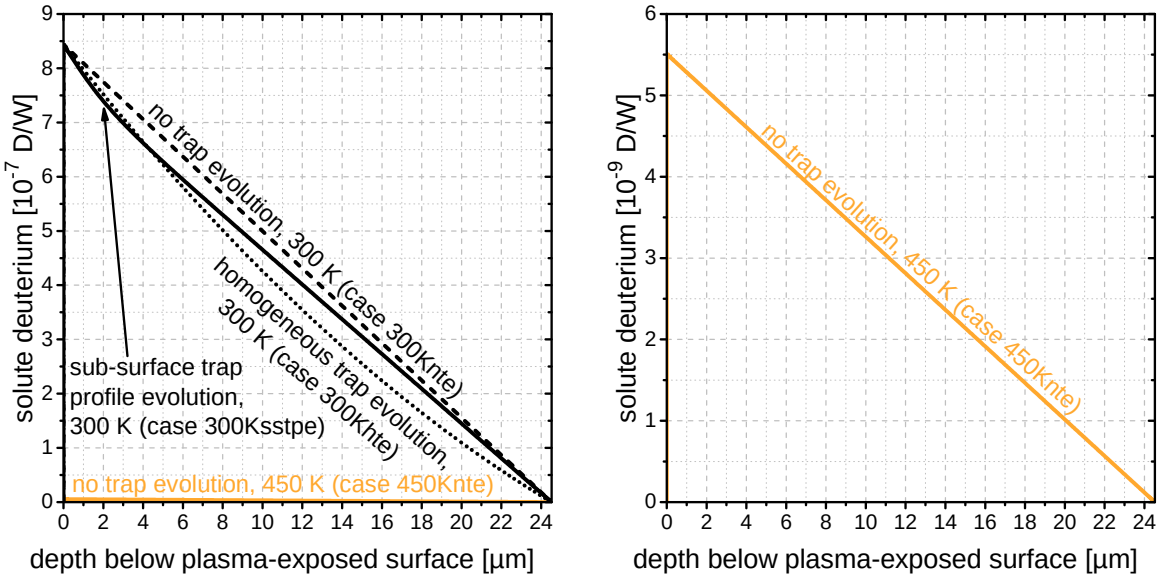

(a) (b)

Figure 6.4.: (a) Simulated ratio of solute-deuterium to tungsten atoms during deuterium-plasma exposure after 192 h for 300 K and 450 K exposure temperature. Without trap evolution, the ratio of solute-deuterium to tungsten atoms decreases linearly from a maximum in the implantation range to zero at the permeation side. With trap evolution, deviations from this linear function are observed. (b) Magnified view of the 450 K data. The data of (a) and (b) was already previously displayed in [47].

6.3.2. Influence of sub-surface-trap-profile evolution on the permeation

Since no physical model was available that is able to quantitatively describe damage and associated trap evolution due to the deuterium-plasma exposure, the trap profile evolution for the case of sub-surface-trap-profile evolution at 300 K (case 300Ksstpe) was included ad-hoc based on experimental results. The number of traps evolving per unit time and area in the NRA range below the plasma-exposed side was chosen according to the upper-limit estimate described in Section 5.2.2 and indicated in Figure 5.7. The shape of the evolving sub-surface trap profile was implemented based on the deuterium-depth-profiles

observed for samples with a zirconium getter, which were displayed in Figure 5.6 and are repeated in Figure 6.5. A simulated trap-profile shape chosen based on these depth profiles appears reasonable, since the corresponding data points in Figure 5.7 are close to the aforementioned upper-limit estimate. In Figure 6.5, the model trap profiles used for the simulations were included in addition to the experimental results of Figure 5.6. These model trap profiles were generated by fitting a continuously differentiable function to the 336 h depth profile and scaling it with time to gain a total number of traps in the NRA range equal to the upper-limit estimate. The continuous differentiability was considered necessary to exclude possible numerical artifacts, which a step profile might have caused in the diffusion-trapping simulations [47].

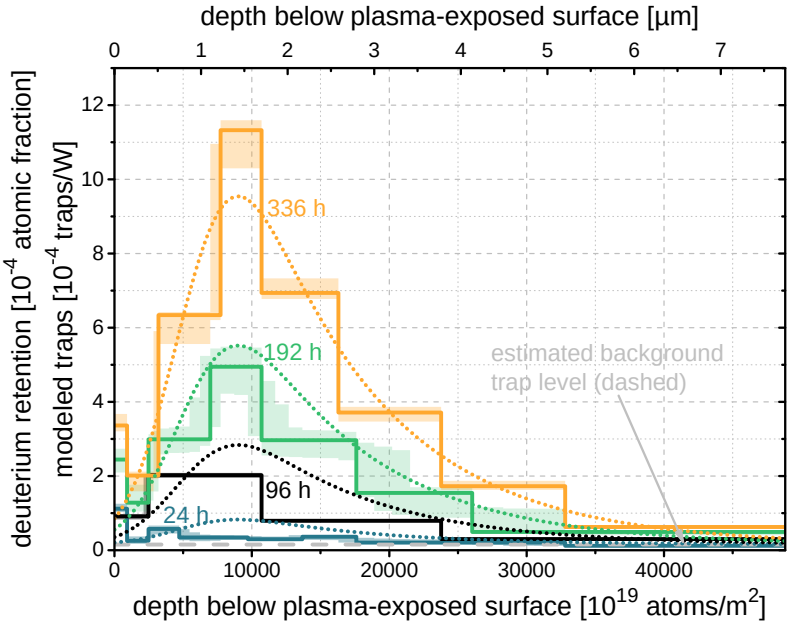

Figure 6.5.: Deuterium depth profiles below the plasma-exposed side of samples with a zirconium getter after different durations of deuterium-plasma exposure at 300 K as already displayed in Figure 5.6 (solid lines). Also included are model trap profiles (dotted lines) determined based on the 336 h experimental depth profile and scaled with exposure time corresponding to the upper-limit estimate in Figure 5.7. The data was already previously displayed in [47].

The function

$$\eta^{\mathrm{tr},i}_{\mathrm{evolve}}(x,t) = f_i(t) \cdot \frac{1}{2\kappa_0} \cdot \exp\left(b_1(x)\right) \cdot \mathrm{erfc}\left(b_2(x)\right) \tag{6.5}$$

with

$$b_1 = \frac{1}{2} \cdot \left(\frac{\sigma_0}{\kappa_0}\right)^2 - \frac{x - x_0}{\kappa_0} \tag{6.6}$$

and

$$b_2 = \frac{1}{\sqrt{2}} \cdot \left(\frac{\sigma_0}{\kappa_0} - \frac{x - x_0}{\sigma_0}\right), \tag{6.7}$$

which is based on an approximation to the exponentially modified Gaussian equation (compare, e.g., [193]), was used as fit function because it gave a good representation of the overall shape of the evolving trap profile. It is not intended to represent any underlying physical model [47].

The model parameters σ_0, κ_0 and x_0 were determined by a least-squares fit of Equation 6.5 to the 336 h deuterium depth profile in Figure 6.5 (excluding the surface layer, compare Section 5.2.1). They were kept constant in all simulations including the evolving sub-surface trap profile. To achieve the desired total number of traps in the NRA range that corresponds to the experimentally determined upper-limit estimate displayed in Figure 5.7, the profile was scaled up linearly with time. For simplicity, the individual contributions of different trap types were defined as $f_i(t) = a_{\mathrm{evolve},i} \cdot t$ for the i-th evolving trap type [47]. This linear up-scaling of the profile with exposure time while keeping the other parameters fixed also ensured that no locally decreasing trap concentrations occur anywhere in the sample, which appeared reasonable since the experimental data did not give any indication for such a local decrease. The determination of σ_0, κ_0 and x_0 based on the 336 h deuterium depth profile in Figure 6.5 appeared justified, also because the 336 h data point for 300 K exposure temperature in Figure 5.7, based on which the upper-limit estimate was defined, was generated using this depth profile.

The inclusion of the evolving sub-surface trap profile in the diffusion-trapping simulations for 300 K exposure temperature leads to only a minor decrease of the steady-state permeation flux from 1.7×10^{14} D/(m^2 s) without trap evolution to 1.6×10^{14} D/(m^2 s). The time development of the permeated deuterium amount is still well within the experimental data scatter, as displayed in Figure 6.3 (case 300Ksstpe). Consequently, the indistinguishability of the permeation flux at 450 K without trap evolution and 300 K with sub-surface-trap-profile evolution within the experimental data scatter was reproduced in the diffusion-trapping simulations [47].

The only slight decrease in the permeation flux due to the sub-surface trap profile evolution compared with the case without trap evolution results from an only slight difference in the slope of the ratio of solute-deuterium to tungsten atoms at the permeation side, as displayed in Figure 6.4. The ratio of solute-deuterium to tungsten atoms is decreased compared with the case without trap evolution (case 300Knte) almost everywhere in the sample. This decrease is less pronounced near the permeation side. At the maximum and at the permeation side, the ratio of solute-deuterium to tungsten atoms approaches essentially the same value as in case 300Knte [47]. This is because the maximum is mainly defined by implantation and re-emission through the plasma-exposed surface and the ratio is pinned to zero at the permeation side by the diffusion-limited boundary condition.

The de-trapping energies of background and evolving traps in the simulations as well as the relative abundances of the evolving trap types were chosen based on the TDS measurements presented in Section 5.2.3. In this process, a frequency pre-factor for de-trapping of $\nu_{\mathrm{TS}} = 10^{13}$ s^{-1} was assumed for all trap types, as it was also done in [41, 179]. Figure 6.6b shows simulated TDS spectra for 300 K exposure temperature with evolving sub-surface trap profile (case 300Ksstpe) and for 450 K exposure temperature without trap evolution (case 450Knte). Using a single constant background trap type with a de-trapping energy of $E_{\mathrm{const}}^{\mathrm{TS}} = 1.5$ eV, the position of the single desorption peak for 450 K exposure temperature is well reproduced, as a comparison of Figure 6.6b with

the experimental TDS spectra for samples without layer system in Figure 6.6a (identical to Figure 5.9) demonstrates. This trap type is assumed to be the only trap type of the constant background traps, which are present during deuterium-plasma exposure at 300 K as well as 450 K [47].

For 300 K exposure temperature, a part of the TDS peak observed at higher desorption temperatures was also ascribed to evolving traps. One type of evolving traps was, therefore, assumed to have the same de-trapping energy as the background traps ($E^{\mathrm{TS}}_{\mathrm{evolve},1} = E^{\mathrm{TS}}_{\mathrm{const}}$). The additional peak (or shoulder) at lower desorption temperatures, which was only present for 300 K exposure temperature, is well reproduced by assuming a second evolving trap type with a de-trapping energy $E^{\mathrm{TS}}_{\mathrm{evolve},2} = 1.25$ eV. Both de-trapping energies are well within the range of literature values reported for de-trapping energies of hydrogen isotopes in tungsten (compare, e.g., [37]) [47].

The relative contributions of the two evolving trap types were implemented with a ratio of $a_{\mathrm{evolve},1}/a_{\mathrm{evolve},2} = 2/1$, since this ratio resulted in a similar peak height of the lower-temperature desorption peak for 12 h exposure at 300 K in simulation and experiment and also yielded a reasonable qualitative agreement of the overall peak-structure shape for 192 h exposure time [47].

It must be emphasized that the uncertainties in the experimental data discussed in Section 5.2.3 lead to significant uncertainties with respect to the determined number of trap types, de-trapping energies and relative abundances for background and evolving traps [47]. The description with one background and two evolving trap types is a model assumption that results in a reasonable agreement of simulation and experiment. A more complex situation that includes additional background and/or evolving trap types may be present in reality. However, a more complex model appears to be unjustified based on the experimental observations and the associated experimental uncertainties. In addition to the uncertainties associated with the choice of the trap types and profiles, it is known that also desorption peaks for hydrogen adsorbed on the tungsten surface can be observed in the same temperature region as the peaks in Figure 6.6a (compare [194]) [47]. This may possibly lead to misinterpretations of the desorption signal if peaks resulting from surface binding or recombination are falsely ascribed to traps in the bulk. However, as already mentioned above, both determined de-trapping energies are well within the range of literature values [37] and thus appear in principle reasonable [47].

The simulated permeation flux is in the end affected by the deuterium retained in the traps and not directly by the traps themselves. The exact number of trap types, values of the trap energies and relative abundances of the trap types are, therefore, of minor importance, as long as the desired retention profile is achieved. In particular with respect to the relative abundances of the evolving traps in the present simulations, this is ensured because both evolving trap types are nearly completely filled in the simulations for 300 K exposure temperature [47].

The overall peak shapes and positions, i.e. a peak around 600 K to 650 K for 300 K and 450 K exposure temperature as well as an additional peak around 460 K to 500 K for 300 K exposure temperature, are well reproduced in the simulations. However, the peak heights partly differ significantly. For 300 K exposure temperature, an important contribution to the differences results from the use of the upper-limit estimate for trap evolution (compare Figure 5.7) used in the simulations. Another source for the different

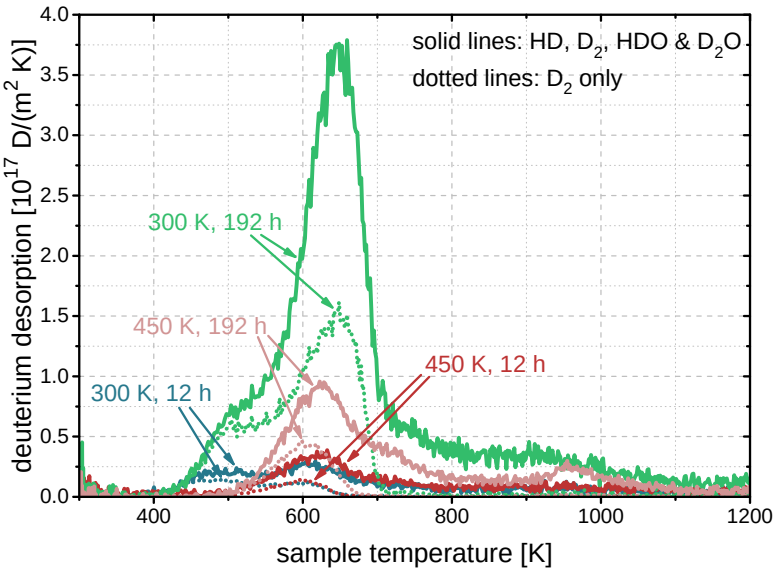

(a) experiment (identical with Figure 5.9)

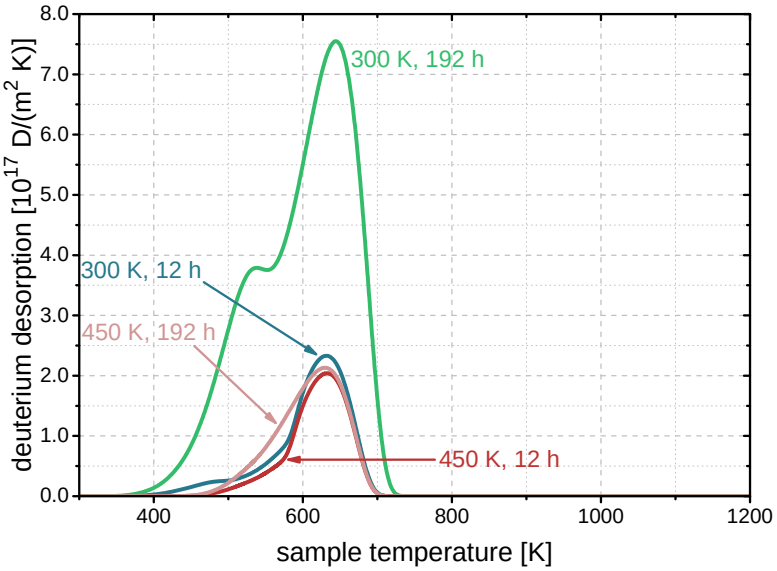

(b) simulation

Figure 6.6.: Experimental (a) and simulated (b) TDS spectra after deuterium-plasma exposure for 12 h and 192 h at 300 K and 450 K. The simulations include an evolving sub-surface trap profile for 300 K exposure temperature (case 300Ksstpe) and no evolving traps for 450 K (case 450Knte). The overall shape of the experimentally determined peak structure is well reproduced in the simulations. Differences in peak heights result from the use of the upper-limit estimate for trap evolution, heavy water contributions and differences between the experimental and simulated retention depth profiles. The data was already previously displayed in [47].

peak heights relevant for both exposure temperatures are the uncertainties associated with the heavy water contributions discussed in Sections 3.8.3 and 5.2.3. Furthermore, differences in the simulated and experimental retention profiles, which are displayed in Figure 6.7 and will be discussed subsequently, contribute to the different TDS peak heights in simulation and experiment [47].

In Figure 6.7b, simulated depth profiles of deuterium trapped in tungsten after deuterium-plasma exposure for 12 h and 192 h at 300 K with sub-surface trap profile evolution (case 300Ksstpe) and at 450 K without trap evolution (case 450Knte) are displayed. They can be compared with the corresponding experimental depth profiles recorded on samples without layer system displayed in Figure 6.7a (identical with Figure 5.5). The overall shape of the experimental and simulated depth profiles is in reasonable agreement. The flat deuterium retention profile below the plasma-exposed side for 192 h exposure at 450 K is well reproduced. Also the peak in the depth profile for 192 h exposure at 300 K is well reproduced. It has a higher maximum in the simulation, which, however, simply results from the use of the upper-limit estimate for trap evolution (compare Figure 5.7) [47].

In contrast to this obvious difference, which can be well explained, other more subtle differences indicate limitations of the used diffusion-trapping model. One indication is that the decrease of the retention profiles in the NRA range below the plasma-exposed side and the negligible retention below the permeation side after 12 h of deuterium-plasma exposure at both exposure temperatures are not correctly reproduced in the simulations. Another indication is that the decrease of the depth profiles to nearly zero below the permeation side that was observed after 192 h of deuterium-plasma exposure at both exposure temperatures is also not reproduced in the simulations. Within the framework of the present diffusion-trapping model, the experimentally observed lower retention far from the plasma-exposed side cannot be understood. The amount of deuterium that has been transported to a certain depth for a given exposure time should be very similar for simulation and experiment because the steady-state permeation flux in simulation and experiment is nearly identical. The indicated deviations of the simulations from the experimental results can possibly be helpful in the future to improve the current diffusion-trapping model [47]. Possibilities for resulting future model improvements will be discussed in Section 6.4.

6.3.3. Influence of homogeneous trap evolution on the permeation

Simulations for 300 K exposure temperature with homogeneous trap evolution throughout the tungsten (case 300Khte) were performed to investigate how the depth of trap evolution influences the impact of the trap evolution on the permeation flux. To ensure comparability, the total number of evolving traps per unit time and area in the case of homogeneous trap evolution at 300 K exposure temperature (case 300Khte) was chosen identical to the case of sub-surface trap profile evolution (case 300Ksstpe) at the same temperature [47].

The homogeneous trap evolution causes a stronger decrease of the steady-state permeation flux than the sub-surface trap profile evolution (compared to the case without trap evolution), as displayed in Figure 6.3. The simulated steady-state permeation flux with homogeneous trap evolution is decreased to 1.1×10^{14} D/(m^2 s) compared to

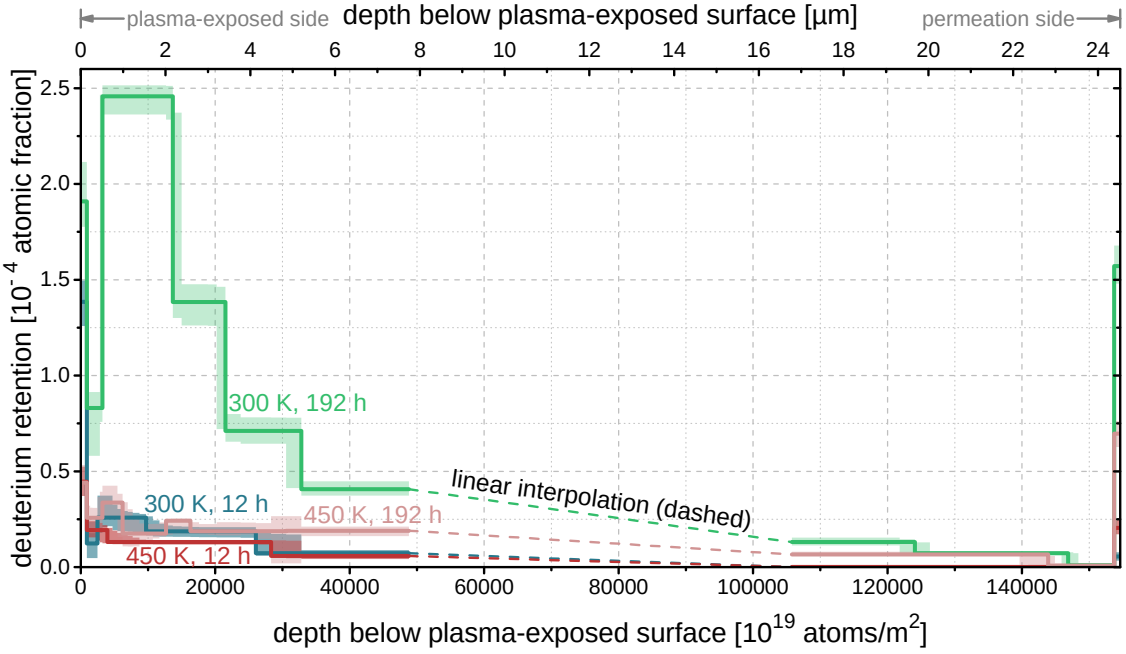

(a) experiment (identical with Figure 5.5)

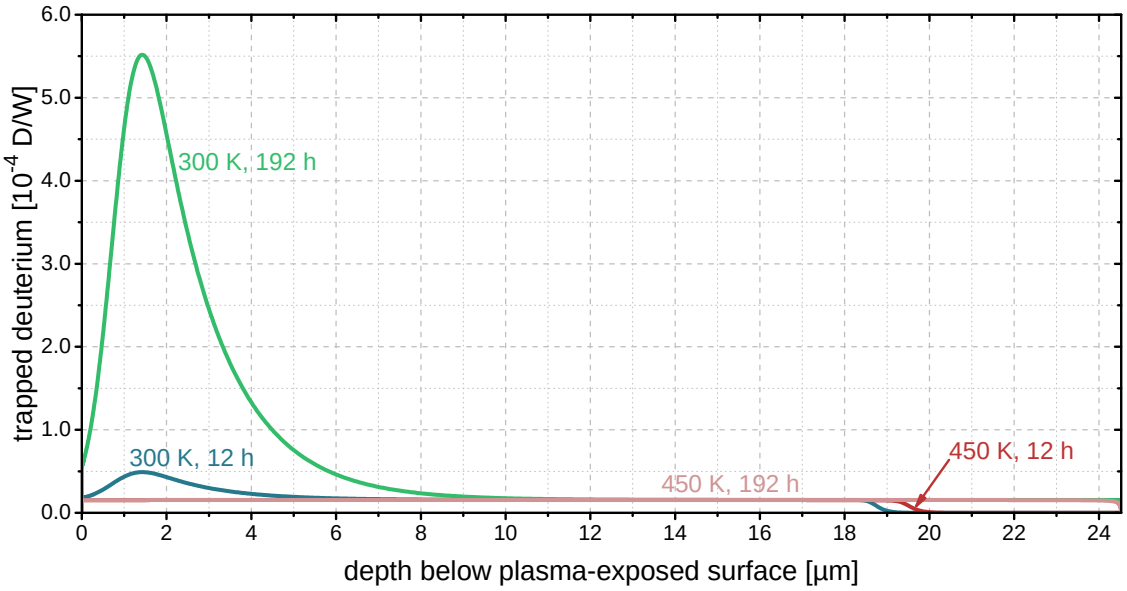

(b) simulation

Figure 6.7.: Experimental (a) and simulated (b) deuterium retention in tungsten after deuterium-plasma exposure for 12 h and 192 h at 300 K and 450 K. The simulations include sub-surface trap profile evolution for 300 K exposure temperature (case 300Ksstpe) and no evolving traps for 450 K exposure temperature (case 450Knte). The overall shape of the experimental profiles is well reproduced by the simulations. The different heights of the retention peaks at 300 K result from the use of the upper-limit estimate for trap evolution (compare Figure 5.7). However, differences between experiment and simulation regarding the retention below the permeation side and the decrease of retention with depth below the plasma-exposed side for 12 h exposure time indicate limitations of the used diffusion-trapping model. The data was already previously displayed in [47].

1.7×10^{14} D/(m^2 s) without trap evolution. The ratio of solute-deuterium to tungsten atoms displayed in Figure 6.4 deviates from the linear function between a maximum below the plasma-exposed side and zero at the permeation side that was observed without trap evolution. In the whole region between the maximum and the permeation side, it is lower than in the case without trap evolution at 300 K. Besides a small region in the vicinity of the maximum of the evolving sub-surface trap profile, the ratio of solute-deuterium to tungsten atoms during homogeneous trap evolution is also lower than that during sub-surface trap profile evolution [47].

The ratio of solute-deuterium to tungsten atoms approaches the same value as without trap evolution at the maximum as well as at the permeation side [47]. For the permeation side this results from the diffusion-limited boundary condition, which pins the solute concentration at the permeation side to zero. For the maximum, this effect results from the fact that the solute concentration directly below the plasma-exposed surface is dominated by implantation and re-emission through the plasma-exposed surface, which are essentially unaffected by trap evolution much deeper in the sample.

The difference in the slope of the ratio of solute-deuterium to tungsten atoms observed at the permeation side compared to the case without trap evolution is more pronounced for homogeneous trap evolution than for sub-surface trap profile evolution. This explains the lower simulated steady-state permeation flux in the case of homogeneous trap evolution compared with the other cases [47].

The effect of the depth in which the evolving traps are located on the amount by which the steady-state permeation flux is reduced, can be understood considering a random walk of deuterium in tungsten. Deuterium atoms that get trapped in evolving traps close to the plasma-exposed surface would, due to the random walk, in any case have had a low probability to reach the permeation side. In contrast, deuterium atoms that get trapped in evolving traps close to the permeation side would have had a high probability to reach the permeation side if they had not been trapped. Therefore, the influence of evolving traps on the permeation flux increases with increasing proximity of the trap evolution to the permeation side [47].

With respect to the curved profiles of the ratio of solute-deuterium to tungsten atoms for cases 300Ksstpe and 300Khte displayed in Figure 6.4, it is important to note that Equation 5.2 is only valid under the assumption of a linear decrease of the ratio of solute-deuterium to tungsten atoms from $r_{\mathrm{D,max}}^{\mathrm{solute}}$ to zero at the permeation side. Trap evolution deeper in the material as well as an even stronger sub-surface trap profile evolution than observed experimentally in the present study can lead to significant deviations of the ratio of solute-deuterium to tungsten atoms from the linear decrease assumed in the derivation of Equation 5.2. Estimates of the ratio of solute-deuterium to tungsten atoms based on the permeation flux using the simple Equation 5.2, therefore, become unreliable, if trap evolution is present during deuterium-plasma exposure [47].

6.4. Summary and conclusions for the modeling results

The possibly surprising negligible influence of sub-surface damage evolution on the steady-state permeation flux described in Chapter 5 was reproduced in one-dimensional diffusion-

trapping simulations performed with the TESSIM [41, 94] code. The evolving trap profile had to be implemented into the simulations ad-hoc because a physical model that quantitatively describes damage and associated trap evolution due to deuterium-plasma exposure of tungsten was not available [47].

The very limited influence of the evolving sub-surface damage on the steady-state permeation flux reported here may appear contradictory to a report by Bauer et al. in [21], where it was demonstrated that blisters can significantly reduce deep diffusion and thus permeation. However, the effect reported in [21] originates from mostly ruptured blisters that represent a loss channel for diffusing deuterium and thus reduce deep diffusion. In contrast, the sub-surface damage presented in this thesis appears to interact with deuterium by forming traps in its vicinity that trap diffusing deuterium from the solute. Therefore, the experiments and simulations presented here are not contradictory to [21], but represent a different regime of damage evolution [47]. In the present case, sub-surface damage evolution has not or possibly not yet developed into blistering. It appears, however, possible that the observed sub-surface damage might develop into blisters for significantly longer exposure times.

The simulations also revealed that traps evolving deeper below the plasma-exposed surface cause a stronger decrease of the steady-state permeation flux than traps evolving close to it. In a fusion reactor, this will be especially relevant for traps generated by neutron damage because they will be generated even deep below the plasma-exposed surface [9, 195]. If the number of traps generated per unit time and area by neutron damage and by sub-surface damage from hydrogen isotopes would be equal, the damage caused deep in the material by neutrons would thus be expected to have a much stronger influence on deep diffusion and steady-state permeation than the damage generated close to the plasma-exposed side by hydrogen isotopes [47].

As expected for the present low incident-ion energies, the implantation simulations performed with SDTrimSP [75] yielded a very shallow implantation profile and thus proved that the observed damage and trap evolution occurred even far beyond the implantation range [47]. This effect is typically ascribed to defect creation caused by an oversaturation with deuterium in the tungsten lattice [39].

When implemented into the diffusion-trapping model, implantation simulations purely based on literature values and the measured incident deuteron flux yielded results for the steady-state permeation flux that were quite close to the experimentally determined value. This suggests that modeling of experiments with diffusion-trapping simulations using an implantation profile determined with SDTrimSP, as was done, e.g., in [57, 94], can yield reasonable results also for deep diffusion and permeation, even for low incident energies in the eV range. However, especially the surface binding energy must be chosen carefully due to its strong influence on the simulation results for such low incident energies. Furthermore, as in the present case, parameter variations should be undertaken to estimate the uncertainty associated with the choice of SDTrimSP input parameters, which can easily lead to variations in the simulated steady-state permeation flux of significantly more than ten percent.

Limitations of the used diffusion-trapping model became apparent in a detailed comparison of simulated and experimental retention profiles. Traps far from the plasma-exposed side and especially close to the permeation side were filled less effectively in the exper-

iments than would be expected based on the simulations. Thermal de-trapping alone, at least as implemented in the present diffusion-trapping model, appears incapable to explain these observations. While de-trapping is strongly temperature-dependent, the measured retention close to the permeation side for exposure temperatures of 300 K and 450 K was very similar. An improvement of the agreement of the simulations with the experimental results might be possible by considering a more complex trapping process. For example, the frequently made assumption that the frequency pre-factor and activation energy for a jump into a trap are the same as for a jump to another interstitial site [39] may not be a good approximation. An alternative explanation for the observed deviations could be enhanced diffusion along grain boundaries as predicted for some types of grain boundaries by molecular dynamics simulations [196]. Since the size of many grains observed on the surfaces of the tungsten samples is comparable to the sample thickness (compare Figures 3.6 and 3.7), grain boundaries exist that connect the plasma-exposed side and the permeation side and deuterium implanted in the adjacent grains will often encounter such a grain boundary during diffusive transport before reaching the permeation side. The latter is a consequence of the random walk of diffusing deuterium atoms in tungsten. If enough of these grain boundaries would enable enhanced diffusion compared to in-grain diffusion, the in-grain-solute-deuterium concentration deep below the plasma-exposed surface could be significantly decreased due to this loss channel. This could decrease the deuterium retention in this region as observed experimentally. At the same time, the measured steady-state permeation flux, which is averaged over the NRA analysis beam spot of about 1 mm^2, should be essentially unaffected [47]. Such grain-boundary effects cannot be represented in one-dimensional diffusion-trapping simulations. Two- or three-dimensional diffusion-trapping simulations could in principle include them, but would be computationally demanding since the number of computation cells scales exponentially with the number of dimensions and the required computation time and/or power scales correspondingly.

To investigate the effect of the tungsten microstructure (e.g. grain boundaries) on the lateral homogeneity of the permeation flux, the sample with a zirconium getter exposed to deuterium plasma at 300 K for 144 h was sent to the Jožef Stefan Institute in Ljubljana (Slovenia), where it was analyzed by nuclear reaction analysis with a very small beam-spot size (microbeam NRA) [197]. The microbeam NRA on the permeation side with the layer system, which had already been suggested in [46], was performed by Sabina Markelj, Primož Vavpetič and Mitja Kelemen. The beam spot with a size of about (5×5) μm^2 was scanned over the surface to generate a two-dimensional map of the signal at different locations of the sample surface. The current of the ^3He analysis beam was 100 pA. Despite measurement times of up to about 20 h, the measurement results unfortunately suffered from insufficient counting statistics and thus did not allow reliable conclusions to be drawn about the influence of the tungsten microstructure on the lateral homogeneity of the permeation flux. A certain lateral inhomogeneity of the deuterium stored in the getter, however, appeared to be present on length scales of tens of µm. It could not finally be clarified, if this inhomogeneity resulted from microstructural features in the tungsten, from some kind of inhomogeneity of the getter layer or statistical fluctuations due to insufficient counting statistics. If counting statistics could be improved significantly, e.g. by a proton detector with larger solid angle or a much higher amount of permeated deuterium,

additional such measurements still appear promising to provide access to information about the influence of the tungsten microstructure on the homogeneity of the deuterium permeation flux.

The maximum ratios of solute-deuterium to tungsten atoms in the diffusion-trapping simulations for the two exposure temperatures are in agreement with the values determined based on the simple analytical formula in Equation 5.2, which requires only the steady-state permeation flux, sample thickness and diffusion coefficient as input. However, the simulations demonstrated that trap evolution leads to a deviation of the solute-deuterium concentration profile from the linear function between a maximum below the plasma-exposed surface and zero at the permeation side, which is expected in the case of diffusion limitation at the permeation side. Since the assumption of such a linear decrease must be fulfilled at least approximately for the simple Equation 5.2 to be valid, Equation 5.2 must be used with caution whenever trap evolution during the permeation measurement cannot be excluded [47].

Based on the results presented in Chapters 4, 5 and 6 and the results of Bauer et al. [21], three experimentally observed regimes [47] can be distinguished for the influence of sub-surface damage evolution on deep diffusion and steady-state permeation during deuterium-plasma exposure of tungsten within the framework of the assumptions made above, e.g. regarding the boundary conditions.

For negligible damage evolution, the deuterium retention is basically determined by filling of the background traps present in the material already before the plasma exposure. For steady-state permeation, the permeation flux saturates at a certain value, which is identical to the steady-state permeation flux without traps as soon as all traps are filled to an equilibrium value [47].

In the regime of moderate but significant sub-surface damage and associated trap evolution, the retention below the plasma-exposed surface is increased due to the additional traps. For a constant trap evolution rate, a steady-state permeation flux can develop, which is reduced compared to the steady-state permeation flux without trap evolution due to continuous trapping of deuterium from the solute into the evolving sub-surface traps. The reduction of the permeation flux results from the fact that the trapping of solute deuterium to the evolving traps modifies the solute-concentration profile, which determines the permeation flux. Despite significant trap evolution and an associated sub-surface deuterium retention increase per area and unit time that is of the order of magnitude of the steady-state permeation flux, the decrease of the steady-state permeation flux can be surprisingly small. The reason for this only small decrease is the proximity of the evolving sub-surface traps to the plasma-exposed surface [47].

Finally, if strong blistering of the surface occurs, ruptured blisters can increase the loss of deuterium at the plasma-exposed side. This can effectively reduce the diffusion of deuterium deeper into the tungsten and consequently also the permeation, as reported by Bauer et al. [21]. However, the reduced permeation flux will probably come at the cost of a significantly increased retention below the plasma-exposed surface due to deuterium stored in not-yet-ruptured blister cavities and defects evolving around the blisters such as those reported in [198]. The deuterium amount trapped in the tungsten in the vicinity of the blisters may still cause significantly increased retention even if most blisters are ruptured [47]. Also additional regimes are possible, especially when deviations from assumptions

made, e.g. with respect to the boundary conditions, occur.

Based on these regimes, the following conclusions can be drawn regarding a desired minimization of the hydrogen-isotope retention and steady-state permeation for tungsten exposed to hydrogen-isotope plasma. Negligible damage evolution appears preferable over moderate sub-surface damage evolution below the plasma-exposed surface because the retention increase in the latter case is not compensated by a sufficient decrease in the permeation flux. Comparing the regimes of negligible damage evolution and strong blistering, both regimes have certain advantages and disadvantages, which must be weighed up. The hindering of deep diffusion by strong blistering appears promising to reduce the permeation as well as the amount of hydrogen isotopes trapped deep in the material. However, sub-surface retention is likely to be increased significantly due to the presence of blisters. Additionally, it is important to note that blistering also endangers the structural integrity of the tungsten surface and thus may lead to a contamination of the plasma with tungsten. Such considerations are also important if conclusions for the wall of fusion reactors shall be drawn, because it was recently demonstrated that blistering does not only occur on polished samples as they are frequently used in laboratory experiments, but also on rough and technical tungsten surfaces [42] as they would be present in a fusion reactor [47].

The conditions of the presented laboratory experiments with respect to the combination of tungsten temperature, incident hydrogen-isotope flux and incident hydrogen-isotope energy distribution are unlikely to be present in a future fusion reactor (compare, e.g., [7, 8, 199, 200]). However, it appears likely that a certain influence on the sub-surface damage evolution can be exerted also for fusion-relevant conditions by controlling device parameters such as the component design and plasma parameters, which affect the wall temperature as well as the incident hydrogen-isotope flux and energy distribution. Despite different conditions, the results presented in this thesis can contribute to the development of guidelines for the optimization of such device parameters. Based on the discussion above, aiming for negligible damage evolution due to hydrogen-isotopes in tungsten appears to be a rewarding optimization goal within a conservative approach, even if strong blistering may appear to offer certain benefits with respect to deep diffusion and permeation [47]. In particular, a sufficiently high wall temperature may help to avoid sub-surface damage evolution due to the presence of hydrogen isotopes in tungsten. A high wall temperature would in addition also be beneficial for the recovery of damage created by neutrons [201, 202].

The ability of future simulations to make reliable predictions for fusion-relevant conditions and thus also for a good choice of fusion-reactor device parameters will depend on further model refinements. These should especially overcome the above-mentioned limitations of the current diffusion-trapping model and include the development of a physical model of trap evolution due to hydrogen-isotope-plasma exposure. Additional effects, such as damage creation by neutrons, possibly different surface boundary conditions and the effect of impurities in the plasma, will also need to be considered in these simulations [47].

7. Summary

The permeation of deuterium through tungsten exposed to deuterium plasma with low incident energies as well as the effect of sub-surface damage evolution on the permeation were investigated by experiments and simulations.

A method to measure the permeation of deuterium through tungsten exposed to deuterium plasma in an existing plasma device typically used for retention studies was developed and validated. The method, which was already previously described in [46, 47], was successfully applied to measure the deuterium permeation through tungsten samples with a mean thickness of about 24.5 µm at 300 K and 450 K that was driven by plasma-based implantation of deuterium ions with incident energies in the eV-range. Following experiments reported in the literature for ion-beam-driven deuterium permeation through stainless steel [153] and nickel [154], a getter layer of either zirconium, titanium or erbium deposited on each of the tungsten samples for permeation measurements was used to accumulate permeated deuterium. As in [153, 154], ion-beam analysis was subsequently applied to determine the deuterium amount in the getter layer and thus the permeated deuterium amount. To prevent a direct uptake of deuterium into the getter from the background gas present during deuterium-plasma exposure, a cover layer system was deposited on the getter layer before deuterium-plasma exposure. This was necessary because the deuterium-plasma exposures were performed at a much higher background pressure than typical ion-beam implantations. The cover layer system was, furthermore, designed such that the energy loss of the incident ^{3}He ions used for ion-beam analysis enabled a distinction of deuterium in the getter and at the cover surface. By exposing various samples for different periods of time to deuterium plasma, the dependence of the permeated deuterium amount on exposure time was studied.

The presented method has been proven to be able to measure a steady-state permeation flux of 1.7×10^{14} D/(m^2 s) [47]. This value is near the lower limit of ion-driven permeation fluxes through tungsten measured using a quadrupole mass spectrometer [23, 26, 30, 150–152]. However, also the measurement of a lower permeation flux appears possible, since the signal in the proton spectra resulting from the nuclear reaction analysis (NRA) was well above noise level. The usability of the method is currently not limited by its sensitivity, but by the data scatter in the measured permeated deuterium amount. The origin of this scatter could not be finally clarified. Future investigations regarding the uncertainties and variations associated with the various experimental parameters may be able to reduce this scatter. The sensitivity could be improved even further by using even longer deuterium-plasma exposures, by increasing the solid angles of the proton detectors and by increasing the ion fluence in the NRA measurements.

Since the determination of the permeated deuterium amount using this method can be performed ex-situ, the plasma source does not need to be in the vicinity of the accelerator used for the ion-beam analysis. Therefore, the plasma exposures could even be performed

at a completely different laboratory than the determination of the permeated deuterium amount. Also, no complex in-situ permeation measurement setup needs to be attached to the plasma source, which may be crucial, e.g. if no space for such a setup is available. Plasma-driven deuterium permeation can thus be investigated with existing plasma devices that are usually used for retention studies without the need for device modifications [46], as it was also the case in the presented experiments. Especially when retention experiments with ion-beam analysis are performed anyways, the presented method can be used to gain also information about the permeation with limited additional effort.

The results of the permeation measurements were combined with the results of a microstructural analysis and measurements of the deuterium retention in tungsten, performed on a number of tungsten samples after deuterium-plasma exposure. Together with a characterization of the incident deuterium-ion flux, these experimental results delivered a quite complete picture of the whereabouts of the implanted deuterium as well as its impact on the tungsten microstructure for the given experimental conditions. They, thereby, enabled an investigation of the influence of sub-surface damage evolution on plasma-driven deuterium permeation through tungsten, as already previously reported in large parts in [47].

Despite low incident energies in the eV-range and a moderate flux of 6.0×10^{19} D/(m^2 s) [47] with which deuterium from the plasma was implanted into the tungsten samples, sub-surface damage evolution due to the deuterium-plasma exposure was observed for an exposure temperature of 300 K. It was, however, not observed for 450 K exposure temperature. The damage was discovered in topview orientation-contrast scanning electron microscopy (SEM) images because it led to in-grain distortions that were visible in this mode of observation. The presence of sub-surface damage below the damage features observed in the topview orientation-contrast images was revealed by a combination of cross-section preparation by FIB and analysis of the cross-section by SEM. The observed damage features were not identified as blisters, because no surface elevations were detected in their vicinity in topographic-contrast SEM images. It appears, however, possible that the observed sub-surface damage may develop into blisters for longer exposure times. The low incident ion energies were chosen to exclude kinetic damage creation due to collision cascades. As revealed by the focused-ion-beam cross-sectioning and SEM analysis, sub-surface damage was observed even far beyond the implantation range. As is commonly assumed [39], its evolution was, therefore, ascribed to the deuterium present in the tungsten lattice during plasma exposure [47].

The sub-surface damage evolution was correlated with an increased deuterium retention below the plasma-exposed surface, which was also only observed for 300 K exposure temperature, but not for 450 K. This correlation justifies the assumption that traps for deuterium were created in the vicinity of the evolving sub-surface damage [47]. The long durations of up to 336 h for which the samples were exposed to deuterium-plasma are considered crucial for the discovery of the observed damage evolution and the associated increased deuterium retention, which would not have been detected for much shorter exposure times of up to about 24 h.

Although the sub-surface damage evolution and the associated increased deuterium retention were only observed for an exposure temperature of 300 K, the steady-state permeation flux at 300 K and 450 K was experimentally indistinguishable. This was the

case even though the upper limit of the rate with which deuterium gets trapped in the evolving traps per unit time and area for 300 K exposure temperature was of the same order of magnitude as the steady-state permeation flux [47].

The experimentally observed negligible influence of the sub-surface trap evolution on the steady-state permeation flux was reproduced in one-dimensional diffusion-trapping simulations performed with the TESSIM [41, 94] code. Diffusion-limited boundary conditions at plasma-exposed and permeation side and an implantation profile and reflection yield determined based on SDTrimSP [75] implantation simulations were found to give a good agreement of the simulated steady-state permeation flux with the experimentally determined value. Only a minor correction of the reflection yield was necessary to fully match the simulated to the experimental steady-state permeation flux for the best set of SDTrimSP input parameters. The evolving trap profile was implemented ad-hoc based on measured deuterium depth profiles, because a physical model that quantitatively describes damage and associated trap evolution due to the deuterium-plasma exposure was not available. The simulations also demonstrated that trap evolution deeper in the material leads to a stronger decrease of the steady-state permeation flux. The damage created by fusion neutrons is, in contrast to typical damage created by hydrogen-isotope implantation, not confined to the region near the implantation surface, but extends deep into the tungsten bulk [9, 195]. Therefore, the presented simulation results may also be relevant in the context of neutron damage in future fusion reactors [47].

Despite the overall good agreement of the simulated deuterium-retention profiles with the experimental ones, small but systematic deviations indicate limitations of the used diffusion-trapping model. They may be caused by a trapping procedure that is more complex than the one implemented in the model. For example, the frequently made assumption that the transition from a regular interstitial site to a trap has the same frequency pre-factor and activation energy as the transition to another regular interstitial site [39] may not be a good approximation. Also, enhanced diffusion along grain boundaries [196] may be the cause of the observed deviations between experiment and simulation [47].

Taking the presented experimental and simulation results as well as results from [21] into account, three regimes [47] were identified for the influence of sub-surface damage evolution during deuterium-plasma exposure of tungsten on the steady-state deuterium permeation flux, within the assumptions made, e.g. the diffusion-limited boundary conditions. In the first regime of negligible damage evolution, the retention is dominated by a constant intrinsic background trap density and the steady-state permeation flux saturates at a certain value, which is unaffected by the traps as soon as they are filled to an equilibrium value. In the second regime, moderate but significant sub-surface damage evolution leads to a continuous increase of the trap density below the plasma-exposed surface. Even if this results in a significant increase of the retained sub-surface deuterium amount, the steady-state permeation flux can remain almost unaffected. Finally, for strong blistering, the permeation flux can be significantly reduced mainly by increased loss of sub-surface solute deuterium due to ruptured blisters [21], while sub-surface retention is expected to be increased due to not-yet-ruptured blisters and defects created in the vicinity of the blisters. Although it appears to be a reasonable assumption, it is not clear if the sub-surface damage observed in the experiments presented here would develop into blisters for

sufficiently long exposure times. The existence of additional regimes is possible. Also, deviations from the assumptions made, e.g. from the diffusion-limited boundary conditions, may lead to additional regimes being present in other experimental configurations.

It is expected that the conditions in a future fusion reactor with respect to the tungsten temperature as well as the incident hydrogen-isotope flux and energy distribution will be significantly different compared to those in the presented laboratory experiments. Still, the insights discussed above can contribute to the development of guidelines for the optimization of fusion reactor device parameters such as component design and plasma parameters by suggesting negligible damage evolution due to hydrogen isotopes in tungsten as a rewarding optimization goal within a conservative approach. This is because, in the presented laboratory experiments, negligible damage evolution turned out to be preferable compared to moderate sub-surface damage evolution if a minimization of hydrogen-isotope retention in and steady-state permeation through tungsten during hydrogen-isotope-plasma exposure is desired. Strong blistering may be advantageous compared to negligible damage evolution with respect to a reduction of deep diffusion and permeation [21], but the retention in the vicinity of the blisters can be expected to be increased compared to negligible damage evolution and with respect to a fusion reactor it must also be considered that blistered tungsten surfaces may lead to enhanced erosion and thus a possible contamination of the plasma with tungsten [47]. Especially the wall temperature, which can be influenced by the choice of different device parameters, is an important factor in sub-surface damage evolution due to hydrogen isotopes in tungsten. If sufficiently high, it may help to avoid such a damage evolution.

Reliable predictions for a good choice of fusion-reactor device parameters will depend on the ability of future simulations to make reliable predictions also for fusion-relevant conditions. Therefore, model refinements will be necessary, which should overcome the limitations of the presented diffusion trapping model and include the development of a physical model of trap evolution due to hydrogen-isotope plasma exposure of tungsten. In these simulations, also additional effects caused, e.g., by neutrons resulting from the fusion reaction, possibly different boundary conditions and plasma impurities must, of course, be taken into consideration [47]. In this context, the reported method for permeation measurements may be a valuable tool that could be used to investigate the influence of plasma impurities on hydrogen-isotope permeation.

It is commonly assumed that the solute concentration, which is difficult to access experimentally, plays a crucial role in the evolution of sub-surface material defects in tungsten during hydrogen-isotope plasma exposure [39]. Based on the permeation measurements presented in this thesis and using Frauenfelder's diffusion coefficient [40], estimates for the maximum ratios of solute-deuterium to tungsten atoms of 8×10^{-7} present during sub-surface damage evolution at 300 K and of 6×10^{-9} present for negligible damage evolution at 450 K were determined [47]. They can be used to test future theories that describe sub-surface damage evolution due to hydrogen-isotope-plasma exposure of tungsten. Their uncertainty, which is mainly caused by the uncertainty of the diffusion coefficient used in their determination, may be reduced by future measurements of the diffusion coefficient [47].

The maximum ratios of solute-deuterium to tungsten atoms present during deuterium-plasma exposure mentioned above were estimated based on the measured steady-state per-

meation flux using a simple analytical formula (Equation 5.2), assuming diffusion-limited transport at the permeation side. The diffusion-trapping simulations yielded maximum ratios of solute-deuterium to tungsten atoms that were consistent with those determined with the simple analytical formula, but also demonstrated that this formula must be used with caution if trap evolution cannot be excluded. This is because a linear decrease of the solute-deuterium concentration from a maximum below the plasma-exposed surface to zero at the permeation side during steady-state permeation was assumed in the derivation of this simple analytical formula. However, as the diffusion-trapping simulations demonstrated, trap evolution may lead to significant deviations from this assumption [47].

The results presented in this thesis form a solid basis for further investigations regarding the plasma-driven permeation of hydrogen isotopes through tungsten and the influence of sub-surface damage evolution on it. They may, furthermore, be helpful to develop a theory that quantitatively describes the evolution of sub-surface damage due to hydrogen-isotope implantation into tungsten and to improve current diffusion-trapping models.

A. Appendix

A.1. SDTrimSP input

The file tri.inp used as input for the SDTrimSP [75] 5.07 simulations is reported subsequently in the version of the final parameter set. It is configured to use an incident energy spectrum defined in the file energy.inp and the surface-binding energies specified in the file mat_surfb.inp. A shortened version of energy.inp, which includes the incident energy spectrum that was determined based on the retarding field analyzer measurements described in Section 3.6 and is displayed in Figure 3.10, is displayed below as well as the file mat_surfb.inp in the version of the final parameter set.

The structure of the files is based on examples given in [75], examples included in the SDTrimSP 5.07 software package and additional information and examples supplied by Andreas Mutzke and Klaus Schmid from the Max-Planck-Institut für Plasmaphysik.

tri.inp

```
standardAB_finalRun_20170911, D -> W
& TRI_INP

text='---elements---'
ncp = 2
symbol = "D", "W"
tableinp = "../../../tables"

text='---beam---'
case_e0 = 1
e0 = 0.0, 0.0
energyinp="./"
qubeam = 1.0, 0.0

case_alpha = 0
alpha0 = 0.0, 0.0

text='---control---'
flc = 731808
flux = 0.605
nh = 1000000
nr_pproj = 1
```

```
idrel = -1

ipot = 1
irc0 = 1
iintegral = 2
ipivot = 8
irand = 42
nx_mat = 1000

text='---target---'
ttarget = 100
nqx = 100
ttemp =450
isbv = 6
inel0 = 3, 3
qu = 0.0, 1.0

e_cutoff = 0.39, 0.39
iq0 = 0
isot = 0
/
```

energy.inp (shortened)

```
energy(eV)          distribution[-]
0.01          5.0385e+14
0.02          5.3848e+14
0.03          5.7537e+14
0.04          6.1467e+14
0.05          6.5652e+14
0.06          7.0108e+14
0.07          7.4851e+14
0.08          7.9898e+14
0.09          8.5269e+14
⋮
```

mat_surfb.inp

```
matrix of surface-binding-energy [eV] ---text
   2          ---number of elements
   1 D        ---Z, symbol for check of input
   74 W       ---Z, symbol for check of input
D             W
0.0           0.0           for D on X
0.0           8.79          for W on X
```

A.2. Fit of the implantation distribution for the final SDTrimSP parameter set

The implantation distribution for the final set of SDTrimSP [75] input parameters (Figure 6.2b) was fitted with an analytical function to implement it into TESSIM [41, 94] for the diffusion trapping simulations. As mentioned in Section 6.1.1, the fitted function was a sum of five Gaussians:

$$f(x) = \sum_{i=1}^{5} a_i \cdot \exp\left(-\frac{(x-b_i)^2}{2c_i^2}\right). \tag{A.1}$$

The fit parameters of Equation A.1 for the final parameter set are summarized in Table A.1.

parameter	value [1/Å]	parameter	value [Å]	parameter	value [Å]
a_1	6008.82808	b_1	3.15702	c_1	1.19344
a_2	6695.27933	b_2	6.70756	c_2	2.3519
a_3	3914.33446	b_3	8.69857	c_3	3.59678
a_4	500.60064	b_4	8.25583	c_4	6.62747
a_5	3885.45744	b_5	5.37252	c_5	1.28973

Table A.1.: Fit parameters for the final SDTrimSP implantation profile.

Bibliography

[1] U.S. Energy Information Administration. International energy outlook 2017. U.S. Energy Information Administration, 1000 Independence Ave, SW Washington, DC 20585, September 2017. URL `https://www.eia.gov/outlooks/ieo/pdf/0484(2017).pdf`. (accessed December 12, 2017).

[2] United Nations. Paris agreement, 2015. URL `http://unfccc.int/files/essential_background/convention/application/pdf/english_paris_agreement.pdf`. (accessed January 02, 2018).

[3] S. W. White and G. L. Kulcinski. Birth to death analysis of the energy payback ratio and CO_2 gas emission rates from coal, fission, wind, and DT-fusion electrical power plants. *Fusion Engineering and Design*, 48(3-4):473–481, 2000. doi:10.1016/s0920-3796(00)00158-7.

[4] M. Kikuchi. *Frontiers in Fusion Research*, chapter Sun on Earth: Endless Energy from Hydrogen, pages 1–14. Springer London, 2011. ISBN 978-1-84996-410-4. doi:10.1007/978-1-84996-411-1_1.

[5] F. F. Chen. *Introduction to Plasma Physics and Controlled Fusion*, chapter Plasma Applications, pages 355–411. Springer International Publishing, 2016. ISBN 978-3-319-22309-4. doi:10.1007/978-3-319-22309-4_10.

[6] P. K. Kaw and I. Bandyopadhyay. The case for fusion. In M. Kikuchi, K. Lackner, and M. Q. Tran, editors, *FUSION PHYSICS*. International Atomic Energy Agency, 2012. ISBN 978-92-0-130410-0.

[7] H. Bolt, V. Barabash, G. Federici, J. Linke, A. Loarte, J. Roth, and K. Sato. Plasma facing and high heat flux materials – needs for ITER and beyond. *Journal of Nuclear Materials*, 307-311:43–52, 2002. doi:10.1016/s0022-3115(02)01175-3.

[8] H. Bolt, V. Barabash, W. Krauss, J. Linke, R. Neu, S. Suzuki, N. Yoshida, and ASDEX Upgrade Team. Materials for the plasma-facing components of fusion reactors. *Journal of Nuclear Materials*, 329-333:66–73, 2004. doi:10.1016/j.jnucmat.2004.04.005.

[9] J. Roth and K. Schmid. Hydrogen in tungsten as plasma-facing material. *Physica Scripta*, T145:014031, 2011. doi:10.1088/0031-8949/2011/t145/014031.

[10] N. Yoshida, H. Iwakiri, K. Tokunaga, and T. Baba. Impact of low energy helium irradiation on plasma facing metals. *Journal of Nuclear Materials*, 337-339:946–950, 2005. doi:10.1016/j.jnucmat.2004.10.162.

[11] A. Kallenbach, M. Balden, R. Dux, T. Eich, C. Giroud, A. Huber, G. P. Maddison, M. Mayer, K. McCormick, R. Neu, T. W. Petrie, T. Pütterich, J. Rapp, M. L. Reinke, K. Schmid, J. Schweinzer, S. Wolfe, the ASDEX Upgrade Team, DIII-D Team, Alcator Team, and JET-EFDA Contributors. Plasma surface interactions in impurity seeded plasmas. *Journal of Nuclear Materials*, 415(1):S19–S26, 2011. doi:10.1016/j.jnucmat.2010.11.105.

[12] M. Mayer, S. Krat, W. Van Renterghem, A. Baron-Wiechec, S. Brezinsek, I. Bykov, P. Coad, Yu. Gasparyan, K. Heinola, J. Likonen, A. Pisarev, C. Ruset, G. de Saint-Aubin, A. Widdowson, and JET Contributors. Erosion and deposition in the JET divertor during the first ILW campaign. *Physica Scripta*, T167:014051, 2016. doi:10.1088/0031-8949/t167/1/014051.

[13] Y. Ueda, J. W. Coenen, G. De Temmerman, R. P. Doerner, J. Linke, V. Philipps, and E. Tsitrone. Research status and issues of tungsten plasma facing materials for ITER and beyond. *Fusion Engineering and Design*, 89(7-8):901–906, 2014. doi:10.1016/j.fusengdes.2014.02.078.

[14] J. Ongena, R. Koch, R. Wolf, and H. Zohm. Magnetic-confinement fusion. *Nature Physics*, 12:398–410, 2016. doi:10.1038/nphys3745.

[15] J. Knaster, A. Moeslang, and T. Muroga. Materials research for fusion. *Nature Physics*, 12:424–434, 2016. doi:10.1038/nphys3735.

[16] R. Neu, A. Kallenbach, M. Balden, V. Bobkov, J. W. Coenen, R. Drube, R. Dux, H. Greuner, A. Herrmann, J. Hobirk, H. Höhnle, K. Krieger, M. Kočan, P. Lang, T. Lunt, H. Maier, M. Mayer, H. W. Müller, S. Potzel, T. Pütterich, J. Rapp, V. Rohde, F. Ryter, P. A. Schneider, J. Schweinzer, M. Sertoli, J. Stober, W. Suttrop, K. Sugiyama, G. van Rooij, and M. Wischmeier. Overview on plasma operation with a full tungsten wall in ASDEX upgrade. *Journal of Nuclear Materials*, 438: S34–S41, 2013. doi:10.1016/j.jnucmat.2013.01.006.

[17] S. Brezinsek, T. Loarer, V. Philipps, H. G. Esser, S. Grünhagen, R. Smith, R. Felton, J. Banks, P. Belo, A. Boboc, J. Bucalossi, M. Clever, J. W. Coenen, I. Coffey, S. Devaux, D. Douai, M. Freisinger, D. Frigione, M. Groth, A. Huber, J. Hobirk, S. Jachmich, S. Knipe, K. Krieger, U. Kruezi, S. Marsen, G. F. Matthews, A. G. Meigs, F. Nave, I. Nunes, R. Neu, J. Roth, M. F. Stamp, S. Vartanian, and U. Samm. Fuel retention studies with the ITER-like wall in JET. *Nuclear Fusion*, 53(8):083023, 2013. doi:10.1088/0029-5515/53/8/083023.

[18] R. A. Pitts, A. Kukushkin, A. Loarte, A. Martin, M. Merola, C. E. Kessel, V. Komarov, and M. Shimada. Status and physics basis of the ITER divertor. *Physica Scripta*, T138:014001, 2009. doi:10.1088/0031-8949/2009/t138/014001.

[19] G. Federici, W. Biel, M. R. Gilbert, R. Kemp, N. Taylor, and R. Wenninger. European DEMO design strategy and consequences for materials. *Nuclear Fusion*, 57 (9):092002, 2017. doi:10.1088/1741-4326/57/9/092002.

[20] V. Kh. Alimov, K. Ertl, and J. Roth. Deuterium retention and lattice damage in tungsten irradiated with D ions. *Journal of Nuclear Materials*, 290-293:389–393, 2001. doi:10.1016/s0022-3115(00)00580-8.

[21] J. Bauer, T. Schwarz-Selinger, K. Schmid, M. Balden, A. Manhard, and U. von Toussaint. Influence of near-surface blisters on deuterium transport in tungsten. *Nuclear Fusion*, 57(8):086015, 2017. doi:10.1088/1741-4326/aa7212.

[22] L. Gao, W. Jacob, U. von Toussaint, A. Manhard, M. Balden, K. Schmid, and T. Schwarz-Selinger. Deuterium supersaturation in low-energy plasma-loaded tungsten surfaces. *Nuclear Fusion*, 57(1):016026, 2017. doi:10.1088/0029-5515/57/1/016026.

[23] Yu. M. Gasparyan, A. V. Golubeva, M. Mayer, A. A. Pisarev, and J. Roth. Ion-driven deuterium permeation through tungsten at high temperatures. *Journal of Nuclear Materials*, 390-391:606–609, 2009. doi:10.1016/j.jnucmat.2009.01.172.

[24] A. A. Haasz, J. W. Davis, M. Poon, and R. G. Macaulay-Newcombe. Deuterium retention in tungsten for fusion use. *Journal of Nuclear Materials*, 258-263:889–895, 1998. doi:10.1016/s0022-3115(98)00072-5.

[25] M. H. J. 't Hoen, M. Balden, A. Manhard, M. Mayer, S. Elgeti, A. W. Kleyn, and P. A. Zeijlmans van Emmichoven. Surface morphology and deuterium retention of tungsten after low- and high-flux deuterium plasma exposure. *Nuclear Fusion*, 54 (8):083014, 2014. doi:10.1088/0029-5515/54/8/083014.

[26] H. T. Lee, E. Markina, Y. Otsuka, and Y. Ueda. Deuterium ion-driven permeation in tungsten with different microstructures. *Physica Scripta*, T145:014045, 2011. doi:10.1088/0031-8949/2011/t145/014045.

[27] F. Liu, H. Zhou, X.-C. Li, Y. Xu, Z. An, H. Mao, W. Xing, Q. Hou, and G.-N. Luo. Deuterium gas-driven permeation and subsequent retention in rolled tungsten foils. *Journal of Nuclear Materials*, 455(1-3):248–252, 2014. doi:10.1016/j.jnucmat.2014.06.005.

[28] G.-N. Luo, W. M. Shu, and M. Nishi. Incident energy dependence of blistering at tungsten irradiated by low energy high flux deuterium plasma beams. *Journal of Nuclear Materials*, 347(1-2):111–117, 2005. doi:10.1016/j.jnucmat.2005.07.014.

[29] A. Manhard, K. Schmid, M. Balden, and W. Jacob. Influence of the microstructure on the deuterium retention in tungsten. *Journal of Nuclear Materials*, 415(1):S632–S635, 2011. doi:10.1016/j.jnucmat.2010.10.045.

[30] H. Nakamura, T. Hayashi, M. Nishi, M. Arita, and K. Okuno. Implantation driven permeation behavior of deuterium through pure tungsten. *Fusion Engineering and Design*, 55(4):513–520, 2001. doi:10.1016/s0920-3796(01)00380-5.

[31] O. V. Ogorodnikova, T. Schwarz-Selinger, K. Sugiyama, T. Dürbeck, and W. Jacob. Deuterium retention in different tungsten grades. *Physica Scripta*, T138:014053, 2009. doi:10.1088/0031-8949/2009/t138/014053.

[32] J. P. Roszell, J. W. Davis, and A. A. Haasz. Temperature dependence of deuterium retention mechanisms in tungsten. *Journal of Nuclear Materials*, 429(1-3):48–54, 2012. doi:10.1016/j.jnucmat.2012.05.018.

[33] C. N. Taylor, M. Shimada, and B. J. Merrill. Deuterium retention and blistering in tungsten foils. *Nuclear Materials and Energy*, 12:689–693, 2017. doi:10.1016/j.nme.2016.12.004.

[34] P. Wang, W. Jacob, L. Gao, S. Elgeti (Lindig), and M. Balden. Deuterium retention in tungsten films deposited by magnetron sputtering. *Physica Scripta*, T159:014046, 2014. doi:10.1088/0031-8949/2014/t159/014046.

[35] Y. Zayachuk, A. Manhard, M. H. J. 't Hoen, W. Jacob, P. A. Zeijlmans van Emmichoven, and G. van Oost. Depth profiling of the modification induced by high-flux deuterium plasma in tungsten and tungsten–tantalum alloys. *Nuclear Fusion*, 54 (12):123013, 2014. doi:10.1088/0029-5515/54/12/123013.

[36] R. Lässer. *Tritium and Helium-3 in Metals*, chapter Introduction, pages 1–6. Springer Berlin Heidelberg, 1989. ISBN 978-3-642-73510-3. doi:10.1007/978-3-642-73510-3_1.

[37] R. A. Causey. Hydrogen isotope retention and recycling in fusion reactor plasma-facing components. *Journal of Nuclear Materials*, 300(2-3):91–117, 2002. doi:10.1016/s0022-3115(01)00732-2.

[38] T. Tanabe. Review of hydrogen retention in tungsten. *Physica Scripta*, T159: 014044, 2014. doi:10.1088/0031-8949/2014/t159/014044.

[39] K. Schmid, J. Bauer, T. Schwarz-Selinger, S. Markelj, U. v. Toussaint, A. Manhard, and W. Jacob. Recent progress in the understanding of H transport and trapping in W. *Physica Scripta*, T170:014037, 2017. doi:10.1088/1402-4896/aa8de0.

[40] R. Frauenfelder. Solution and diffusion of hydrogen in tungsten. *Journal of Vacuum Science and Technology*, 6(3):388–397, 1969. doi:10.1116/1.1492699.

[41] K. Schmid, V. Rieger, and A. Manhard. Comparison of hydrogen retention in W and W/Ta alloys. *Journal of Nuclear Materials*, 426(1-3):247–253, 2012. doi:10.1016/j.jnucmat.2012.04.003.

[42] A. Manhard, M. Balden, and U. von Toussaint. Blister formation on rough and technical tungsten surfaces exposed to deuterium plasma. *Nuclear Fusion*, 57(12): 126012, 2017. doi:10.1088/1741-4326/aa82c8.

[43] V. Kh. Alimov, J. Roth, and M. Mayer. Depth distribution of deuterium in single- and polycrystalline tungsten up to depths of several micrometers. *Journal of Nuclear Materials*, 337-339:619–623, 2005. doi:10.1016/j.jnucmat.2004.10.082.

[44] V. Kh. Alimov, W. M. Shu, J. Roth, K. Sugiyama, S. Lindig, M. Balden, K. Isobe, and T. Yamanishi. Surface morphology and deuterium retention in tungsten exposed to low-energy, high flux pure and helium-seeded deuterium plasmas. *Physica Scripta*, T138:014048, 2009. doi:10.1088/0031-8949/2009/t138/014048.

[45] S. Lindig, M. Balden, V. Kh. Alimov, T. Yamanishi, W. M. Shu, and J. Roth. Sub-surface morphology changes due to deuterium bombardment of tungsten. *Physica Scripta*, T138:014040, 2009. doi:10.1088/0031-8949/2009/t138/014040.

[46] S. Kapser, A. Manhard, and U. von Toussaint. Measuring deuterium permeation through tungsten near room temperature under plasma loading using a getter layer and ion-beam based detection. *Nuclear Materials and Energy*, 12:703–708, 2017. doi:10.1016/j.nme.2016.11.019.

[47] S. Kapser, M. Balden, T. Fiorini da Silva, S. Elgeti, A. Manhard, K. Schmid, T. Schwarz-Selinger, and U. von Toussaint. Influence of sub-surface damage evolution on low-energy-plasma-driven deuterium permeation through tungsten. *Nuclear Fusion*, 58:056027, 2018. doi:10.1088/1741-4326/aab571.

[48] W. Assmus and S. Brühne. Rudiments of crystallography. In W. Martienssen and H. Warlimont, editors, *Springer Handbook of Condensed Matter and Materials Data*, pages 27–41. Springer Berlin Heidelberg, 2005. ISBN 978-3-540-30437-1. doi:10.1007/3-540-30437-1_3.

[49] H. Ibach and H. Lüth. *Solid-State Physics*, chapter Structure of Solid Matter, pages 21–49. Springer Berlin Heidelberg, 2009. ISBN 978-3-540-93804-0. doi:10.1007/978-3-540-93804-0_2.

[50] W. Massa. *Crystal Structure Determination*, chapter Crystal Lattices, pages 3–11. Springer Berlin Heidelberg, 2004. ISBN 978-3-662-06431-3. doi:10.1007/978-3-662-06431-3_2.

[51] E. Lassner and W.-D. Schubert. *Tungsten*, chapter The Element Tungsten, pages 1–59. Springer US, 1999. ISBN 978-1-4615-4907-9. doi:10.1007/978-1-4615-4907-9_1.

[52] A. H. M. Krom and A. Bakker. Hydrogen trapping models in steel. *Metallurgical and Materials Transactions B*, 31(6):1475–1482, 2000. doi:10.1007/s11663-000-0032-0.

[53] J. D. Verhoeven. *Fundamentals of Physical Metallurgy*, chapter Description of Crystals, pages 5–31. John Wiley and Sons, Inc., 1975. ISBN 0-471-90616-6.

[54] W. Borchardt-Ott. *Crystallography*, chapter Crystal Defects, pages 293–300. Springer Berlin Heidelberg, 2011. ISBN 978-3-642-16452-1. doi:10.1007/978-3-642-16452-1_14.

[55] J. Pelleg. *Mechanical Properties of Materials*, chapter Introduction to Dislocations, pages 85–146. Springer Netherlands, 2012. ISBN 978-94-007-4342-7. doi:10.1007/978-94-007-4342-7_2.

[56] E. J. Mittemeijer. *Fundamentals of Materials Science*, chapter Recovery, Recrystallization and Grain Growth, pages 463–496. Springer Berlin Heidelberg, 2010. ISBN 978-3-642-10500-5. doi:10.1007/978-3-642-10500-5_10.

[57] A. Manhard. *Deuterium Inventory in Tungsten After Plasma Exposure: A Microstructural Survey*. doctoral thesis, Universität Augsburg, 2013. URL `https://nbn-resolving.org/urn:nbn:de:bvb:384-opus4-19817`.

[58] J. F. Ziegler, J. P. Biersack, and U. Littmark. *The Stopping and Range of Ions in Solids*, chapter Nuclear Stopping Cross-Sections, pages 14–65. Pergamon Press, 1985. ISBN 0-08-021603-X.

[59] B. Schmidt and K. Wetzig. *Ion Beams in Materials Processing and Analysis*, chapter Ion–Solid Interactions, pages 7–31. Springer Vienna, 2012. ISBN 978-3-211-99356-9. doi:10.1007/978-3-211-99356-9_2.

[60] K. Gärtner. Ion-solid interaction. In W. Wesch and E. Wendler, editors, *Ion Beam Modification of Solids*, pages 3–62. Springer International Publishing, 2016. ISBN 978-3-319-33561-2. doi:10.1007/978-3-319-33561-2_1.

[61] H. R. Verma. *Atomic and Nuclear Analytical Methods*, chapter Nuclear Reaction Analysis and Particle-Induced Gamma-Ray Emission, pages 269–293. Springer Berlin Heidelberg, 2007. ISBN 978-3-540-30279-7. doi:10.1007/978-3-540-30279-7_7.

[62] W. Eckstein. *Computer Simulation of Ion-Solid Interactions*, chapter The Binary Collision Model, pages 4–32. Springer Berlin Heidelberg, 1991. ISBN 978-3-642-73513-4. doi:10.1007/978-3-642-73513-4_2.

[63] J. F. Ziegler, J. P. Biersack, and U. Littmark. *The Stopping and Range of Ions in Solids*, chapter Electronic Stopping Cross-Sections, pages 66–108. Pergamon Press, 1985. ISBN 0-08-021603-X.

[64] O. S. Oen and M. T. Robinson. Computer studies of the reflection of light ions from solids. *Nuclear Instruments and Methods*, 132:647–653, 1976. doi:10.1016/0029-554x(76)90806-5.

[65] J. Lindhard and M. Scharff. Energy dissipation by ions in the kev region. *Physical Review*, 124(1):128–130, 1961. doi:10.1103/physrev.124.128.

[66] W. Eckstein. *Computer Simulation of Ion-Solid Interactions*, chapter Inelastic Energy Loss, pages 63–72. Springer Berlin Heidelberg, 1991. ISBN 978-3-642-73513-4. doi:10.1007/978-3-642-73513-4_5.

[67] W. J. Weber and E. Wendler. Modelling effects of radiation damage. In W. Wesch and E. Wendler, editors, *Ion Beam Modification of Solids*, pages 105–136. Springer International Publishing, 2016. ISBN 978-3-319-33561-2. doi:10.1007/978-3-319-33561-2_3.

[68] W. Eckstein. *Computer Simulation of Ion-Solid Interactions*, chapter Classical Dynamics Model, pages 33–39. Springer Berlin Heidelberg, 1991. ISBN 978-3-642-73513-4. doi:10.1007/978-3-642-73513-4_3.

[69] W. Eckstein. *Computer Simulation of Ion-Solid Interactions*, chapter Programs Based on the Classical Dynamics Model, pages 108–110. Springer Berlin Heidelberg, 1991. ISBN 978-3-642-73513-4. doi:10.1007/978-3-642-73513-4_8.

[70] W. Eckstein. *Computer Simulation of Ion-Solid Interactions*, chapter Thermal Vibrations and Specific Energies, pages 73–82. Springer Berlin Heidelberg, 1991. ISBN 978-3-642-73513-4. doi:10.1007/978-3-642-73513-4_6.

[71] W. D. Wilson, L. G. Haggmark, and J. P. Biersack. Calculations of nuclear stopping, ranges, and straggling in the low-energy region. *Physical Review B*, 15(5):2458–2468, 1977. doi:10.1103/physrevb.15.2458.

[72] G. Molière. Theorie der Streuung schneller geladener Teilchen I. *Zeitschrift für Naturforschung*, 2a:133–145, 1947. doi:10.1515/zna-1947-0302. URL `https://www.degruyter.com/view/j/zna.1947.2.issue-3/zna-1947-0302/zna-1947-0302.xml`.

[73] S. T. Nakagawa and Y. Yamamura. Interatomic potential in solids and its applications to range calculations. *Radiation Effects*, 105(3-4):239–256, 1988. doi:10.1080/00337578808229950.

[74] W. Eckstein. *Computer Simulation of Ion-Solid Interactions*, chapter Interaction Potentials, pages 40–62. Springer Berlin Heidelberg, 1991. ISBN 978-3-642-73513-4. doi:10.1007/978-3-642-73513-4_4.

[75] A. Mutzke, R. Schneider, W. Eckstein, and R. Dohmen. SDTrimSP Version 5.00. IPP Report 12/8, Max-Planck-Institut für Plasmaphysik, Garching, Germany, 2011. URL `http://hdl.handle.net/11858/00-001M-0000-0026-EAF9-A`.

[76] Y. Fukai. *The Metal-Hydrogen System: Basic Bulk Properties*, chapter Phase Diagrams and Statistical Thermodynamics of Binary M-H Systems, pages 9–53. Springer Berlin Heidelberg, 2005. ISBN 978-3-540-28883-1. doi:10.1007/3-540-28883-X_2.

[77] M. P. Puls. *The Effect of Hydrogen and Hydrides on the Integrity of Zirconium Alloy Components*, chapter Solubility of Hydrogen, pages 109–152. Springer London, 2012. ISBN 978-1-4471-4195-2. doi:10.1007/978-1-4471-4195-2_4.

[78] R. G. Mortimer. *Physical Chemistry*, chapter Multicomponent Systems, pages 203–260. The Benjamin/Cummings Publishing Comapny, Inc., 1993. ISBN 0-8053-4560-4.

[79] P. W. Atkins. *Physical Chemistry*, chapter The nature of matter: orientation and background, pages 1–15. Oxford University Press, 3rd edition, 1986. ISBN 0-19-855196-7.

[80] M. Shimada, G. Cao, Y. Hatano, T. Oda, Y. Oya, M. Hara, and P. Calderoni. The deuterium depth profile in neutron-irradiated tungsten exposed to plasma. *Physica Scripta*, T145:014051, 2011. doi:10.1088/0031-8949/2011/t145/014051.

[81] A. Sieverts. Über Lösungen von Gasen in Metallen. *Zeitschrift für Elektrochemie und angewandte physikalische Chemie*, 16(17):707–713, 1910. doi:10.1002/bbpc.19100161706. URL `http://onlinelibrary.wiley.com/doi/10.1002/bbpc.19100161706/abstract`.

[82] P. L. Andrew and A. A. Haasz. Models for hydrogen permeation in metals. *Journal of Applied Physics*, 72(7):2749–2757, 1992. doi:10.1063/1.351526.

[83] Y. Fukai. *The Metal-Hydrogen System: Basic Bulk Properties*, chapter Diffusion, pages 303–400. Springer Berlin Heidelberg, 2005. ISBN 978-3-540-28883-1. doi:10.1007/3-540-28883-X_6.

[84] K. Heinola and T. Ahlgren. Diffusion of hydrogen in bcc tungsten studied with first principle calculations. *Journal of Applied Physics*, 107(11):113531, 2010. doi:10.1063/1.3386515.

[85] B. S. Bokstein, M. I. Mendelev, and D. J. Srolovitz. *Thermodynamics and Kinetics in Materials Science: A Short Course*, chapter Diffusion, pages 165–188. Oxford University Press, 2005. ISBN 0-19-852803-5.

[86] S. A. Steward. Review of hydrogen isotope permeability through materials. August 1983. doi:10.2172/5277693. Technical Report, Lawrence Livermore National Laboratory, Livermore, USA.

[87] H. Wipf. Diffusion of hydrogen in metals. In H. Wipf, editor, *Topics in Applied Physics - Hydrogen in Metals III: Properties and Applications*, pages 51–91. Springer Berlin Heidelberg, 1997. ISBN 978-3-540-69988-0. doi:10.1007/bfb0103401.

[88] W. M. Franklin. Classical and quantum theory of diffusion in solids. In *Diffusion in Solids*. Academic Press, 1975. ISBN 0-12-522660-8.

[89] B. L. Doyle. A simple theory for maximum H inventory and release: A new transport parameter. *Journal of Nuclear Materials*, 111-112:628–635, 1982. doi:10.1016/0022-3115(82)90277-x.

[90] O. K. Brice and B. L. Doyle. Steady state hydrogen transport in solids exposed to fusion reactor plasmas. *Journal of Nuclear Materials*, 120(2-3):230–244, 1984. doi:10.1016/0022-3115(84)90061-8.

[91] W. M. Shu, K. Okuno, and Y. Hayashi. General model for ion-driven permeation at steady state: new transport parameters. *The Journal of Physical Chemistry*, 97 (17):4497–4499, 1993. doi:10.1021/j100119a040.

[92] T. Tanabe, Y. Furuyama, and S. Imoto. Hydrogen ion driven permeation through metals. *Journal of Nuclear Materials*, 145-147:305–308, 1987. doi:10.1016/0022-3115(87)90349-7.

[93] Ch. A. Wert. Trapping of hydrogen in metals. In G. Alefeld and J. Völkl, editors, *Topics in Applied Physics - Hydrogen in Metals II: Application-Oriented Properties*, pages 305–330. Springer Berlin Heidelberg, 1978. ISBN 978-3-540-35801-5. doi:10.1007/3-540-08883-0_24.

[94] K. Schmid. Diffusion-trapping modelling of hydrogen recycling in tungsten under ELM-like heat loads. *Physica Scripta*, T167:014025, 2016. doi:10.1088/0031-8949/t167/1/014025.

[95] S. T. Picraux and F. L. Vook. Deuterium lattice location in Cr and W. *Physical Review Letters*, 33(20):1216–1220, 1974. doi:10.1103/physrevlett.33.1216.

[96] A. Založnik, S. Markelj, T. Schwarz-Selinger, and K. Schmid. Deuterium atom loading of self-damaged tungsten at different sample temperatures. *Journal of Nuclear Materials*, 496:1–8, 2017. doi:10.1016/j.jnucmat.2017.09.003.

[97] A. Mézin, J. Lepage, and P. B. Abel. An analytical solution for non-steady-state diffusion through thin films. *Thin Solid Films*, 272(1):124–131, 1996. doi:10.1016/0040-6090(95)06969-0.

[98] J. B. Condon and T. Schober. Hydrogen bubbles in metals. *Journal of Nuclear Materials*, 207:1–24, 1993. doi:10.1016/0022-3115(93)90244-s.

[99] D. Kato, H. Iwakiri, and K. Morishita. Formation of vacancy clusters in tungsten crystals under hydrogen-rich condition. *Journal of Nuclear Materials*, 417(1-3): 1115–1118, 2011. doi:10.1016/j.jnucmat.2010.12.211.

[100] D. F. Johnson and E. A. Carter. Hydrogen in tungsten: Absorption, diffusion, vacancy trapping, and decohesion. *Journal of Materials Research*, 25(02):315–327, 2010. doi:10.1557/jmr.2010.0036.

[101] S. C. Middleburgh, R. E. Voskoboinikov, M. C. Guenette, and D. P. Riley. Hydrogen induced vacancy formation in tungsten. *Journal of Nuclear Materials*, 448(1-3):270–275, 2014. doi:10.1016/j.jnucmat.2014.02.014.

[102] V. Kh. Alimov, W. M. Shu, J. Roth, S. Lindig, M. Balden, K. Isobe, and T. Yamanishi. Temperature dependence of surface topography and deuterium retention in tungsten exposed to low-energy, high-flux D plasma. *Journal of Nuclear Materials*, 417(1-3):572–575, 2011. doi:10.1016/j.jnucmat.2011.01.088.

[103] H. Y. Xu, W. Liu, G. N. Luo, Y. Yuan, Y. Z. Jia, B. Q. Fu, and G. De Temmerman. Blistering on tungsten surface exposed to high flux deuterium plasma. *Journal of Nuclear Materials*, 471:51–58, 2016. doi:10.1016/j.jnucmat.2015.12.025.

[104] S. Markelj, T. Schwarz-Selinger, A. Založnik, M. Kelemen, P. Vavpetič, P. Pelicon, E. Hodille, and C. Grisolia. Deuterium retention in tungsten simultaneously damaged by high energy W ions and loaded by D atoms. *Nuclear Materials and Energy*, 12:169–174, 2017. doi:10.1016/j.nme.2016.11.010.

[105] Y. K. Yap. Physical vapor deposition. In B. Bhushan, editor, *Encyclopedia of Nanotechnology*, pages 2069–2075. Springer Netherlands, Dordrecht, 2012. ISBN 978-90-481-9751-4. doi:10.1007/978-90-481-9751-4_362.

[106] M. Konuma. *Film Deposition by Plasma Techniques*, chapter Physical Vapor Deposition Under Plasma Conditions, pages 126–148. Springer Berlin Heidelberg, 1992. ISBN 978-3-642-84511-6. doi:10.1007/978-3-642-84511-6_6.

[107] R. T. Haasch. X-ray photoelectron spectroscopy (XPS) and Auger electron spectroscopy (AES). In M. Sardela, editor, *Practical Materials Characterization*, pages 93–132. Springer New York, 2014. ISBN 978-1-4614-9281-8. doi:10.1007/978-1-4614-9281-8_3.

[108] H. R. Verma. *Atomic and Nuclear Analytical Methods*, chapter X-Ray Photoelectron Spectroscopy, pages 213–241. Springer Berlin Heidelberg, 2007. ISBN 978-3-540-30279-7. doi:10.1007/978-3-540-30279-7_5.

[109] R. Reichelt. Scanning electron microscopy. In P. W. Hawkes and J. C. H. Spence, editors, *Science of Microscopy*, pages 133–272. Springer New York, 2007. ISBN 978-0-387-49762-4. doi:10.1007/978-0-387-49762-4_3.

[110] J. I. Goldstein, D. E. Newbury, P. Echlin, D. C. Joy, C. E. Lyman, E. Lifshin, L. Sawyer, and J. R. Michael. *Scanning Electron Microscopy and X-ray Microanalysis*. Springer US, 2003. ISBN 978-1-4615-0215-9. doi:10.1007/978-1-4615-0215-9.

[111] T. E. Everhart and R. F. M. Thornley. Wide-band detector for micro-microampere low-energy electron currents. *Journal of Scientific Instruments*, 37(7):246–248, 1960. doi:10.1088/0950-7671/37/7/307.

[112] F. A. Stevie, L. A. Giannuzzi, and B. I. Prenitzer. The focused ion beam instrument. In *Introduction to Focused Ion Beams*, pages 1–12. Springer US, 2005. ISBN 978-0-387-23313-0. doi:10.1007/0-387-23313-x_1.

[113] J. Orloff, M. Utlaut, and L. Swanson. *High Resolution Focused Ion Beams: FIB and its Applications*, chapter Practical Focused Ion Beam Optics and Systems, pages 147–203. Springer US, 2003. ISBN 978-1-4615-0765-9. doi:10.1007/978-1-4615-0765-9_6.

[114] J. Orloff, M. Utlaut, and L. Swanson. *High Resolution Focused Ion Beams: FIB and its Applications*, chapter Applications of Focused Ion Beams, pages 205–290. Springer US, 2003. ISBN 978-1-4615-0765-9. doi:10.1007/978-1-4615-0765-9_7.

[115] M. W. Phaneuf. FIB for materials science applications - a review. In L. A. Giannuzzi and F. A. Stevie, editors, *Introduction to Focused Ion Beams*, pages 143–172. Springer US, 2005. ISBN 978-0-387-23313-0. doi:10.1007/0-387-23313-x_8.

[116] F. A. Stevie, D. P. Griffis, and P. E. Russell. Focused ion beam gases for deposition and enhanced etch. In L. A. Giannuzzi and F. A. Stevie, editors, *Introduction to Focused Ion Beams*, pages 53–72. Springer US, 2005. ISBN 978-0-387-23313-0. doi:10.1007/0-387-23313-x_3.

[117] A. Manhard, T. Schwarz-Selinger, and W. Jacob. Quantification of the deuterium ion fluxes from a plasma source. *Plasma Sources Science and Technology*, 20(1): 015010, 2011. doi:10.1088/0963-0252/20/1/015010.

[118] R. Wilhelm. ECR plasma sources. In C. M. Ferreira and M. Moisan, editors, *Microwave Discharges: Fundamentals and Applications*, pages 161–179. Springer US, 1993. ISBN 978-1-4899-1130-8. doi:10.1007/978-1-4899-1130-8_11.

[119] M. Schmidt and H. Conrads. Plasma sources. In R. Hippler, H. Kersten, M. Schmidt, and K.H. Schoenbach, editors, *Low Temperature Plasmas. Fundamentals, Technologies, and Techniques*. Wiley-VCH Verlag GmbH & Co. KGaA, 2nd edition, 2008. ISBN 978-3-527-40673-9.

[120] L. Gao, W. Jacob, T. Schwarz-Selinger, and A. Manhard. Deuterium implantation into tungsten nitride: Negligible diffusion at 300K. *Journal of Nuclear Materials*, 451(1-3):352–355, 2014. doi:10.1016/j.jnucmat.2014.04.029.

[121] M. Mayer. SIMNRA user's guide. IPP Report 9/113, Max-Planck-Institut für Plasmaphysik, Garching, Germany, 1997. URL `http://hdl.handle.net/11858/00-001M-0000-0027-6157-F`.

[122] M. Mayer. Improved physics in SIMNRA 7. *Nuclear Instruments and Methods in Physics Research Section B: Beam Interactions with Materials and Atoms*, 332: 176–180, 2014. doi:10.1016/j.nimb.2014.02.056.

[123] H. R. Verma. *Atomic and Nuclear Analytical Methods*, chapter Rutherford Backscattering Spectroscopy, pages 91–141. Springer Berlin Heidelberg, 2007. ISBN 978-3-540-30279-7. doi:10.1007/978-3-540-30279-7_2.

[124] B. Schmidt and K. Wetzig. *Ion Beams in Materials Processing and Analysis*, chapter Materials Analysis by Ion Beams, pages 301–376. Springer Vienna, 2012. ISBN 978-3-211-99356-9. doi:10.1007/978-3-211-99356-9_6.

[125] T. F. Silva, C. L. Rodrigues, M. Mayer, M. V. Moro, G. F. Trindade, F. R. Aguirre, N. Added, M. A. Rizzutto, and M. H. Tabacniks. MultiSIMNRA: A computational tool for self-consistent ion beam analysis using SIMNRA. *Nuclear Instruments and Methods in Physics Research Section B: Beam Interactions with Materials and Atoms*, 371:86–89, 2016. doi:10.1016/j.nimb.2015.10.038.

[126] M. Mayer. personal communication.

[127] M. Mayer, E. Gauthier, K. Sugiyama, and U. von Toussaint. Quantitative depth profiling of deuterium up to very large depths. *Nuclear Instruments and Methods in Physics Research Section B: Beam Interactions with Materials and Atoms*, 267 (3):506–512, 2009. doi:10.1016/j.nimb.2008.11.033.

[128] B. Wielunska, M. Mayer, T. Schwarz-Selinger, U. von Toussaint, and J. Bauer. Cross section data for the D(^{3}He,p)^{4}He nuclear reaction from 0.25 to 6 MeV. *Nuclear Instruments and Methods in Physics Research Section B: Beam Interactions with Materials and Atoms*, 371:41–45, 2016. doi:10.1016/j.nimb.2015.09.049.

[129] T. Schwarz-Selinger, A. von Keudell, and W. Jacob. Plasma chemical vapor deposition of hydrocarbon films: The influence of hydrocarbon source gas on the film properties. *Journal of Applied Physics*, 86(7):3988–3996, 1999. doi:10.1063/1.371318.

[130] H.-M. Kuan, T. W. Bonner, and J. R. Risser. An investigation of the C^{12} + He^3 reactions at bombarding energies between 1.8 and 5.4 MeV. *Nuclear Physics*, 51: 481–517, 1964. doi:10.1016/0029-5582(64)90289-5.

[131] M. Mayer, K. Arstila, and U. von Toussaint. Skewness of energy-loss straggling and multiple-scattering energy distributions. *Nuclear Instruments and Methods in Physics Research Section B: Beam Interactions with Materials and Atoms*, 268(11-12):1744–1748, 2010. doi:10.1016/j.nimb.2010.02.057.

[132] W. Hösler and R. Darji. On the nonlinearity of silicon detectors and the energy calibration in RBS. *Nuclear Instruments and Methods in Physics Research Section B: Beam Interactions with Materials and Atoms*, 85(1-4):602–606, 1994. doi:10.1016/0168-583x(94)95890-4.

[133] K. Schmid and U. von Toussaint. Statistically sound evaluation of trace element depth profiles by ion beam analysis. *Nuclear Instruments and Methods in Physics Research Section B: Beam Interactions with Materials and Atoms*, 281:64–71, 2012. doi:10.1016/j.nimb.2012.03.024.

[134] V. Rakić and L. Damjanović. Temperature-programmed desorption (TPD) methods. In A. Auroux, editor, *Calorimetry and Thermal Methods in Catalysis*, pages 131–174. Springer Berlin Heidelberg, 2013. ISBN 978-3-642-11954-5. doi:10.1007/978-3-642-11954-5_4.

[135] A. Turnbull, R. B. Hutchings, and D. H. Ferriss. Modelling of thermal desorption of hydrogen from metals. *Materials Science and Engineering: A*, 238(2):317–328, 1997. doi:10.1016/s0921-5093(97)00426-7.

[136] A. M. de Jong and J. W. Niemantsverdriet. Thermal desorption analysis: Comparative test of ten commonly applied procedures. *Surface Science*, 233(3):355–365, 1990. doi:10.1016/0039-6028(90)90649-s.

[137] J. Kołaczkiewicz and E. Bauer. Thermal desorption spectroscopy of Ni, Cu, Ag and Au from W(110). *Surface Science*, 175(3):508–519, 1986. doi:10.1016/0039-6028(86)90009-9.

[138] E. Salançon, T. Dürbeck, T. Schwarz-Selinger, F. Genoese, and W. Jacob. Redeposition of amorphous hydrogenated carbon films during thermal decomposition. *Journal of Nuclear Materials*, 376(2):160–168, 2008. doi:10.1016/j.jnucmat.2008.02.070.

[139] P. Wang, W. Jacob, L. Gao, T. Dürbeck, and T. Schwarz-Selinger. Comparing deuterium retention in tungsten films measured by temperature programmed desorption and nuclear reaction analysis. *Nuclear Instruments and Methods in Physics Research Section B: Beam Interactions with Materials and Atoms*, 300:54–61, 2013. doi:10.1016/j.nimb.2013.01.057.

[140] John Skilling. Calibration and interpolation. *AIP Conference Proceedings*, 872(1): 321–330, 2006. doi:10.1063/1.2423290.

[141] HIDEN ANALYTICAL LTD. *Relative Sensitivity.* HIDEN ANALYTICAL LTD, 420 Europa Boulevard, Warrington, WA5 7UN, England. URL `https://www.hidenanalytical.de/wp-content/uploads/pdf/RS_Measurement_of_Gases_-_Hiden_Analytical_App_Note_282.pdf`. Gas Analysis Application Note 282, (accessed April 13, 2017).

[142] R. Frauenfelder. Permeation of hydrogen through tungsten and molybdenum. *The Journal of Chemical Physics*, 48(9):3955–3965, 1968. doi:10.1063/1.1669720.

[143] G. Benamati, E. Serra, and C. H. Wu. Hydrogen and deuterium transport and inventory parameters through W and W-alloys for fusion reactor applications. *Journal of Nuclear Materials*, 283-287:1033–1037, 2000. doi:10.1016/s0022-3115(00)00202-6.

[144] A. P. Zakharov, V. M. Sharapov, and E. I. Evko. Hydrogen permeability of polycrystalline and monocrystalline molybdenum and tungsten. *Soviet Materials Science*, 9 (2):149–153, 1975. doi:10.1007/bf00715727. Translated from Fiziko-Khimicheskaya Mekhanika Materialov, Vol. 9, No. 2, pp. 29-33, March-April, 1973.

[145] T. Ikeda, T. Otsuka, and T. Tanabe. Hydrogen permeation in metals near room temperature by a tritium tracer technique. *Journal of Nuclear Materials*, 417(1-3): 568–571, 2011. doi:10.1016/j.jnucmat.2010.12.116.

[146] S. Markelj, A. Založnik, T. Schwarz-Selinger, O. V. Ogorodnikova, P. Vavpetič, P. Pelicon, and I. Čadež. In situ NRA study of hydrogen isotope exchange in self-ion damaged tungsten exposed to neutral atoms. *Journal of Nuclear Materials*, 469: 133–144, 2016. doi:10.1016/j.jnucmat.2015.11.039.

[147] O. V. Ogorodnikova, S. Markelj, V. S. Efimov, and Yu. M. Gasparyan. Deuterium removal from radiation damage in tungsten by isotopic exchange with hydrogen atomic beam. *Journal of Physics: Conference Series*, 748:012007, 2016. doi:10.1088/1742-6596/748/1/012007.

[148] J. Bauer. *Hydrogen Isotope Exchange in Tungsten at Low Temperatures*. doctoral thesis, Technische Universität München, 2018. URL `http://nbn-resolving.de/urn/resolver.pl?urn:nbn:de:bvb:91-diss-20180118-1399472-1-5`.

[149] A. Manhard, S. Kapser, and L. Gao. Electrochemical study of hydrogen permeation through tungsten near room temperature. *Journal of Nuclear Materials*, 463:1057–1061, 2015. doi:10.1016/j.jnucmat.2014.10.018.

[150] H. T. Lee, H. Tanaka, Y. Ohtsuka, and Y. Ueda. Ion-driven permeation of deuterium through tungsten under simultaneous helium and deuterium irradiation. *Journal of Nuclear Materials*, 415(1):S696–S700, 2011. doi:10.1016/j.jnucmat.2010.12.023.

[151] Y. Ueda, H. T. Lee, H. Y. Peng, and Y. Ohtsuka. Deuterium permeation in tungsten by mixed ion irradiation. *Fusion Engineering and Design*, 87(7-8):1356–1362, 2012. doi:10.1016/j.fusengdes.2012.03.006.

[152] R. A. Anderl, D. F. Holland, G. R. Longhurst, R. J. Pawelko, C. L. Trybus, and C. H. Sellers. Deuterium transport and trapping in polycrystalline tungsten. *Fusion Technology*, 21(2P2):745–752, 1992. doi:10.13182/fst92-a29837.

[153] W. Möller, B. M. U. Scherzer, and R. Behrisch. The application of ion beam methods to diffusion and permeation measurements. *Nuclear Instruments and Methods*, 168 (1-3):289–294, 1980. doi:10.1016/0029-554x(80)91267-7.

[154] P. Børgesen, B. M. U. Scherzer, and W. Möller. Permeation of implanted deuterium through Ni near room temperature. *Journal of Applied Physics*, 57(8):2733–2738, 1985. doi:10.1063/1.335415.

[155] D. Levchuk, S. Levchuk, H. Maier, H. Bolt, and A. Suzuki. Erbium oxide as a new promising tritium permeation barrier. *Journal of Nuclear Materials*, 367-370: 1033–1037, 2007. doi:10.1016/j.jnucmat.2007.03.183.

[156] B. Predel. Er-W (Erbium-Tungsten). In O. Madelung, editor, *Dy-Er – Fr-Mo (part of Landolt-Börnstein - Group IV Physical Chemistry - Volume 5E)*. Springer-Verlag Berlin Heidelberg, 1995. doi:10.1007/10474837_1239.

[157] B. Predel. Cu-W (Copper-Tungsten). In O. Madelung, editor, *Cr-Cs – Cu-Zr (part of Landolt-Börnstein - Group IV Physical Chemistry - Volume 5D)*. Springer-Verlag Berlin Heidelberg, 1994. doi:10.1007/10086090_1131.

[158] B. Predel. W-Zr (Tungsten-Zirconium). In O. Madelung, editor, *Pu-Re – Zn-Zr (part of Landolt-Börnstein - Group IV Physical Chemistry - Volume 5J)*. Springer-Verlag Berlin Heidelberg, 1998. doi:10.1007/10551312_2877.

[159] P. Franke and D. Neuschütz. W-Zr (Tungsten - Zirconium). In P. Franke and D. Neuschütz, editors, *Binary Systems. Part 5: Binary Systems Supplement 1 (part of Landolt-Börnstein - Group IV Physical Chemistry - Volume 19B5)*. Springer-Verlag Berlin Heidelberg, 2007. doi:10.1007/978-3-540-45280-5_106.

[160] J. L. Murray. The Ti-W (Titanium-Tungsten) system. *Bulletin of Alloy Phase Diagrams*, 2(2):192–196, 1981. doi:10.1007/BF02881477.

[161] B. Predel. Ti-W (Titanium-Tungsten). In O. Madelung, editor, *Pu-Re – Zn-Zr (part of Landolt-Börnstein - Group IV Physical Chemistry - Volume 5J)*. Springer-Verlag Berlin Heidelberg, 1998. doi:10.1007/10551312_2843.

[162] R. L. Beck and W. M. Mueller. Zirconium hydrides and hafnium hydrides. In W. M. Mueller, J. P. Blackledge, and G. G. Libowitz, editors, *Metal Hydrides*. Academic Press, New York, 1968.

[163] W. M. Mueller. Titanium hydrides. In W. M. Mueller, J. P. Blackledge, and G. G. Libowitz, editors, *Metal Hydrides*. Academic Press, New York, 1968.

[164] W. M. Mueller. The rare-earth hydrides. In W. M. Mueller, J. P. Blackledge, and G. G. Libowitz, editors, *Metal Hydrides*. Academic Press, New York, 1968.

[165] J. P. Blackledge. An introduction to the nature and technology of hydrides. In W. M. Mueller, J. P. Blackledge, and G. G. Libowitz, editors, *Metal Hydrides*. Academic Press, New York, 1968.

[166] S. Yamanaka, T. Tanaka, and M. Miyake. Effect of oxygen on hydrogen solubility in zirconium. *Journal of Nuclear Materials*, 167:231–237, 1989. doi:10.1016/0022-3115(89)90446-7.

[167] S. Yamanaka, Y. Sato, T. Tanaka, and M. Miyake. *Fusion Technology*, 2:1249, 1988.

[168] S. Yamanaka, H. Ogawa, and M. Miyake. Effect of interstitial oxygen on hydrogen solubility in titanium, zirconium and hafnium. *Journal of the Less Common Metals*, 172-174:85–94, 1991. doi:10.1016/0022-5088(91)90436-8.

[169] E. A. Gulbransen and K. F. Andrew. Diffusion of hydrogen and deuterium in high purity zirconium. *Journal of The Electrochemical Society*, 101(11):560, 1954. doi:10.1149/1.2781154.

[170] R. J. Wasilewski and G. L. Kehl. Diffusion of hydrogen in titanium. *Metallurgia*, 50:225–230, 1954.

[171] H. J. Christ, M. Decker, and S. Zeitler. Hydrogen diffusion coefficients in the titanium alloys IMI 834, Ti 10-2-3, Ti 21 S, and alloy C. *Metallurgical and Materials Transactions A*, 31(6):1507–1517, 2000. doi:10.1007/s11661-000-0161-8.

[172] S. Nagata, A. Inouye, S. Yamamoto, B. Tsuchiya, K. Takano, K. Toh, and T. Shikama. Hydrogen incorporation and gasochromic coloration of tungsten oxide films. *Journal of Alloys and Compounds*, 446-447:558–561, 2007. doi:10.1016/j.jallcom.2007.01.039.

[173] H. F. Winters and E. Kay. Gas incorporation into sputtered films. *Journal of Applied Physics*, 38(10):3928–3934, 1967. doi:10.1063/1.1709043.

[174] P. Børgesen, B. M. U. Scherzer, and W. Möller. A sensitive method for measuring surface recombination of hydrogen isotopes implanted into metals. *Nuclear Instruments and Methods in Physics Research Section B: Beam Interactions with Materials and Atoms*, 9(1):33–40, 1985. doi:10.1016/0168-583x(85)90774-8.

[175] W. A. Lanford, H. P. Trautvetter, J. F. Ziegler, and J. Keller. New precision technique for measuring the concentration versus depth of hydrogen in solids. *Applied Physics Letters*, 28(9):566–568, 1976. doi:10.1063/1.88826.

[176] M. Balden, S. Lindig, A. Manhard, and J.-H. You. D_2 gas-filled blisters on deuterium-bombarded tungsten. *Journal of Nuclear Materials*, 414(1):69–72, 2011. doi:10.1016/j.jnucmat.2011.04.031.

[177] W. M. Shu, E. Wakai, and T. Yamanishi. Blister bursting and deuterium bursting release from tungsten exposed to high fluences of high flux and low energy deuterium plasma. *Nuclear Fusion*, 47(3):201–209, 2007. doi:10.1088/0029-5515/47/3/006.

[178] W. M. Shu, A. Kawasuso, Y. Miwa, E. Wakai, G.-N. Luo, and T. Yamanishi. Microstructure dependence of deuterium retention and blistering in the near-surface region of tungsten exposed to high flux deuterium plasmas of 38 eV at 315 K. *Physica Scripta*, T128:96–99, 2007. doi:10.1088/0031-8949/2007/t128/019.

[179] K. Schmid, U. von Toussaint, and T. Schwarz-Selinger. Transport of hydrogen in metals with occupancy dependent trap energies. *Journal of Applied Physics*, 116 (13):134901, 2014. doi:10.1063/1.4896580.

[180] K. Heinola, T. Ahlgren, K. Nordlund, and J. Keinonen. Hydrogen interaction with point defects in tungsten. *Physical Review B*, 82(9), 2010. doi:10.1103/physrevb.82.094102.

[181] T. J. Finlay, J. W. Davis, T. Schwarz-Selinger, and A. A. Haasz. The effect of high energy ion beam analysis on D trapping in W. *Physica Scripta*, T170:014057, 2017. doi:10.1088/1402-4896/aa9139.

[182] A. Manhard, U. v. Toussaint, T. Dürbeck, K. Schmid, and W. Jacob. Statistical analysis of blister bursts during temperature-programmed desorption of deuterium-implanted polycrystalline tungsten. *Physica Scripta*, T145:014038, 2011. doi:10.1088/0031-8949/2011/t145/014038.

[183] O. V. Ogorodnikova, T. Schwarz-Selinger, K. Sugiyama, and V. Kh. Alimov. Deuterium retention in tungsten exposed to low-energy pure and helium-seeded deuterium plasmas. *Journal of Applied Physics*, 109(1):013309, 2011. doi:10.1063/1.3505754.

[184] S. Ryabtsev, Yu. Gasparyan, M. Zibrov, A. Shubina, and A. Pisarev. Deuterium thermal desorption from vacancy clusters in tungsten. *Nuclear Instruments and Methods in Physics Research Section B: Beam Interactions with Materials and Atoms*, 382:101–104, 2016. doi:10.1016/j.nimb.2016.04.038.

[185] I. Takagi, K. Kodama, K. Shin, K. Higashi, H. Zushi, T. Mizuuchi, T. Senjyu, M. Wakatani, and T. Obiki. Deuterium plasma-driven permeation in heliotron E during discharge cleaning and in a small plasma device. *Fusion Technology*, 25(2): 137–146, 1994. doi:10.13182/fst94-a30263.

[186] R. D. Kolasinski, D. F. Cowgill, and R. A. Causey. A continuum-scale model of hydrogen precipitate growth in tungsten plasma-facing materials. *Journal of Nuclear Materials*, 415(1):S676–S679, 2011. doi:10.1016/j.jnucmat.2010.10.077.

[187] R. D. Kolasinski, M. Shimada, Y. Oya, D. A. Buchenauer, T. Chikada, D. F. Cowgill, D. C. Donovan, R. W. Friddle, K. Michibayashi, and M. Sato. A multi-technique analysis of deuterium trapping and near-surface precipitate growth in plasma-exposed tungsten. *Journal of Applied Physics*, 118(7):073301, 2015. doi:10.1063/1.4928184.

[188] W. Eckstein. Sputtering, reflection and range values for plasma edge codes. IPP Report 9/117, Max-Planck-Institut für Plasmaphysik, Garching, Germany, 1998. URL `http://hdl.handle.net/11858/00-001M-0000-0027-6091-4`.

[189] A. F. Holleman and N. Wiberg. *Lehrbuch der anorganischen Chemie*, chapter XXVII Die Chromgruppe, pages 1438–1478. de Gruyter, 101. edition, 1995. ISBN 3-11-012641-9.

[190] O. V. Ogorodnikova, S. Markelj, and U. von Toussaint. Interaction of atomic and low-energy deuterium with tungsten pre-irradiated with self-ions. *Journal of Applied Physics*, 119(5):054901, 2016. doi:10.1063/1.4940678.

[191] A. Lasa, C. Björkas, K. Vörtler, and K. Nordlund. MD simulations of low energy deuterium irradiation on W, WC and surfaces. *Journal of Nuclear Materials*, 429 (1-3):284–292, 2012. doi:10.1016/j.jnucmat.2012.06.012.

[192] Z. Yang, Q. Xu, R. Hong, Q. Li, and G.-N. Luo. Molecular dynamics simulation of low-energy atomic hydrogen on tungsten surface. *Fusion Engineering and Design*, 85(7-9):1517–1520, 2010. doi:10.1016/j.fusengdes.2010.04.018.

[193] D. Hanggi and P. W. Carr. Errors in exponentially modified gaussian equations in the literature. *Analytical Chemistry*, 57(12):2394–2395, 1985. doi:10.1021/ac00289a051.

[194] P. W. Tamm and L. D. Schmidt. Binding states of hydrogen on tungsten. *The Journal of Chemical Physics*, 54(11):4775–4787, 1971. doi:10.1063/1.1674753.

[195] W. R. Wampler and R. P. Doerner. The influence of displacement damage on deuterium retention in tungsten exposed to plasma. *Nuclear Fusion*, 49(11):115023, 2009. doi:10.1088/0029-5515/49/11/115023.

[196] U. von Toussaint, S. Gori, A. Manhard, T. Höschen, and C. Höschen. Molecular dynamics study of grain boundary diffusion of hydrogen in tungsten. *Physica Scripta*, T145:014036, 2011. doi:10.1088/0031-8949/2011/t145/014036.

[197] P. Pelicon, P. Vavpetič, N. Grlj, I. Čadež, S. Markelj, S. Brezinsek, A. Kreter, T. Dittmar, E. Tsitrone, B. Pégourié, P. Languille, M. Rubel, and T. Schwarz-Selinger. Fuel retention study in fusion reactor walls by micro-NRA deuterium mapping. *Nuclear Instruments and Methods in Physics Research Section B: Beam Interactions with Materials and Atoms*, 269(20):2317–2321, 2011. doi:10.1016/j.nimb.2011.02.049.

[198] A. Manhard, U. von Toussaint, M. Balden, S. Elgeti, T. Schwarz-Selinger, L. Gao, S. Kapser, T. Płociński, J. Grzonka, M. Gloc, and Ł. Ciupiński. Microstructure and defect analysis in the vicinity of blisters in polycrystalline tungsten. *Nuclear Materials and Energy*, 12:714–719, 2017. doi:10.1016/j.nme.2016.10.014.

[199] G. Federici, J. N. Brooks, D. P. Coster, G. Janeschitz, A. Kukuskhin, A. Loarte, H. D. Pacher, J. Stober, and C. H. Wu. Assessment of erosion and tritium codeposition in ITER-FEAT. *Journal of Nuclear Materials*, 290-293:260–265, 2001. doi:10.1016/s0022-3115(00)00627-9.

[200] R. Behrisch, G. Federici, A. Kukushkin, and D. Reiter. Material erosion at the vessel walls of future fusion devices. *Journal of Nuclear Materials*, 313-316:388–392, 2003. doi:10.1016/s0022-3115(02)01580-5.

[201] L. K. Keys and J. Moteff. Neutron irradiation and defect recovery of tungsten. *Journal of Nuclear Materials*, 34(3):260–280, 1970. doi:10.1016/0022-3115(70)90193-5.

[202] M. W. Thompson. The damage and recovery of neutron irradiated tungsten. *Philosophical Magazine*, 5(51):278–296, 1960. doi:10.1080/14786436008235842.

Acknowledgments

I would like to thank Prof. Dr. Rudolf Neu for the supervision of this thesis as well as for his support and advice in its preparation. Furthermore, I am grateful to the Max-Planck-Institut für Plasmaphysik (IPP) for funding and enabling my research and in particular to Prof. Dr. Ulrich Stroth for the possibility to join the E2M division. In particular, I would also like to thank Dr. Wolfgang Jacob, the leader of the PMI group at the IPP, for his continuous support, his advice and valuable scientific discussions. The PMI group offered me an inspiring and pleasant working environment.

Especially, I would like to thank Dr. Armin Manhard for his support throughout the preparation of this thesis, including many fruitful scientific discussions as well as practical advice on various experimental techniques. I am also especially grateful to Dr. Udo von Toussaint for his advice and continuous support, many valuable scientific discussions and the patience he showed in answering my questions.

Moreover, I would like to thank Dr. Klaus Schmid for his support, in particular with NRADC, SDTrimSP and TESSIM. I also appreciate the support from Dr. Thomas Schwarz-Selinger and in particular his valuable advice on the ion-beam analysis and the TDS measurements. To Dr. Matej Mayer and Dr. Tiago Fiorini da Silva, I am thankful for valuable scientific discussions, support and advice especially regarding SIMNRA and MultiSIMNRA, respectively.

Also, I would like to thank Dr. Martin Balden, Stefan Elgeti and Gabriele Matern for their support, in particular with the microstructural analysis with SEM and FIB. I would additionally like to express my gratitude to Thomas Dürbeck and Till Höschen for their support especially with the TDS measurements and the XPS measurements, respectively. To Freimut Koch I am grateful for his advice, in particular regarding sputter deposition.

For operating the tandem accelerator, which I used in the ion-beam analysis measurements, I thank Joachim Dorner, Michael Fußeder and Stefan Schindler. I am also grateful to Dr. Andreas Mutzke for advice on SDTrimSP and to Dr. Cleber Rodrigues from the Instituto de Física da Universidade São Paulo (Brazil) for modifications implemented in MultiSIMNRA. I thank Rupert Brüderl and the Technical Support Team for realizing my construction projects and for manifold technical support.

Furthermore, I would like to thank Dr. Sabina Markelj, Dr. Primož Vavpetič and Mitja Kelemen from the Jožev Stefan Institute in Ljubljana (Slovenia) for performing microbeam NRA measurements on one of the samples presented in this thesis.

I would also like to thank all my other colleagues at the IPP, especially Dr. Liang Gao, Dr. Johannes Bauer, Dr. Hans Maier, Dr. Gerd Meisl, Rodrigo Arredondo Parra, Karsten Schlüter, Georg Holzner, Barbara Wielunska, Vassily Burwitz, Mikhail Zibrov, Alexander von Müller, Hanns Gietl as well as the other participants of the scientific round table and of the PWI meeting. I am grateful to them for valuable scientific discussions as well as valuable advice, support and feedback. Moreover, I thank the co-authors of my

publications for their contributions to these publications and the unknown referees of my publications for their valuable comments.

I am also grateful to the International Helmholtz Graduate School for Plasma Physics (HEPP), which is associated with the TUM Graduate School, for support and especially the possibility to participate in a number of scientific conferences.

Finally, I would like to thank my family. In this context, I especially thank my parents and my sister for their steady support. And last but not least, I am exceptionally grateful to my fiancée Ingrid for her patience, advice and outstanding continuous support over the past years.